Magnetic configurations, reconnection and energy transfers in space plasmas

Sid Fadanelli

THESIS

submitted in partial fulfilment of the requirements for the degree of

Philosophiæ Doctor

jointly conferred by

Université Toulouse III - Paul Sabatier

Università di Pisa

---

presented by Sid FADANELLI

Magnetic configurations, reconnection and energy transfers in space plasmas

---

JURY

Mme Denise PERRONE	*Rapporteur*
M. Fouad SAHRAOUI	*Rapporteur*
Mme Maria Federica MARCUCCI	*Examinateur*
M. Vincent GENOT	*Examinateur*
M. Benoît LAVRAUD	*Directeur de thèse*
M. Francesco CALIFANO	*Co-directeur de thèse*

Discussion date	13.oct.2020
Doctoral School	SDU2E
Speciality	Astrophysics, Space Science, Planetology
Research Unit	IRAP

Mais ce jour-là, vers onze heures du matin, Nicholl ayant laissé échapper un verre de sa main, le verre, au lieu de tomber, resta suspendu dans l'air.
« Ah ! » s'écria Michel Ardan « voilà donc un peu de physique amusante ! »

J. G. V.

Acknowledgements

The lifespan of a Ph.D. student is not long, a little more than thousand days if one does the maths, a short time in which one is bound to experience an incredibly vivid craze of work and coffee, terrible and wonderful at the same time. Now that my work is done, now that the Ph.D. is discussed and the line has been drawn, now that the thesis can't get any better nor any worse, now it is the knowledge that I will gradually loose the feeling of these days what makes it so that I feel my very first duty to preserve and maintain at least their current impression, unaltered at best, and I think the most effective way is by remembering all those who in this time have shaped my life, and taking this occasion to thank them deeply for their support and presence.

In sharing blame and glory for this three-year craze of mine, the first ones I have to mention and thank are Benoît and Francesco, who not only gave me this one incredible opportunity but also allowed me a great liberty of action and so many possibilities, the like of which wasn't always the case for my colleagues. Wasn't it for your help and understanding, who knows what mess would have come out of all this. Another debt of gratitude is to the members of my examining commission, who found time and patience to read and comment this work in which I have invested so much, and which now means so much to me. Thanks are due also to the reviewers of my papers for every time they've been enthusiastic, unmerciful or even pretended to be deadly stupid because (especially in the two latter cases) they allowed me to have those second, third and fourth thoughts on them which made me really aware of a hundred little subtleties hidden in the physics.

If my coming to Toulouse proved to be a happy one, I know that it is especially due to the extraordinary people who "lived" in the desks closest to mine: Yoann and Issaad first, who were always able to light up my day, and Mika, Kevin, Athanasios and Nico, our truly solar guys. Then, Michael (dur-dur!) and Om, Mathieu and Léa, who I've always seen as my senior references. Can't forget to mention then the most wonderful battalion of "petits" stagiaires: Lydia, Vincent, Guillaume and Ilona, and the ones in PEPS that I most closely worked with: Aurelie, Christian, Manu and Alain (the only one who understood what I was whistling: honour to you!), and Alexis, who I truly enjoyed talking with. Also, the MMS community and ISSI 442 team deserve a special mention for the happiness I found in interacting with them (how cannot you love dr. Phan?), and the special Biarritz-organisation team of Quentin, Sergio and Naïs. On a weirder note at this point I need to quote Jérémy, who cannot be cathegorised properly, I feel, since we found each other in Toulouse first and then he anticipated me in Pisa, where I found he had merged within one of the most terrific research groups ever: Manuela, Giulia, Peppe, Job, Louis, Silvio and Roby who showed me how to survive an AGU meeting. And Fra, of course, who I must thank for our unforgettable "zingarata" between Rome, Genoa, Milan and Strasbourg. Not physically "in" the group but in my heart then remain Andrea dr. Macchi, Daniele Del Sarto, professors Pegoraro and Cornolti whom I tormented for answers, Pisco and Federico (who I must note here to keep track of our contract), Pier and obviously Paula, who will never cease to surprise me. Even further from my field, but possibly even closer, I cannot forget Sujay, Torito

and Tiziana, Gabi who showed me what it means to fight for a thesis, Jakob, Sacha, Lucy, Evgeny, Daria, Chen Lin, and Andrés of course, the big guy on whose success I surely bet. At parties, in Bordeaux, on the Pyreneés: wherever this group was, there I felt at my best. Similar familiarity I could feel only with my longer time friendships, in Trentino and in Pisa: Ferro, Prada, Shkelzen, Davide, Valentina and Capitani, monsieur Palazzo, dr. Testa, Antonino and dr. Votino (whether he likes this or not), prof. Gervasi, Desmond, and Ambra whose presence in Paris and Palermo made it possible many beer-drinking pit-stops in my wild triangulations across Europe as I moved between couches, hotels and homes. Speaking of homes, I cannot but remember and thank here my homies of Pisa, Manellone and Trillocco, who showed me how to BBQ on the balcony, Anaïs and Mathias who saved me from mononucleosis in full quarantine, and Arnaud, Valery and professor Delage, the "ingegnere" who taught me so much. My last thought goes then to my family, to those in Riva and those living in the mountains, to all those who always thought I was the "ok-with-school" kid and slowly forged this truth: maybe it was the inertia of this thought the ultimate reason for me to attempt the step of getting this degree. Had it not been for that, however, I wouldn't have known him who has brought me the first really great summer in these years - and I mean not only the one in Syracuse or Scopello with the boys - so cheers to you, Ale, and to us; to our trips and adventures, those in the past and those hopefully and happily to come.

So, here it is, this poor dissertation, this thesis of mine and of so many others. Here's the manuscript which has been my burden and pride, my life and shame, here's my last sin in attempting research. And while I know, I recognise that maybe it could have taken just a little bit more of care to make this thesis better, more precise or more detailed, yet in front of the gay progress of science I do also realise that others will certainly come to do this in my place, and surely better than I could have. Large margins, these are what science needs, blanks that someone at some time will coherently fill up, so that this ephemeral synthesis of partial knowledge can be eventually amended and corrected until not a thing in it remains the same anymore. As this work will get buried, hidden in the multitude of those similar to it, however, let me add here one hope and one wish only: even if these pages will not succeed in being of help before getting old, still may their readers get to love this piece of physics as deeply and truly as I have.

Summary (EN, FR, IT)

Throughout interplanetary space, plasma particles and magnetic fields play an endless game of re-shaping themselves and exchanging energy. A key process in this regard is magnetic reconnection. The complex dynamics resulting from this process is responsible for particle acceleration and entry into the Earth's magnetosphere, potentially dangerous for people and machinery, and is the basic subject of this thesis. In the first part of the work, I focus on the local shape of magnetic configurations. To this aim, I devise a technique to retrieve relevant local characteristics of magnetic configurations, which I apply to multi-spacecraft data, demonstrating its efficacy. In the second part of the thesis I discuss how energy is exchanged among its different forms in the neighbourhood of a reconnection site using a numerical simulation. I show in particular how different energy conversions are statistically related to one another and to local features of the system.

Dans l'espace interplanétaire, particules chargées et champs magnétiques sont en continu sujet à des remodelages et échanges d'énergie. Un processus clé dans ce contexte est la reconnexion magnétique. La dynamique complexe résultant de ce processus est responsable de l'accélération des particules et de leur entrée dans la magnétosphère terrestre, ce qui est potentiellement dangereux pour les personnes et la technologie, et constitue le sujet de cette thèse. Dans la première partie de mon travail, je me concentre sur la structure locale du champ magnétique. J'ai conçu une technique pour déterminer les caractéristiques locales de la configuration du champ magnétique, et je l'applique à des données multi-satellites, démontrant son efficacité. Dans la deuxième partie de la thèse, j'étudie comment l'énergie est échangée entre ses différentes formes, près d'un site de reconnexion magnétique avec une simulation numérique. Je montre en particulier comment les différentes conversions d'énergie sont statistiquement liées les unes aux autres et aux caractéristiques locales du système.

Nello spazio interplanetario, particelle cariche e campi magnetici sono continuamente soggetti a processi fisici responsabili di scambi di energia e che ne modellano le configurazioni. Un processo chiave in questo contesto è la riconnessione magnetica. La complessa dinamica che ne risulta, responsabile dell'accellerazione delle particelle e della loro entrata nella magnetosfera terrestre (il che è potenzialmente pericoloso per alcune tecnologie ed il personale che se ne occupa) costituisce il soggetto principale di questa tesi. Nella prima parte del lavoro, il focus è la struttura locale del campo magnetico. Si mette a punto una tecnica per determinare le caratteristiche locali della configurazione di campo magnetico e la si applica a dati raccolti da satellite, dimostrandone l'applicabilità e l'efficacia. Nella seconda parte del lavoro di tesi vengono studiati i trasferimenti di energia fra campo elettromagnetico e plasma in prossimità di un sito di riconnessione, con l'aiuto di una simulazione numerica. In particolare si dimostra come i diversi canali di trasferimento dell'energia sono legati statisticamente gli uni agli altri, e correlati alle caratteristiche locali del sistema.

Introduction (FR)

Au cours des cent dernières années, il est devenu de plus en plus clair que les espaces interstellaires et interplanétaires ne sont pas de simples « vides » dans lesquels les particules orbitent librement, mais plutôt qu'ils sont le lieu d'une dynamique complexe et variée de particules chargées et de champs électromagnétiques ou, en d'autres termes, ils sont typiquement peuplés d'un plasma ténu en perpétuelle évolution. La caractéristique principale de la dynamique des plasmas spatiaux est leur forte liaison avec le champ magnétique : d'un côté, le champ détermine comment les particules sont accélérées, chauffées ou refroidies tandis que d'un autre côté, c'est le champ magnétique qui est façonné par les courants induits par les particules.

Dans toute cette dynamique, le processus de reconnexion magnétique occupe une position centrale. En effet, alors que la reconnexion est déclenchée par une dynamique à petite échelle (celle des électrons), elle finit par affecter les plus grandes échelles du système. Sous l'effet de la reconnexion, au lieu d'évoluer « en douceur », les structures magnétiques s'ouvrent ou finissent par être sectionnées, libérant d'importantes quantités d'énergie dans le processus.

Les conséquences de la dynamique violente qui résulte de la reconnexion peuvent être observées dans une variété de phénomènes physiques. Par exemple, lors des éruptions solaires, c'est la reconnexion qui permet à une partie du plasma de la couche externe du Soleil d'échapper au confinement exercé par les champs magnétiques solaires, explosant dans l'espace. Les aurores sont également des conséquences de la reconnexion - dans ce cas, celle qui réorganise le champ magnétique de la queue de la magnétosphère terrestre, accélérant le plasma et le faisant précipiter aux hautes latitudes pour éclairer les nuits des régions polaires.

Cependant, en libérant du matériel solaire ou en éclairant le ciel polaire, la reconnexion peut également devenir une menace, en particulier pour les réseaux électriques au sol et les satellites et les hommes dans l'espace. Les satellites peuvent être endommagés partiellement ou de manière permanente par les radiations induites par les particules accélérées par la reconnexion. Pour cette raison, à une époque où l'on dépend de plus en plus de l'électronique et des satellites, il est fondamental de modéliser et prédire la dynamique du plasma proche de la Terre et donc, en particulier, de comprendre la reconnexion.

Cette thèse s'intéresse à la façon dont les champs magnétiques se forment lorsqu'ils interagissent avec les particules du plasma et comment l'énergie est échangée pendant cette interaction. Ces deux thèmes sont fondamentaux en physique des plasmas, en particulier en ce qui concerne le processus de reconnexion magnétique. D'un côté, en effet, c'est la forme locale du champ magnétique qui joue un rôle fondamental pour le déclenchement de la reconnexion et son evolution. D'un autre côté, la compréhension des transferts d'énergie induits par la reconnexion est la clé pour déterminer de quelle manière le système évolue après la reconnexion.

Afin d'étudier les configurations magnétiques, dans la première partie de ma thèse, j'introduis une procédure par laquelle on peut décrire la forme du champ magnétique local, et je l'applique aux données des satellites de la mission MMS de la NASA. De cette façon, j'ai pu obtenir la configuration locale du champ magnétique dans le plasma près de la Terre. Dans la deuxième partie de la thèse, j'exploite des simulations numériques pour étudier le transfert d'énergie au voisinage d'un site de reconnexion. En particulier, je détermine la corrélation statistique entre les termes décrivant différents types de transferts d'énergie, et je montre également comment

ces transferts sont corrélés avec l'échelle locale du système.

Conclusion (FR)

Dans cette thèse, je montre comment il est possible de mener une analyse approfondie des configurations magnétiques et des transferts d'énergie dans les plasmas spatiaux, proches de la Terre. Dans cette optique, j'ai mené deux projets principaux, ainsi que quelques autres en parallèle.

Concernant le premier sujet, je me suis concentré sur la forme locale du champ magnétique qui, dans un plasma magnétisé, entraîne l'évolution de grandes structures, régule la propagation des ondes et joue un rôle fondamental dans la détermination des instabilités qui peuvent être excitées dans un plasma. Afin de réaliser ça, j'ai dérivée une nouvelle méthode, que j'ai appelé « Magnetic Configuration Analysis » (MCA) et grâce à laquelle on peut caractériser la configuration locale du champ magnétique en termes de trois longueurs caractéristiques et trois directions caractéristiques. La particularité de la méthode MCA est que les trois longueurs caractéristiques ne sont déterminées que par la forme de la configuration et non par l'intensité du champ magnétique.

En appliquant MCA sur des données collectées par les satellites de la mission Magnetospheric Multiscale (MMS) de la NASA, j'ai étudié les configurations locales du champ magnétique dans la magnétosphère, la magnétogaine et le vent solaire proche de la Terre. En particulier, j'ai effectué deux études différentes, l'une centrée sur l'analyse des données à haute fréquence, l'autre consacrée aux tendances statistiques dans un ensemble de données plus large composé de mesures à plus basse fréquence. Mes résultats démontrent la capacité et soulignent l'utilité de la technique MCA pour l'analyse de données multi-satellites.

La deuxième partie de ma thèse porte sur le problème de la conversion d'énergie dans un plasma magnétisé sans collision. Contrairement à la plupart des travaux précédents, l'approche adoptée ici est basée sur l'évaluation des dérivées lagrangiennes des densités d'énergies en chaque point, afin de suivre leur évolution à l'intérieur du chaque élément fluide. Cette approche nous permet d'étudier les corrélations entre les différents canaux de conversion d'énergie et avec chaque autre quantité ou paramètre du plasma défini point par point.

L'analyse des échanges d'énergie s'est poursuivie en considérant un site de reconnexion dans une simulation numérique Vlasov-hybride. Les résultats montrent que les variations locales d'énergie cinétique sont généralement faibles, car elles nécessitent la rupture d'une condition de quasi-équilibre des forces. De plus, je démontre que la variation moyenne de l'énergie interne peut être attribuée à un comportement approximativement polytropique, mais dans ce cas les écarts deviennent important. Le caractère local de l'analyse réalisée a également permis de déterminer les dépendances des transferts de densité d'énergie à l'échelle locale du système. L'équilibre des forces a tendance à être valide statistiquement à toutes les échelles, conduisant ainsi à une conservation moyenne des densités d'énergie cinétique. Mais il existe, cependant, une tendance pour la densité d'énergie interne ionique à diminuer à grande échelle et augmenter à petite échelle. J'ai également mis en exergue une tendance des taux de conversion d'énergie à être plus élevés à mesure que la longueur caractéristique diminue.

Tout en travaillant sur les deux projets mentionnés précédemment, j'ai également contribué à

divers degrés dans un certain nombre d'autres travaux. Je les résume ici brièvement.

L'instabilité de Kelvin-Helmholtz qui se développe au niveau des flancs magnétosphériques peut être un acteur de premier plan dans la dynamique de la magnétopause, excitant un grand nombre de processus secondaires et contribuant potentiellement à la pénétration du vent solaire dans la magnétosphère. Dans un projet que j'ai dirigé, les instabilités de Kelvin-Helmholtz et la dynamique associée ont été examinées selon leur développement latitudinal, via une simulation réalisée avec un code bi-fluides (de que j'ai finalisé cette étude pendant les premiers mois de ma thèse , l'article résultant de ce travail est rapporté en annexe). La configuration initiale est façonnée de manière à reproduire le confinement latitudinal de la bande instable Kelvin-Helmholtz (les cisaillements de vitesse et de champ magnétique sont les plus intenses à proximité des régions équatoriales et deviennent moins instables lorsque l'on s'éloigne progressivement de celle-ci). Les simulations montrent lors du développement de l'instabilité de Kelvin-Helmholtz que les perturbations les plus excitées présentent un vecteur d'onde incliné par rapport au plan équatorial, et s'étendent de manière asymétrique loin de l'équateur. Le décalage latitudinal de les perturbations de Kelvin-Helmholtz démontre que ce n'est pas seulement le cisaillement magnétique initial qui détermine où le système développera des vortex, mais aussi l'advection différentielle des lignes de champ magnétique, qui doit être prise en compte.

La reconnexion magnétique a également été observée dans la simulation discutée, à différents endroits et sous diverses configurations (dans le vortex principal de Kelvin-Helmholtz mais également à l'intérieur de régions plus « secondaires »). Notablement, nous avons trouvé que la reconnexion induite par l'instabilité de Kelvin-Helmholtz s'étend de manière continue à travers une large gamme de latitudes. Par conséquent, par rapport à des résultats similaires connus, la reconnexion induite par les tourbillons principaux dans le cas présent doit être comprise comme un processus hybride qui combine les caractéristiques de deux cas bien connus, à savoir la reconnexion de type I et la reconnexion à moyenne-latitude. En effet, alors que dans les deux cas précités, la reconnexion est contrôlée soit par l'angle de cisaillement magnétique à travers la couche du courant, soit par la compression, dans la situation analysée les deux phénomènes sont en jeu simultanément et ils forment une sorte de continuum. De plus, dans le régime non linéaire de l'instabilité, le nombre de sites de reconnexion augmente en raison du développement d'instabilités secondaires. Cela permet également de créer des lignes doublement reconnectées, qui permettent le piégeage du vent solaire dans la magnétosphère. Cette considération suggère notamment que la dynamique liée à une perturbation Kelvin-Helmholtz à grande échelle peut conduire à un transport de matière très efficace entre le vent solaire et la magnétosphère.

Toujours en exploitant les codes développés à l'Université de Pise, j'ai entrepris le projet « Magnetospheric Multiscale Turbulence » (MMT), visant à générer des simulations de turbulence plasma directement comparables aux observations des satellites MMS. Ce projet est toujours en cours, comme aussi le développement de routines spécifiquement conçues pour analyser les simulations (projet « fibo »), avec le but de standardiser et d'organiser systématiquement plusieurs routines développées au cours de mes années de thèse.

Contents

Chapter 1

Introduction

1.1 Setting the scene: plasmas in the solar system

This section is meant as an overview on the topic of plasma dynamics in the solar system, accessible to pretty much everyone, at least in its general traits. After an introduction to plasmas in space (subsection 1.1.1) I provide a basic, qualitative description of the solar system as a plasma environment, organised in two steps. First, I revise briefly where we can recognise the main plasma sources and magnetised bodies, drawing a large-scale scenario of plasma motions within this panorama (subsection 1.1.2). Second, I recall some of the characteristic perturbations of this system (subsection 1.1.3). The section ends stressing the relevance of studying the so-called "space weather" science and applications, noting in which regards it is important to predict plasma dynamics in the solar system and plan strategies to face its consequences (subsection 1.1.4).

1.1.1 Astrophysical plasmas

What is a plasma? In physics, this term is used to indicate any system of multiple charges, neutral overall, in which the main driver of dynamics are collective electromagnetic interactions - i.e. where dynamics is dominated by long-range Lorentz forces (see Tonks (1967), Mott-Smith (1971) and Langmuir *et al.* (1928)). Such systems are observed whenever negatively charged electrons are prevented to bound stably with positively charged ions, which is generally the case when the system possesses high thermal energy or is kept under impinging radiation. Such situations are found in many contexts: in lightnings, in the core of flames, in some lamps and in most stars we can observe. Somewhat surprisingly, however, also the low-density medium that extends through the vast regions of interstellar and interplanetary space is composed of charged particles that fulfil all requirements to be plasma. In conclusion, therefore, throughout the vast majority of the universe we live in, there's plasma (see Fitzpatrick (2014)).

By definition, the main driver of plasma dynamics is the large-scale, many-body interaction sprouting from the electromagnetic field. In astrophysical context, however, not only particle-particle interactions (which from now on I shall call "collisions" for brevity) can generally be neglected, but also Coulombian effects tend to be secondary

at most lengths and timescales of interest (due to the overall neutrality). In most space plasma scenarios, therefore, the most important factor in determining particle dynamics is the magnetic field. This is especially the case in the interplanetary regions of our solar system, on which I will focus for the remainder of this first section of the introduction.

1.1.2 Plasma environments of the solar system

In our solar system, the main source of charged particles is the Sun, which produces the so-called "solar wind" by continuously pushing its outermost layer - the "corona" - into space. Ionisation of solar material, reached thanks to high temperatures, is well preserved as the plasma expands and its density falls, since electrons and ions interact too scarcely in couples for allowing an efficient recombination into neutral atoms (see Meyer-Vernet (2007) at page 327). Secondary sources of plasma in the interplanetary medium arise due to ultraviolet photons or energetic ions ionising neutral gas incoming from interstellar space or escaping from the atmospheres of planetary bodies, which come to be surrounded by the so-called "ionospheres" (see Meyer-Vernet (2007), section 6.5.3). One particularly visible example of the ionisation of escaping gas can be found close to comets: one of the two tails, the one pointing always in the anti-sunward direction, is created by this mechanism. Ionisation of planetary, interplanetary or interstellar gas, however, when compared with the expanding corona gives an effect so feeble that it can be neglected in drawing a large-scale picture of the plasma configuration in the solar system, except when considering its outer boundaries.

A number of bodies in the solar system sustain their own magnetic fields. So does the Sun, which generates the most powerful, but so also do Mercury, the Earth, Jupiter, Saturn and the icy planets (see Lang (2011), page 107). Planetary magnetic fields are in good approximation dipolar, change over secular times and their orientation is approximately fixed with respect to planetary rotation (thus defining magnetic poles). In contrast, the solar magnetic field exhibits complex shape and evolution. First of all, it does not appear generally as a dipole but rather in a strong multi-polar shape. Secondly, it varies sensibly over an eleven-year cycle, passing from a "more" dipolar state to a "less" dipolar one to return in the former with reversed polarity (see Lang (2013), section 9.1.2). Inside the complex "heliosphere" i.e. the region in which the solar magnetic field prevails, the sharp transition to zones dominated by planetary magnetism - the "magnetospheres" - are known as "magnetopauses". All the magnetic structures just presented are impacted upon by the streaming plasma, which induces currents causing them to stretch, bend, twirl and locally break down. This we will see in some detail in the next paragraphs.

What are the deformations that plasma induces on the solar magnetic field? In the region closest to the Sun, the expanding plasma deforms the arches of the multipolar solar field, with some of these assuming a rather ogee-like shape, thus generating the so-called "coronal streamers". Since this kind of deformation affects in particular the dipolar component of the Sun's field, the expanding solar wind induces a sharp

reversal of magnetic polarity approximately in correspondence of the dipole's equatorial plane and produces the so-called heliospheric current sheet (HCS). As the Sun's rotation axis and dipole moment are misaligned, the innermost portion of the HCS is subject to regular swinging and this results in a large-scale, wave-like bending of the electromagnetic structure when considered as a whole (much like the skirt of a rotating ballerina). Solar rotation stands also at the basis of another characteristic deformation of the Sun's magnetic field - the so-called "Parker spiral" - which is generated as solar wind experiences a progressive reduction of angular velocity while it expands outward from our star. At Earth's average orbital distance, therefore, the solar magnetic field generally lays over a plane with its normal on the ecliptic and about 45° away from the sunward/anti-sunward direction, changing its orientation in such plane so to follow the change in HCS orientation.

When the solar wind impacts onto some un-magnetised object, if such object is large enough, it creates a piled-up-plasma "sheath" region terminating upwind with a shock ("bow-shock") and downwind with a wake (i.e. a region depleted of plasma). The interplanetary magnetic field and its interaction with the body somehow influence the shapes of both these regions, but in good approximation one can model the bow-shock as a paraboloid (hence the name) and the wake as a cone. When the planet, satellite or asteroid possesses its own magnetic field, however, interaction becomes more complex since also the object's magnetosphere goes into the picture (see for instance Siscoe (2011)). On the upwind side, for instance, not only the bow shock develops, but also the so-called "Chapman-Ferraro" current system builds up at the magnetopause in response to the solar wind's ram pressure, bending the axis of the magnetospheric dipole so to turn sunward both its high-latitude "cusps" (see Fig. 1.1). On the downwind side, coupling of planetary and interplanetary magnetic fields results into another (Θ-shaped) current system, which stretches the magnetosphere into an elongated "magnetotail" pointing away from the Sun (again, see Fig. 1.1). In the Earth's case, for instance, a magnetosphere which is about ten Earth-radii wide in the sunward direction extends up to several hundreds Earth-radii in length with its anti-sunward magnetotail.

Due to strong coupling with the streaming solar wind, the interplanetary magnetic field and planetary ionospheres, magnetospheres generally exhibit a complex, dynamical behaviour (see Eastwood *et al.* (2015), Borovsky & Valdivia (2018)). For instance, as the interplanetary magnetic field is traversed by the solar wind, so inside each magnetosphere a characteristic plasma circulation is induced. A variety of processes, combined in different fashion, contribute to magnetospheric stirring. In the Earth's case, the dominant magnetospheric "engine" is given by the coupling processes at the magnetic boundary, where the interplanetary magnetic field streaming in the solar wind forces the outermost portion of the magnetospheric system into a dayside-nightside motion. Counter-streaming with respect to this motion, plasma in the central portion of the magnetotail tends to advect slowly toward the planet, and there it compensates for plasma advected tailward (the famous "Dungey convection" is part of such processes - see, again, Siscoe (2011)). Also, planetary rotation can be an important energy source for magnetospheric motions - this being the case especially for giant and icy planets (see Griton & Pantellini (2020) for instance). The buildup of a magnetospheric circu-

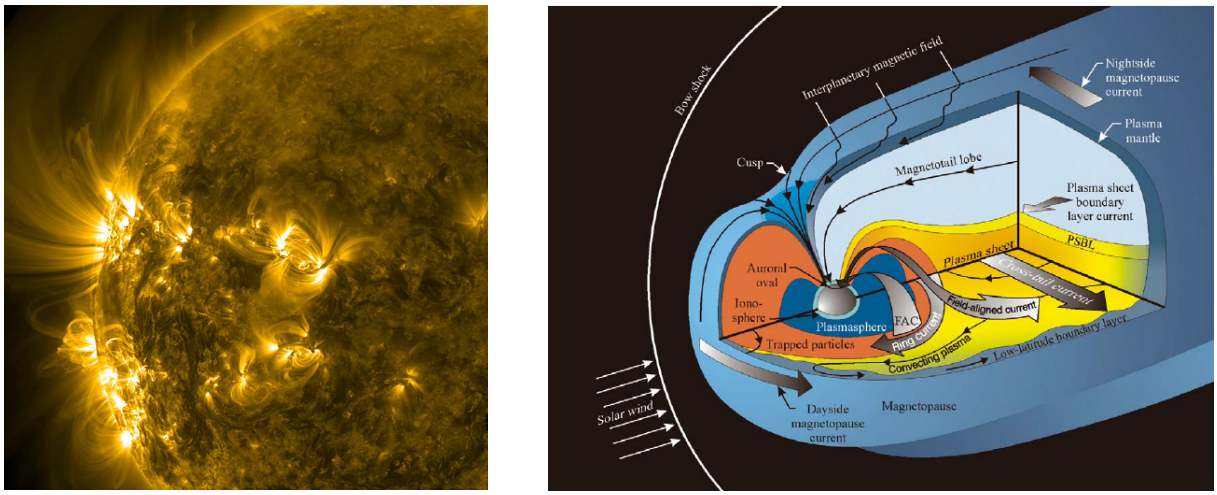

FIGURE 1.1: Left: a "photography" of our Sun's corona, taken in ultraviolet light (image by NASA Goddard Space Flight Center from Greenbelt, MD, USA - Sweeping Arches and Loops, Public Domain, https://commons.wikimedia.org/w/index.php?curid=51482839). Note that the luminous structures are indicative of the presence of extremely hot plasma, which emits light in the wavelength used to take this picture. As hot plasma streams along magnetic field lines, it is easy to recognise two main types: the arched, closed ones and the more "straight" ones which constitute an "open" way for the plasma to escape the Sun.
Right: schematic diagram of the sunward portion of Earth's magnetosphere (the long magnetotail expanding out from the right margin of the figure). The many labels highlight the complex system of currents arising from moving plasma which re-shapes the Earth's dipolar field into the complex elongated configuration of the magnetosphere. Note that the front magnetosphere is surrounded by a region called "magnetosheath" that extends up to a bow shock: in this volume the solar wind impacting the magnetosphere is compressed and slowed down, piling up as it slowly moves around the magnetopause (image from Birn *et al.* (2012)).

lation is generally accompanied by the development of more current systems (such as the "ring current" or various "field-aligned currents" reported in Fig. 1.1) which shape the internal structure of a magnetosphere and regulate its interaction with the planet (see for instance Tanaka *et al.* (2016)).

1.1.3 Major perturbations of plasma environments

To overview major plasma perturbations in the solar system, let me start from the so-called "magnetic clouds" i.e. fast bunches of plasma, magnetically structured, which propagate away from the Sun, shocking the plasma on which they impact. The origin of magnetic clouds resides in solar dynamics: as the coronal plasma moves, it "drags" the Sun's arched magnetic field lines whose footpoints are "anchored" and slowly advected in lower solar layers. Since footpoint motion cannot follow the pace imposed by coronal dynamics, some of the magnetic arches get stretched until the point of collapse, i.e. until a "solar flare" is produced. Solar flares are the main processes characterising the corona, and come in a wide range of dimensions, with the smallest and less energetic proportionally more frequent than large-scale highly-energetic events. Some solar flares in particular result into a "coronal mass ejection" (CME) i.e. the expulsion of a magnetic arch's central portion into the solar wind. As part of a magnetic arch exits from the corona, some of its energy gets released so to accelerate the rest of the

structure and the plasma it carries: this is how the corona produces a magnetic cloud (see Priest (2017)).

In planetary magnetospheres, major perturbations are geomagnetic "storms" and "substorms", which lead to heating of magnetospheric plasma and cause the precipitation of energetic particles onto the planets. On one hand, storms are generated whenever a magnetosphere gets hit by a magnetic cloud, with the magnetic cloud's energy affecting all the delicate mechanism of plasma circulation and electric currents inside the magnetosphere. On the other hand, substorms happen in magnetospheres subject to a slowly changing or steady solar wind, their source of energy being the configuration of the magnetosphere itself (with solar wind conditions - at best - acting as a trigger). A substorm happens whenever stretched magnetic lines, which store large amounts energy, get severed and re-arranged. This way, while a portion of the magnetosphere accelerates away from the planet, relaxation of the remaining portion leads to plasma heating and drives particles toward the inner magnetospheric regions (see Ebihara & Tanaka (2020)).

Alongside the large-scale dynamics just described, a plethora of small-scale perturbations develops nearly ubiquitously in both the solar wind and planetary magnetospheres. In the solar wind, for instance, it is common to form shock structures, which sometimes interact with each other in complex ways. Impact of these and other perturbations on a planetary magnetosheath causes "hot flow anomalies" or "high-speed jets" which can eventually also impact on the magnetopause (see Hietala & Plaschke (2013), Eastwood *et al.* (2015), Hietala *et al.* (2018)). Also the magnetopause by itself might be unstable to perturbations: a classic example is the flow-induced Kelvin-Helmholtz instability which develops predominantly on the magnetospheric flanks (see Farrugia *et al.* (1998), Faganello & Califano (2017)). At magnetopauses, perturbations can cause the so-called "flux transfer events" (see section 10.3 of Priest & Forbes (2000)) by which portions of plasma are exchanged between a magnetosphere and the interplanetary medium around it, and that have been for long an object of intense study, as they allow the denser solar wind to penetrate into the environment magnetically connected to the planet.

As energy accumulated in the magnetospheres gets released in storms or substorms, particles can get accelerated along field lines and induce the most famous consequence of magnetospheric disturbances: an aurora (see Fig. 1.2). Auroras are the result of beams of charged, high-energy particles which reach the upper atmosphere while streaming along field lines, and there they excite the atmospheric particles: as energised atoms relax, they emit photons at characteristic wavelengths and this way they produce the northern and southern lights. Since the basic ingredients for auroras are simply an atmosphere and a planetary magnetic field, auroral displays are found not only on Earth but also on Jupiter, Saturn, Uranus and Neptune, each aurora being characterised by peculiarities of the case (see Lang (2011) section 3.7). While it is clear that an intensification of auroral phenomena generally follows from major perturbations of a magnetosphere (such as storms and substorms), the exact sequence of processes by which magnetic perturbations excite the precipitation of high-energy particles is - as of today

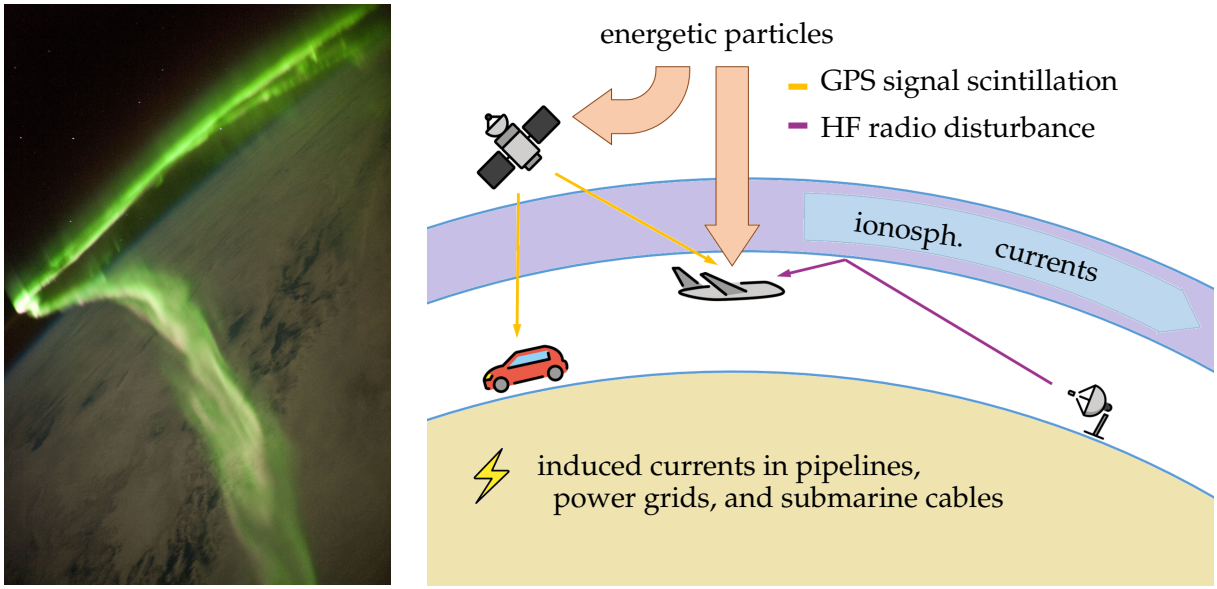

FIGURE 1.2: Left: an aurora, photographed from the International Space Station (image from ISS Expedition 23 crew - Mission: ISS023 Roll: E Frame: 58455 Mission ID on the Film or image: ISS023, Public Domain, https://commons.wikimedia.org/w/index.php?curid=10691965).
Right: info-graphic presenting hazards related to geomagnetic storms. Energetic particles and ionospheric currents resulting from high geomagnetic activity impact telecommunications, aerial transports, pipelines and power networks (own image, with emojis from https://openmoji.org/).

- still a matter of debate (see Birn *et al.* (2012)).

1.1.4 Space weather: monitoring and predicting plasma dynamics

Between the 1st and the 2nd of September 1859, most of the night sky was turned into day-like brightness as green and red auroras blazed in the northern and southern hemisphere, stretching nearly from pole to pole. Auroral sightings were reported by the press in Colombia and Cuba, in Australia, Canada and throughout the United States: the phenomenon was so strong that "ordinary print could be read by its light" while voltage differences induced by auroral currents through the telegraphic network succeeded into injuring the operators and destroying some equipment (see Inc. (1859)). In spite of the incomplete understanding of electromagnetism and solar system physics at the time, the chain of events leading to such an extraordinary phenomenon was grasped by amateur astronomer R. Carrington, who supposed such auroras being a consequence of a bright solar flare he had witnessed just the day before (see Carrington (1859)).

As of today, in spite of the scarce amount of data we dispose, the 1859 geomagnetic storm ("Carrington event") continues being actively studied (see for instance Tsurutani (2003) and references therein), and so it happens for many others which we have traced in historical records (see Stephenson *et al.* (2019)). Far from being academic curiosity, each testimony of strong geomagnetic activity nowadays provides us with a reference for situations that at some point in the future we will surely need to face; situations which could lead to widespread damage for satellites, wireless communica-

tions, power grids and electronic devices (see Fig. 1.2); situations which risk to cost us billions of dollars in the case we should not act in advance to properly protect our technology (see Eastwood *et al.* (2017)). So, while it is now understood that 1859-like phenomena are statistically rare, a consistent effort has been put in their study and, more in general, in the whole of the "space weather" science and applications, i.e. the monitoring, analysing and predicting possibly harmful effects of plasma dynamics in the solar system.

Understanding the state of interplanetary plasma, however, is far from being a simple task. The interaction of magnetised plasma structures tend to display a highly nonlinear nature, which together with complex geometries, poses a formidable challenge to analytical modelling, numerical simulations or experimental probing. One more difficulty, however, needs to be mentioned, that is the incomplete knowledge of some of the plasma processes at play in these systems. Space weather forecasting, therefore, is at the moment a research field as challenging as necessary to our society (see Lyon (2000), Song *et al.* (2001)).

1.2 Presentation of this thesis

After having set the scene, with this section I introduce the reader to this thesis. The thesis' main topics, i.e. magnetic field configurations and local energy transfers in a plasma, are presented first (subsection 1.2.1), followed by an overview of the general structure of the work (subsection 1.2.2).

1.2.1 Magnetic configurations, reconnections, energy transfers: why?

The two main topics of this thesis are the way magnetic fields get shaped as they interact with plasma particles and how energy gets exchanged during this interaction. Both these themes are fundamental in plasma physics, but especially so when one is dealing with the process of magnetic reconnection, as I will shortly discuss hereafter.

The process of magnetic reconnection is one of the most studied in plasma physics. Magnetic reconnection happens whenever the behaviour of a magnetised plasma cannot be characterised as a smooth motion of magnetic-line-tied ions and electrons, i.e. whenever the "magnetic connectivity" of plasma elements locally breaks down. Now, even if this break is localised and happens only at small scales, it can easily have consequences up to the largest scales of the system: wherever reconnection acts, magnetic structures that would evolve "smoothly" get opened instead, exchanging plasma with their surroundings or getting severed into pieces. Solar flares, coronal mass ejections, the cutting of magnetotails: all these are possible just thanks to reconnection. Magnetic reconnection, therefore, is to be recognised at the root of geomagnetic storms and substorms alike - but more in general, such a number of processes has been understood to induce reconnection or to interact with it that we could simply state that it is patho-

logical to any dynamics of magnetised plasma (see Vaivads *et al.* (2009), Zweibel & Yamada (2016), Hesse & Cassak (2020)).

Given the ubiquity of magnetic reconnection, in plasma physics it is of fundamental importance being capable of understanding the exact conditions in which it develops and its consequences on the particles. Hence, it is in especially in this regard that retrieving the local shape of the magnetic field and understanding how energy gets redistributed in a plasma becomes paramount. This consideration is at the basis of the whole thesis, which discusses magnetic configurations, reconnections and energy transfers in space plasmas.

1.2.2 Aim and structure of the work

This thesis consists basically of two projects: in the first, I investigate the local shape of the magnetic field, and in the second I analyse energy conversions around a reconnection site. To this aim, first I develop specific techniques for each of these analyses and then I put them at work on different datasets, namely, satellite data and the results from numerical simulations.

Adopting different datasets, it must be noted, allows one to tackle the open problems of plasma physics in a more effective way. On one side, indeed, analytical studies cannot provide but very limited models concerning only a simplified treatment of very restricted areas. On another side, numerical experiments are forcedly limited in either their accuracy or in the size of the considered box because of the enormous extension of the overall system with respect to its smallest scale lengths - this basically calls for a trade-off between precision in detail and realistic boundary conditions. Finally, not even in-situ measurements are able to give us the "whole truth" on reconnection physics, due to the intrinsic limitations of harvested data: the probes' trajectories cutting one-dimensionally through the system, the data they collect cannot provide us with its three-dimensional time-evolving shape.

The large-scale structure of this thesis is as follows. After the general introduction of this chapter 1, in chapter 2 I shall summarise some elements of plasma physics, and in chapter 3 I will present the characteristics of spacecraft and numerical codes which provided the data for my analyses. The research projects conducted during the Ph.D. training are presented in chapters 4 and 5, the former focusing on magnetic configurations, the latter dealing with the energetics of magnetic reconnection. Finally, chapter 6 will draw the conclusions of this work, and sketch some of today's perspectives on further developments of the projects I worked on, and chapter 7 will provide additional material to expand the view on many of the topics presented.

In all this work, I will use Gaussian units for all formulas, while results from numerical experiments and spacecraft-collected data will be presented each in the most convenient way, as specified case by case. I hereby cut the chat, and leave the remainder of this work to the reader's guts and patience.

Chapter 2

Theoretical background

2.1 Plasma models

Here I overview some basic theory of plasma dynamics. This brief summary starts from kinetic and fluid equations to model the material (subsection 2.1.1), then discusses the apparatus to model the evolution of electromagnetic fields coupled to the plasma (subsection 2.1.2). Finally, I briefly present a noteworthy plasma model called "magnetohydrodynamics" (MHD), which has been used extensively in space physics to derive the large-scale characteristics of plasma environments (subsection 2.1.3). Such presentation is particularly important in view of the magnetised plasma dynamics discussed in the rest of this chapter.

2.1.1 Representing the plasma: kinetic and fluid descriptions

By definition, a plasma is in first instance a physical system constituted by a very large number of charges, but neutral overall, with the foremost role in its dynamics played by long-range, multi-particle electromagnetic interactions (see subsection 1.1.1). Of course, since trying to solve such a system in a deterministic fashion is ultimately a "hopeless task" (quoting Fitzpatrick (2014)), for practical applications we must content ourselves with investigating plasma physics within a statistical framework. In other words, for any particle with mass m and charge q we do not seek to know its position $\vec{r}$ and velocity $\vec{v}$ at a given time, but rather its probability to be found at some position within δ_r from $\vec{r}$ and within δ_v from $\vec{v}$ at each moment, this way defining the distribution function $\mathfrak{f}$ of the particle population over phase space. Now, from the definition of plasma follows that it is possible to regulate the scales δ_r and δ_v to be large enough so that the portion of phase space which they cover can be faithfully described in statistical fashion (i.e. the typical number of particles in it is required to be much larger than one), but at the same time this phase space zone is also smaller than the characteristic dimensions linked to multi-particle interactions. Since all dynamics presented from here onward will neglect all scales below δ_r and δ_v, from this point every physical quantity will be understood as the local average over this "phase space unit" (see Boyd & Sanderson (2003), section 7.1).

The evolution of $\mathfrak{f}$ can be determined from the electric and magnetic fields $\vec{E}$ and $\vec{B}$ and

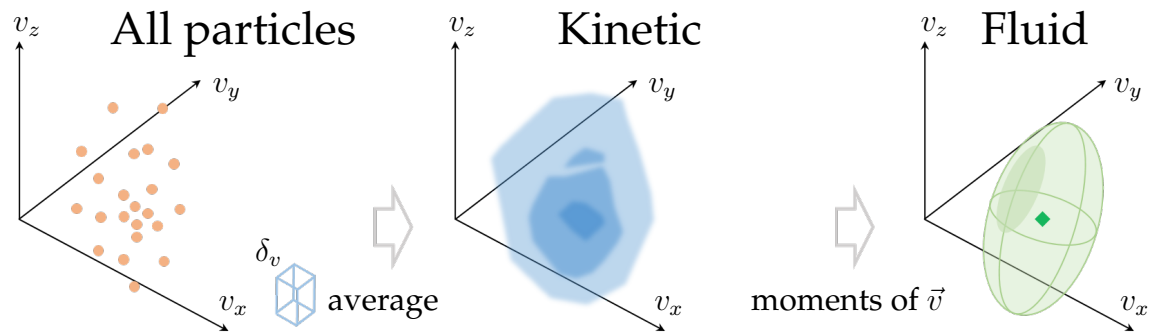

FIGURE 2.1: Schematic showing the way in which different plasma models deal with particle velocities in a small parcel of plasma, of characteristic dimension δ_r (own image).
Left: each orange dot is meant to indicate the $\vec{v}$ of some particle. In other words the kinematic state of the plasma parcel can be represented by a distribution composed by a sum of Dirac deltas, of which here is represented only the velocity-space projection.
Centre: averaging the phase space distribution over boxes of dimension δ_v it is possible to retrieve a continuous distribution $\mathfrak{f}$ which represents statistically the kinematic state of the system. The darker the colour in this schematic, the higher the probability density.
Right: an approximate version of the distribution function $\mathfrak{f}$ is all that remains in the fluid description of a plasma, where instead of the full $\mathfrak{f}$ only some of its low-order moments are retained. In other words, while one forgets the actual shape of $\mathfrak{f}$ in $\vec{v}$, still some characteristics of the distribution are known: this is represented here by a diamond encompassed in an ellipsoid with coloured surface. Now, n is proportional to the diamond's colour intensity, while the velocity $\vec{u}$ follows from the diamond's position. Pressure and heat flux are represented by the ellipsoid's shape and by its colouration, respectively.

a source $\dot{\mathfrak{f}}$. With ∂_t, $\vec{\nabla}$ and $\vec{\nabla}$ for partial differentiation over time, space and velocity:

$$\left[\partial_t + \vec{v}\cdot\vec{\nabla} + \frac{q}{m}\left[\vec{E} + \frac{\vec{v}\times\vec{B}}{c}\right]\cdot\vec{\nabla}\right]\mathfrak{f} = \dot{\mathfrak{f}} \tag{2.1}$$

known as the "kinetic equation" describes how $\mathfrak{f}$ evolves in time (for this denomination, see section 7.1 in Boyd & Sanderson (2003) and/or Fitzpatrick (2014), section 4.1). The source term generically includes the average of all phenomena with characteristic scale below the δ_r and δ_v limit, and will be called "collisions" from now on (see Boyd & Sanderson (2003), section 7.1). Now, from the definition of plasma it follows that the right-hand side "collisional" term must be negligible with respect to the terms on the left-hand side. In this work I will exploit brutally this fact, and therefore neglect completely collisional effects by setting the source term to zero. In this case, the kinetic equation becomes known as "Vlasov equation" (see Fitzpatrick (2014), section 4.1).

While the statistical approach just introduced allows for very precise description of any plasma, one can recognise that even a less-accurate description can be deemed sufficient in many situations of interest. The most common of methods to provide an useful approximate model of plasma is that of integrating the probability distribution over velocity coordinates so to pass into a fluid plasma framework. As sketched in Fig 2.1, the basic idea behind a fluid approach to plasma is that any $\mathfrak{f}$ can be approximated by its low-order moments, the approximation being more and more precise the more moments are considered. For this reason, the fluid description of a plasma is constructed on the following quantities, that combine into the various velocity moments

of the $m\mathfrak{f}$ distribution:

$$\begin{aligned} &\text{density: } n && && mn = \int m\mathfrak{f}\, d\vec{v} \\ &\quad\text{velocity: } \vec{u} && && mn\vec{u} = \int m\mathfrak{f}\, \vec{v}\, d\vec{v} \\ &\quad\quad\text{pressure: } \vec{\vec{P}} && \text{such that} && mn\vec{u}\vec{u} + \vec{\vec{P}} = \int m\mathfrak{f}\, \vec{v}\vec{v}\, d\vec{v} \\ &\quad\quad\quad\text{heat flux: } \vec{\vec{\vec{Q}}} && && mn\vec{\vec{\vec{u}}} + [\vec{u}\vec{\vec{P}}]^{+} + \vec{\vec{\vec{Q}}} = \int m\mathfrak{f}\, \vec{v}\vec{v}\vec{v}\, d\vec{v} \end{aligned} \tag{2.2}$$

where the superscript "+" is meant to indicate the sum over all positive permutations of the tensor indices. Integrating also the Vlasov equation on velocity coordinates provides us with a series of fluid evolution laws, each one specifying the time derivative of some moment of $m\mathfrak{f}$. For instance, one can obtain:

$$\partial_t[mn] + \vec{\nabla}\cdot[mn\vec{u}] = 0 \tag{2.3}$$

$$\partial_t[mn\vec{u}] + \vec{\nabla}\cdot[mn\vec{u}\vec{u} + \vec{\vec{P}}] = qn\left[\vec{E} + \vec{u}\times\vec{B}/c\right] \tag{2.4}$$

$$\partial_t[mn\vec{u}\vec{u} + \vec{\vec{P}}] + \vec{\nabla}\cdot[mn\vec{\vec{\vec{u}}} + [\vec{u}\vec{\vec{P}}]^{+} + \vec{\vec{\vec{Q}}}] = qn\left[\vec{u}\vec{E} + [mn\vec{u}\vec{u} + \vec{\vec{P}}]\times\vec{B}/mnc\right]^{+} \tag{2.5}$$

for the zeroth, first and second velocity moments (aside: Eq. 2.3 in particular is known as "continuity equation" as it expresses mathematically the requirement that the number of particles must be conserved in time, which is a constraint on the evolution of n). By combining such equations one easily retrieves also the laws which describe the evolution of each of the fluid variables, such as:

$$mn\left[\partial_t + \vec{u}\cdot\vec{\nabla}\right]\vec{u} = -\vec{\nabla}\cdot\vec{\vec{P}} + qn\left[\vec{E} + \vec{u}\times\vec{B}/c\right] \tag{2.6}$$

$$\left[\partial_t + \vec{u}\cdot\vec{\nabla}\right]\vec{\vec{P}} = -\vec{\vec{P}}\vec{\nabla}\cdot\vec{u} - [\vec{\vec{P}}\cdot\vec{\nabla}\vec{u}]^{+} - \vec{\nabla}\cdot\vec{\vec{\vec{Q}}} + qn\left[\vec{\vec{P}}\times\vec{B}/mnc\right]^{+} \tag{2.7}$$

for the fluid velocity and pressure respectively (aside: Eq. 2.6, which can be regarded as the "fluid equivalent" of Newton's second law of dynamics, is known as "Euler equation" after Euler (1761)). Writing the series of fluid equations, however, it is evident that a fluid plasma model cannot simply be realised by considering some number of low-order moments of $m\mathfrak{f}$ and the corresponding evolution equations, since in the equation for the highest-order moment considered also the next moment of $m\mathfrak{f}$ appears. In other words, a complete fluid model needs to be closed by considering one equation which does not follow from the integration of the distribution function: such relation is the so-called "closure" of the fluid system. In the simplest examples of closure for a fluid system, the dynamics is described by Eqs. 2.3, 2.6 and the closure replaces Eq. 2.7 in providing the temporal evolution of the pressure tensor. Whenever one is in need of a more detailed fluid description, Eq. 2.7 might be retained and closures might be found for the heat flux, or the heat flux evolution might be modelled by moments of Landau's equation and closures might be at higher order moments (see for instance Sulem & Passot (2015)).

Let me introduce here briefly a noteworthy example of pressure closure based on the polytropic assumption, a closure which I will also need in the following of the thesis. In order to write such closure, the underlying idea is to assume, in analogy with thermodynamics, that the pressure tensor is governed by polytropic relations i.e. (more precisely) supposing that combinations of its components evolve so to keep a quantity $Pn^{-\gamma}$ constant - a condition which can also be expressed by:

$$[\partial_t + \vec{u} \cdot \vec{\nabla}]P = -\gamma P \vec{\nabla} \cdot \vec{u} \tag{2.8}$$

with the polytropic factor γ being an adimensional constant expressing the kind of thermodynamic transformation that undergoes any fluid element as it evolves. In particular, at $\gamma = 0$ we have isobaric behaviour, $\gamma = 1$ implies isothermal variations while $\gamma = 5/3$ is the adiabatic case. In the limit $\gamma \to \infty$ we retrieve perfect isocore, that is incompressible behaviour - the last expression usually being given in terms of the equivalent $\vec{\nabla} \cdot \vec{u} = 0$ requirement (see for instance Frühauff *et al.* (2017)).

Before closing this section, one last important note regards how it is useful, sometimes, to separate or merge fluid species. Indeed, if by considering more and more of the fluid moments one always gets a better and better approximation of every $\mathfrak{f}$, in some cases the same approximation can be more easily attained by separating the $\mathfrak{f}$ as a sum of different distributions and approximating each of these into a fluid quasi-species. Having a fluid species represented as multiple quasi-species (each with its own density, velocity etc.) can be of advantage also when it comes to close the fluid system, since many low-order closures, one for each quasi-species, can attain the same precision of of a high-order closure for the species considered as a whole (see for instance Le *et al.* (2009) and Le *et al.* (2010a), summarised in the review by Egedal *et al.* (2013), or Goldman *et al.* (2020)). The merging of fluid species can also help to simplify the plasma description (you get one density instead of many, one velocity in place of many, etc.), but this is usually obtained at the expense of detail in the overall plasma model. While the separation of fluid species can be done quite straightforwardly, however, note that merging species with different m and q means that you need new expressions for charge and current density of the merged species, which cannot be represented as nq and $nq\vec{u}$ anymore, and one must establish arbitrarily the new m and q of the overall fluid.

2.1.2 Describing electromagnetic fields and their evolution

As the plasma builds up charge and current densities ϱ and $\vec{J}$, it contributes to the electromagnetic fields $\vec{E}$ and $\vec{B}$ which determine its evolution: this accounts for the need to couple the material equations just introduced to equations describing the dynamics of electromagnetic fields. As for the material equation, I will overview here several models which allow for such a description, differing by the approximations which they assume valid.

Let me begin by reminding Maxwell's system of equations, constituted by Gauss's laws for the electric and magnetic field (on the left column, top to bottom) and Faraday's and

Ampére's laws (column on the right, also top to bottom):

$$\begin{aligned} \vec{\nabla} \cdot \vec{E} &= 4\pi\, \varrho & c\, \vec{\nabla} \times \vec{E} &= -\,\partial_t \vec{B} \\ \vec{\nabla} \cdot \vec{B} &= 0 & c\, \vec{\nabla} \times \vec{B} &= +\,\partial_t \vec{E} + 4\pi\, \vec{J} \end{aligned} \tag{2.9}$$

The form in which the Maxwell equations are written here highlights the fact that (by Helmholtz's theorem) knowledge of divergence and curl are necessary and sufficient to determine completely the electric and magnetic fields. Coupling with material equations is achieved by expressing ϱ and $\vec{J}$ in terms of the material variables (i.e. the distribution functions if we adopt a kinetic plasma model, the fluid moments of all species if we consider plasma from a fluid standpoint - see for instance Mangeney *et al.* (2002)).

As for material equations, also the Maxwell system can be simplified once ascertained the regime in which we are operating, by removing from the equations all those terms relative to the dynamics at too high frequencies or too small wavelengths to be effectively coupled with the plasma dynamics at the characteristic scales considered. Notably, for most practical applications one can neglect light waves. One way to prevent light waves from being included in the model consists in replacing the electric field appearing in Ampère's law with its irrotational component (this breaks the coupling of electric and magnetic fields in Ampère's and Faraday's laws, from which light waves follow). This operation is known as the "Darwin approximation" of the Maxwell system (originally devised in Darwin (1920) - for an introduction, see Hewett (1985)). Now, while the details of this approximation are not important to this work, it might be worth noting that solving the Darwin-approximated system requires that ϱ and $\vec{J}$ are specified in terms of material quantities, just as happened for the Maxwell system (see for instance Pezzi *et al.* (2019)). In other words, eliminating light waves from the description of electromagnetic fields does not require a change of the information provided by the material equations in order to determine the electromagnetic part of the dynamics.

Another important simplification follows from supposing that the material is quasineutral, i.e. the overall charge density is negligible at the scales considered, everywhere and at any time throughout the system. When this approximation is performed after Darwin's, i.e. for nonrelativistic plasmas, it is clear that the equation system governing the evolution of $\vec{E}$ and $\vec{B}$ gets heavily impacted. Indeed, with a vanishing ϱ, also the electrostatic (i.e. irrotational) component of $\vec{E}$ disappears, and thus the Darwin-Ampère's law gets reduced to a relationship between $\vec{B}$ and $\vec{J}$ only. While in theory it could be possible to solve for $\vec{E}$ and $\vec{B}$ once $\vec{J}$ is expressed in terms of the material quantities, another approach is generally more convenient, i.e. to construct a formula which provides $\vec{E}$ from the plasma characteristics, so to obtain $\vec{B}$ by time-integration of Faraday's law and thus reducing $\vec{J}$ to a dummy variable, defined by Ampère's equation. Within the approach just described, the formula providing $\vec{E}$ as function of plasma quantities is known as "generalised Ohm's law" and can be thought somewhat similar to a closure for fluid equations in the sense that depending on the information one uses in building it, it can be used more or less successfully in different plasma regimes (aside: note that even if the $\vec{E}$ produced by a generalised Ohm's is not

solenoidal, it is only its solenoidal component which contributes to determining the electromagnetic dynamic).

A particularly interesting form of generalised Ohm's law, that I will call "resistive" from now on, is the following:

$$\vec{E} = -\vec{u} \times \vec{B}/c + \eta \vec{J} \tag{2.10}$$

and physically "means" that in the reference co-moving with the velocity field $\vec{u}$ the electric field and current density are directly proportional by the constant "resistivity" η. Now, one could argue that this form of generalised Ohm's law in Eq. 2.10 is not particularly accurate for a plasma, physically speaking, since collisions are, by definition, secondary effects in plasma dynamics, and hence collisional resistivity tends to be generally negligible. Yet, a widely-observed characteristic of plasmas is that wherever the length scale is above some threshold value (generally species-dependent) then the electric field can be transformed away with the passage of the frame co-moving with the fluid velocity. Whenever this is the case, the plasma is said "ideal". Now, the introduction of a "resistivity" parameter is a very "cheap" expression by which one can reproduce this fact, i.e. that at large-scales plasma is generally ideal. For this reason Eq. 2.10 has known a discrete fortune as generalised Ohm's law, with the caveat that the parameter η does not usually match the actual resistivity of the medium but is introduced as a simple way of mimicking a widely observed plasma behaviour.

2.1.3 A noteworthy approach: magnetohydrodynamics

Up to now, I have discussed how it is possible to represent a multi-species plasma and determine its evolution alongside that of the electromagnetic field by which it interacts. Moreover, I also mentioned how it is possible to simplify the models just presented so to adapt these representations to different plasma regimes. In this subsection, however, I am going to work along the guidelines just presented so to reach a particularly successful plasma model, dubbed "magnetohydrodynamics" or, in short "MHD". While introduced first in the study of liquid metals, it came to fortune in a variety of fields, among which space plasma physics (see Goedbloed & Poedts (2005), Molokov *et al.* (2007), Galtier (2016)).

The basic idea of magnetohydrodynamics is to describe the large-scale behaviour of a quasineutral plasma in a single-fluid framework completed with an electromagnetic evolution described via a generalised Ohm's law: in this way, basically, one is interpreting the system like a moldable magnet, hence the name. In other words, the magnetohydrodynamic plasma model is obtained by casting all species into a single fluid and coupling the system obtained with the quasineutral, Darwin-approximated description of the electromagnetic fields. Note that, while the merging of all plasma species into one means that the charge density and current density cannot be obtained by combining n and $\vec{u}$, yet the assumptions taken to model the electromagnetic fields don't require these quantities to be explicited in the system of the MHD equations.

As an example of MHD system, here I am going to write down explicitly the equations which describe a polytropic-resistive magnetohydrodynamic plasma with scalar pressure, i.e. the continuity equation and Euler's law (Eqs. 2.3 and 2.6) alongside with a polytropic closure (Eq. 2.8) and Faraday's equation (top right in Eq. 2.9) combined with the resistive, generalised Ohm's law (Eq. 2.10):

$$[\partial_t + \vec{u}\cdot\vec{\nabla}]n = -n\vec{\nabla}\cdot\vec{u} \tag{2.11}$$

$$mn\,[\partial_t + \vec{u}\cdot\vec{\nabla}]\vec{u} = -\vec{\nabla}[P + B^2/8\pi] + \vec{B}\cdot\vec{\nabla}\vec{B}/4\pi \tag{2.12}$$

$$[\partial_t + \vec{u}\cdot\vec{\nabla}]P = -\gamma P\vec{\nabla}\cdot\vec{u} \tag{2.13}$$

$$[\partial_t + \vec{u}\cdot\vec{\nabla}]\vec{B} = \vec{B}\cdot\vec{\nabla}\vec{u} - \vec{B}\vec{\nabla}\cdot\vec{u} + [c^2/4\pi]\vec{\nabla}\times[\eta\vec{\nabla}\times\vec{B}] \tag{2.14}$$

where m here is defined as the sum of all species' particle masses, weighted by average relative abundances. Note that the quantities $\vec{E}$ and $\vec{J}$, which do not appear explicitly, can be easily retrieved from n, $\vec{u}$, P and $\vec{B}$, the first by the generalised Ohm's law, the second by the reduced Ampère's law. This system completely determines the evolution of the four physical quantities n, $\vec{u}$, P and $\vec{B}$ from any appropriate initial state, with the quantities:

$$\text{Thermal velocity} \quad c_T := [2P/mn]^{1/2} \tag{2.15}$$

$$\text{Sound velocity} \quad c_S := [\gamma P/mn]^{1/2} \tag{2.16}$$

$$\text{Alfvèn velocity} \quad c_A := [B^2/4\pi mn]^{1/2} \tag{2.17}$$

playing a fundamental role in defining its regimes, i.e. determining which are the characteristic features of the dynamics which the system develops (aside: for a thorough definition of regimes, see subsection 7.1.2)

Magnetohydrodynamic models, though sometimes really simple in form, notably succeed in representing all most relevant aspects of the large scale dynamics in very different plasma systems: the interstellar medium as well as the outer strata of stars, planetary magnetospheres, and magnetically confined plasmas for thermonuclear controlled fusion. In our case, the most important quality of such models is that we can exploit them to describe the large-scale behaviour of space plasma close to Earth.

2.2 An overview of magnetised plasma dynamics

In this section I provide the reader with a very short overview to some relevant aspects of the dynamics of a magnetised plasma, considering the plasma from a fluid perspective. To this aim, first I discuss two characteristic regimes in the dynamics of magnetised plasmas (subsection 2.2.1), then I define magnetic reconnection and present a characteristic reconnection site (subsection 2.2.2 - this exposition of reconnection has been kept to the bare minimum which is necessary to understand the rest of the work: the interested reader is referred to the appendix section for a number of insights on this topic). To conclude, I report on some characteristic structures arising in the evolution of a magnetised plasma, and note how reconnection affects them (subsection 2.2.3)

2.2.1 Frozen magnetic field and magnetic diffusion

In a magnetised plasma dynamics, one of the most peculiar features is that under some circumstances all particles can be regarded as moving "with" the magnetic field, meaning that all fluid elements of a same plasma species which are sitting on the same magnetic field line at some instant will retain this "magnetic connectivity" as the system evolves. In order to understand the physics which leads to the preservation of magnetic connectivity, consider the temporal variation of magnetic flux through the infinitesimal surface advected with some plasma species (see subsection 7.1.1), which is written:

$$d_t\vec{B} + \vec{B}\vec{\nabla}\cdot\vec{u} - \vec{B}\cdot\vec{\nabla}\vec{u} = \partial_t\vec{B} - \vec{\nabla}\times[\vec{u}\times\vec{B}] = -\vec{\nabla}\times[c\vec{E} + \vec{u}\times\vec{B}]$$

Since fluid elements which sit over a given field line can be individuated by the intersection of the plasma populations disposed over two magnetic surfaces, if magnetic flux across a material surface does not change in time, then we can conclude that plasma also realises a "perfect advection" of the line. In other words, magnetic connectivity is preserved wherever it is negligible the field-perpendicular component of the magnetic flux variation just introduced. In particular, since this situation is found wherever the plasma is ideal, it is interesting to recognise that plasma preserves its connectivity throughout most of the near-Earth space environment (see Lundin *et al.* (2005)).

Before moving on, it is useful to introduce also some of the terminology linked with the preservation of magnetic connectivity just discussed. Whenever the plasma species considered is in a connectivity-preserving regime, the material is said to be locally "frozen" inside the magnetic field. While allowing material on nearby field lines to evolve even very differently from each other, the frozen plasma condition poses a very strong limitation on the configurations that can be reached from any given initial state: the magnetic field can bend, twist and twirl but only as long as the plasma follows all its movements. The frozen behaviour can disappear only provided that the plasma becomes nonideal. For instance, if the generalised Ohm's law considered is resistive, then the connectivity constraint might disappear as the $\eta\vec{J}$ term becomes relevant and therefore $\vec{B}$ evolves as in a diffusive fashion with respect to the plasma. In analogy with resistive breakage of the frozen condition, with a slight abuse of language we will call "diffusion region" ("DR" for short) any volume where line connectivity is not preserved in time, and this regardless of the mechanism by which this is happening. Appearance of diffusion regions turns off the strong topological requirement given by the frozen plasma condition, and allows the system to reach a much larger number of states.

2.2.2 Magnetic reconnection and a reconnection site

Suppose that the plasma under study exhibits a frozen behaviour throughout most of the system considered. In such a scenario, a "magnetic reconnection" is the process by which a localised diffusion region allows some of the fluid elements to change magnetic connectivity while most of the plasma is strictly frozen (this according to the

definition in Schindler *et al.* (1988) - for details, see subsection 7.3.1).

A fundamental parameter in studying reconnection is the so-called "reconnection rate" $\mathcal{R}$ which estimates "how much" the localised diffusion region allows to break the frozen plasma condition. Since the preservation of line connectivity is equivalent to magnetic flux conservation when we restrict ourselves in a localised nonideal region (demonstration in Hesse & Schindler (1988)), $\mathcal{R}$ is naturally defined as the variation of magnetic flux that a reconnection site can induce across a material surface gradually advected through it by the plasma. Depending on the specific characteristics of every reconnection site, obviously, one can rely on one or more of such surfaces to estimate one or more reconnection rates (see subsection 7.3.2).

Reconnection sites can be found in many different contexts, since the "diffusivity" they require can be easily generated by many of the processes leading to a local shrinkage of plasma scales, and the states in which the system is allowed by such a local de-freezing of plasma happen often to be energetically convenient. Instead of discussing more in detail which processes might concur to establishing a diffusion region, or in which situations the system favours reconnection as a mean to reach a least energetic state (see subsection 7.3.3), here I will present the reader with a simple case of reconnection (more cases can be found in subsection 7.3.4). To this aim, I focus on the two-dimensional system sketched in Fig. 2.2. A hyperbolic null of the in-plane magnetic field (X-point) allows us to recognise four field lines ("separatrices") dividing the system into four (unequal) quadrants. Movement of all plasma species is organised into an hyperbolic flow system (two inflows, two outflows), with a zero (S-point) not far from the magnetic null, so that plasma elements which entered the box connected with each other end up sitting on different lines as they flow away on the two sides. Given this kind of flow and the two-dimensional nature of the system, reconnection rate is evaluated here on any surface constructed on a in-plane curve with one extreme positioned on the X-point and the other in any point of the ideal region: by an easy computation it is found that this reconnection rate $\mathcal{R}$ is equal to the value of cE_z at the X-point (see Eq. 7.8 for reference). It is important to recognise that in this setup every plasma species must exhibit a diffusion region in the central part of this system, where the local scales shrink and ideality is broken, meaning that all plasma can undergo reconnection (see Vasyliunas (1975)), and that reconnection is convenient as long as the electromagnetic field inside the outflow regions can transfer energy to plasma thanks to the $\vec{B} \cdot \vec{\nabla}\vec{B}/4\pi$ term (which contributes to the Lorentz force $\vec{J} \times \vec{B}$).

In order to be just a little bit more quantitative in this presentation, let me show now some characteristic of this reconnection site which emerge once a very simplified, steady-state configuration has been assumed for it (I am adopting the so-called "kinematic" approach, which is legitimate as long as the portion of plasma we consider is sufficiently small compared to the larger system in which it is embedded - as noted in section 3.3 of Biskamp (2005)). So, let me assume that all quantities are uniform across inflows and outflows, sufficiently far away from the X-point, and describe the plasma by resistive, incompressible MHD. Integrating the MHD equations over a rectangular box, of dimensions $\ell^{\text{in}} \times \ell^{\text{out}}$ with vertices on the separatrices and large enough to con-

tain the MHD diffusion region, allows to obtain a series of relations between inflow and outflow values. Assuming a configuration with perfectly symmetric inflows, with the reference frame specified in Fig. 2.2, let me set:

$$\vec{u}^{\text{in}} = \mp u^{\text{in}}\vec{e}_x + \dots \vec{e}_y \qquad \vec{B}^{\text{in}} = \pm B^{\text{in}}\vec{e}_y + \dots \vec{e}_x$$
$$\vec{u}^{\text{out}} = \pm u^{\text{out}}\vec{e}_y + \dots \vec{e}_x \qquad \vec{B}^{\text{out}} = \pm B^{\text{out}}\vec{e}_x + \dots \vec{e}_y$$

while density and pressure are supposed constant everywhere (aside: for the sake of this analysis, some of the components of $\vec{u}$ and $\vec{B}$ need not to specified and therefore they have been plainly ignored). Integrating the four equations of the resistive incompressible MHD, one gets:

$$u^{\text{in}}/\ell^{\text{out}} = u^{\text{out}}/\ell^{\text{in}} \qquad \text{from either mass continuity, either the incompressible closure}$$
$$mn\, u^{\text{in}}u^{\text{out}} = B^{\text{in}}B^{\text{out}}/4\pi \qquad \text{from Euler's law, equating magnetic tension and convection}$$
$$u^{\text{in}}B^{\text{in}} = u^{\text{out}}B^{\text{out}} \qquad \text{from Faraday's law}$$

from which it is possible to estimate, for instance, that the outflow velocity u^{out} is about c_A^{in} (i.e. in this simplified model all magnetic energy released by the annihilation of the in-plane magnetic field ends up accelerating the outflowing plasma). Perhaps more interestingly, note that from these relation one can deduce $\mathcal{R}$ in terms of the system's parameters. Indeed the steady state hypothesis implies that E_z is uniform over the whole domain, thus it is possible to write $\mathcal{R}$ as:

$$\mathcal{R} = cE_z = [c_A^{\text{in}}\, B^{\text{in}}][u^{\text{in}}/u^{\text{out}}] = [c_A^{\text{in}}\, B^{\text{in}}][\ell^{\text{out}}/\ell^{\text{in}}] = [c_A^{\text{in}}\, B^{\text{in}}][B^{\text{out}}/B^{\text{in}}]$$

where the $c_A^{\text{in}}\, B^{\text{in}}$ term is usually interpreted as a "dimensional" factor multiplying the normalised reconnection rate (see for comparison Karimabadi et al. in Balogh *et al.* (2014)). The scheme just presented, one of the simplest for the X-point reconnection site, is known as the "Sweet-Parker" model of X-point reconnection (see subsection 2.1.1 in Birn & Priest (2007)).

Compared to the simple, didactic model just presented, the actual picture of a reconnection site is generally really complicated, including asymmetries, varying fields, multiple particle species and the plasma generally exhibiting more than one regime throughout it. While numerical experiments and satellites have agreed in drawing a rich and interesting picture of reconnection physics (see subsections 7.5.1 and 7.5.2 for an overview), however, the full understanding of such a picture is still largely to come, since the models are not completely able to keep up with satellites and computations. Obviously, it is exactly the quantity and variety of open questions (e.g. the recurrent 0.1 normalised rate for X-point reconnection - see Cassak *et al.* (2017)) that makes reconnection physics such an interesting field of research (see Hesse & Cassak (2020)).

2.2.3 Characteristic structures in near-Earth plasma

In studying near-Earth plasma systems it is common to search for characteristic structures: for this reason, here I will briefly introduce the two of them which are the most

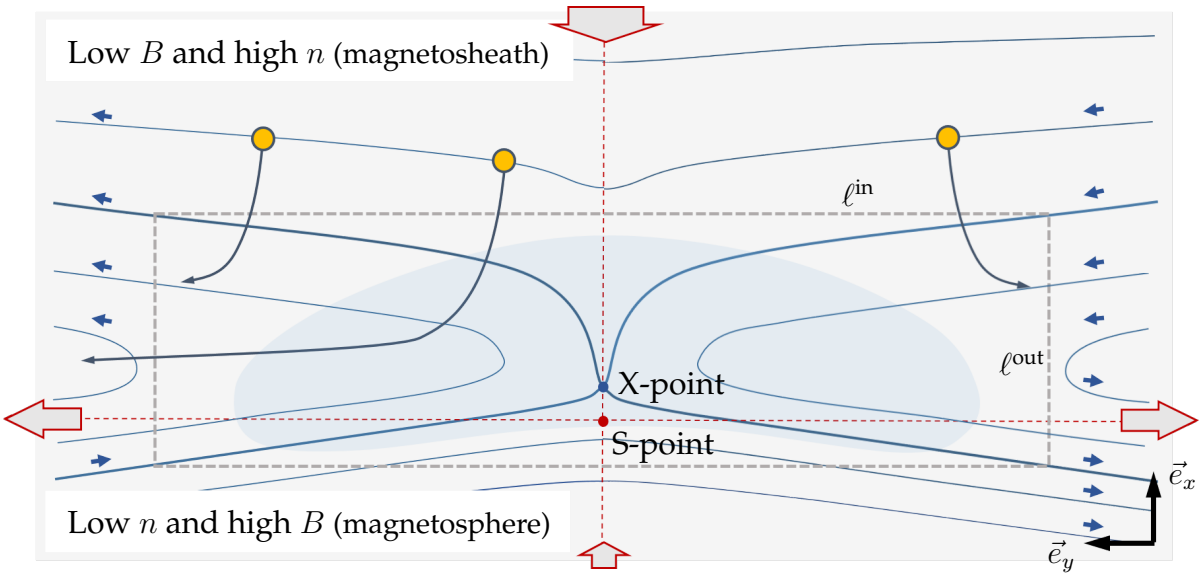

FIGURE 2.2: Schematic representation of a two-dimensional reconnection region constituted of an in-plane null surrounded by a non-ideal region, assumed stationary (own image). Blue lines indicate the in-plane projection of magnetic field lines, with the separatrices made thicker, and blue arrows show the direction of the projected magnetic field. Red dashed lines determine the "skeleton" of the hyperbolic flow, with red-grey arrows indicating the direction in which the material circulates into the reconnection site and out of it. The diffusion region is shaded in azure. Light-grey dashed lines highlight integration boxes used for reconnection budget analyses, with dimensions ℓ^{in} and ℓ^{out}.
Note that for generality reconnection here is supposed with asymmetric inflow conditions, even though without a significant out-of-plane (guide) field - a situation similar to that at the subsolar magnetopause (hence the small labels in parenthesis, indicating magnetosphere and magnetosheath). In particular, asymmetry makes it so that the X-point of magnetic degeneracy does not coincide with the S-point where the fluid stagnates: this can be recognised as the point at the centre of the red dashed line intersection does not coincide with that in which the four magnetic separatrices converge. The three yellow points and their arrows are intended to represent the displacement of three different fluid elements, initially all magnetically connected, exit the box on three different magnetic field lines.

recurrent, namely current sheets and flux ropes. Recognising the presence of such structures, as I will remark, can allow us to infer (to some degree at least) where reconnection could have acted or where it might start.

Current sheets can be individuated whenever the magnetic field is locally present in a sheared configuration, as one can understand considering Ampère's law in the quasineutral and nonrelativistic approximation, where $\vec{J}$ is proportional the curl of $\vec{B}$ (see Fig. 2.3). Now, by compressing some portion of the current sheet one can obtain that the local scale shrinks, nonideality arises and field lines from either part of the sheet end up reconnecting with each other developing an X-point configuration (subsection 2.2.2). Out of all processes which can induce reconnection by locally compressing a current sheet, the most famous is the so-called "tearing" instability (see Furth *et al.* (1963)), even if it is possible also to find many other perturbation modes under which the current sheet is unstable and therefore develops reconnection (see for instance the "resistive kink" modes or the "ideal" tearing in Pucci & Velli (2013), Tenerani *et al.* (2015), Pucci *et al.* (2017)).

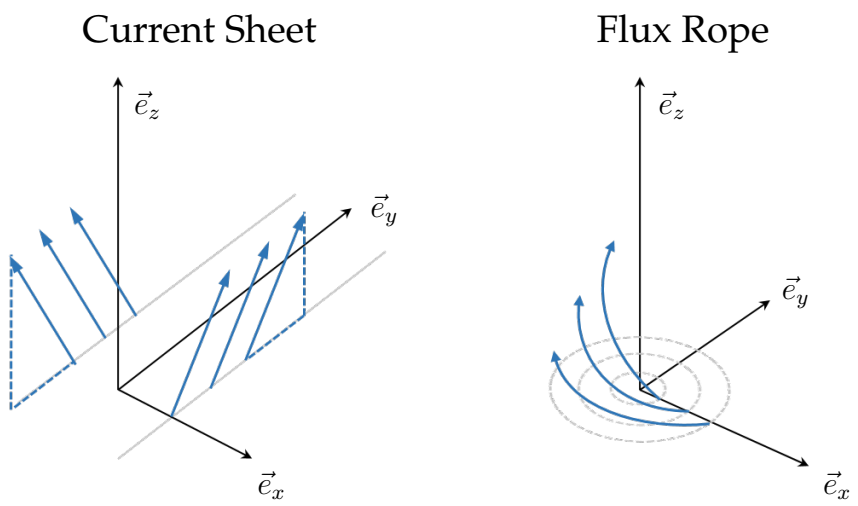

FIGURE 2.3: Schematic of a current sheet and flux rope, structures characteristically found in the magnetic field (own image). In both cases, $\vec{J}$ is aligned with the z axis. Note that the current sheet can be considered a one-dimensional system, since the magnetic field is invariant in two directions (y and z). The flux rope, instead, is translationally invariant only along its axis (parallel to z) and hence must be considered generally a two-dimensional system.

In near-Earth plasma, tearing and/or tearing-like perturbations have been individuated in many locations and circumstances (see for instance Liu *et al.* (2013) or Nakamura *et al.* (2017b)), with the most important cases being the disruption of current sheets at the magnetopause and in the magnetotail (see subsection 1.1.2). In particular, one can note that at the magnetotail the guide field can be generally considered negligible and so is the asymmetry between the inflows, since the north and south lobes can be usually approximated symmetric. At the magnetopause, instead, inflow situations are strongly asymmetric (Fig. 2.2 is representative of this) and in general also higher guide field values can be attained. These tendencies, which can be intuitively understood by considering the large-scale picture of the magnetosphere (as drawn, for instance, in subsection 1.1.2) have been recognised in both observations and simulations (see for reference all chapter 4 of Birn & Priest (2007)).

Flux ropes are structures in which the magnetic field is organised in a helical fashion, winding around a central axis along which current flows (see Fig. 2.3, and Vinogradov *et al.* (2016) for an example of analytical description). Flux ropes are very easily found in plasma environments where reconnection operates, since it is generally convenient for the severed magnetic tubes to possess or develop the flux-rope twirl (see Priest *et al.* (2016), Threlfall *et al.* (2018)).

Flux ropes have been individuated in both simulations and observations of the near-Earth plasma dynamics, both at the front magnetopause and the magnetotail. In the subsolar magnetopause, for instance, it is recognised that flux transfer events generally have flux ropes in their cores (in the case of a localised reconnection, the flux-rope

results as the newly generated flux tube acquires twist by "rolling" along the magnetopause - in the case of multiple reconnections the creation of flux ropes is very similar to the formation of two-dimensional magnetic islands in between two X-points). In the magnetotail, instead, flux ropes can be usually found in the core of plasmoids, i.e. inside those sections of the magnetosphere that reconnections have been severed and drift away into the passing solar wind. Literature on the subject is large, so I shall only provide here a very quick list of recent research papers: Hoilijoki *et al.* (2017), Juusola *et al.* (2018), Sun *et al.* (2019a), Ebihara & Tanaka (2020) for simulations, and Stawarz *et al.* (2018), Hwang *et al.* (2018), Sun *et al.* (2019b), Fargette *et al.* (2020) for satellite observations.

Chapter 3

Spacecraft data and numerical experiments

3.1 The MMS mission and data analysis techniques

Spacecraft data from NASA's Magnetospheric Multiscale mission (MMS) have been extensively used in this thesis. Therefore, in this section I introduce the reader to MMS and to some of the techniques presently used to analyse the data it provides, with particular attention to the detection and characterisation of spacecraft passages close to reconnection regions. After a general introduction of the MMS mission, presenting its objective, orbits and the general characteristics of its data products (subsection 3.1.1), I provide some detail on the different instruments aboard (subsection 3.1.2). This is followed by a recapitulation of reference frames generally adopted when dealing with spacecraft data in the near-Earth environment (subsection 3.1.3). The section ends with an overview of the principal methods to analyse the data provided by spacecraft mission (subsection 3.1.4), and in particular how to detect reconnections close to the spacecraft, and how to characterise them (subsection 3.1.5). Note that several of the methods which I mention in the last two subsection are not introduced in view of some use in subsequent analyses but rather for the sake of completeness and in order to provide the reader with a full panorama of this topic.

3.1.1 The MMS mission: general characteristics

The Magnetospheric Multiscale mission (see Burch *et al.* (2016b)) has been designed specifically for the purpose of investigating the electron-scale physics of reconnection processes occurring in the boundary regions of the Earth's magnetosphere (see Cassak (2016)). Such an aim is extremely challenging from the technical viewpoint because the full three-dimensional and time-wise characterisation of plasma physics at this scale requires to sample the plasma and electromagnetic fields with a tremendous precision at different points in close locations (down to few kilometers) and with an extremely high measurement rate (up to hundreds of times per second). To face such requirements, the MMS mission is composed by four satellites set to orbit in close formation, and each equipped with a complete, state-of-the-art collection of scientific instruments.

To maximise scientific outcome, the MMS mission is required to operate in a variety

of key regions of the near-Earth plasma environment: the nose, flank and tail of the magnetosphere, the magnetosheath and the close solar wind. For this reason, the mission's time has been divided into phases and sub-phases, each focusing on a different near-Earth region and thus requiring the satellites' orbits being re-adjusted accordingly (see Figure 3.1 for the general idea and Fuselier *et al.* (2016) for details on the orbits). Since probing different regions requires the ability to sample different temporal and spatial scales the four-spacecraft formation has been made adjustable both in shape and size, hence the "multiscale" denomination (for more on characteristic scales and their proper sampling, see subsections 7.1.2 and 7.1.3).

While an extremely high resolution is necessary for the detailed study of DRs, if MMS instruments were to operate at full regime during the whole mission, there would be no way to downlink all data produced. Downlink limitations forced the MMS project to rely on a series of data selection procedures, the first being the individuation of restricted "regions of interest" (ROIs) within each orbit and limit to these the high-frequency measurement mode. However, not even ROI-limited data can be fully downloaded. This calls for the necessity of a second, continuous data-selection process - one which is set to be man-made. Therefore, at each orbit MMS is required to keep new measures at full resolution in the aboard memory while it sends to the ground only a low resolution copy of these. On ground, the selection crew - known as "Scientists-In-The-Loop" (SITL) team - uses this preliminary data to assign downlink priorities known as "figures of merit" (FOM) to each data interval. Data which have been assigned the highest FOM values are downloaded at full-resolution during the following orbit.

Instrument operation modes and data selection procedures result into the availability of data products with different resolutions, as detailed in Baker *et al.* (2016). At the basic level, "slow survey" data cover all non-ROI intervals, while the higher resolution "fast survey" product is available only throughout ROIs. In addition to these products, every ten seconds a comprehensive set of so-called "trigger data" is created automatically. It is the ensemble of trigger and survey data that is initially transmitted to Earth for being examined by the SITL team. Full-resolution measures which have been downlinked thanks to high FOMs are known as the "burst mode" data (see Figure 3.1 for a schematic summary of different MMS data products).

Data products do not only differ in terms of temporal resolution, but also for the amounts of post-processing they have passed through. First, "level-1" products are obtained by eliminating communication artifacts and then by applying engineering calibration to ground-transmitted measures. All these operations are carried on automatically upon reception of data to the ground. A longer procedure of further calibration, however, is necessary to attain research-grade material. In this process, dedicated algorithms must refine level-1 products into "level-2" data. Since production of level-2 data is generally time-consuming, the scientific community is also given a lower-grade product, dubbed "QuickLook", which is automatically generated and not suitable for research, but should nonetheless display the relevant features of every data interval. From level-2 data, any further elaboration (for instance combining measurements from

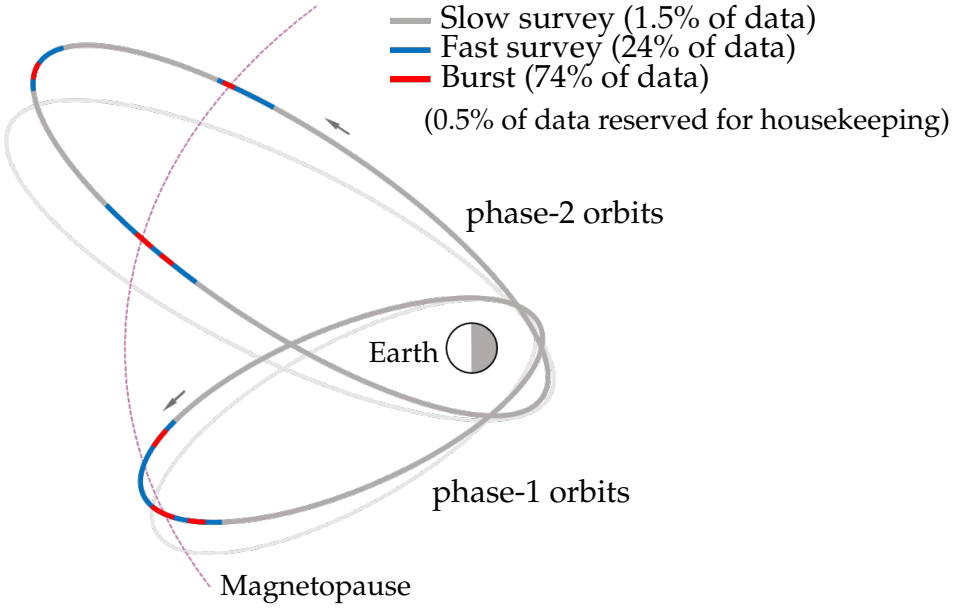

FIGURE 3.1: A MMS orbit scheme, visualising the plane individuated by GSE x and y axes. Different colours highlighting regions of different operation modes (own image, inspired by the similar in Burch *et al.* (2016b)). The orbits drawn are representative of phase-1 and phase-2 of the MMS mission, with the thin grey "shadow" drawn to highlight the spacecraft's precession.

multiple instruments) must be referred to as a "level-3" product. Throughout this thesis, data from MMS will be used at level-2, both at "burst" and "survey" frequency.

In spite of the complex routine of data processing and refinement just presented, in many cases even high-level products display some signatures which are not indicative of the plasma environment in itself but rather emerge from plasma-spacecraft interactions. All these, obviously, should not be confused with the real features of the environment and must be kept in mind whenever analysing MMS data. As an example, here I will just mention to the reader some of the artifacts resulting from the electric charging of satellites, a consequence from exposure to plasma and solar radiation (to understand charge buildup, consider that while radiation stimulates the production of photoelectrons, also ions and electrons impacting the satellite result in accumulation of charge at a rate that depends on spacecraft potential and plasma temperatures: given the parameters of magnetospheric and magnetosheath environments, equilibrium between these processes is achieved only as the spacecraft potential builds up of several volts, i.e. with an excess of positive ions residing on the satellites). An obvious consequence of spacecraft charging is that positive ions will appear to instrumentation as less energetic than they actually are in the environment, while at the same time the electron energy spectrum will be shifted towards higher values, thus posing problems to probing probability distribution (see Lavraud & Larson (2016)). More in detail, the complex overall shape of the spacecraft (see Figure 3.2 for reference) means that the electrostatic potential will not act uniformly on different instruments and its effect on measures can even vary as function of time. This happens, notably, when spacecraft rotation gets in the game, leading to the generation of periodic features in the signals recorded by

particle instruments (see for instance Barrie *et al.* (2019) and Toledo-Redondo *et al.* (2019)).

3.1.2 An overview of MMS instrumentation

From Figure 3.2 the reader can get an overall look at the main components of each MMS spacecraft, that we can roughly split into four main systems. First, each spacecraft is given a propulsion system, made up by fuel tanks, thrust tubes and the related electronics, so to regulate the formation of MMS fleet and - occasionally - to change orbit. Second, eight solar panels are set to power the spacecraft's electronic. Third, a communication system is implemented in order to receive instructions from the ground and send back scientific and technical data. Fourth, scientific probes and ancillary systems provide field and plasma measurements throughout the environments crossed by the spacecraft. Let us now plunge in more detail through these, which belong to the large family of plasma measurement devices for space exploration (see Parks (2018)).

Aboard each spacecraft, there are three major suites of particle sensors and one for electromagnetic fields. These are the following.

- Fast Plasma Investigation (FPI) includes four dual-spectrometers for electrons (the so-called DES) and four dual-spectrometers for ions (DIS), both in the form of top-hat electrostatic analyser, enabling each spacecraft to get a full-sky panorama of ion and electron distribution functions (for details on this kind of instruments, see appendix A1 in Bruno & Carbone (2016) or McFadden *et al.* (2008)). Both distribution functions are sampled at 32 energy levels, from 0.01 to 30 keV, for electrons every 30 ms and for ions at 150 ms (for all details, see Pollock *et al.* (2016) - note that IRAP has contributed hardware to the mission through the provision and calibration of the set of micro-channel plate detectors for the ion instruments).

- Hot Plasma Composition Analyser (HPCA) is constituted by one instrument per spacecraft, which combines an electrostatic energy analyser with a carbon-foil time-of-flight unit to measure ion energy and mass relative to ion charge for each angle of arrival. This allows HPCA to resolve 3D ion energy distributions for H^+, He^{++}, He^+ and O^+ separately, between 0.001 and 40 keV (see Young *et al.* (2016)).

- Energetic Particles Detector (EPD) produces a full-sky view of energetic ions and electrons. On each spacecraft this suite counts one Energetic Ion Spectrometer (EIS) and two probes constituting the Fly's Eye Energetic Particle Spectrometer (FEEPS). Together, EIS and FEEPS provide a three dimensional distribution of charged particles up to 500 keV - the lowest energy sampled being 25 keV for electrons, 20 keV for protons and 45 keV for O^+ ions (see Mauk *et al.* (2016) and Blake *et al.* (2016)).

- FIELDS is dedicated to the measure of electric and magnetic fields through a wide frequency range. For the magnetic field two flux-gate magnetometers (AFG

and DFG) provide data up to 0.064 kHz while a search-coil magnetometer (SCM) covers frequencies up to 6 kHz (for an overview on the principles about flux-gate magnetometers, see appendix A2 in Bruno & Carbone (2016)). Precision in magnetic field measurement is 0.1 nT. For the electric field MMS is equipped with two sets of double-probe sensors (SDP and ADP), each operating up to 100 kHz and with 0.5 mV/m accuracy. Alongside with the sensors just presented, the Electron Drift Instruments (EDI) is used to determine offsets between electric and magnetic field data, and cross-calibrate them (see Torbert *et al.* (2016) for an overview, and all papers therein for details on the specific MMS instruments).

Alongside with probes, the scientific instrumentation aboard each spacecraft is completed by one more suite of instruments, the so-called "Active Spacecraft Potential Control" (ASPOC) which is a system to change the spacecraft's charge by ejecting indium ions. Basically, activating ASPOC should enable MMS potential to be kept under 4 V and therefore for all scientific probes to operate within limited bias. However, since operating ASPOC has also impact on some instruments, in practice it has been seldom activated in the mission (see Andriopoulou *et al.* (2016), Nakamura *et al.* (2017a)).

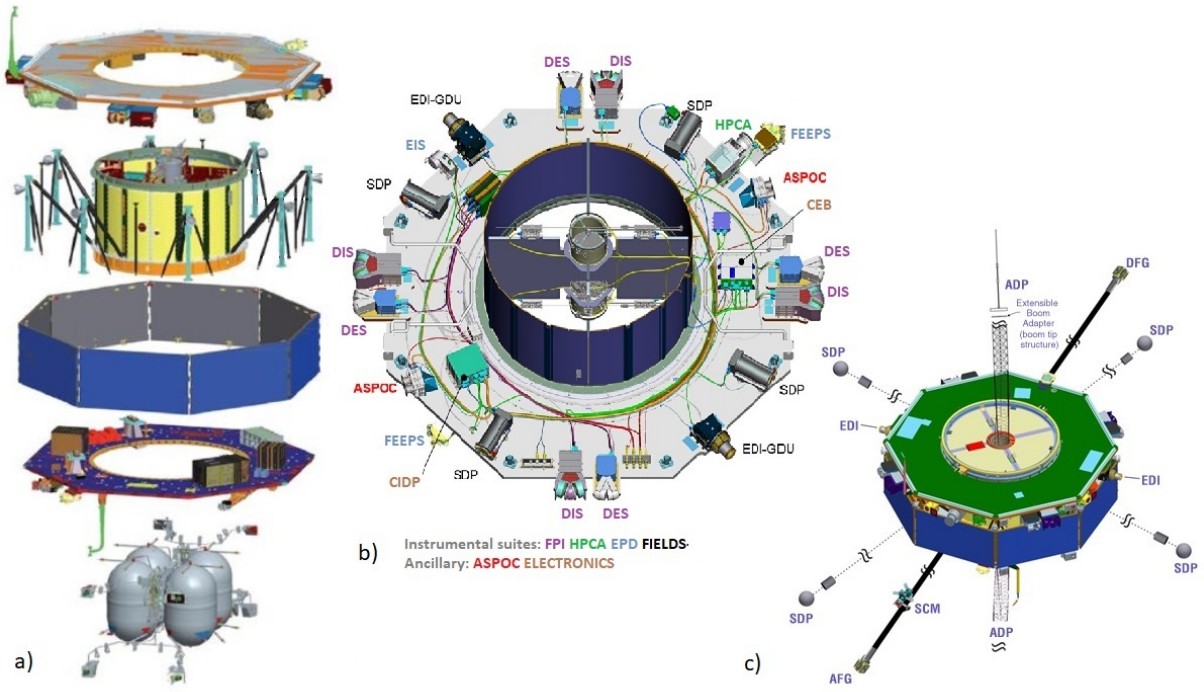

FIGURE 3.2: a) Exploded representation of a MMS satellite, drawn without wire booms and antennas for simplicity. The five vertical levels, from top to bottom, show the top deck, the frame or "skeleton" of the spacecraft, its eight solar panels, the bottom deck and the propulsion module, with well visible the four fuel reservoirs (image from the MMS website https://mms.gsfc.nasa.gov/index.html).
b) Detail on the top deck and central frame of MMS, seen from below. Here all the instruments hosted on the spacecraft's main body are recognisable (adapted from Burch *et al.* (2016b)).
c) A MMS satellite fully assembled, in flight configuration, i.e. after that antennas and booms, reclined during the launch, have been fully deployed. While plasma probes can be set just below the top deck, measurements of fields need the spacecraft to be equipped with booms and/or antennas to achieve maximum efficacy (image from Torbert *et al.* (2016)).

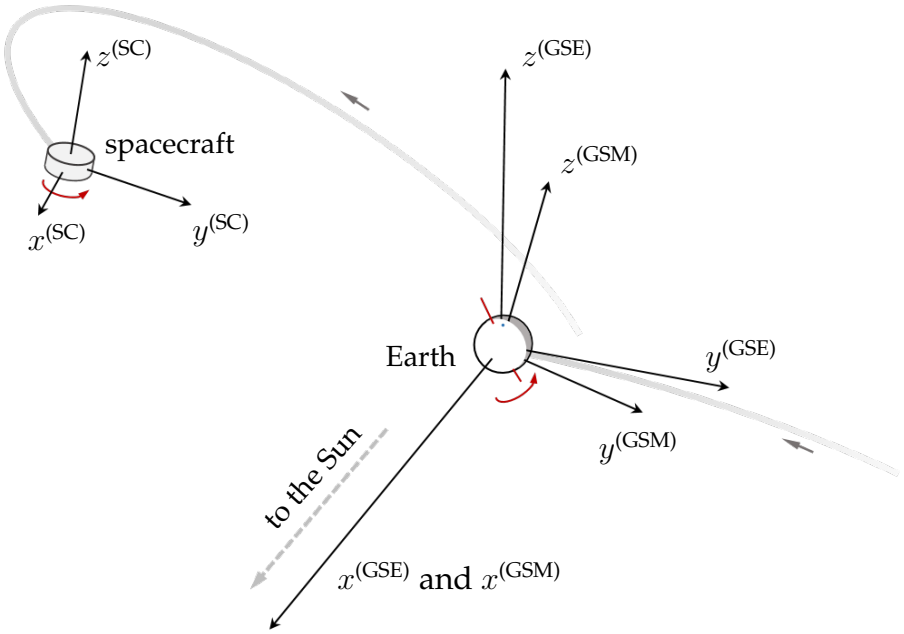

FIGURE 3.3: Schematic of different coordinate systems, with GSE, GSM and the spacecraft-relative frames represented (own image). The Earth's revolution is sketched by the grey trace, and lies in the plane defined by GSE x and y axes. The blue dot on the Earth's surface represents the north geomagnetic pole, which is kept in the plane defined by GSM x and z axes. Due to the rotation of the Earth around its axis, here sketched in red, the GSE and GSM frames change orientation with respect to each other during the day. Similarly, motion and rotation of the spacecraft change the frame transformations between the satellite-solidal reference, GSE and GSM.

3.1.3 Reference frames in the near-Earth environment

In magnetospheric physics, several reference frames are useful to visualise the data (see for instance in the appendix of Kivelson & Russell (1995)). Therefore, even if measures are taken in a frame which is solidal to the spacecraft, in order to interpret them it is best to transform them into other frames. Here I will briefly summarise some of these "other" frames, generally adopted while interpreting spacecraft data.

When considering the large-scale picture of the near-Earth plasma system, the two references the most used are the following.

- Geocentric-Solar-Ecliptic (GSE): is centred at the Earth's centre, with the x axis pointed toward the Sun. The z axis is then set perpendicular to the x axis, such that the ecliptic's normal fits into the plane defined by x and z. The y axis is set orthogonal to the other two, so to complete a right-handed triad (see Fig. 3.3). This reference frame can be understood as the most natural one to follow the Earth's revolution, since the ecliptic (the approximate plane in which the Earth orbits the Sun) is always given by the x and y axes of this reference. For this reason, GSE is generally used to describe trajectories of satellites when these orbits are firstly regulated by the gravitational pull of the Sun and of the Earth.

- Geocentric-Solar-Magnetospheric (GSM): is centred at the Earth's centre, with the x axis pointed into the Sun (as in the previous case). The z axis is set in the plane perpendicular to x so that the Earth's dipole falls into the plane defined by z and x. The y axis completes a orthogonal, right-handed triad with the other two (see Fig. 3.3). This reference, as already noted, shares the x axis with GSE, while the y and z axes are oriented such that the Earth's magnetic equator falls into the plane defined by axes x and y. This means that over one rotation of the Earth, the GSM y and z oscillate back and forth with respect to their GSE counterparts. Even if GSM is not the best frame for satellite motions, it comes very useful when one is interested into the large-scale structure of the magnetopause: indeed, the only effect of Earth's rotation over the magnetic dipole is that this oscillates back and forth in the plane defined by GSM x and z axes (for more detail on this coordinate system, and on similar ones which align with the Earth's magnetic field. see Laundal & Richmond (2017)).

Now, whenever one analyses specific structures in the plasma environment, it is possible to devise specific frames, oriented according to the symmetries of the system under study. For instance, with flux ropes and current sheets the references adopted would be those sketched in Fig. 2.3 or equivalent ones. In the specific case of a current sheet, the three unit vectors are usually called $\vec{e}_L$, $\vec{e}_M$, $\vec{e}_N$ instead of the classic $\vec{e}_x$, $\vec{e}_y$ amd $\vec{e}_z$, with the unit vector $\vec{e}_N$ being aligned with the direction of main variation (the current sheet normal) and $\vec{e}_M$ in the direction of least change. To this aim, it is fundamental to develop techniques to devise how these frames are oriented based on the spacecraft's data: this I will briefly discuss in the following subsection.

3.1.4 Analysis techniques for spacecraft data

Here I will draw a quick summary of analysis techniques for spacecraft data series, keeping the focus mainly on methods based on multi-spacecraft measurements. While throughout the text the reader is referenced to the original publications for all these procedures, it must be noted that many of these methods are well explained and discussed in the excellent books editored by Paschmann and Daly (original version: Paschmann & Daly (1998), update: Paschmann & Daly (2008)).

Before entering into spacecraft analysis techniques, a fundamental note is due on the so-called "Taylor hypothesis" (so-called after its first appearance in an early study of fluid turbulence, Taylor (1938)) which in near-Earth plasmas has been generally confirmed to hold at MMS operational scales (see Perri *et al.* (2017)). Basically, working under the Taylor hypothesis means assuming it is possible to picture the spacecraft as crossing through a "fixed" plasma configuration, and therefore that time-series of measurements are equivalent to measurements taken all at the same time along a curve cutting through a stationary plasma. Many techniques for multi-spacecraft data analysis are based on this assumption, as it will become evident in the following of this section.

Whenever a fleet of many spacecraft operates in sufficiently close formation it is possible to suppose that all physical quantities vary according to a linear combination of known functions in the region surrounding the probes, with the coefficients of such combination being determined from the measures. In other words, let us assume to dispose of all measures at some instant in time, i.e. to know the values Ψ_α of the generic quantity Ψ at each of the probes' positions, α being the index denoting each probe; then the value of Ψ can be estimated as a linear combination of characteristic functions μ_α for any position $\vec{r}$ in the surroundings of the fleet:

$$\Psi(\vec{r}) \simeq \sum_\alpha \mu_\alpha(\vec{r})\Psi_\alpha \qquad \text{with} \qquad \begin{cases} \mu_\alpha(\vec{r}_\beta) = 1 & \text{for } \alpha = \beta \\ \mu_\alpha(\vec{r}_\beta) = 0 & \text{for } \alpha \neq \beta \end{cases} \tag{3.1}$$

Obviously, different choices are possible for the definition of the μ_α, with each of them resulting into different estimates of the spatial shape of any Ψ (note the linear and quadratic μ_α in chapter 14 of Paschmann & Daly (1998), for instance). The accuracy of any of these Ψ estimates in reproducing the real physics at a certain scale depends primarily on factors such as the precision of the probe from which the Ψ_α are derived and inter-probe separations, with better performance if all such separations are similar to each other (for a more general discussion on the subject, the reader is referred to subsection 7.1.3).

Disposing of four spacecraft, the easiest choice is assuming μ_α to be linear:

$$\mu_\alpha(\vec{r}) = 1 + \vec{\kappa}_\alpha \cdot (\vec{r} - \vec{r}_\alpha) \qquad \text{where} \qquad \begin{aligned} \vec{\kappa}_1 &= \frac{[\vec{r}_3 - \vec{r}_2] \times [\vec{r}_4 - \vec{r}_2]}{[\vec{r}_1 - \vec{r}_2] \cdot [[\vec{r}_3 - \vec{r}_2] \times [\vec{r}_4 - \vec{r}_2]]} \\ \vec{\kappa}_2 &= \frac{[\vec{r}_4 - \vec{r}_3] \times [\vec{r}_1 - \vec{r}_3]}{[\vec{r}_4 - \vec{r}_1] \cdot [[\vec{r}_2 - \vec{r}_3] \times [\vec{r}_1 - \vec{r}_3]]} \\ \vec{\kappa}_3 &= \frac{[\vec{r}_1 - \vec{r}_4] \times [\vec{r}_2 - \vec{r}_4]}{[\vec{r}_3 - \vec{r}_4] \cdot [[\vec{r}_1 - \vec{r}_4] \times [\vec{r}_2 - \vec{r}_4]]} \\ \vec{\kappa}_4 &= \frac{[\vec{r}_2 - \vec{r}_1] \times [\vec{r}_3 - \vec{r}_1]}{[\vec{r}_4 - \vec{r}_1] \cdot [[\vec{r}_2 - \vec{r}_1] \times [\vec{r}_3 - \vec{r}_1]]} \end{aligned} \tag{3.2}$$

where the $\vec{\kappa}_\alpha$ have been defined by requiring that the function μ_α evaluated at $\vec{r}_\beta$ has value one if $\alpha = \beta$ and vanishes if $\alpha \neq \beta$ instead. Given this choice of μ_α, it is easy to recognise that the gradient of Ψ in the approximation given by Equation 3.1, can be estimated by:

$$\vec{\nabla}\Psi(\vec{r}) \simeq \sum_\alpha \vec{\kappa}_\alpha \Psi_\alpha \tag{3.3}$$

which is constant in space due to the linearity of the μ_α chosen. Limitations and strengths of this estimates have been addressed in specific studies (for short, I refer only to Kieokaew *et al.* (2018) and Chanteur (2000)).

Historically, an overwhelming majority of gradient, curl and divergence estimates from four-spacecraft data follows from the linear interpolation just presented. In particular, most estimates of current density come by applying the previous analysis on magnetic field measures, in a procedure exploiting the MHD approximation of Ampère's law (see Section 2.1.3) famously known as the "curlometer" method (see Dunlop *et al.* (1988)). From knowledge of fields' gradients, however, it is also natural to

develop some machinery that provides selected information on the geometrical configuration of the plasma environment traversed, and this has been done extensively (see Shen *et al.* (2003), Shi *et al.* (2005), Shen *et al.* (2007a), Rezeau *et al.* (2018), Fadanelli *et al.* (2019) and especially Shi *et al.* (2019) for a review - anyway, all such methods will be presented in more detail through subsection 4.1.3).

Let us now suppose that the Taylor hypothesis holds, making it possible to imagine the data as resulting from each spacecraft traversing a fixed plasma structure along some curve. In this case it is possible to determine a relative velocity between the plasma structure and the probes. This possibility has been explored in particular with a focus on the magnetic field, i.e. for the determination of a "magnetic structure velocity" $\vec{c}_X$ (a quantity which is thoroughly discussed in subsection 7.2.3). In this procedure, however, even slight departures from a "perfect" Taylor behaviour can lead to misleading results (as recently shown by Manuzzo *et al.* (2019)).

Always supposing the Taylor hypothesis, a robust analysis of the plasma environment surrounding a spacecraft is that of variances. The idea is that the variance of the values of some physical vector field $\vec{\Psi}$ can indicate the dimensionality and orientation of the plasma structure encountered by the spacecraft. To be clearer, let angle brackets indicate average over the data segment relative to the spacecraft crossing the structure and recall that the variance ellipsoid from this segment of measurements is the rank-3 symmetric tensor:

$$\vec{\vec{\mathcal{C}}}_{\vec{\Psi}} := \langle \vec{\Psi}\vec{\Psi} \rangle - \langle \vec{\Psi} \rangle \langle \vec{\Psi} \rangle \tag{3.4}$$

with $\vec{\Psi}$ as a reference vector field. Now, $\vec{\vec{\mathcal{C}}}_{\vec{\Psi}}$ is characterised by three orthogonal eigenvectors $\pm\vec{e}_{\text{min}}$, $\pm\vec{e}_{\text{med}}$, $\pm\vec{e}_{\text{max}}$ each specifying a direction. Over the measures' set, the three components of $\vec{\Psi}$ in the directions individuated have null co-variances with respect to each other. Moreover, over the same set of measures, each component of $\vec{\Psi}$ separately has the variance specified by the eigenvector associated with the eigenvalue determining the direction considered. Hence, if the structure is approximately one-dimensional then one of the eigenvalues will be much larger than the other two, and if the structure is about two-dimensional then one of the eigenvalues will be much smaller than the others. Only three well-separated eigenvalues imply a fully three-dimensional plasma structure. As for structure velocity, the first historical use of variance analysis has been with the magnetic field as $\vec{\Psi}$ (see Sonnerup & Cahill (1967)). As robustness of the general framework has lead to its widespread success, variance analysis has been performed also onto many other fields (see for instance Paschmann *et al.* (1990), the appendix of Mozer & Retinò (2007), Haaland *et al.* (2004a)).

Another possibility to obtain information about the local shaping of fields around some spacecraft consists in comparing the time-series of data, with some reference function, obtained from a theoretical model of the structure we think to have crossed. Since structure models are generally time-stationary, usually the Taylor hypothesis is needed for this kind of operations. Analyses of this kind allow, for instance, to identify current sheets and flux ropes from magnetic field measurements. While it is possible to identify and characterise flux ropes with one single time-series (e.g. Rong *et al.* (2013)

and Huang *et al.* (2018)), the orientation of current sheets can be retrieved only by comparing multi-spacecraft data, either via gradient-based techniques (such as Shen *et al.* (2007b)), either by performing a so-called "timing analyses" (see chapter 12 in Paschmann & Daly (1998)). Strong and weak points of all these methods have been tested several times (see Haaland *et al.* (2004b), Denton *et al.* (2018)).

To conclude, here I will list some of the techniques one can exploit to retrieve more characteristics of the plasma structures encountered by the satellites if we assume not only the Taylor hypothesis, but when we also combine measures of different physical quantities. Given the difficulty of this task, this has generally been done under the simplifying assumptions one-dimensionality or two-dimensionality.

Studying one-dimensional structures (as current sheets), when disposing of both the electric and magnetic field, one can retrieve normal and velocity of an approximately one-dimensional structure by individuating a "deHoffman-Teller" frame (see Sonnerup *et al.* (1987)) or by minimisation of various "residues" i.e. quantities that should be always null over the whole of the data interval relative to the probe traversing an "idealised" discontinuity (see for instance the "Minimum Faraday Residue" in Khrabrov & Sonnerup (1998), the "Minimum Mass flux Residue" in Sonnerup (2004)) Other common analysis techniques involve the check of momentum and energy balances (see for instance Paschmann *et al.* (1986)). Passing to two-dimensional structures (as flux ropes), it is worthy here to quote only a discretely fortunate technique; the so-called "Grad-Shafranov reconstruction" (see for instance Hasegawa *et al.* (2017)). This method provides plasma characteristics throughout a neighbourhood of the spacecraft, and it does so by assuming magnetohydrodynamic equilibrium and the some trajectory of the probe, generally taken as a straight segment.

3.1.5 Finding and analysing reconnections in spacecraft data

Given the fundamental role played by reconnection in space plasma physics, several analysis techniques have been developed with the precise intent of detecting and/or characterising reconnection sites from spacecraft measurements.

As of nowadays, a systematic method to individuate automatically the passage of spacecraft close to reconnection sites is still in course of development, even if in many cases it has been documented that the satellites have transited in the vicinity of a reconnection (see chapter 12 of Balogh *et al.* (2014) for an overview on CLUSTER results, while with MMS I refer to Burch *et al.* (2016a) for the first detection of a EDR and Webster *et al.* (2018) for a longer catalogue of EDR encounters). Basically, in all cases in which proximity to reconnection has been ascertained, multiple features have been considered at once, and only from the overall picture it has been concluded that reconnection was close. So, in spite of several quantities being known as indicative of reconnection (as for instance the field-parallel heat fluxes for electrons, or more complicated, ad-hoc proxies - see Scholer *et al.* (1981), Lavraud *et al.* (2006) and the chapter by Scudder in Gonzalez & Parker (2016) or Wendel *et al.* (2018)), the most promising road seems to be that of train some artificial intelligence to the scope of individuating recon-

nections. This methods, already implemented for the automatic detection of several characteristic signatures in spacecraft-collected data (such as in Nguyen *et al.* (2019) and Argall *et al.* (2020)), however, call first for the production of training databases in which a large number of passages close to reconnections are registered, which are currently in the making (see Paschmann *et al.* (2018)).

Once reconnection sites have been identified, specific methods have been devised to study them. On one hand these methods can focus on the determination of spacecraft trajectory within a reconnecting environment, either assumed to be linear around the X-point, either simulated by some ad-hoc numerical experiment (see Wendel & Reiff (2009), Denton *et al.* (2016a), Alm *et al.* (2017), Shuster *et al.* (2017)). On the other hand, some techniques also aim at the estimate of relevant reconnection parameters, and in particular the reconnection rate (see Nakamura *et al.* (2018) or Genestreti *et al.* (2018a)). Also these methods, however, constitute a branch of space plasma physics in which there is currently active research.

3.2 Numerical experiments with the HVM code

Since this thesis has been based also on the analysis of numerical experiments, this section is devoted to a brief presentation of the HVM code, developed at the Pisa university, which has produced the data I analysed. To this end, first I introduce the reader to the plasma model the code exploits (subsection 3.2.1), and then I add some technical detail on discretisations and normalisations adopted (subsection 3.2.2). Finally, I describe a numerical experiment conducted via the HVM code, from which comes the data used in my analyses (subsection 3.2.2), and I conclude by reviewing some of the techniques to identify and characterise reconnection in simulated plasma (subsection 3.2.4). As for the techniques presented to analyse spacecraft data, so in this overview the underlying spirit is to provide the reader with a panorama of the situation in the field.

3.2.1 Plasma model and phase space in the code

The hybrid Vlasov-Maxwell code HVM (see Valentini *et al.* (2007)), developed mainly at the University of Pisa, models the collisionless dynamics of a non-relativistic, quasi-neutral ion-electron plasma, as prescribed by a generalised Ohm's law, by integrating the Vlasov equation for the ions and solving a system of fluid equations (with different possible closures) for the electrons (aside: note that since the characteristic lengths of ion dynamics are larger than those for the electrons, if one wants to resolve the system at the same scales for both species then the description of ions must be more accurate than that for electrons). This combination allows for a good compromise between computational demands, stability and accuracy in the results, making it so that the code has been widely used and expanded for over twelve years as of now (see Servidio *et al.* (2015) and references therein).

Let me be clearer now on the characteristics of the plasma model implemented in the code. First, as said before, ion dynamics is taken care of by Vlasov's equation, and this way it can be assumed to be "perfect" up to the code's resolution (which, by the way, is noteworthy as it follows a direct, Eulerian algorithm). Electrons being fluid, instead, call for the need of a closure - the three possibilities implemented, as of now, are an isothermal (i.e. a polytropic with $\gamma = 1$ - see subsection 2.1.1), a double polytropic (see for instance in Del Sarto & Pegoraro (2018)) and a Landau-fluid (as described in Sulem & Passot (2015)). Since only two species are present and quasineutrality is assumed, the electron density and velocity can be immediately obtained by combining ion density, ion velocity and current density. This implies that it is not necessary to solve the first two fluid moments of Vlasov for the electrons (read: Eqs. 2.3 and 2.4) but only it is required to implement the equations relative to higher moments. Moreover, the generalised Ohm's law by which $\vec{E}$ is obtained (see 2.1.2) follows from a clever combination of Euler's equation for ions and Euler's equation for electrons. This can be obtained if one multiplies Eq. 2.6 by the factor q/m and then sums up over the species: since the partial temporal derivatives combine into the term $\partial_t \vec{J}$ which one can understand as $-c^2\,\vec{\nabla} \times (\vec{\nabla} \times \vec{E})$ thanks to Ampère and Faraday's laws, the overall resulting equation can be solved for the electric field, and therefore it constitutes a valid possibility as generalised Ohm's law.

Solving plasma dynamics in the model just presented calls for the initial setting of the magnetic field $\vec{B}$, ion distribution functions at each point and specify all electron moments from the pressure upwards (depending on the closure adopted). As the ions are set to be initially Maxwellian, the only parameters to regulate are local number density (which will be the same for electrons), fluid velocity and pressure, everywhere through the physical space modelled (usually with the prescription that the configuration chosen is a slightly perturbed equilibrium). Physical space over which the code is run can be represented in all generality as a three-dimensional orthogonal box with periodic boundaries, of lengths L_x, L_y and L_z respectively (aside: setting the L_z to zero is also a viable possibility, making the box two-dimensional). In velocity space, instead, the code covers a cubic domain, centred on the origin of Cartesian axes and extending to some $\pm v_{\text{max}}$ in all directions. The value of v_{max} is set so that $\mathfrak{f}$ assumes negligible values (below 10^{-13}) at the boundary of the velocity space considered in the computation.

3.2.2 Normalisations and discretisations

In numerical experiments, on one side the phase space must be discretised so to be resolved up to the required accuracy (see subsections 7.1.2 and 7.1.3) and on the other side all quantities must be normalised so that their values do not exceed computational capabilities. The equations implemented in the code, together with the initial conditions posed force our hand on normalisations and discretisations used throughout the simulation. In particular, given a unitary length $\ell_\varnothing$ and a unitary time $\tau_\varnothing$ as well as a unitary mass $m_\varnothing$ and a unitary charge $q_\varnothing$ one can deduce the unitary values for each

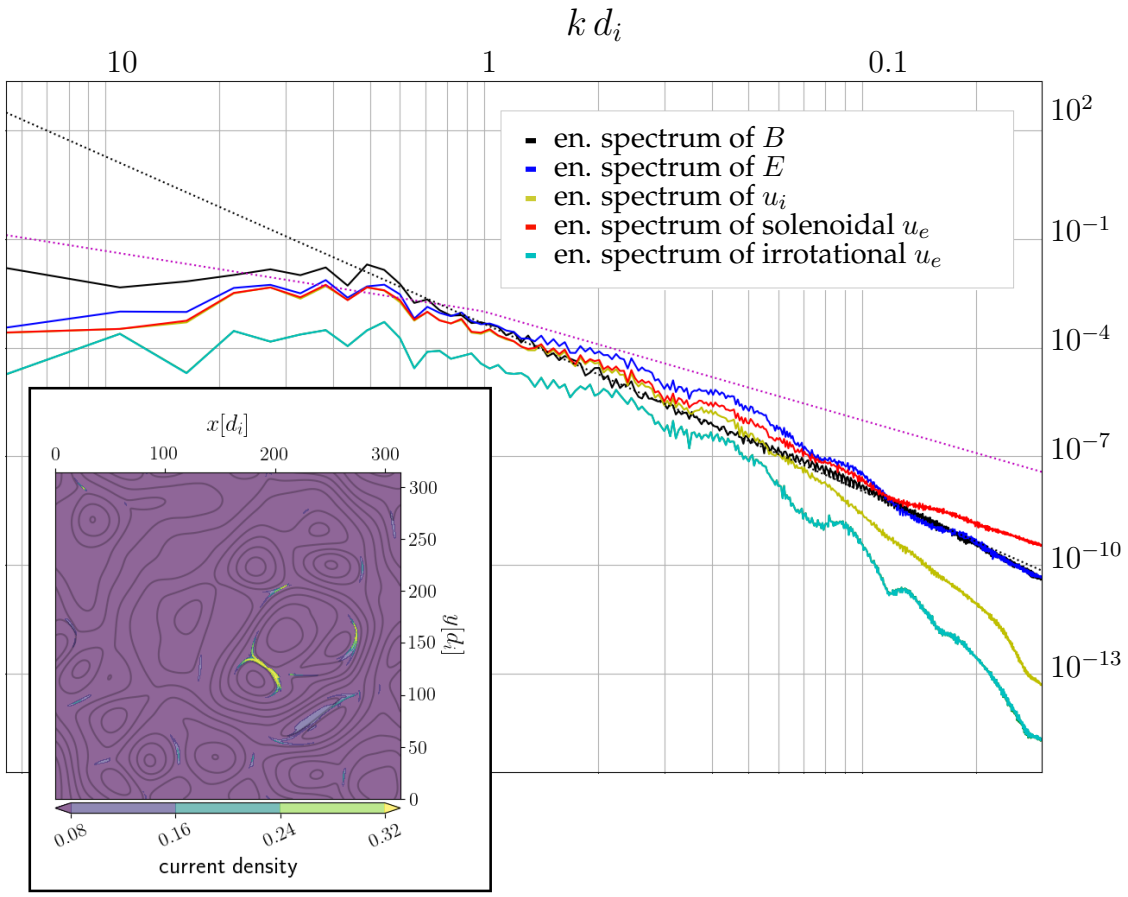

FIGURE 3.4: A snapshot a turbulence simulation presented in the text, and the energy spectra of fluctuations in B, E, u_i and u_e (own image - see inset for the legend on specific colours). In the snapshot, taken at 170 τ_i after the beginning of the simulation, the grey lines represent in-plane projections of magnetic field lines, while the different colours indicate zones of higher and lower current density. It can be recognised that the system's overall appearance is that of a series of magnetic "bubbles" i.e. "islands" or "vortices". The local scale of the system is the larger inside the vortices, and smaller in between vortices.

physical quantity, as:

$$n_\varnothing = m_\varnothing c^2/4\pi\ell_\varnothing^2 q_\varnothing^2 \qquad E_\varnothing = m_\varnothing \ell_\varnothing/q_\varnothing\tau_\varnothing^2$$
$$u_\varnothing = \ell_\varnothing/\tau_\varnothing \qquad B_\varnothing = m_\varnothing c/q_\varnothing\tau_\varnothing$$
$$P_\varnothing = m_\varnothing c^2/4\pi\tau_\varnothing^2 q_\varnothing^2$$

Therefore, once that the four parameters $\ell_\varnothing$, $\tau_\varnothing$, $m_\varnothing$ and $q_\varnothing$ have been chosen, one gets the normalisation values to be used for all quantities.

Given the plasma regime in which it is meant to operate, HVM normalises lengths to the ion inertial length ℓ_{di}, times to the proton cyclotron period τ_{gi}, masses to the proton mass and charges to the proton charge. Since ℓ_{di} depends only on the average initial density $n_\star$ and τ_{gi} is determined solely by the average initial intensity of the magnetic field $B_\star$, the two parameters $n_\star$ and $B_\star$ alone determine normalisation conditions in HVM codes. In other words, given $n_\star$ and $B_\star$ one can determine $\ell_\varnothing = \ell_{di}$ and $\tau_\varnothing = \tau_{gi}$ and the unitary values of all quantities, which follow according to the previous equations. In particular, note that the unitary density is the average initial density $n_\varnothing = n_\star$

and similarly $B_\varnothing = B_\star$ i.e. the average initial intensity of the magnetic field is one in code units.

In order to resolve the timescales and lengths of interest, the phase space domain is discretised as follows. The physical space $[0, L_x] \times [0, L_y] \times [0, L_z]$ is sampled by $N_x \times N_y \times N_z$ grid points, with approximately 10 points for ℓ_{di}. The velocity space, instead, is discretised in each direction by a number of points which is deemed sufficient to allow a satisfactory description of the distribution function. In order to be effective, timestep must comply with the CFL condition for the numerical stability of the Vlasov algorithm (see Peyret & Taylor (1983)).

3.2.3 Numerical experiments: reproducing turbulence

As an example of the capabilities of the HVM code, here I describe the results of a numerical experiment run in a two-dimensional geometry. The spatial domain is set to be square, with $L_x = L_y = 100\pi d_i$, and the cube portion of velocity domain which computations cover extends with v_{max} being set five times the initial ion Alfvén velocity (the ion distribution function will be set so to "fit" inside this cube). Discretisation of the spatial domain is carried on with $N_x = N_y = 3072$ points, while the velocity space is approximated on a grid of $51 \times 51 \times 51$ points. As initial conditions, it has been set that the system has uniform values of density, pressure, magnetic field, and that it is completely at rest (aside: note that a strong-enough guide-field is necessary when one performs the choice of two-dimensional geometry, because it is when an ambient $\vec{B}$ is present that perturbations tend to develop bidimensionally). Ion and electron pressures are set equal, and such that the ratio $(c_T/c_A)^2$ also known as "plasma beta", is one. This allows the ion distribution function, which is set gaussian, to "fit" into the cube of velocity space which is covered by calculations. Turbulence is then initiated by a sum of magnetic fluctuations, statistically isotropic, resulting from a random combination of the first five Fourier modes of the box (corresponding to the largest wave lengths admitted by the system).

As turbulence develops, the large-scale perturbations excite a cascade of fluctuations towards smaller and smaller scales. A strong indication of this behaviour is usually found by investigating the evolution of "energy spectra" (i.e. the distributions of the Fourier transformed intensity relative to the wavenumbers' modules) of several physical quantities (see Frisch (1995)). In Fig. 3.4, the development of small-scale perturbations is evident as the modes at high wavenumber, which were not excited at the initial time, are present. Moreover, however, it must also be noted that small-scale fluctuations in plasma tend to concentrate in some portions of the system, displaying a behaviour generally known as intermittency (see chapter 8 of Frisch (1995)). Hints of intermittency can be seen also in the simulation just presented, for instance in the fact that the system generates current sheets which are distributed in a non-homogeneous way (see Fig. 3.4). Similar performances of the code can be found in other runs or simulations, both two-dimensional and three-dimensional, exploited and discussed in several publications (I refer the reader to Servidio *et al.* (2015) and references therein for a review of similar results obtained by HVM).

3.2.4 Detection of reconnections in simulations

Alongside with flux ropes and current sheets, in plasma turbulence magnetic reconnection develops, hence the need of methods to individuate reconnection sites.

To individuate reconnection sites, if one searches for physical signatures, it must be always kept in mind that these will be limited by the amount of physics which the code reproduces, i.e. in the HVM case, substantially by the fact that electronic behaviour is not completely modelled. Therefore, while some of the physics-based indicators can in general be exploited (again, I refer to Scudder in Gonzalez & Parker (2016), Goldman *et al.* (2016), Wendel *et al.* (2018) as examples, but also to Lapenta *et al.* (2015a) and Daughton *et al.* (2014)), still it is generally preferred to go for the magnetic null points (in-plane hyperbolic nulls for the two-dimensional case, generic nulls if one is three-dimensional).

Looking for null points, one of the most used methods is by a generalisation of the well-known bisection procedure (see Greene (1992) - the idea behind this kind of search is that if a magnetic null is present in some volume, then the values which $\vec{B}$ attains over the surface of this volume should identify, in the space defined by $\vec{B}$ components, a surface which must encompass the origin). If the configuration is two-dimensional, however, one can also find in-plane magnetic nulls by finding critical points of the flux function (see subsection 7.2.1). In particular, X-points in which we are interested can be found in correspondence of saddles in the flux function (as it is done, for instance, in Servidio *et al.* (2009)), and different techniques exist to identify these. One possibility, for instance, is to investigate the values attained by the flux function on contours of surfaces: a positive-negative-positive-negative pattern individuates the presence of a saddle of the function at some point inside the surface (see Peucker & Douglas (1975)). The other technique generally implemented is the so-called "watershedding" i.e. an analysis of integral curves of the flux function's gradient (see section 11.3 of Rana (2004)). In all cases just presented, however, for the good outcome of such analyses it must be noted that it is crucial to work on a "smoothed enough" function, i.e. finding the correct methods for filtering noise out of the data with care enough to maintain all relevant features nonetheless (see for instance the procedure presented in Servidio *et al.* (2010), for smoothing the flux function - for generalities to keep in mind while performing this kind of analysis, see subsections 7.1.2 and 7.1.3).

Chapter 4

The local configuration of magnetic fields

4.1 Motivation and outlook

This section introduces the reader to my work on magnetic configurations. To this aim, first I recall how it is possible to represent a magnetic configuration, introducing the reader to the three techniques of MDD, MRA and MCA (subsection 4.1.1). After some technical details (subsection 4.1.2) I compare the three techniques presented, and this concludes my introduction to the local study of magnetic configurations (subsection 4.1.3).

4.1.1 The local analysis of magnetic configurations

In a magnetised plasma the local configuration of the magnetic field plays a key role in the system's dynamics at all scales, in particular, by controlling the evolution of large structures, regulating how waves propagate and feeding most of the instabilities that can be excited. Moreover, magnetic configurations can bear the footprint of plasma relaxation processes and provide significant insight not only into the possible dynamical evolution of the system but also relative to its past history. Therefore, when studying the dynamics of near-Earth plasmas, in the terrestrial magnetosphere, in its magnetosheath and in the solar-wind, it is of fundamental importance to understand how the magnetic field is locally shaped. To this end, it is particularly useful to define methodologies which provide us with some kind of "measure" of the local magnetic configuration.

While several possibilities exist to characterise the local magnetic field configuration, here I will consider the topic by reviewing two techniques first, the "Magnetic Directional Derivative" (MDD) procedure presented in Shi *et al.* (2005) and the Magnetic Rotational Analysis (MRA) by Shen *et al.* (2007a), then conclude by introducing the Magnetic Configuration Analysis (MCA) from Fadanelli *et al.* (2019) on which I have relied. Since the common "root" of all these techniques lays in the idea that the characterisation of magnetic configurations can be attained by thorough examination of magnetic field gradients, in theory MDD, MRA and MCA can be applied to any set of measures which includes the magnetic field's gradient, hence both to multi-spacecraft

data and the results of numerical simulations.

In order to characterise a magnetic configuration, MDD focuses on the square of the directional derivatives of $\vec{B}$. By identifying a generic direction by the unit vector $\vec{e}$, the square of the directional derivative along $\vec{e}$ is given by:

$$I_{\text{MDD}}(\vec{e}) := [\vec{e} \cdot \vec{\nabla}\vec{B}]^2 = \vec{e} \cdot [\vec{\nabla}\vec{B}] \cdot [\vec{\nabla}\vec{B}]^T \cdot \vec{e} =: \vec{e} \cdot \vec{\vec{\mathcal{C}}}_{\text{MDD}} \cdot \vec{e} \tag{4.1}$$

where the superscript "T" indicates the transpose and the configuration tensor $\vec{\vec{\mathcal{C}}}_{\text{MDD}}$ has been defined as the scalar product between the gradient of $\vec{B}$ and this same tensor, transposed. In particular, noting that this last tensor "contains" the square of any directional derivative, the MDD paradigm regards it as the carrier of all information about local magnetic configurations (and as such, it has been the starting point of dimensional analyses of magnetic environments, such as in Rezeau *et al.* (2018)).

Now, what can be regarded as a "weak" point of the MDD method when investigating magnetic configurations is its dependence on the local intensity of the magnetic field and not only on the magnetic field local shape. For example, let us assume we perform MDD on some magnetic configuration, then change (globally) the intensity of $\vec{B}$ and perform MDD again. While the MDD outcome (that is, the configuration tensor) has changed between these two calculations, one could still say that the "magnetic configuration" in the two cases is exactly the same. In other words, interpreting magnetic configurations by a MDD analysis allows to recognise the "absolute" spatial rates of change of the magnetic field - and yet, this might not always be the information one is interested into.

A different way to deal with magnetic field configuration is the "Magnetic Rotational Analysis" (MRA), introduced by Shen *et al.* (2007a) as a development of the "geometrical" characterisation of the local magnetic field based on the field's curvature in Shen *et al.* (2003). Basically, MRA consists in carrying out the very same analysis as MDD but on the normalised magnetic field $\vec{e}_B := \vec{B}/B$ instead than using $\vec{B}$ itself. The idea behind MRA is to focus primarily on the "magnetic rotation rate" along the generic $\vec{e}$ direction, i.e. the square root of:

$$I_{\text{MRA}}(\vec{e}) := [\vec{e} \cdot \vec{\nabla}\vec{e}_B]^2 = \vec{e} \cdot [\vec{\nabla}\vec{e}_B] \cdot [\vec{\nabla}\vec{e}_B]^T \cdot \vec{e} =: \vec{e} \cdot \vec{\vec{\mathcal{C}}}_{\text{MRA}} \cdot \vec{e} \tag{4.2}$$

Similar to $\vec{\vec{\mathcal{C}}}_{\text{MDD}}$ in MDD, in MRA the configuration tensor $\vec{\vec{\mathcal{C}}}_{\text{MRA}}$ carries all information related to all possible "rotation rates" in all directions for each point in space and, therefore, in MRA it can be understood as the "holder" of all information regarding the local magnetic configuration.

While not depending on local magnetic field intensity, however, MRA cannot describe the fully three-dimensional nature of magnetic configurations. This can be shown once considered that the $\vec{e}_B$ field (on which MRA is built) has only two degrees of freedom: because of this its configuration tensor is degenerate, that is, its determinant must be zero and therefore one of the MRA eigenvalues is always null (as detailed in Appendix

A of Fadanelli *et al.* (2019)). In conclusion, by construction, the configuration tensor of MRA would describe a three-dimensional configuration only by two characteristic lengths.

To overcome the limitations of both MDD and MRA while investigating local three-dimensional magnetic field configurations, in Fadanelli *et al.* (2019) it was suggested that an effective "Magnetic Configuration Analysis" (MCA) could be obtained by considering a "normalised MDD" method based on the directional derivative divided by the local magnetic field intensity:

$$I_{\mathrm{MCA}}(\vec{e}) := \frac{[\vec{e}\cdot\vec{\nabla}\vec{B}]^2}{B^2} = \vec{e}\cdot\frac{[\vec{\nabla}\vec{B}]\cdot[\vec{\nabla}\vec{B}]^T}{B^2}\cdot\vec{e} =: \vec{e}\cdot\vec{\vec{C}}_{\mathrm{MCA}}\cdot\vec{e} \tag{4.3}$$

Since $\vec{\vec{C}}_{\mathrm{MCA}}$ does not change under re-scaling of $\vec{B}$ (thanks to the factor appearing at the denominator in its definition) nor it is forcedly degenerate (i.e. it provides three different values to characterise a three-dimensional shape), it can be understood as sufficient for describing any local magnetic configuration. In other words, by performing MCA one is provided with spatial rates of change which are not absolute but rather relative to the configuration examined.

4.1.2 How to deal with rank-3 symmetric tensors

As we have seen, all the three methods of MDD, MRA and MCA end up representing local magnetic configurations by rank-3 symmetric tensor fields. So - before proceeding - let me point out some basic characteristics of these (such as in 8.2.4 of Paschmann & Daly (1998)). Firstly, any rank-3 symmetric tensor is totally determined by its three "proper directions" (eigenvectors) and "proper values" (eigenvalues):

σ_{max}	maximum eigenvalue	$\pm\vec{e}_{\mathrm{max}}$	direction of max. eigenvector
σ_{med}	intermediate eigenvalue	$\pm\vec{e}_{\mathrm{med}}$	direction of int. eigenvector
σ_{min}	minimum eigenvalue	$\pm\vec{e}_{\mathrm{min}}$	direction of min. eigenvector

A somewhat intuitive way to deal with the information contained in these quantities is to visualise a symmetric tensor field as a set of ellipsoids, one for each point in space, constructed so that ellipsoid's axes are everywhere aligned along the local eigenvectors, the axes' lengths inversely proportional to the square roots of the corresponding eigenvalues - see Fig. 4.1. Regardless whether one uses MDD, MRA or MCA to construct the configuration tensor, the "variation ellipsoid" corresponding to it will provide an immediate graphical representation of the local magnetic configuration, as intended by the underlying construction method. In particular, the more stretched an ellipsoid in some direction, the more gentle the variation of magnetic field in that same direction, and the more elongated there the magnetic configuration. Vice-versa, in the directions where the ellipsoid is thinner, there the magnetic field changes the most abruptly and hence one interprets the magnetic configuration to be compressed. Finally, ellipsoids of the same shape, but scaled, are understood to represent similar configurations, the one being a scaled version of the other.

In order to turn the previous statements into a more rigorous form, it is convenient to introduce specific evaluators for shape and scale of magnetic configurations. Regarding how the configuration scales, any of the three eigenvalues could be taken as reference. However, noting that the characteristic lengths of a configuration scale as the inverse of square roots of the eigenvectors, local scale will be well represented by $1/\sqrt{\sigma_{\max}}$ (that is the smallest length in the magnetic configuration). Focusing on shapes instead, an intuitive way is to define the following two parameters:

$$\begin{aligned} \text{elongation} \qquad & \mathscr{E} := 1 - \sqrt{\sigma_{\min}/\sigma_{\text{med}}} \\ \text{planarity} \qquad & \mathscr{P} := 1 - \sqrt{\sigma_{\text{med}}/\sigma_{\max}} \end{aligned} \tag{4.4}$$

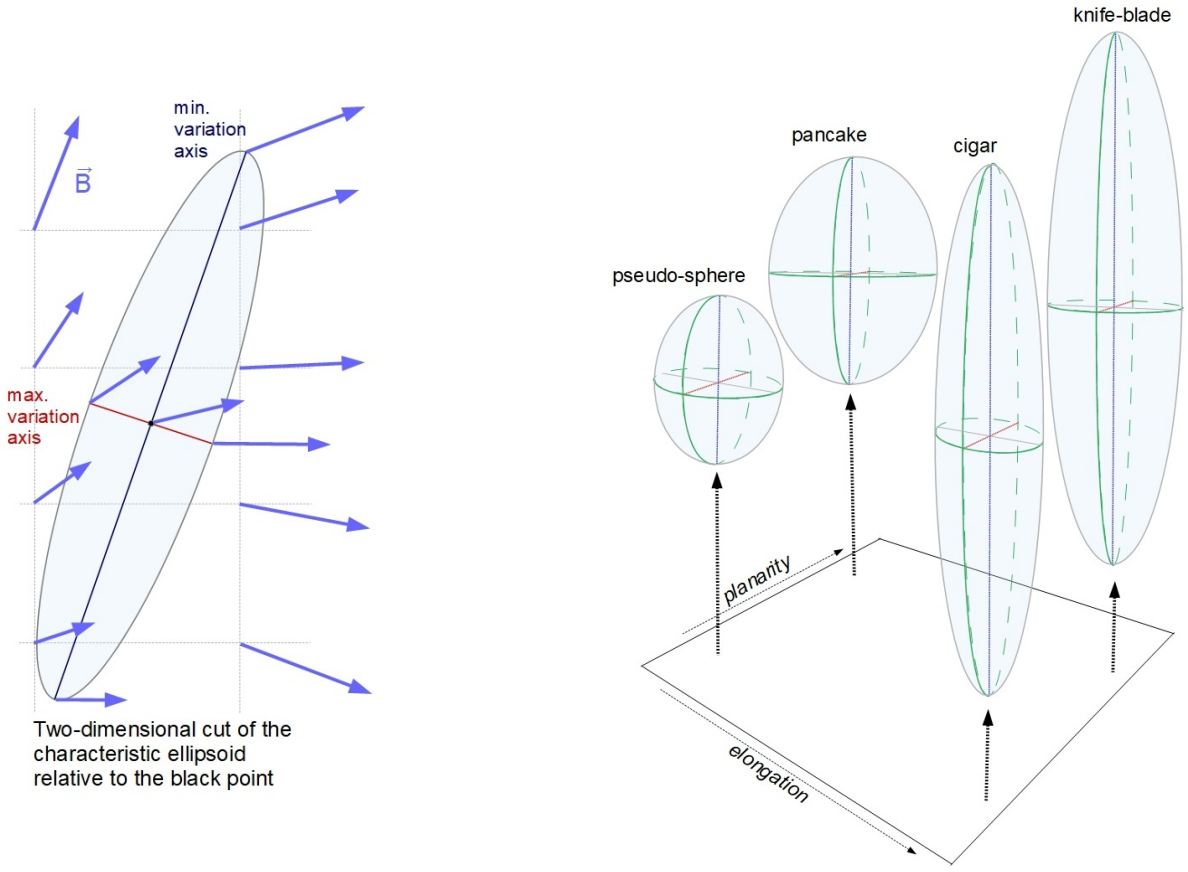

FIGURE 4.1: Schematic of magnetic configurations (own image, also in Fadanelli *et al.* (2019)).
Left: a sketch showing how MCA constructs a characteristic variation ellipsoid for the magnetic field around the point highlighted in black, with the local magnetic configuration suggested by blue arrows. Differences between the magnetic field at the centre of the ellipsoid (black point) and that at the endpoints of its axes are the same for each of the axes. Note that for simplicity we have made the choice of drawing only a two-dimensional (plane) cut of the three-dimensional field and ellipsoid. The other three methods presented - MVA, MDD and MRA - obtain configuration ellipsoids in a similar fashion.
Right: schematic representation of the different "standard" shapes of variation ellipsoids: pancake, knife-blade, pseudo-sphere, and cigar. The maximum and minimum variation axes all highlighted in red and blue, respectively. For a pancake shape (low $\mathscr{E}$, high $\mathscr{P}$) the maximum and intermediate lengths in the configuration are nearly equal, while in a "cigar" (high $\mathscr{E}$, low $\mathscr{P}$), it is the intermediate and minimum ones that are similar. The case of well-separated lengths (high $\mathscr{E}$, high $\mathscr{P}$) falls under the denomination of "knife-blade," while "pseudo-sphere" i.e. for three similar axes (low $\mathscr{E}$, low $\mathscr{P}$).

as elsewhere in the literature (see chapter 13 of Paschmann & Daly (1998) and references therein). These parameters measure the tendency of the local rotation ellipsoid to squeeze toward some one-dimensional elongated form ($\mathscr{E} \to 1$) or to flatten into a quasi-two-dimensional surface ($\mathscr{P} \to 1$). Therefore, the (local) shaping of $\vec{B}$ may be represented by a point in the $\mathscr{E} - \mathscr{P}$ parameter space (Fig. 4.1, panel b). We also decide to classify the local shape of $\vec{B}$ by picking up the terminology used for spacecraft tetrahedrons: "pseudo-spheres" (low $\mathscr{E}$, low $\mathscr{P}$), "cigars" (high $\mathscr{E}$, low $\mathscr{P}$), "pancakes" (high $\mathscr{P}$, low $\mathscr{E}$) and "knife blades" (high $\mathscr{E}$, high $\mathscr{P}$) – the more generic "potato" (intermediate $\mathscr{E}$ and $\mathscr{P}$) being left out of our discussions for the sake of simplicity (for a visual representation of this classification, see Fig. 4.1).

This shape classification naturally leads to the possibility of recognising local approximate "dimensionalities" for the magnetic field configuration. For example, where $\vec{B}$ displays a pancake shape, we know that its variation in one direction is much more pronounced than in the other two and thus the local magnetic environment is quasi one-dimensional. Conversely, finding a cigar shape suggests that variations in $\vec{B}$ along the longest of the ellipsoid's axes can be neglected with respect to those in the directions perpendicular to it, and thus the local magnetic structure can be thought of as two-dimensional. Note that the axes of our characteristic ellipsoids have been defined as the characteristic variation lengths of the magnetic field, and therefore "dimensionalities" are determined by the shortest rather than the longest of the ellipsoid's scales.

At this point, an important issue to introduce is that of error estimation, i.e. how does one assess to which extent the eigenvalues and eigenvectors detected can be assumed to be precise. Whenever the magnetic field gradient is calculated from multiple measures of $\vec{B}$ taken at a distance ℓ_{sep} apart, a simple estimate of the minimal eigenvector one can resolve is:

$$\min_{\text{res}} \sigma_{\text{MDD}} = \left[\frac{\delta B}{\ell_{\text{sep}}}\right]^2 \qquad \min_{\text{res}} \sigma_{\text{MRA}} = \min_{\text{res}} \sigma_{\text{MCA}} = \left[\frac{\delta B}{\ell_{\text{sep}} B}\right]^2 \tag{4.5}$$

with δB being the sensitivity of magnetic field probes and B the average local intensity of the magnetic field (see Fadanelli *et al.* (2019)). Interpretation of the previous formulas is immediate: given the instrumental error and inter-probe separation, this is the smallest eigenvalue which can be resolved by our measurement apparatus.

To recognise whether a characteristic direction is well-defined or not, instead, not only error threshold for eigenvalues are important but also considerations on shape and dimensionality. Indeed, mathematically, a "bad" definition of characteristic variance and directions happens whenever two eigenvalues are degenerate, as in that case it is not possible to individuate clearly two eigenvectors corresponding univocally to the eigenvalues. For practical applications, therefore, we must recognise that our capability to distinguish two of the characteristic directions from each other worsens each time that any two of σ_{min}, σ_{med} and σ_{max} approach each other, or equivalently, the closer that any of $\mathscr{P}$ and $\mathscr{E}$ gets to zero. This way, for instance, we understand that the only well-defined directions are the longest axis in "cigars" and "knife blades" and the shortest axis in "knife blades" and "pancakes". So, whenever we observe a series of "knife

blade" and "pancake" shapes through some data interval, there $\vec{e}_{\text{max}}$ provides a clear maximum angular variance direction, while only through intervals consisting of "knife blades" and "cigars" $\vec{e}_{\text{min}}$ determines a clear direction of approximate invariance.

Let me conclude this subsection with a two notes, the first regarding a possible way in which one can present eigenvectors as oriented unitary vectors. Whenever we intend to present proper variance directions by unitary vectors, indeed, then we need some orientation criterion. Now, a somewhat "natural" prescription could be to orient each axis to minimise the angle between the resulting unitary vector and some other unitary vector $\vec{e}_{\text{ref}}$ taken as reference. This criterion, however, can lead to small changes in the original ellipsoid provoking sudden $180°$ reversals in the resulting oriented unitary vectors. To avoid this, whenever dealing with time-series one can simply require the angle between two consecutive eigenvectors to be minimal. Once the orientation of the first vector has been arbitrarily selected, this prescription avoids sudden $180°$ reversals, therefore ensuring a "smooth transition" between consecutive unitary vectors (aside: in Huynh (2009) the interested reader can find a wider discussion on the problem of defining which triple of vectors is "the closest" to any other one). In the presence of not-simply-ordered data-sets, however, it must be recognised that this latter criterion cannot be simply applied, and one might well revert to the former.

The second note to conclude this subsection regards a possible way to deal with the statistical characteristics of sets of eigenvectors (which can be presented as "$\pm$" unit vectors). In most situations, the strategy I found the easiest has been to define an arbitrary, fixed direction $\vec{e}_{\text{ref}}$ and perform statistics on $|\cos(\theta)|$ where θ is the angle formed by some eigenvector and the reference direction $\vec{e}_{\text{ref}}$. Obviously, the cases of θ and $\pi - \theta$ come to be considered as equivalent when determining such absolute-valued-cosine distributions, since $|\cos(\theta)| = |\cos(\pi - \theta)|$. A further point of easiness is given once considered that perfectly random angles θ, which are distributed as $\sin(\theta)$, form naturally a flat distribution in the space of $|\cos(\theta)|$ (see for instance Wasserman (2004), section 2.11). In particular, since a random distribution of θ results into an uniform distribution for $|\cos(\theta)|$, from now on I will intend any statistical parameters relative to the set of angles (such as averages, variances, etc.) as the product of applying the $\arccos$ function to the corresponding quantities calculated from the distribution of $|\cos(\theta)|$ values.

4.1.3 Comparative performance of configuration analyses

A number of works has been dedicated to the evaluation of techniques which estimate the local magnetic field configuration, in particular starting from the MDD method (see Denton *et al.* (2010), Denton *et al.* (2012), and in particular the excellent review by Shi *et al.* (2019) which offers an overview of most of them). Here we will shortly discuss how MDD, MRA, and MCA do perform on the same event. For this experiment (or exercise) I chose to review an event that displays a great variation in magnetic field magnitude and therefore can highlight at best the differences among MDD, MRA, and MCA outcomes.

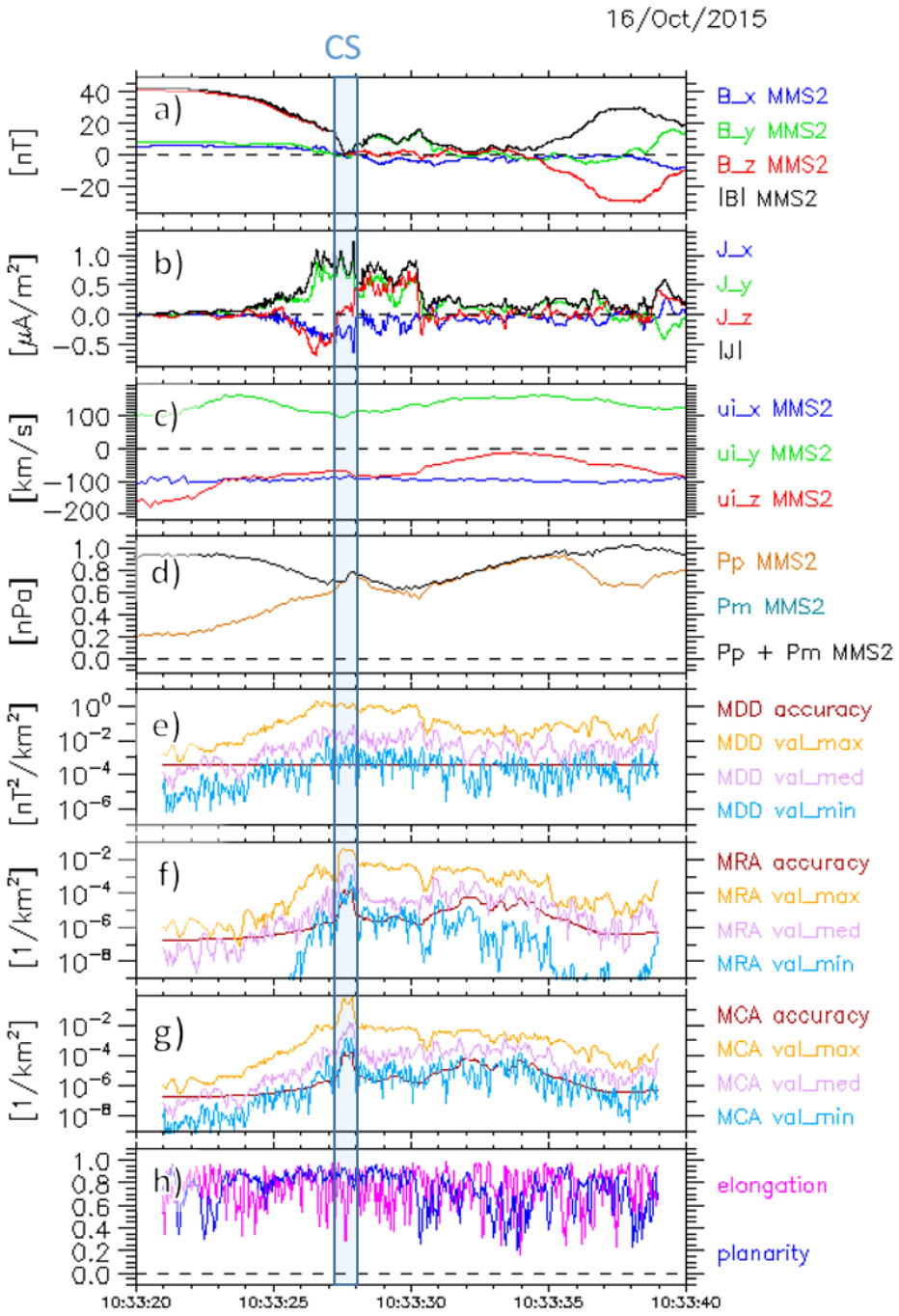

FIGURE 4.2: Data recorded by MMS2 between 11:33:20 and 11:33:40 UT on 16 October 2015, and results of the (four spacecraft) MDD, MRA and MCA analyses on the same data interval (image also in Fadanelli *et al.* (2019)). The four upper panels show characteristic plasma quantities: a) magnetic field, b) current from particle measurements, c) bulk ion flow (in GSE coordinates) and d) the three plasma "pressures" (thermal, magnetic and total). The four lower panels display results from configuration analyses: e) MDD eigenvalues, f) MRA eigenvalues, g) MCA eigenvalues, h) shape parameters (E and P) referred to MCA (or, equivalently, to MDD). Note that the additional line in the eigenvalue plot estimates the expected accuracy threshold (see Eq. 4.5 for its definition). Notice that MCA shows the presence of very small scales between 11:33:27 and 11:33:28 while MRA only partially recognises this and MDD does not consider it at all. The overall planar character of magnetic configurations traversed between 11:33:25 and 11:23:32 is also evident

In Fig. 4.2, panels (a) to (d) show characteristic plasma quantities: magnetic field, current density, ion velocity, and pressures. By these one can figure out that the spacecraft, which is trailing the subsolar magnetopause, is crossing here from the magnetosphere to the magnetosheath passing across the exhaust of an asymmetric reconnection site (see Lavraud *et al.* (2016)). This kind of movement is clearly suggested by the strong diminution of magnetic field intensity one can observe in the data, accompanied by a rotation of $\vec{B}$ which at the beginning is directed perfectly northward (see that the GSE-z component is strongly predominant) but at the end rotates southward and then even westward. An increase of plasma pressure also highlights the fact that the satellite is exiting the magnetosphere and entering the magnetosheath. The ion velocity is also suggesting a magnetopause which is moving towards Earth (note the constant negative component in the GSE-x direction, and the similarly constant positive GSE-y velocity, which also is indicative of a receding magnetopause since the satellites are located on the dusk side of Earth). Electron velocity is not directly reported, but can be inferred from the current density: wherever J is low, there electrons have the same velocity as ions: this happens at the beginning of the data interval, when the satellites are in magnetosphere, and in the second half of the data-set, when thy have crossed into the magnetosheath. A current sheet separates clearly these two low-current regions. In Fig 4.2, the data interval highlighted in azure and indicated by "CS" represents the core of this current sheet, which corresponds to a neat drop in magnetic field intensity.

Panels (e) to (h) of Fig. 4.2 show MDD, MRA, and MCA eigenvalues, respectively, along with the shape factors elongation and planarity relative to MCA and MDD. The accuracy thresholds follow the prescriptions in Eq. 4.5. Now, by examining MCA, one can easily recognise the presence of some small-scale configuration traversed between 10:33:27 and 10:33:28, whose shape somewhat oscillates between knife-blade and pancake since planarity is in general close to one and elongation behaves unsteadily. The notable similarity between MRA and MCA eigenvalues points out that the greatest contribution to the magnetic field gradient is given by differences in the direction of $\vec{B}$ between one spacecraft and the others, while differences in magnitude are in general less important. Average magnitude, however, is of fundamental importance since by neglecting its effects (that is, when performing MDD) one ends up losing track of some relevant features in magnetic configurations (like the small-scale region pointed out before).

4.2 Performing MCA on MMS data

Here I illustrate the results of two studies carried on via MCA on MMS data. In the first, I investigate how the local magnetic configuration is rendered by MCA in characteristic magnetic structures (flux ropes and current sheets) encountered by the spacecraft, thus assessing limitations and capabilities of the method in this situation (subsection 4.2.1). In the second, I perform statistics on the local configurations encountered by the spacecraft fleet (subsection 4.2.2). A short recapitulation of results concludes the section (subsection 4.2.3). All data hereafter has

been made available, and in some case plotted, via the CL program, developed and maintained by E. Penou at IRAP in Toulouse.

4.2.1 Case studies

In Fig. 4.3 is plotted a data-set containing two ion-scale flux-ropes which were observed within a reconnection exhaust at the magnetopause, as discussed by Eastwood *et al.* (2016). The magnetosphere, sampled at the beginning of the interval, is recognisable thanks to clearly positive values of B_z in GSE coordinates; the magnetosheath appears at the end of the interval (negative B_z). The flux ropes were identified thanks to bipolar variations in the B_x and B_z magnetic field components (see panel a) and peaks in both magnetic and total pressures (panel d). The crossings of the flux ropes are identified in Fig. 4.3 by the two-second shadings with labels "FR 1" and "FR 2" (FR for "flux rope"). We also show the FPI current (panel b) and the ion velocity (panel c), for context.

In the last four panels we display MCA results: the three eigenvalues (panel e), the two shape parameters $\mathscr{E}$ and $\mathscr{P}$ (panel f), the direction of $\vec{e}_{\text{max}}$ (panel g) and that of $\vec{e}_{\text{min}}$ (panel h) both expressed as unitary vectors. All MCA data presented here are presented using a 10-point moving window average, in order to smooth out some minor spiky oscillations. The thin, dark red line in the eigenvalue plot represents an expected lower accuracy limit that is analytically derived using an absolute magnetic field accuracy of 0.1 nT (see Eq. 4.5). Since the least MCA eigenvalue lays usually close or even below this threshold, in general we would not expect it to bear precise information – a limitation that is reflected therefore also in the values retrieved for the $\mathscr{E}$ parameter, but not necessarily in $\vec{e}_{\text{min}}$ since this eigenvector can be determined by vector product of the remaining two.

Aware of these caveats, let us compare MCA performance to that of known analyses on this event. In particular, one would expect $\vec{e}_{\text{min}}$ to identify the axis direction of flux ropes (as explained in subsection 4.1.2). This is indeed what we observe when investigating statistically the angle between the axis obtained in Eastwood *et al.* (2016) and the minimal MCA eigenvector direction around 13:04:34 UT (when the spacecraft was passing closest to the flux-rope core, as highlighted by the shading in the figure). Indeed, the angle distribution shows a sharp peak at $15°$ (the so-called "statistical mode" value), and for 50% of the data points in the interval considered this same angle is below $20°$.

In Fig. 4.4 we plot the same quantities as in Fig. 4.3 for a crossing of a current sheet embedded within a larger-scale compressive structure. While a first glance at the quantities in panels a) to d) might suggest that this event is similar to the previous one (note in particular similarities in the pressures), strong differences in the plasma properties before and after the magnetic field peak led Kacem *et al.* (2018) to identify this structure as the collision of two separate flux tubes. The thin current sheet in the middle of the event around 14:16:41 UT arises from the interaction of the flux tubes (the shaded two-second interval labelled "CS") and was demonstrated to be reconnecting (in Fig.

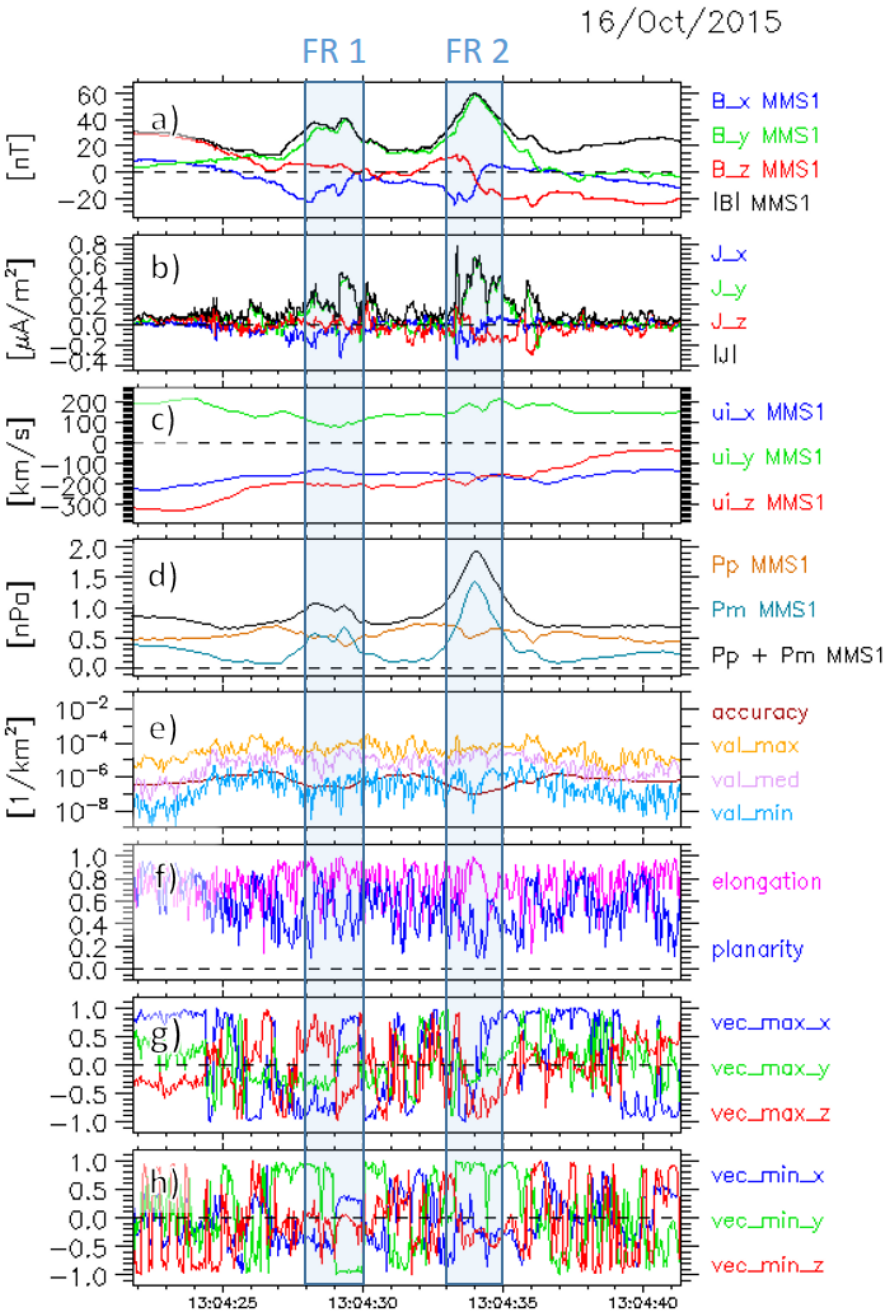

FIGURE 4.3: Data recorded by MMS2 between 13:04:20 and 13:04:45 UT on 16 October 2015, and results of the (four spacecraft) MCA analysis on the same data interval (image also in Fadanelli *et al.* (2019)). Two flux rope crossings can be recognised in the data highlighted by the shaded strips and labelled "FR 1" and "FR 2". The four upper panels show characteristic plasma quantities: a) magnetic field, b) current from particle measurements, c) bulk ion flow (in GSE coordinates) and d) the three plasma "pressures" (thermal, magnetic and total). The four lower panels display MCA results: e) eigenvalues, f) shape parameters ($\mathscr{E}$ and $\mathscr{P}$) and g)- h) the three components of the maximal and minimal normalised eigenvectors, respectively. The dark red line in the eigenvalue plot (panel e) estimates the expected accuracy threshold (presented in subsection 4.1.2). Notice that the "least variance" direction given by $\pm\vec{e}_{\text{min}}$ is well aligned with the flux rope axis estimated by Eastwood *et al.* (2016) through all the traversal of the second flux rope, highlighted by the shading. Spatial scales of flux ropes do not stand out as markedly different from those of the surrounding plasma, as indicated by the generally constant behaviour of MCA eigenvalues.

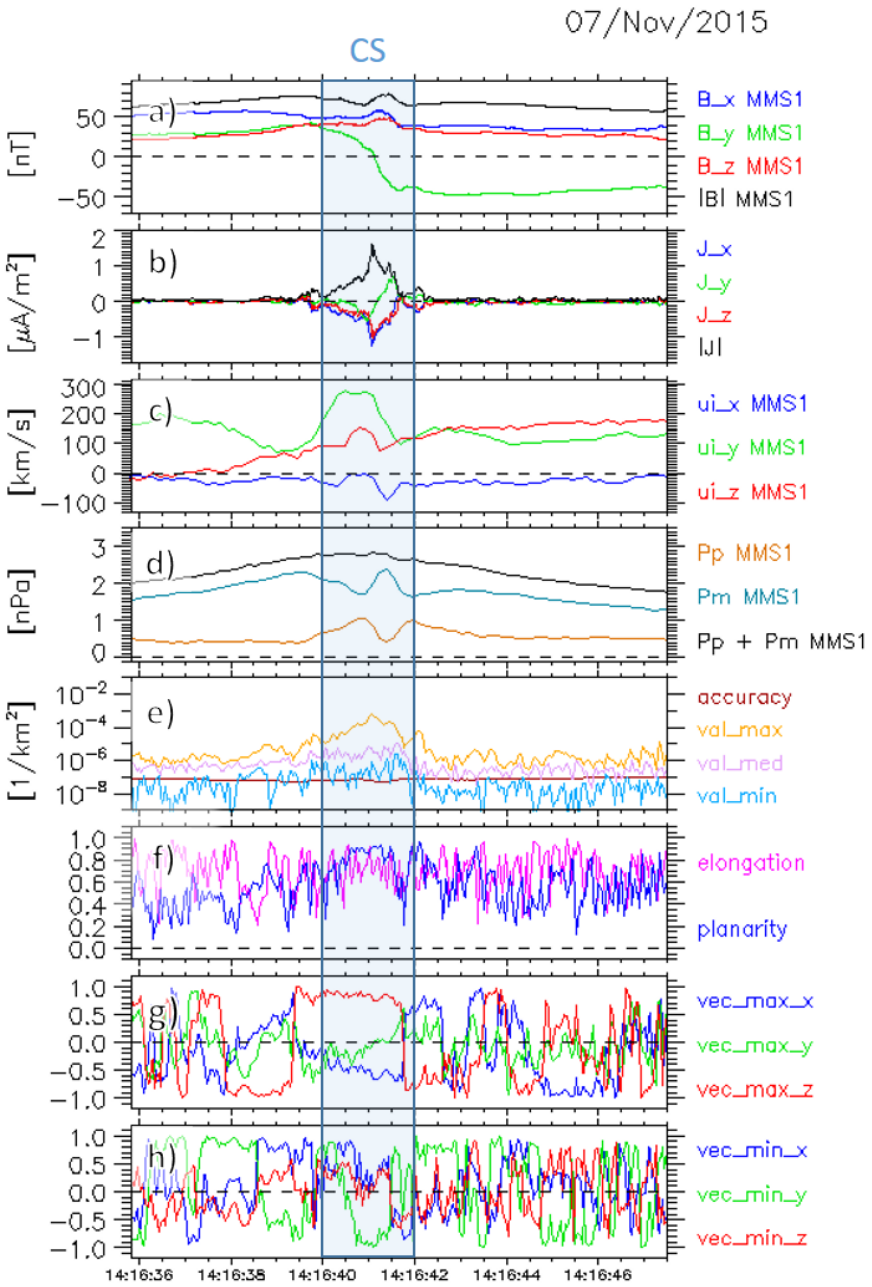

FIGURE 4.4: Overview of MMS2 observations and MCA results between 14:16:25 and 14:16:55 UT on 7 November 2015, with the shaded time interval labelled "CS" identifiable as a current sheet crossing (image also in Fadanelli *et al.* (2019)). All quantities presented in the panels are the same as in Fig. 4.3. The peaking of $\sigma_{\max}$ at the time of the highlighted interval (see panel e) indicates that one of the characteristic scales in the local magnetic field configuration is much lower inside the current sheet than in its surroundings. The direction in which $\vec{B}$ develops its smallest variation scale, indicated by $\pm\vec{e}_{\max}$ (see panel g), is consistent with the one found via MVA as reported by Kacem *et al.* (2018) during all the entire, highlighted current sheet traversal.

4.4 this can be seen in particular by looking at the ion flow, consistent with a reconnection exhaust). A thorough study of this event can be found also in Zhou *et al.* (2018a).

Again, here MCA can be tested by comparing directions individuated by MCA eigenvalues inside the current sheet with known results, and again MCA is found coherent with expectations. Indeed, while $\vec{e}_{\text{min}}$ oscillates (note that the more elongation differs from one, the worst the minimum rotation rate is determined, see subsection 4.1.2), $\vec{e}_{\text{max}}$ points nearly along the current sheet normal calculated by Kacem *et al.* (2018). Statistics on the angle between the normal from timing estimate and MCA show a distribution sharply peaked at 10° (statistical mode), with values falling below 12° for 50% of the data points.

Having ascertained that MCA preforms consistently with known analysis methods, let us now focus on its results regarding local shapes and scales of magnetic configuration. In the first event examined, especially the second flux rope shows a tendency for the magnetic field to be very elongated with little planarity (Fig. 4.3, panel f). Apart from this, however, not much stands out during the whole interval, meaning that the detectable local configuration of the magnetic field does not change much between the inside of these structures and their surroundings. Passing on the second event, we note that in spite of a very similar behaviour in the usual average plasma parameters, results from MCA differ greatly between this current sheet traversal (panels e to h of Fig. 4.4) and the flux rope crossings discussed previously (panels e to h of Fig. 4.3). In particular, in correspondence with the current sheet traversal studied by Kacem *et al.* (2018) and Zhou *et al.* (2018a) we observe that both σ_{max} and $\mathscr{P}$ rise, thus indicating that magnetic configurations inside current sheets display smaller scale and more planar shapes than in the surrounding environment. In other words, known magnetic structures might be associated to some average configuration signature that one obtains as mean of MCA eigenvalue / shape parameter values.

These analyses have been replicated on a number of other events containing current sheets or flux ropes previously studied in the literature, as well as on crossings of magnetic holes (see Fadanelli *et al.* (2019)). Each time I found that MCA behaves consistently with published studies, in particular reproducing for current sheet and flux rope traversals all behaviours described for the two cases just presented. In particular, the direction of MCA eigenvalues agrees with the orientation of the magnetic structure as retrieved by differential timing techniques. These results show that the local configuration determined by MCA is in agreement with the expected shape of the magnetic field for a number of characteristic structures encountered in near-Earth plasmas.

4.2.2 Statistical analysis

We investigate here the statistical behaviour of MCA parameters for different near-Earth regions: the magnetosphere, the magnetosheath and the solar wind. Since "burst" resolution is available only on short data intervals corresponding to the crossing of particular structures (see subsection 3.1.1), the MCA method is here only applied to a "fast survey" mode data-set. Results of this analysis are nonetheless generally con-

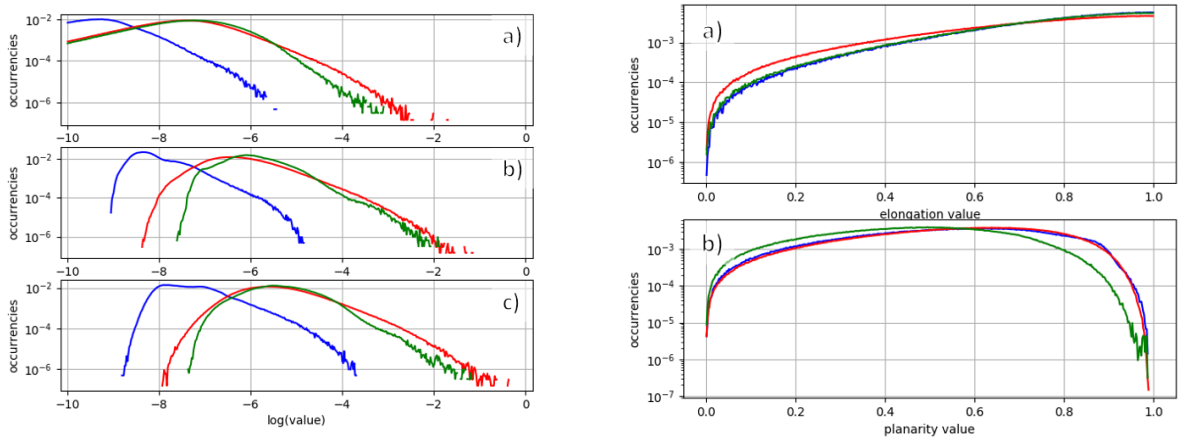

FIGURE 4.5: Statistics of magnetic configurations, by environment (image also in Fadanelli *et al.* (2019)). Left column: occurrence distribution of MCA eigenvalues: a) σ_{min}, b) σ_{med}, c) σ_{max}. The three coloured lines indicate statistics corresponding to each of the three plasma environments sampled: blue for the magnetosphere, red for the magnetosheath, green for the solar wind. From this statistics it appears that in general the smallest scales are found in the magnetosheath, and the largest in the magnetosphere. Right column: occurrence distribution of MCA shape factors: a) elongation $\mathscr{E}$, b) planarity $\mathscr{P}$. As in the left column, the three lines indicate statistics corresponding to each of the three plasma environments sampled: blue for the magnetosphere, red for the magnetosheath, green for the solar wind. From panel b we notice that markedly planar configurations are more frequent in the magnetosphere and less frequent in the solar wind.

sistent with those obtained on burst mode data (from the considerations in subsection 7.1.3 one deduces that only dynamics with $\ell_{\text{sep}}/\tau_{\text{mea-fast}} < \ell_{\Delta}/\tau_{\Delta} < \ell_{\text{sep}}/\tau_{\text{mea-burst}}$ is resolved by "burst" data but not in "fast" resolution).

Data selected for this study have been chosen to be representative of the magnetosphere, magnetosheath and solar wind, all sampled sunward from the terminator during the five-month period between November 2017 and March 2018 (see Fadanelli *et al.* (2019) for the complete list). Magnetosphere, magnetosheath and the solar wind data intervals were selected based on ion density, ion velocity and magnetic field values, preferring continuous hour-long takes. Inside the selected data intervals (covering 690 hours overall, 500 in the solar wind, 105 in the magnetosheath and 85 in the magnetosphere), a further selection has been made by considering only segments in which at least two of the MCA eigenvalues are above the accuracy threshold as defined in Eq. 4.5 (reducing effective data to 180 hours, 50 in the solar wind, 90 in the magnetosheath and 35 inside the magnetosphere). Indeed, in many cases σ_{min} is below the threshold set by the prescribed instrumental resolution, corresponding to an elongation larger than what can be resolved (more precisely, this happens for around 65% of all time spent in the magnetosheath, and practically always when MMS is traversing the magnetosphere and solar wind). Consequentially, if we were to restrict our statistics on data where all three MCA eigenvalues are properly determined (above the purported threshold), then the results would be not representative of the overall plasma features: this is the reason for which we require that there are at least two well-resolved MCA eigenvalues. Given this selection choice, the only statistical information we can get for σ_{min} is that the largest variation scale of magnetic configurations generally tends to

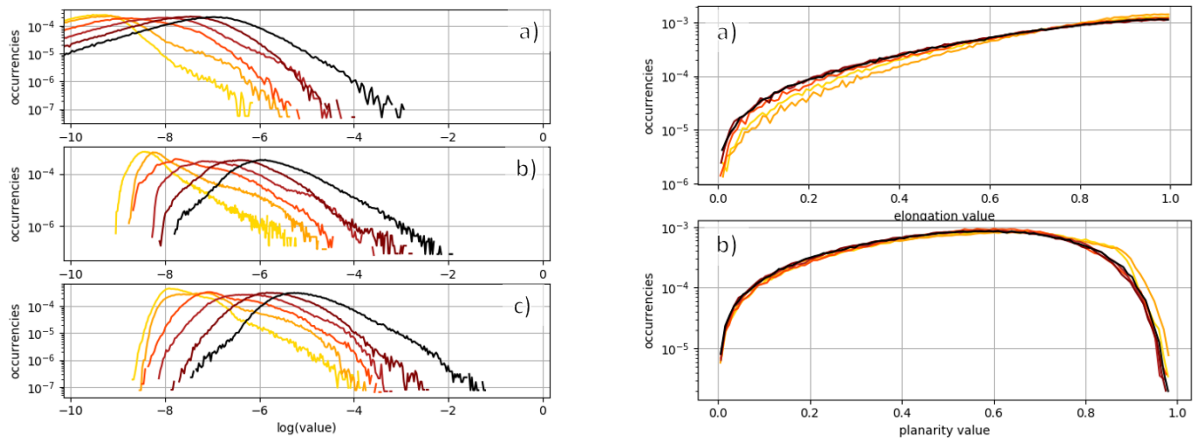

FIGURE 4.6: Statistics of magnetic configurations, by plasma beta (image also in Fadanelli *et al.* (2019)). Left column: occurrence distribution of MCA eigenvalues: a) $\sigma_{\min}$, b) σ_{med}, c) $\sigma_{\max}$. The six lines indicate statistics corresponding to data within the same interval of plasma beta, the six intervals being $(0, 0.4)$, $(0.4, 0.75)$, $(0.75, 1.25)$, $(1.25, 2.5)$, $(2.5, 10.0)$, and all the rest above 10.0. Darker colours are those associated to higher beta values. It appears clearly that the higher the beta, the smaller the characteristic magnetic field scales observed.
Right column: occurrence distribution of MCA shape factors: a) elongation $\mathscr{E}$, b) planarity $\mathscr{P}$. As in the left column, the five coloured lines indicate statistics corresponding to five sets of data grouped together based on plasma beta values. The binning considered is the same exploited for the left column. Magnetic configurations show a tendency to develop higher planarities the smaller the local value of beta.

exceed the detection capabilities of MMS. In other words, magnetic configurations traversed are usually so elongated in one direction that it can be properly approximated as two-dimensional when sampled on the MMS scale.

In Fig. 4.5 I present the statistical distributions of all MCA parameters, as obtained by analysing separately the magnetosphere, magnetosheath and solar wind data segments. In particular, the left column of Fig. 4.5 shows the occurrence distributions of the three MCA eigenvalues, different colours standing for different environments. Similarly, in the right column of Fig. 4.5 I show the overall occurrences of the $\mathscr{P}$ and $\mathscr{E}$ values, separately, colours again identifying magnetosphere, magnetosheath and solar wind statistics. In order to display statistics about the overall shape, I have also plotted the joint distributions of shape parameters, which can be found in Fig. 4.7 with the three panels corresponding to magnetosphere, magnetosheath and solar wind data respectively. Statistics of joint occurrences are presented as spectrograms in the $\mathscr{E} - \mathscr{P}$ plane, with brighter colour being associated here to the most frequent parameter values.

Of the three environments, the magnetosphere and solar wind show marked differences in their occurrence distributions of MCA eigenvalues, and to some lesser extent regarding local magnetic field shaping. Indeed, the magnetosphere tends to display remarkably smaller MCA eigenvalues than the solar wind, meaning that characteristic variation lengths inside the magnetopause are generally longer than outside. High

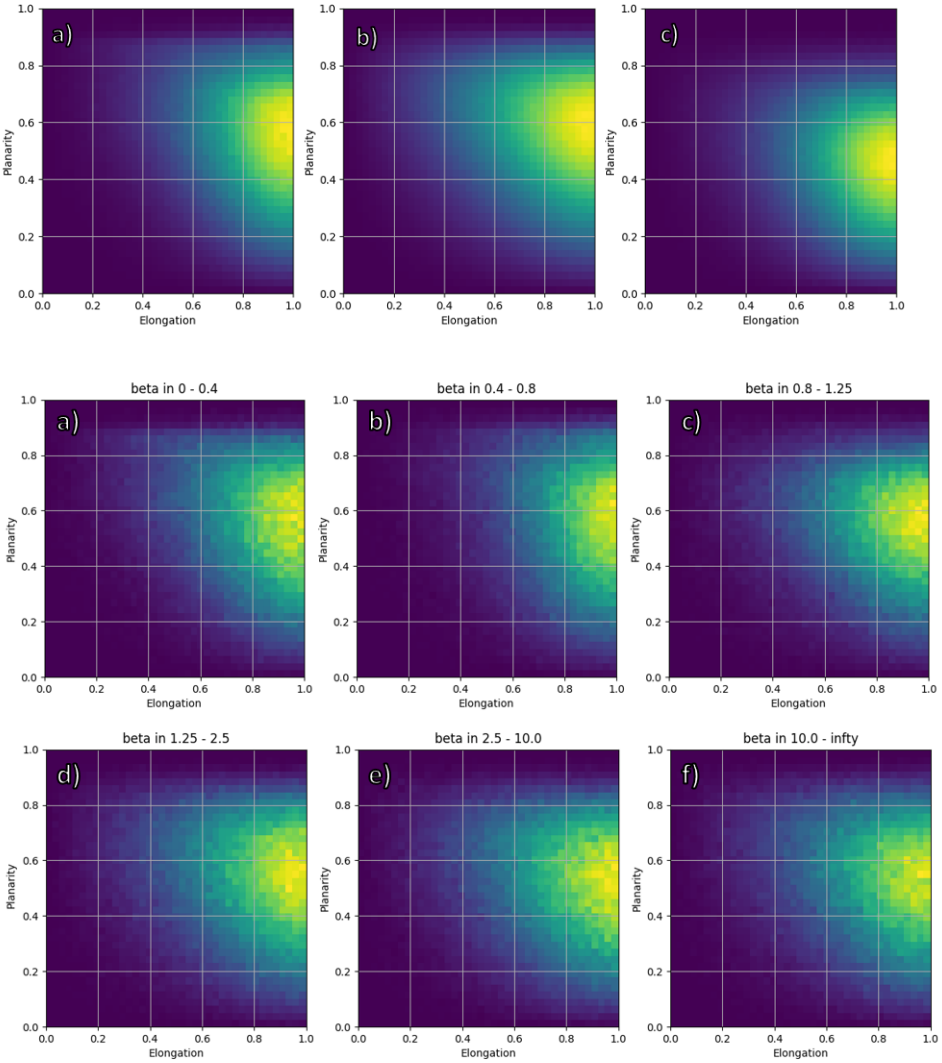

FIGURE 4.7: Statistics of magnetic configurations, by environment and plasma beta (image also in Fadanelli *et al.* (2019)).
Top row: occurrence distribution of MCA shapes on the $\mathscr{E} - \mathscr{P}$ plane, for the three sampled plasma environments: a) magnetosphere, b) magnetosheath, c) solar wind. Lighter colours indicate higher number of samples while the dark blue areas correspond to regions where less samples are present. The three distributions have been retrieved by using the same number of data points for each environment, so to make them easily comparable with each other.
Middle and bottom rows: occurrence distribution for MCA shapes, as in the top row but as a function of 6 ranges of plasma beta values. Again, lighter colours indicate higher number of samples while blue areas are the least populated. As in the top row, all six distributions have been drawn out of the same number of data points, so to make them easily comparable with each other. The six plasma beta intervals used in panels a) to f) are delimited by values of 0.0, 0.4, 0.75, 1.25, 2.5, and 10.0.

planarity values are generally missing in the solar wind, indicating that configurations resolved by MMS are more likely planar inside the magnetosphere. In the magnetosheath, we notice two different behaviours depending on whether we look at MCA eigenvalues or if we consider the shape parameters. Indeed, magnetosheath statistics on MCA eigenvalues shows some remarkable similarity to the solar wind while the distribution of MCA shape parameter is closer to that in the magnetosphere. Overall,

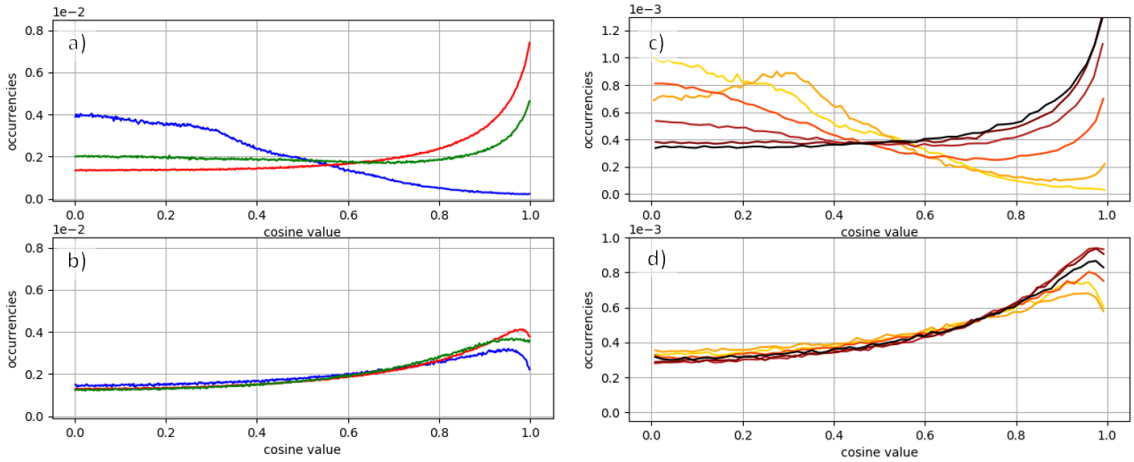

FIGURE 4.8: Statistics on the direction of $\vec{B}$ and $\vec{J}$ relative to $\vec{e}_{\max}$ from MCA (image also in Fadanelli *et al.* (2019)), i.e. occurrence distribution of $|\vec{e}_B \cdot \vec{e}_{\min}|$ (panels a, c) and $|\vec{e}_J \cdot \vec{e}_{\min}|$ (panels b, d). The peak in correspondence of the value one indicates that b and j tend to align in the same direction as $\vec{e}_{\min}$. Colours of the lines indicate occurrence distributions relative to different regions in panels a and b (blue for the magnetosphere, red for the magnetosheath, green for the solar wind) and to different beta bins in panels c and d (from light to dark colours: $(0, 0.4)$, $(0.4, 0.75)$, $(0.75, 1.25)$, $(1.25, 2.5)$, $(2.5, 10.0)$, and all the rest above 10.0).

the distributions found for the magnetosheath are thus a sort of mix, or average, of the tendencies found on one side in the solar wind and on the other in the magnetosphere.

Clearer trends in eigenvalue and shape factor distributions are observed when the data are merged together and re-categorised in terms of the plasma β (the parameter $(c_T/c_A)^2$ i.e. the ratio of thermal to magnetic pressures - note that here the plasma is intended in a single-fluid model, hence only one temperature, comprehensive of ions and electrons, is present). Occurrence distributions of each parameter are shown in Fig. 4.6 as a function of the local plasma β using six ranges of values: $(0, 0.4)$, $(0.4, 0.75)$, $(0.75, 1.25)$, $(1.25, 2.5)$, $(2.5, 10.0)$, and all the rest above 10.0. As for the environment-based statistics, random selection of data within these beta intervals has been performed, so that one can compare an equal number of data for each beta interval (this reduces the overall number of data used in this section to about 10% of the selected points). Solar wind data have been left out of this analysis since the ion moments used for calculating the plasma β are deemed not statistically reliable in that region.

As anticipated, here a more general trend is present: small β implies larger MCA scales and more planar shapes (knife-blades and pancakes), while high β leads to smaller scales and the appearance of much less planar configurations. We recall here that $\sigma_{\min}$ is typically not well determined, as it is generally below the measurement error estimated analytically for a magnetic field accuracy of 0.1 nT. This suggests that $\sigma_{\min}$ may often be overestimated, which in turn means that the $\mathscr{E}$ may often be underestimated, resulting in the deformation of statistics towards more elongated structures.

Focusing on MCA eigenvectors, we have studied a possible relationship between their orientation and that of the measured background magnetic field at the same time. In

Fig. 4.8, panels a and c, we show the occurrence distribution of $|\vec{e}_B \cdot \vec{e}_{\text{min}}|$. Remembering that uncorrelated unitary vectors result in uniform cosine distributions (from subsection 4.1.2), we see that the least variance direction (given by $\vec{e}_{\text{min}}$) and that of the magnetic field (i.e $\vec{e}_B$) are correlated. Moreover, correlations between these two directions are different in the magnetosphere, magnetosheath and solar wind. The two vectors are usually parallel to each other in the magnetosheath and solar wind but are mostly perpendicular to each other inside the magnetosphere. Reproducing all the previous procedure with the current density direction $\vec{e}_J := \vec{J}/J$ instead of $\vec{e}_B$, one obtains panels b and d in Fig. 4.8 (where the current density follows from applying the curlometer technique - see subsection 3.1.4). Again, a correlation is found between the two quantities, meaning that generally $\vec{J}$ and $\vec{e}_{\text{min}}$ tend to align (here regardless of the environment sampled).

Alignment of $\vec{J}$ and $\vec{e}_{\text{min}}$ can be generally expected for all near-Earth plasma environments, since by definition the derivatives of $\vec{B}$ perpendicular to $\vec{e}_{\text{min}}$ are the strongest, and $\vec{J}$ is in good approximation proportional to the curl of $\vec{B}$ (in the physical regimes we study displacement current is negligible). Instead, to explain the various behaviours of $\vec{B}$ we need to recall that in the framework of magnetohydrodynamics, plasma systems are expected to relax in states where $\vec{B}$ and $\vec{J}$ are aligned with each other (the so-called Taylor relaxation, see Taylor (2000)). Now, since we find $\vec{B}$ aligned with $\vec{J}$ in the solar wind and in the magnetosheath, we can conjecture that Taylor relaxation can effectively operate only when no large-scale constraint is imposed. By contrast, the Earth's strong and compressed magnetic field in the dayside magnetosphere might well impede relaxation of the system toward states with $\vec{B}$ and $\vec{J}$ aligned.

4.2.3 Recapitulation of the study

The project just presented consisted in evaluating the performance of the MCA method applied on MMS data. To this aim, I have first estimated linearly the magnetic field gradient (see the method described in subsection 3.1.4) and then constructed the MCA fundamental tensor from spacecraft measures, this for case studies focusing on short time intervals sampled at high frequency and statistical analyses over lower frequency data covering a series longer time intervals.

Using case studies, I have assessed first that MCA does indeed work on MMS data (subsection 4.2.1). This has been done by showing that magnetic shaping deduced by MCA is in agreement with what is expected for a series of characteristic structures (here flux ropes and current sheets). In particular, planar magnetic configurations are found inside current sheets where the smallest of the configuration's scale length shrinks (i.e. the thickness of current sheets is generally much smaller than characteristic lengths of the surrounding magnetic structures).

Furthermore, a statistical analysis revealed trends in the preferential magnetic configurations observed in the magnetosphere, magnetosheath and solar wind environments, as well as the correlation of these magnetic configurations with different plasma β

values (subsection 4.2.2). In particular, in correspondence with low plasma β values MCA finds more frequent appearance of high planarities and the largest characteristic length scales. This supports the idea that magnetically-driven plasma dynamics tend to develop naturally into approximately uniform regions separated by current sheets. Moreover, the same statistical analysis also showed that magnetic configurations are consistently aligned with the mean electric current, that is, that the spatial variance of $\vec{B}$ in the direction parallel to the mean current is significantly lower than in the directions perpendicular to it. The alignment of the most invariant direction with the electric current can be interpreted as following from the fact that a MHD system tends to relax into states where $\vec{J}$ and $\vec{B}$ are parallel to each other. Indeed, whenever the absence of large-scale constraints allows a magnetic configuration to relax the system will tend to a state in which the electromagnetic force on the plasma is null, a situation which in MHD is denoted by $-\vec{\nabla}B^2/8\pi + \vec{B}\cdot\vec{\nabla}\vec{B}/4\pi = \vec{0}$ (from Eq. 2.12) which is equivalent to $\vec{J}\times\vec{B} = \vec{0}$. Both behaviours I have discussed - the approximate force-free condition $\vec{J}\times\vec{B} \simeq \vec{0}$ and the supposed development of current sheets separating approximately uniform regions - support the idea that most of the environment observed is Taylor-relaxed, i.e. it has developed into the lowest energy state attainable under the constraint of constant magnetic helicity (see Parker (2004)).

Chapter 5

Energy transfers in reconnection zones

5.1 Energy transfers in plasma

In this section, I consider the problem of energy transfers (conversions) in reconnection zones. First I introduce the reader to the description of energy transfers in a multi-fluid plasma framework (subsection 5.1.1). Then I present two possible methodologies to examine energy transfers in reconnection regions: the one leading to the definition of an "energy budget" by performing integration over some portion of the system (subsection 5.1.2), the other aiming at a statistic of point-by-point conversions (subsection 5.1.3). The section is closed by considerations on the merits of both these approaches (subsection 5.1.4).

5.1.1 The fluid approach to energy transfers in plasmas

Depending on the plasma model assumed, many approaches are possible to the problem of energy transfers in a plasma: single particle, kinetic and fluid, just to quote some. Here, I will focus only on energy transfer as it is understandable from a fluid framework, occasionally quoting results from studies performed with a different perspective.

In order to consider energy conversions processes in a fluid framework, let me begin by defining the kinetic and internal energy densities for a generic plasma species:

$$\begin{aligned} K &:= (1/2)\, mnu^2 && \text{kinetic energy density} \\ U &:= (1/2)\, \vec{\vec{1}} : \vec{\vec{P}} = (3/2)\, nT =: (3/4)\, mnc_T^2 && \text{internal energy density} \end{aligned} \tag{5.1}$$

where also the thermal energy c_T has been introduced, and then report the equations which regulate their evolution (as in Birn & Hesse (2010) or Yang *et al.* (2017)):

$$d_t K := [\partial_t + \vec{u}\cdot\vec{\nabla}]K = -K\vec{\nabla}\cdot\vec{u} - \vec{u}\cdot\vec{\nabla}\cdot\vec{\vec{P}} + qn\vec{u}\cdot\vec{E} \tag{5.2}$$

$$d_t U := [\partial_t + \vec{u}\cdot\vec{\nabla}]U = -U\vec{\nabla}\cdot\vec{u} - \vec{\vec{P}} : \vec{\nabla}\vec{u} - \vec{\nabla}\cdot\vec{Q}/2 \tag{5.3}$$

where I refer to a generic fluid species, n is its density, $\vec{u}$ the fluid velocity, $\vec{\vec{P}}$ the pressure tensor and $\vec{Q}$ the heat flux vector, obtained by contracting any two indices of the

heat flux tensor already presented. Finally, q and m are charge and mass per particle, as usual.

Let me now briefly note what each term in these equations accounts for. In particular, since energy density variations in the streaming fluid, given by Lagrangian derivatives, always appear as the only left-hand side term, then all terms on the right-hand sides account for different effects that change energy densities in the streaming plasma, i.e. in a given fluid element.

- First, the two terms $-K\vec{\nabla}\cdot\vec{u}$, $-U\vec{\nabla}\cdot\vec{u}$ account for changes in energy densities due to compression or expansion of the fluid element, when no net energy flux is considered trough its boundary.

- Second, kinetic energy density may change because of either $-\vec{u}\cdot\vec{\nabla}\cdot\vec{\vec{P}}$ or $qn\vec{u}\cdot\vec{E}$. In the former case, the fluid is accelerated/decelerated either by the presence of a pressure gradient, in the latter this happens because of an electric field.

- Third, changes in internal energy of a fluid element can be caused by $-\vec{\vec{P}}:\vec{\nabla}\vec{u}$ and/or $-\vec{\nabla}\cdot\vec{Q}/2$ i.e. as consequence of thermodynamic work of converging/diverging velocity patterns, and/or when incoming and outgoing heat fluxes are not balanced: noting the nature of these terms makes us interpret Eq. 5.3 as the first law of thermodynamics expressed in microscopic form.

Furthermore, in multi-species plasma the electromagnetic field cannot impact directly the internal energy of any of the species when considered separately, but it can nonetheless increase or decrease the internal energy with respect to the common plasma barycenter. This follows from the fact that summing Eq. 2.4 over different species changes its right-hand site (as noted in subsection 2.1.1) and can be taken into account by an appropriate "dissipation" measure (introduced by Zenitani *et al.* (2011)). In my case, however, this will not be necessary, since I will stick to the multi-fluid framework.

5.1.2 Overall energy budgets: integrating energy exchanges

One of the long-known possibilities to approach the issue of energy transfers in a reconnecting plasma is that to draw an "energy budget" of the reconnection region, that clarifies how much kinetic, internal and electromagnetic energies are affected by reconnection. This is achieved by evaluating the volume integrals of all terms appearing in the two following equations. The first equation describes the overall energy flow in the plasma, is obtained by summing Eqs. 5.2 and 5.3 and reads:

$$\partial_t[K+U]+\vec{\nabla}\cdot[\vec{\mathcal{K}}+\vec{\mathcal{U}}+\vec{u}\cdot\vec{\vec{P}}+\vec{Q}/2]=qn\vec{u}\cdot\vec{E} \tag{5.4}$$

where $\vec{\mathcal{K}}:=\vec{u}K$ and $\vec{\mathcal{U}}:=\vec{u}U$ are the energy fluxes relative to kinetic and internal energy, respectively. The second equation, also known as "Poynting theorem", describes the evolution of electromagnetic energy density and reads:

$$\partial_t[E^2/8\pi+B^2/8\pi]+\vec{\nabla}\cdot\vec{\mathcal{S}}=-\vec{J}\cdot\vec{E} \tag{5.5}$$

in which the "Poynting flux" $\vec{\mathcal{S}} := (c/4\pi)\vec{E} \times \vec{B}$ can be intended as the momentum of the electromagnetic field.

Different choices have been made, historically, regarding the integration volume to consider for the energy budget.

- The first possibility I list is that of defining an integration zone centered onto a specific reconnection (this way, energy partition has been addressed both from the MHD point of view, such as in Birn & Hesse (2010) and Birn *et al.* (2010), and from a multiple-fluid perspective as in Aunai *et al.* (2011a) for ions and in Shay *et al.* (2014) for electrons - a somewhat refined version of this approach, such as in Wang *et al.* (2018) and Pucci *et al.* (2018), includes a set of integration boxes instead of a single one to determine a certain degree of spatial dependencies in the energy repartition mechanisms).

- A second approach to investigate energy partition is that of focusing on the behaviour of single flux tubes, i.e. performing integration not over a box but rather cutting the system accordingly to the magnetic field (this has been done especially for studies of internal energy, either concentrating on polytropic relations as in Hoshino (2018), Frühauff *et al.* (2017) and references therein, either studying plasma entropy evolution like in Birn *et al.* (2006), Ma & Otto (2014)).

- A third way is that of investigating not one single reconnection site alone, but many at the same time, performing an integration over the whole of a simulation with many reconnections acting contemporaneously (this has been done, for instance, by Yang *et al.* (2017), Du *et al.* (2018), Du *et al.* (2019)).

Of these three possibilities, let me now focus on the first one only, which historically has been the most adopted, and discuss how it performs when applied to the study of a reconnecting X-point assumed stationary and surrounded by ideal plasma, as the one shown in Fig. 2.2 (note that this corresponds to adopting the "kinematic" approach also employed in subsection 2.2.2). Since the system is assumed time-stationary, its energy budget is completely determined by the incoming and outgoing energy fluxes. In particular, denoting total of fluxes over inflows and outflows by indices "in" and "out" respectively, it is by the following coefficients:

$$\begin{aligned} \mathcal{D}_S &:= \frac{\mathcal{S}^{\text{out}} - \mathcal{S}^{\text{in}}}{\mathcal{S}^{\text{in}}} \\ \mathcal{D}_K &:= \frac{\mathcal{K}^{\text{out}} - \mathcal{K}^{\text{in}}}{\mathcal{S}^{\text{in}}} \\ \mathcal{D}_U &:= \frac{\mathcal{U}^{\text{out}} - \mathcal{U}^{\text{in}}}{\mathcal{S}^{\text{in}}} \end{aligned} \tag{5.6}$$

that we will characterise the energy budget in a stationary X-point reconnection site (similar to what is done in Shay *et al.* (2014)).

It is possible to link $\mathcal{D}_S$, $\mathcal{D}_K$ and $\mathcal{D}_U$ to the characteristics of the plasma around the X-

point by assuming some model of the reconnection site (this is similar to the approach taken in the MHD analysis of subsection 2.2.2). In particular, let me align x with the inflows, y with the outflows and z in the out-of-plane direction. Then I consider a $\ell^{\text{in}} \times \ell^{\text{out}}$ box with vertices on the separatrices and encapsulating the whole diffusion region, and suppose that B_x and u_y are uniform over the box's boundary in the outflows while B_y and u_x are uniform over its inflow-crossing sides. The values of these quantities will be denoted by the indices I, II for the two inflows and "out" in the two outflows, supposed symmetric (i.e. B^{I}, B^{II} are the y components $\vec{B}$ in the inflows and B^{out} is the x component of $\vec{B}$ in the outflows; u^{I}, u^{II} are the x components $\vec{u}$ in the inflows and u^{out} is the y component of $\vec{u}$ in the outflows).

In order to estimate $\mathcal{D}_S$, $\mathcal{D}_K$ and $\mathcal{D}_U$ under all assumptions just listed, let me begin by introducing the three quantities c_A^{in}, u^{in} and c_T^{in}:

$$\frac{m(c_A^{\text{in}})^2}{2} := \frac{B^{\text{I}}+B^{\text{II}}}{8\pi}\frac{B^{\text{I}}B^{\text{II}}}{n^{\text{I}}B^{\text{II}}+n^{\text{II}}B^{\text{I}}} = \frac{B^{\text{I}}+B^{\text{II}}}{8\pi}\frac{cE_z}{n^{\text{I}}u^{\text{I}}+n^{\text{II}}u^{\text{II}}} \tag{5.7}$$

$$\frac{m(u^{\text{in}})^2}{2} := \frac{n^{\text{I}}m(u^{\text{I}})^2B^{\text{II}}+n^{\text{II}}m(u^{\text{II}})^2B^{\text{I}}}{n^{\text{I}}B^{\text{II}}+n^{\text{II}}B^{\text{I}}} = \frac{n^{\text{I}}m(u^{\text{I}})^3+n^{\text{II}}m(u^{\text{II}})^3}{n^{\text{I}}u^{\text{I}}+n^{\text{II}}u^{\text{II}}} \tag{5.8}$$

$$\frac{m(c_T^{\text{in}})^2}{2} := \frac{n^{\text{I}}T^{\text{I}}B^{\text{II}}+n^{\text{II}}T^{\text{II}}B^{\text{I}}}{n^{\text{I}}B^{\text{II}}+n^{\text{II}}B^{\text{I}}} = \frac{n^{\text{I}}T^{\text{I}}u^{\text{I}}+n^{\text{II}}T^{\text{II}}u^{\text{II}}}{n^{\text{I}}u^{\text{I}}+n^{\text{II}}u^{\text{II}}} \tag{5.9}$$

where the second equality of each equation follows from multiplying numerator and denominator by $u^{\text{I}}u^{\text{II}}$, then using the ideality condition at the box boundary and the uniformity of E_z which follows from time-stationarity (i.e. $u^{\text{I}}B^{\text{I}} = cE_z = u^{\text{II}}B^{\text{II}}$). Then, thanks to mass continuity, integrated over the box:

$$2\ell^{\text{out}}n^{\text{out}}u^{\text{out}} = \ell^{\text{in}}[n^{\text{I}}u^{\text{I}}+n^{\text{II}}u^{\text{II}}]$$

the incoming energy fluxes can be written as:

$$\begin{aligned}
(1/2)\,\mathcal{S}^{\text{in}} &= m(c_A^{\text{in}})^2\ell^{\text{in}}[n^{\text{I}}u^{\text{I}}+n^{\text{II}}u^{\text{II}}]/2 &&= mn^{\text{out}}(c_A^{\text{in}})^2\ell^{\text{out}}u^{\text{out}}\\
\mathcal{K}^{\text{in}} &= m(u^{\text{in}})^2\ell^{\text{in}}[n^{\text{I}}u^{\text{I}}+n^{\text{II}}u^{\text{II}}]/2 &&= mn^{\text{out}}(u^{\text{in}})^2\ell^{\text{out}}u^{\text{out}}\\
(2/3)\,\mathcal{U}^{\text{in}} &= m(c_T^{\text{in}})^2\ell^{\text{in}}[n^{\text{I}}u^{\text{I}}+n^{\text{II}}u^{\text{II}}]/2 &&= mn^{\text{out}}(c_T^{\text{in}})^2\ell^{\text{out}}u^{\text{out}}
\end{aligned}$$

while the outgoing fluxes are:

$$\begin{aligned}
(1/2)\,\mathcal{S}^{\text{out}} &= mn^{\text{out}}(c_A^{\text{out}})^2\ell^{\text{out}}u^{\text{out}}\\
\mathcal{K}^{\text{out}} &= mn^{\text{out}}(u^{\text{out}})^2\ell^{\text{out}}u^{\text{out}}\\
(2/3)\,\mathcal{U}^{\text{out}} &= mn^{\text{out}}(c_T^{\text{out}})^2\ell^{\text{out}}u^{\text{out}}
\end{aligned}$$

and $\mathcal{D}_S$, $\mathcal{D}_K$ and $\mathcal{D}_U$ can be expressed as:

$$\begin{aligned}
\mathcal{D}_S &= \frac{(c_A^{\text{out}})^2-(c_A^{\text{in}})^2}{(c_A^{\text{in}})^2}\\
\mathcal{D}_K &= \frac{1}{2}\frac{(u^{\text{out}})^2-(u^{\text{in}})^2}{(c_A^{\text{in}})^2}\\
\mathcal{D}_U &= \frac{3}{4}\frac{(c_T^{\text{out}})^2-(c_T^{\text{in}})^2}{(c_A^{\text{in}})^2}
\end{aligned} \tag{5.10}$$

and this concludes our analysis.

In literature, the energy budget of stationary reconnection has been pursued both from simulations and spacecraft data. While simulations allow to determine such an energy budget via "direct" measurement of the fluxes $\mathcal{D}_S$, $\mathcal{D}_K$ and $\mathcal{D}_U$ (i.e. since one can perform integration, fluxes can follow from their very definitions in Eq. 5.6), however, studies based on spacecraft data cannot perform explicitly the spatial integration and must rely on some model of the reconnection site instead. In other words, the only way to determine $\mathcal{D}_S$, $\mathcal{D}_K$ and $\mathcal{D}_U$ from spacecraft data is to assume that the reconnection site probed fits some theoretical model and then extrapolate $\mathcal{D}_S$, $\mathcal{D}_K$ and $\mathcal{D}_U$ thanks to relations such as those of Eq. 5.10 which have been deduced in the model's framework. This last consideration accounts for the fact that there is only a general agreement on the values of $\mathcal{D}_S$, $\mathcal{D}_K$ and $\mathcal{D}_U$ and/or on their dependence on external parameters (compare Birn & Hesse (2010), Eastwood *et al.* (2013), Phan *et al.* (2013), Shay *et al.* (2014), Phan *et al.* (2014), Wang *et al.* (2018) and the review by Yamada et al. in Gonzalez & Parker (2016)).

5.1.3 Local energy transfers: going point-by-point

Another approach to investigate energy conversion between the electromagnetic field and matter is that to evaluate all the terms in Eqs. 5.2 and 5.3 at every point in the system considered. This way it is possible to determine an "infinitesimal energy budget" i.e. what happens at each point: for this reason from now on I will refer to this procedure calling it a "point-by-point" analysis.

Through such analysis, the quantities $-\vec{u}\cdot\vec{\nabla}\cdot\vec{\vec{P}}$, $+qn\vec{u}\cdot\vec{E}$, $-\vec{\vec{P}}:\vec{\nabla}\vec{u}$ and $-\vec{\nabla}\cdot\vec{Q}/2$, will be called "energy conversion rates" and receive particular attention. Indeed, only these four terms denote effective energy changes inside a fluid element, contrary to $-K\vec{\nabla}\cdot\vec{u}$ and $-U\vec{\nabla}\cdot\vec{u}$ which evaluate how much energy density must vary due to compression and rarefaction processes. Before going on, one last "perfectionist" remark is due, namely, that in order to determine correctly the point-by-point energy transfers it is necessary to evaluate all terms in Eqs. 5.2 and 5.3 separately, i.e. one should escape the temptation of casting terms together in some combinations. For instance, it is common practice to sum the terms describing compression/decompression with those evaluating convection, so to obtain the terms $\vec{\nabla}\cdot[\vec{u}K]$ and $\vec{\nabla}\cdot[\vec{u}U]$ (e.g. Birn & Hesse (2010), Yang *et al.* (2017)). Another custom is that of adding to either of these terms also the sum of thermodynamic work densities (the one for K and the one for U), which can also be expressed by a divergence (again, see Birn & Hesse (2010) and Yang *et al.* (2017), for instance). Here, however, I will avoid such practice, understanding that it is only by recognising explicitly all Lagrangian derivatives and considering separately thermodynamic work densities resulting in acceleration and heating, that it is possible to retain all information on the precise way by which K and U change along the material streamlines.

Let me now introduce a quantity comparing $-\vec{u}\cdot\vec{\nabla}\cdot\vec{\vec{P}}$ and $+qn\vec{u}\cdot\vec{E}$, determining which one between thermodynamic and electric work contributes the most to the total

variation of kinetic energy:

$$\mathcal{A}_K := \frac{-\vec{u}\cdot\vec{\nabla}\cdot\vec{\vec{P}}}{qn\vec{u}\cdot\vec{E}} \qquad \simeq -1 \tag{5.11}$$

where the value of this quantity is expected to be -1 since we can generally suppose that force balance approximately holds everywhere in the plasma. In other words, since we expect force balance, also the energy conversion rates contributing to K should balance each other. This situation is indeed coherent with the studies in which it is found that force balance approximately holds throughout the plasma (see Birn & Hesse (2005) and Birn & Hesse (2010)).

Changes in internal energy density are achieved by $-\vec{\vec{P}} : \vec{\nabla}\vec{u}$ and $-\vec{\nabla}\cdot\vec{Q}/2$. As for variations in kinetic energy density, also in this case we can introduce a quantity expressing the correlation between these energy conversion rates, and suppose its value by physical considerations. Indeed, let us define the local polytropic index γ (so-called for its association to the polytropic index already encountered in subsection 2.1.1) and the ratio δ by:

$$\gamma := \frac{d_t U}{-U\vec{\nabla}\cdot\vec{u}} \qquad \delta := \frac{\vec{\vec{P}} : \vec{\nabla}\vec{u} - (2/3)\, U\vec{\nabla}\cdot\vec{u}}{\vec{\vec{P}} : \vec{\nabla}\vec{u}} \tag{5.12}$$

Now, γ is widely known as a way to characterise the kind of thermodynamic transformation that a fluid element is undergoing (see also in Pudovkin *et al.* (1997)), and the quantity δ can be interpreted as sort of a "normalised" version of the "Pi-D" index (defined by Yang *et al.* (2017)) accounting for the effects of anisotropy and off-diagonal terms in the pressure tensor. Since one can write:

$$\mathcal{A}_U := \frac{-\vec{\nabla}\cdot\vec{Q}/2}{-\vec{\vec{P}} : \vec{\nabla}\vec{u}} \qquad = \frac{3\gamma - 5}{2 - 2\delta} - \delta \tag{5.13}$$

it is possible to conclude that the ratio of $-\vec{\nabla}\cdot\vec{Q}/2$ over $-\vec{\vec{P}} : \vec{\nabla}\vec{u}$ must be uniform throughout our reconnection neighbourhood if γ and δ are uniform themselves. This situation is indeed what one could expect, since plasma can generally be approximated polytropic and non-compressional work is generally a negligible percentage of the total (see Yang *et al.* (2017)). Under these hypotheses, we can set $\delta = 0$ and check which values are attained by $\mathcal{A}_U$ if γ changes. In particular, note that in the isothermal $\gamma = 1$ case $\mathcal{A}_U = -1$ and there's no neat change in internal energy, while the adiabatic $\gamma = 5/3$ and isocore $\gamma \to \infty$ scenarios imply $\mathcal{A}_U = 0$ and $\mathcal{A}_U \to \infty$ respectively, i.e. that all change in U is due to mechanical work in the first case and to heat exchange in the second. Being generally understood that the local variations in U are approximately adiabatic in the near-Earth plasma (see for instance the results of Birn *et al.* (2006), Ma & Otto (2014), Frühauff *et al.* (2017), Hoshino (2018)), in that situation one can expect $\mathcal{A}_U$ to be close to zero, meaning that the mechanical work is the preferential factor in determining variations of internal energy density.

In contrast to the rich literature addressing a reconnection's energy budget, there is still scarcity of point-by-point analyses of all energy conversion channels, meaning that a

correct statistics on $\mathcal{A}_K$ and $\mathcal{A}_U$ has not been assessed up to now. Rather, point-by-point analyses have generally focused on the recognition of how different processes might contribute to generate the $qn\vec{u}\cdot\vec{E}$ conversion rate alone which assesses energy exchanges from matter-field interactions (see for reference Eq. 5.4 - decomposing the $qn\vec{u}\cdot\vec{E}$ has usually been done from the perspective of gyrofluid theory, see Dahlin *et al.* (2014), Li *et al.* (2015), Li *et al.* (2017), Li *et al.* (2018)), or through the guiding centre approach to single-particle energisation, see Wang *et al.* (2016) or Dahlin *et al.* (2015), Dahlin *et al.* (2016), Beresnyak & Li (2016) and Dahlin *et al.* (2017)). In conclusion, however, the absolute and relative importance of all energy conversion rates has never been thoroughly discussed.

5.1.4 To integrate or not to integrate?

In the previous two subsections I have presented the two methodologies aiming at the study of energy transfers in plasmas. Avoidance of volume integration in favour of a point-by-point analysis of energy conversions means, on one side, that no direct and obvious extrapolations may be made regarding global energy budgets. On the other, however, it may also present several major advantages with respect to the more traditional, integration-based "energy budget" approach.

First, not requiring the choice of an integration box makes any results obviously independent of the procedure by which the integration volume is chosen: the method is robust. Second, not requiring integration implies that this procedure can be carried on in all such situations in which integration cannot be performed, such as for satellite data analysis: the method is easily portable. Third, by retaining values of all terms estimated locally at any time one can adopt a statistical approach to the energy conversion problem, the energy conversion areas can be mapped in detail and the link between the energy conversion and the small-scale features of the system can be enlightened. This last characteristic of the procedure is particularly suitable to advance in the understanding of the nature of all localised energy conversion processes: for this reason in the following analyses I will adopt the "point-by-point" approach rather than going for an "energy budget" evaluation.

5.2 Energy transfers in numerical experiments

This section is devoted to an analysis of energy transfers in the neighbourhood of a reconnection site, performed via statistics on point-by-point conversions as shown in the result of a numerical experiment. To this end, I present first the simulation used, in particular focusing on a reconnection site which can be individuated inside it (subsection 5.2.1), then describe spatial patterns shown by energy densities and their conversion rates (subsection 5.2.2). After this, I present two statistical analyses of energy conversions, the first retrieving correlations between energy conversion terms (subsection 5.2.3) and the second investigating correlations between such terms and a characteristic length of the system (subsection 5.2.4). The section ends with a

quick recapitulation of the main results (subsection 5.2.5).

5.2.1 Overview of the simulation and reconnection site

In order to give a practical example of the technique just presented, here I discuss energy densities and energy conversion rates as they appear in the neighbourhood of a reconnection site in the two-dimensional, hybrid simulation presented through subsection 3.2.3. While choosing to base my analysis on such a reconnection site means that the boundary conditions relative to the reconnection might be interpreted as somewhat realistic, however, the reproduction of plasma dynamics via computer simulation needs also to assume some simplifications with respect to the real-world scenario.

Two assumptions in particular characterise the present simulation, namely that of bidimensionality and that connected with the fluid model assumed for electrons. Both these assumptions greatly help both in terms of computation time required. Moreover, while two-dimensionality implies a certain departure from reality, it also helps subsequent analyses by providing a numerical experiment in which magnetic topology can be easily recognised (see subsection 7.2.1) in which the interpretation plasma dynamics is much easier than in the three-dimensional case. Finally, given the accuracy of the generalised Ohm's law adopted, even if not all behaviours of electrons are completely reproduced yet a good number of features of plasma dynamics are present in this numerical experiment (see Valentini *et al.* (2007)).

The following analyses will focus $170\,\tau_i$ after initialisation, and in the neighbourhood of the X-point located about $(193, 125.5)$ the most prominent feature is a strong current sheet which shows a number of characteristics consistent with ongoing reconnection. In Fig. 5.1, top row, I show a broad perspective on this current sheet: number density, magnetic field intensity and current density magnitude. The X-point is observed in the projected magnetic field lines drawn in the figure. An asymmetry between magnetic field strength in the two reconnecting vortices (moving lower left to upper right, B_z passes from about unity to 0.85 while the in-plane field changes from 0.27 to 0.12) implies that the upper right separatrices are more bent than the lower left ones. Exhausts are recognisable as the regions where both number density and current density are enhanced.

By looking at Equations 5.2 and 5.3 we observe that some of the terms are not frame-invariant. Therefore, in order to carry on our analysis of energy conversions it is of paramount importance to establish first a "good" reference frame. Here we set this reference frame as the one co-moving with the X-point, i.e. the one in which at the X-point $\vec{c}_X$ velocity defined by Eq. 7.4 is zero (see all subsection 7.2.3 for more).

Changing to the frame in which X-point velocity is zero, a number of characteristic reconnection signatures appear. This is clearly shown in the bottom row of Fig. 5.1. First, notice that the in-plane component of the electron velocity shows a stagnation point less than $1\,d_i$ away from the X-point, consistent with the commonly accepted picture of reconnection. The in-plane ion velocity is also stagnating near the X-point, but

at about $3\,d_i$ downstream in the bottom-right exhaust (see panel e). This displacement, which is yet consistent with asymmetries due to large-scale ion dynamics, implies in particular that ions must drift across the X-line: such a drift, however, does not impede reconnection. A further confirmation of the validity of this reference is given by the flow of the "in-plane $\vec{c}B$" i.e. the in-plane flux velocity $\vec{c}_\psi$ set with $\upsilon = 0$ (defined in subsection 7.2.2) which also presents a stagnation-like structure at the X-point (aside: note that it is impossible that $\vec{c}_\psi$ assumes zero value at the X-point exactly because it must diverge wherever the in-plane field vanishes). All these facts considered, we deem this frame as appropriate for our analysis, and from now on we shall always adopt it.

5.2.2 Spatial patterns of K, U, d_tK and d_tU

In this subsection we describe the patterns of energy densities and their Lagrangian derivatives around the reconnection site. These are visible in Fig. 5.2. Discussing which shows the kinetic and internal energy densities of ions and electrons in the vicinity of the reconnection region, we intend to provide a detailed presentation of

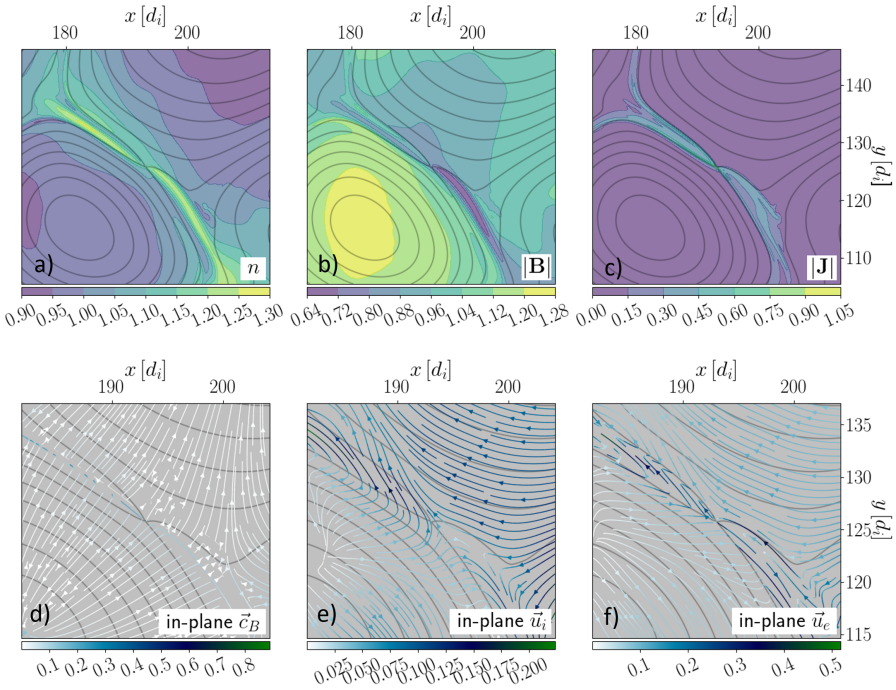

FIGURE 5.1: Simulation results of reconnection within a turbulent plasma, at time $170\,\tau_i$ of the simulation (own image). First row offers a wide perspective on the reconnection site (with frame-invariant quantities) while the second row shows a close-up of several in-plane velocities (all frame-dependent, evaluated in the reference co-moving with the X-point as described in the text). Panel a: number density (equal for ions and electrons), panel b: magnetic field intensity, panel c: absolute value of current density. Panel d: in-plane magnetic flux velocity. Panels e and f: ion and electron in-plane velocities. All quantities are evaluated in the reference frame where the X point velocity $\vec{c}_X$ is null (X point is situated at approximately $193, 125.5$). projected magnetic field lines are shown in black.

the reconnection site on which we will later perform statistical analyses. Only using Lagrangian derivatives, we remind, one may identify where fluid elements get energised or de-energised.

Let us start by first discuss the ion kinetic energy density, K_i, which shows increment in both that one of the exhausts, even if one of these clearly displays a stronger (more developed) ion jet (top left corner of Fig. 5.2, panel a). To explain this asymmetry, let us remind that reconnection is sometimes unable to fully develop ion jets, in particular when constrained in a limited spaces. This was highlighted in the recent work of Sharma Pyakurel *et al.* (2019), that estimated ten-to-twenty d_i as the minimum exhaust length required for ion acceleration whenever one reconnection is started in a small, periodic system. In our case, though the local boundary conditions for this reconnection are non-periodic, still we note that a similar scale argument might apply. The fully-developed ion jet (upper left in Fig. 5.2) is hosted in an exhaust that runs straight for about $20\,d_i$, while the slower outflow is bent and does not extend as much owing to larger scale constraints (nearby vortex dynamics). This unequal ion acceleration in the two outflows is consistently supported by the Lagrangian derivative of K_i (panel e), which shows that the ions in the lower-right outflow are locally experiencing a limited increase of K_i while those in the upper-left outflow get consistently accelerated instead.

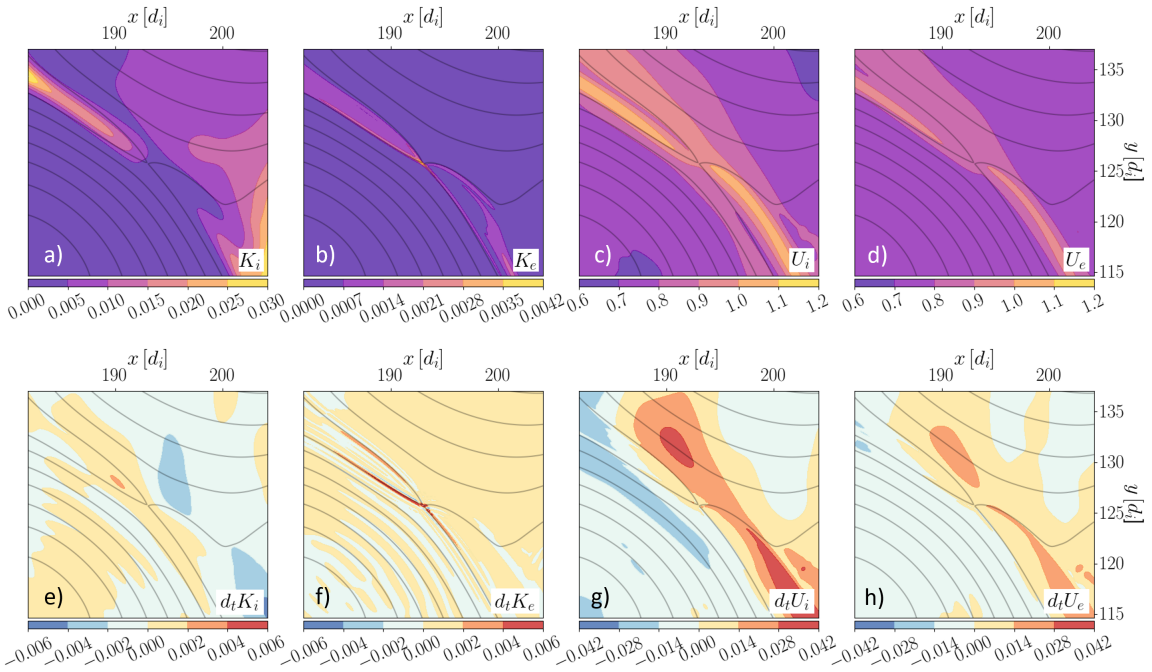

FIGURE 5.2: Ion and electron energy densities (top row) and their Lagrangian derivatives (bottom row) in the close proximity of the reconnection region, at time $170\,\tau_i$ (own image). Panels a, b: kinetic energy densities of ions and electrons respectively; panels c, d: ion and electron internal energy density. Panels e, f, g, h: Lagrangian derivatives of quantities in panels a, b, c, d respectively (calculated as sum of the right-hand side terms in Equations 5.2 and 5.3). In-plane projections of magnetic field lines are shown in black, and all terms have been evaluated in the reference frame where the $\vec{c}_X$ velocity at the X-point is null, as described in the text.

On the other hand, electron kinetic energy density (panel b of Fig. 5.2) and its Lagrangian derivative (panel f) show that electrons react to reconnection building up very localised regions of high velocity along the separatrices. The Lagrangian derivative of K_e (panel f) shows that acceleration takes place in the closest proximity to the X-point, as expected in high guide-field reconnection (see for instance Pucci *et al.* (2018)), and that accelerations and decelerations display a patchy structure. This last pattern – we note – may be similar to what has been reported (albeit in situations with lower guide field), in spacecraft data, albeit with lower guide field (see Burch *et al.* (2018a) and Cozzani *et al.* (2019)), and in simulations (see of Swisdak *et al.* (2018)).

The ion internal energy density displays an overall symmetric spatial distribution that peaks in the exhausts, in correspondence with local enhancements in number density (see panel c). High density due to accumulation of material in the narrow exhausts and heating due to the release of magnetic energy are both well-known from literature. Values of $d_t U_i$ (panel g), however, appear to be asymmetrically distributed in both the inflow and outflow regions alike, and pretty much de-correlated from U_i. A possible way out from this conundrum comes from the check of the in-plane ionic flows (from Fig. 5.1 panel e). Indeed, a "diagonal" component of ion velocity makes it so that most of the upper left exhaust is characterised by material moving from high-U_i to low-U_i regions, with the only exception being a narrow band close to its lower separatrix. By such motion, we note, one can explain both the negative $d_t U_i$ values observed for most of this exhaust and the thin region of positive $d_t U_i$ close to the its lower separatrix.

In contrast to the net differences in kinetic energies, remarkable similarities are present between U_i and U_e, as well as between $d_t U_i$ and $d_t U_e$. This is a primary consequence of the quasi-neutrality and of the isothermal electron assumption, together preventing the development of specific electronic signatures around this reconnection site. Given this consideration, we shall not discuss electron internal energy, whose properties thus fall outside of the scope of the present analysis.

5.2.3 Point-by-point correlations of energy conversions

Let us now focus on the causes of plasma energisation, in particular on those processes leading to effective energy changes inside a fluid element. Such processes are described by the terms on the right-hand sides of Equations 5.2 and 5.3, apart from $-K\vec{\nabla}\cdot\vec{u}$ and $-U\vec{\nabla}\cdot\vec{u}$ which denote energy density variations due to compression and rarefaction. For the sake of clarity, from now on we will name "energy conversion rates" all those terms.

Fig. 5.3 displays electromagnetic work (ionic in panel d, electronic in panel e) and pressure work (for ions in panel a, for electrons in panel b) that accelerate/decelerate the material, alongside with the heat flux divergence (for ions only, panel c) and thermodynamic work (ions only, panel f) relative to heating/cooling. Hence, effective energy changes result from the sum of the conversion rate terms which are plotted in panels a and d for K_i, b and e for K_e, c and f for U_i. The third row of Fig. 5.3 displays the cor-

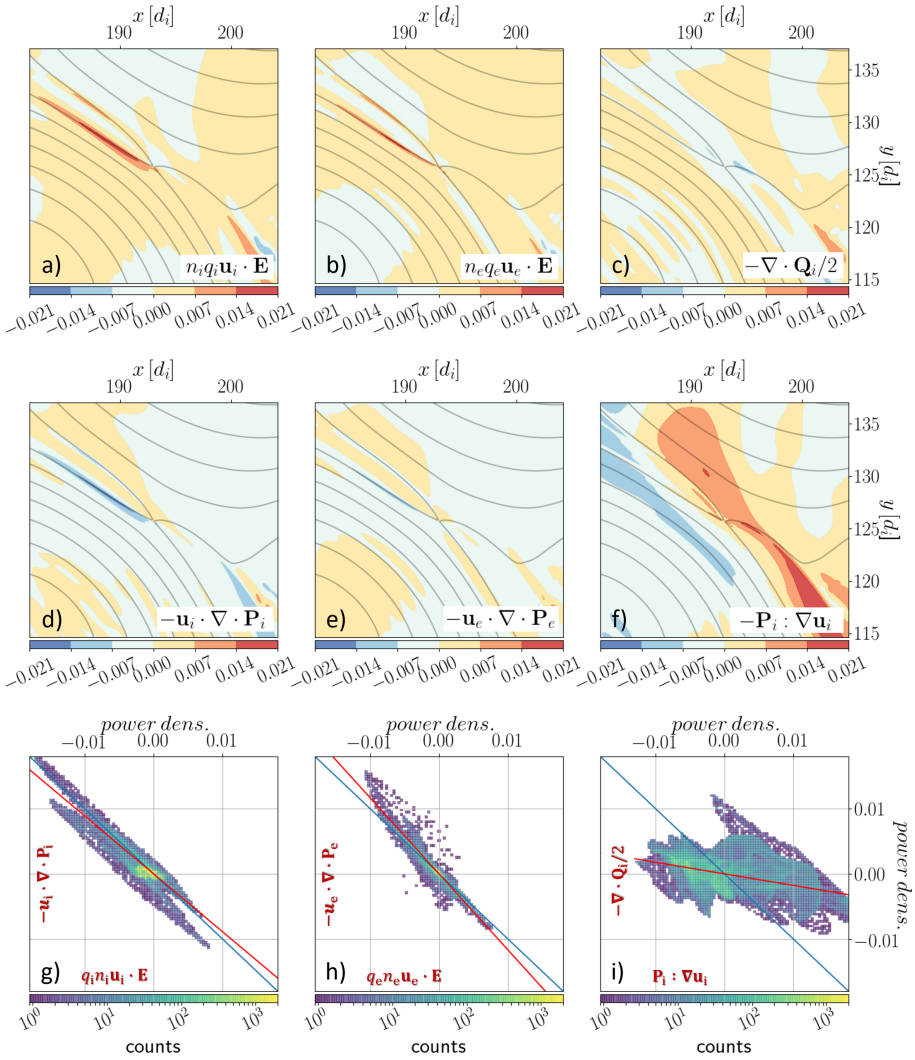

FIGURE 5.3: Comparison of ion energy conversion rates in the neighbourhood of a reconnection region, with projected magnetic field lines in dark grey (own image). First row, panels a, b: work done by electromagnetic field on ions and electrons; panel c: heating/cooling processes following from heat fluxes imbalance, for ions. Second row, panels d, e: thermodynamic work to accelerate ions and electrons; panel f: ion heating following from thermodynamic work. Third row: scatter-plot histograms showing the correlation of the terms plotted in the two upper rows, panels g, h for ion and electron kinetic energies, panel i for ion internal energy. In other words, panels in the third row show the parameter space defined by coupled conversion rates, the colour of each bin indicating for how many points of real space the values of energy conversion rates fall within the portion of parameter space covered by the bin (aside: notice that the colour-scale adopted is logarithmic). Red lines fit the most representative ratio in each sample, while blue lines are the diagonals that mark the frontier of no-net-energy-transfer i.e. they separate overall energy gain (upper-right region) from energy loss (lower-left).

relation of terms plotted in the first and second row, that is, the statistical occurrence of values in the parameter space defined by coupled energy conversion terms. Colour of the dots in each of panels g, h, i corresponds to the number of data points falling within each of the bins that cover the parameter space. The red lines superposed to all three distributions of the last row are obtained by performing linear regressions,

setting by default that the line must pass through the origin and lowering noise by excluding data from within a circle of radius 0.0035 centered in the origin (this threshold has been found to be the lowest to allow good fitting). The result of linear regression will be regarded as the "highest-confidence" ratio between coupled energy conversion rates.

Fitting data from the simulation, it appears that approximate balance of energy conversion rates is indeed observed, with a higher accuracy for electrons rather than for ions. Indeed, linear regression fits indicate that the highest-confidence value for $\mathcal{A}_K$ is -0.75 for ions and -1.19 for electrons, with the electron data-set being slightly better correlated (the R^2 estimator, which is the square of correlation coefficient and approaches unity as the relationship between two variables approaches perfect linearity, scores 0.74 for ions and 0.96 for electrons). In the present example, so, despite small local departures from the diagonal, the two terms tend to compensate each other very precisely, confirming the validity of Eq. 5.11 in this case.

Let us now pass to changes in internal energy densities, starting with U_e. In our simulation, the isothermal electron assumption corresponds to $\gamma_e = 1$, while the absence of diagonal terms in the electron pressure tensor implies $\delta_e = 0$. Therefore, in our case $\mathcal{A}_U = -1$ for electrons, and no internal energy is effectively gained or lost in any compressions or decompressions of the electron fluid. Wishing to proceed in the same way for ions, we begin by evaluating γ_i and δ_i. Fig. 5.4 shows that both γ_i and δ_i are well defined throughout the reconnection neighbourhood, and their values being 1.61 and 0.10 (with R^2 of 0.97 and 0.66, respectively) we expect $\mathcal{A}_U$ to be about -0.19 from Eq. 5.13. The small value of δ_i is overall consistent with the possibility of neglecting non-compressional work terms, while γ_i just less than $5/3$ means that heat exchanges are generally negligible with respect to the thermodynamic work, which in the case of reconnection would ultimately result into an increase of U_i since the passage of plasma

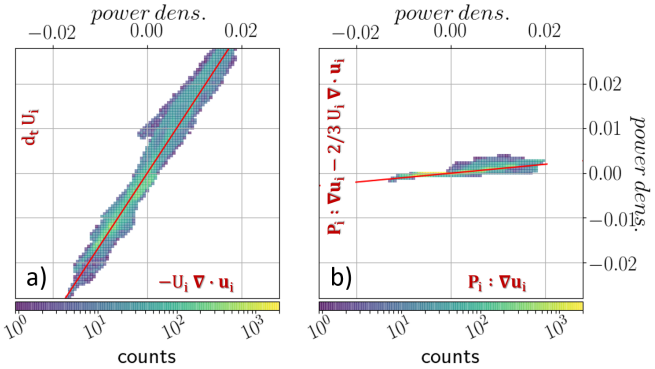

FIGURE 5.4: Evaluation of ratios γ_i and δ_i in the surrounding of the X-point (own image). The diagrams are scatterplot histograms showing point-by-point relationships of the numerator and denominator terms defining γ_i and δ_i (similar to panels in the third row of Fig. 5.3). In other words, as each bin covers some portion of the parameter space defined by the denominator and numerator values, and its colour is proportional to the number of points in real space in for which denominator and numerator values fall within the bin. Red lines fit the most representative ratio in each sample.

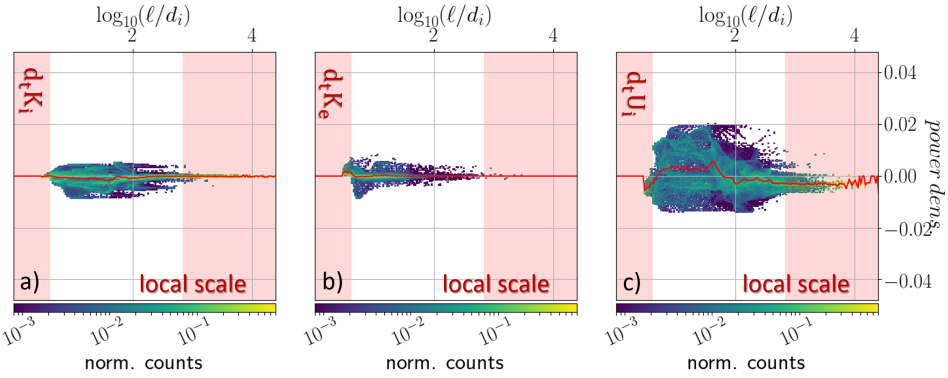

FIGURE 5.5: Statistics of conversion rates relative to local scale (own image). Energy conversion rates are in ordinates, local scales of the plasma are in abscisse (logarithmic axis). In these scatterplot-like histograms, colour scale is normalised for each "vertical cut" i.e. yellow colour highlights the most probable values attained by energy conversion rates at each scale along the abscissa, while blue colour indicates the lowest frequency of observed values for each scale separately. Statistics is performed over the same neighbourhood of the reconnection region depicted in Fig. 5.3. Panels a and b refer to total conversion rates of kinetic energy, for ions and electrons. Panel c refers to total conversion rates of ion internal energy. Total conversion rates for electron internal energy, we remind, is identically zero at every scale because of the isothermal prescription implemented in the code. Red shading highlights data point statistics below 200.

close to the X-point is accompanied with its compression. These considerations on δ_i and γ_i do concord with the overall trends seen in Fig. 5.3, panel i, since the observed value of $\mathcal{A}_U$ is -0.18 and most of the reconnection neighbourhood exhibits an overall increase of U_i (most of the data points arrange on the right and above the blue line). However, when plotting the heat flux divergence against thermodynamic work density it must also be recognised that the correlation observed is as best a weak one (see Fig. 5.3, panel i) with the linear regression slope sporting a low R^2 likelihood (only 0.19). Since both hypotheses leading to Equation 5.13 (i.e. polytropic behaviour or negligible δ_i) are quite well satisfied, I suggest that the weak correlation observed must not be attributed to some failure in having approximately uniform values of δ_i and γ_i close to the reconnection, but should rather be interpreted as the result of combining small and localised deviations from near-constant behaviours (possibly pointing at the complex fine structure of the reconnection neighbourhood).

5.2.4 Energy transfers and characteristic lengths

While in the previous analyses I focused mainly over correlations between different contributions to energy conversion rates, here I will try to link these values to some parameter describing the local configuration of the system. In particular, here I will consider the scale length $\ell_n := n/|\vec{\nabla} n|$, which quantifies the local fluctuation length of the plasma density n.

In Fig. 5.5 I report the distribution of total energy conversion rates as a function of the characteristic length just defined, showing which is the percentage of points where ℓ attains some given value of energy conversion in the same neighbourhood of the X-

point considered up to this point. The red lines show the averaged energy transfer, at each given scale. Considering that one must ascertain that the number of points displaying a given scale ℓ is sufficient for statistics to be relevant, some intervals of scales with low statistics have been highlighted in shaded red (less than 200 data points).

Several trends appear consistently. For kinetic energy densities (panels a and b), we find an overall balance between energy gains and losses through most scales (note that the red line generally is very close to zero). For ion internal energy density, instead, the trend is to decrease at large scales and to increase at small scales (note the red line again, passing from generally positive to generally negative at about $100\,d_i$).

5.2.5 Recapitulation of the study presented

Throughout the whole of this section, I showed how it is possible to exploit data from a numerical simulation of plasma turbulence to study energy transfers close to a reconnection site. To this aim, I first individuated the site and a reference frame solidal with it (subsection 5.2.1) and proceeded to recognise characteristic patterns of K, U, d_tK and d_tU so to prove its coherence with known models (subsection 5.2.2). In the case examined, in contrast of the difficulty in performing conclusively an "energy budget" analysis, basically due to the fact that it is unclear which "inflow" and "outflow" values one should adopt one can well perform a statistical study of point-by-point energy conversion rates.

In particular, studying correlations of energy conversion channels with each other (subsection 5.2.3) I retrieved that in very first approximations force balance and polytropic behaviour do indeed describe how energy is exchanged, in accord with theoretical expectations (subsection 5.1.3). While force balance in general tends to be well maintained trough the system, however, strong deviations are seen locally from a nearly-polytropic behaviour.

Determining point-by-point energy exchanges also allows for the research of correlations between energy conversions and other quantities defined point-by-point, such as characteristic scales (subsection 5.2.4). Comparing the characteristic scale of density perturbations with energy conversions, I retrieved that the extreme values of d_tK and d_tU generally correlate with lowest characteristic scales, and the average contribution of these extreme values is an increase of kinetic and internal energy densities. Most other scales generally have a zero average contribution to K and/or U, possibly with a slight loss observed in the average d_tU at the largest scales.

Chapter 6

Conclusions and perspectives

6.1 Looking back

In this section I draw some general conclusions on the research projects I carried on. I discuss first the research activity on magnetic configurations and the project on energy conversions (subsection 6.1.1). Other projects are presented at the end (subsection 6.1.2).

6.1.1 On the main projects

In the first part of my thesis, I focused on the local shape of the magnetic field, which in a magnetised plasma drives the evolution of large structures, regulates how waves propagate and plays a fundamental role in determining which instabilities can be excited. To this aim, I adopted a procedure derived from the MDD and MRA methods (see Shi *et al.* (2005) and Shen *et al.* (2007a) respectively), which I called "MCA" (Magnetic Configuration Analysis) and by which one can describe local magnetic field configurations in terms of three characteristic lengths and three characteristic directions. The particularity of MCA is that the three characteristic lengths it individuates are determined only by the configuration's shape and not by magnetic field intensity: the re-scaling of the magnetic field, under which MDD would return different values, does not impact on MCA results. While also MRA would be unaffected by re-scaling, yet MRA provides only two characteristic scales only, not three as MCA, and therefore cannot completely characterise the field's shape.

Using MCA with data collected by the Magnetospheric Multiscale mission (see Burch *et al.* (2016b)), I retrieved the configuration of the local magnetic field in the dayside magnetosphere, the magnetosheath and the near-Earth solar wind. In particular, I performed two different studies, one focused on the analysis of high-frequency data, the other devoted to statistical trends in a larger data-set composed by low-frequency measurements. My findings demonstrate the capabilities and highlight the usefulness of the MCA technique for the analysis of multi-satellite data. In particular, the statistical application of MCA to MMS data supports the idea that near-Earth plasma is found in a Taylor-relaxed state, i.e. it is at the lowest possible energy attainable while conserving total helicity (see Parker (2004)).

The second main project of my thesis focused on the problem of energy conversion in a collisionless magnetised plasma. Unlike most previous works, the approach adopted here is based on evaluating the Lagrangian derivatives of energy densities at each data point, so to follow their evolution relative to each fluid element. This approach allows us to study correlations of energy conversion channels with each other and with every other quantity which is defined point by point.

The analysis of energy exchanges was carried on by analysing a reconnection site in a Vlasov-hybrid numerical simulation of plasma turbulence. The results show that local kinetic energy variations in plasmas are usually small, as they require the breaking of an approximate force balance condition between work done by the pressure and that from the electric field. Moreover, it has been shown that the average variation of internal energy can be ascribed to an approximately polytropic behaviour, with deviations due to the non-compressional thermodynamic work. The local character of the analysis performed also offered the opportunity to determine dependencies of energy density transfers on the local scale of the system. In the close surroundings of the reconnection site, force balance tends to appear statistically at each scale, hence leading to an average conservation of kinetic energy densities. In the same region, a trend with large-scale decrease and small-scale increase is evident instead for ion internal energy density. Also, I found a trend toward larger energy conversion rates as the characteristic length diminishes, even if to identify it clearly it was necessary to extend the number of points considered for statistics.

6.1.2 Other projects

While working on the previously mentioned projects, I also contributed to various extent in a number of others. Here I will summarise them briefly.

Kelvin-Helmholtz instabilities developing at the magnetospheric flanks can be a foreground player in magnetic boundary dynamics, exciting a vast number of secondary processes and potentially contributing to the entering of solar wind material into the magnetosphere. In a project I led, Kelvin-Helmholtz instabilities and the related dynamics have been examined in their latitudinal development, via a simulation performed with a two-fluid code (the paper resulting from this work is reported as annex in reason of the several months of Ph.D. thesis spent on it). The initial configuration is shaped so to reproduce in latitude the latitudinal confinement of the Kelvin-Helmholtz unstable band (the shears of velocity and magnetic field are the most intense close to the equatorial regions and gradually diminishes away from it). Simulations show the onset and development of the Kelvin-Helmholtz instability. Perturbations exhibit a wavevector of maximal growth tilted with respect to the equatorial plane, and extends asymmetrically away from the equator. The latitudinal shift of the Kelvin-Helmholtz band highlights how it is not only the initial magnetic shear that determines where the system will develop vortices, but also differential advection of magnetic field lines must be taken into account (see Fadanelli *et al.* (2018)).

Magnetic reconnection has also been observed in the simulation discussed, in differ-

ent sites and under various local fluid configurations (i.e. within the main Kelvin-Helmholtz vortex but also inside secondary draped regions with enhanced flud shear). Specific to the reconnection induced by Kelvin-Helmholtz here is that such process has been found ranging continuously across zones at different latitudes, not confined to some latitude band (as in Faganello *et al.* (2012)). Therefore, when compared to known similar results, reconnection induced by principal vortices in the present case is to be understood as somewhat of a hybrid process that combines features of two well-known cases, that are type-I reconnection and mid-latitude reconnection. Indeed, while in the aforementioned two cases, reconnection is given by a magnetic shear enhancement driven by an increase in shear angle or by the compression of some pre-existing sheared configuration, in the analysed situation both phenomena are at play simultaneously and they form a sort of continuum. In the nonlinear vortex regime, reconnection is typically enhanced by the development of secondary instabilities. The increase of reconnection processes makes also it possible to create doubly reconnected lines, which eventually result into the trapping of solar wind material within the magnetosphere. This consideration suggests in particular that the dynamics following a large-scale Kelvin-Helmholtz perturbation can lead to a very effective material transport between the solar wind and the magnetosphere (see Fadanelli *et al.* (2018)).

Always exploiting codes developed at the University of Pisa, I have undertaken the "Magnetospheric Multiscale Turbulence" (MMT) project, aimed at generating simulations of plasma turbulence directly comparable with observations from the MMS satellites. This project is still ongoing, as it is the development of routines specifically designed to analyse the simulations ("fibo" project), carried on with the aim of standardising and systematically organising multiple routines developed during the years.

6.2 Moving forward

After having summarised results and outcomes of the work during my Ph.D. thesis, here I outline briefly which perspectives have been opened by such work. In this regard, I am presenting first the direct development of the main projects I've worked on, starting from the one on the recognition of local magnetic configurations (subsection 6.2.1) and then a more general outlook on magnetospheric research (subsection 6.2.2).

6.2.1 On the local configuration of the magnetic field

In the project presented up to now, local configurations have been analysed only in spacecraft data. The MCA method applied to satellite fleets, however, can be used in a similar way in simulations, in particular with the aim to assess further its limits and capabilities. Simulations are really useful as they can provide an overall view of the magnetic configuration, to compare with the local one of MCA. For the moment, one project is mainly focusing on determining whether it is possible to retrieve the shape of current peaks by performing MCA on a subset of its points or, more in general, how

does the local MCA correlates with the overall shape of the current peak. The ability to point at some overall shape once the local configuration is known would been particularly significant for the analysis of spacecraft data.

Always for MCA, another possible development is to determine by simulations whether it can be statistically linked with other estimators of local magnetic shape, such as the "exponentiation" measure (see Boozer (2012b)). Again, any correlation could help to retrieve hints of these nonlocal features from local measurements, meaning new possibilities for analysis of data from satellites and simulations, and in particular as reconnection proxies. In this regard, it can be useful to note that MCA can, at need, be "reduced" i.e. at each point one can choose a direction, and perform MCA only perpendicular to that direction (basically, instead of looking for the three eigenvalues and eigenvectors one can project the tensor onto a plane and find the two eigenvalues and eigenvectors of the projected tensor). This fact can be exploited to define, in particular, a $\vec{B}$-perpendicular MCA, possibly more useful in the circumstances just introduced.

Anyway, information retrieved by performing MCA on satellite data may be of crucial importance in all those studies for which either we make hypotheses on local magnetic configurations, or for which we need to estimate characteristic length scales of the system. In the former category we can put all those studies that focus on specific structures (current sheets, flux ropes etc.), and for which MCA could be used both as an additional identification diagnostic and/or to provide characteristic properties (for reference, consider theoretical works such as Zhang *et al.* (2015) or data-based analyses like in Chasapis *et al.* (2018)). In the latter category, we find most studies that focus on local frame determination, alongside with all works focusing specifically on characteristic magnetic scales (e.g. Rappazzo & Parker (2013), Rappazzo (2015)). In all these cases, retrieving and expressing three-dimensional features of the local magnetic field opens new possibilities for event-oriented and statistical analyses in near-Earth plasmas.

6.2.2 On energy conversions

Work on energy conversions presented up to now has been only carried on simulations. A natural further development is the comparison of my results with the high resolution observations provided by MMS. This project, currently underway, basically aims at determining to which extent do simulations reproduce satellite data. In particular, the local polytropic index via the relation Eq. 5.12 could be compared with those obtained via other methodologies, as discussed in literature (see for instance Frühauff *et al.* (2017), Livadiotis (2018), Nicolaou *et al.* (2019)).

Always on the topic of energy conversions, it is easy to recognise that a limit to the study just presented is given by the isothermal closure assumed for the electrons in the simulation, meaning that effects at very small scales (both spatial and temporal) are not retrieved here, as well as all effects driven by electron pressure anisotropy and all electron heating physics (for a review of electron-driven effects near reconnection sites see for instance see subsection 7.5.2). Another limitation is given by the

two-dimensional geometry of the simulation considered, which constrains the overall system evolution. Two-dimensional setups, indeed, in many case lead to qualitatively similar results of fully three-dimensional simulations (see Wan *et al.* (2015) or Servidio *et al.* (2015)) even if sometimes appear to affect the relative weight of the different phenomena (see Dahlin *et al.* (2015) discussing how the field-to-matter energy exchanges vary between two-dimensional and three-dimensional systems). Also, the choice of a reconnection site which is generated and then remains constrained within a turbulent dynamics must be considered just as a different approach with respect to numerical works analysing reconnection in a more laminar regime, in which the X-point emerges from an initially prepared large-scale current sheet (Harris-sheet-like). These two approaches may not be directly compared, while both remaining valid with applicability to different plasma regimes. Our approach, for instance, impedes exhaust jets from fully developing and reaching the Alfvèn speed (both for ions and electrons), as mentioned previously. It might also be responsible for the difference observed in ion and electron acceleration. For this reason, further work on this subject conducted from simulation data should consider fully three-dimensional systems, possibly use a plasma model including kinetic electrons and might consider a setup involving a single current sheet instead of a turbulence simulation.

Chapter 7

Appendices

7.1 The basics of continuum theory

This section is intended to be a reminder of some features of continuum mechanics. Initially, it briefly presents the way in which one can write relations expressing temporal change of field integrals over infinitesimal lines, surfaces or volumes, ending into the definition of "frozen-in" fields (subsection 7.1.1). After the definition of characteristic scales and fluid elements (subsection 7.1.2), the section ends with a discussion on how well a discretely sampled continuum can be resolved (subsection 7.1.3). This last consideration in particular is fundamental whenever one is interested in studying the continuum via numerical simulations and/or multi-satellite measurements.

7.1.1 Evolution laws in the continuum

Given a generic field, we denote with ∂_t the operator that gives us its variation in time, point by point. Similarly, evolution "in the fluid's reference" can be easily found by operating a "local" frame change, and is given by the so-called "Lagrangian derivative" operator, that is:

$$d_t := [\partial_t + \vec{u} \cdot \vec{\nabla}]$$

with $\vec{u}$ being the fluid velocity considered. Now, integrate a generic field over lines, surfaces or volumes which are also transported with the fluid velocity $\vec{u}$ (and thus dubbed "material"). Any change in these integrals will depend not only on the evolution of the field along streamlines, but can also be due to how fluid advection affects the integration domain. The expressions representing these variations are:

$$\begin{aligned} \text{for change over infinitesimal lines:} \quad & d_t\vec{\Psi} + \vec{\Psi} \cdot \vec{\nabla}\vec{u} + \vec{\Psi} \times [\vec{\nabla} \times \vec{u}] \\ \text{for change over infinitesimal surfaces:} \quad & d_t\vec{\Psi} + \vec{\Psi}\vec{\nabla} \cdot \vec{u} - \vec{\Psi} \cdot \vec{\nabla}\vec{u} \\ \text{for change over infinitesimal volumes:} \quad & d_t\Psi + \Psi\vec{\nabla} \cdot \vec{u} \end{aligned}$$

where Ψ and $\vec{\Psi}$ are generic fields (see section 2.2 of Birn & Priest (2007) for reference, or Abraham *et al.* (2003) for a more comprehensive treatment).

Let us notice in particular that field lines of $\vec{\Psi}$ are materially transported whenever the change in the flux of $\vec{\Psi}$ through any infinitesimal surface is either zero, or parallel to the vector field itself (indeed, field lines might well be intended as intersection of surfaces with normals perpendicular to $\vec{\Psi}$). That is, if the change of $\vec{\Psi}$ over perpendicular infinitesimal surfaces is proportional to the flux itself, then integral lines of $\vec{\Psi}$ will be perfectly transported. This consideration leads us to distinguish the following two scenarios:

- frozen-line dynamics when $\vec{u}$ is such to advect integral lines of $\vec{\Psi}$,
- frozen-flux dynamics when $\vec{u}$ preserves the flux of $\vec{\Psi}$ through any surface,

that will come out to be particularly important especially while dealing with the evolution of magnetic fields, and in particular to define the process of magnetic reconnection.

7.1.2 Characteristic scales and simplification criteria

Given a generic field Ψ we can define a characteristic temporal scale τ_Δ and a characteristic length ℓ_Δ by requiring that over such time and distance on average the said field varies of a quantity $\Delta\Psi$. In other words, to find a variation of $\Delta\Psi$ one must either move of a distance ℓ_Δ or wait for a time τ_Δ to pass (the concept of characteristic scale is somewhat similar to the incremental ratio).

Differential equations in which Ψ appears can be simplified once the $\Delta\Psi$ of interest has been chosen and the relative temporal and spatial scales τ_Δ and ℓ_Δ have been determined. In particular, it is often convenient to combine τ_Δ and ℓ_Δ with physical parameters regulating the system (e.g. the viscosity or a characteristic velocity) so to obtain adimensional quantities (or "numbers"). For instance, the ratio between ℓ_Δ/τ_Δ and a characteristic velocity is called "Mach number" while that of $\ell_\Delta^2/\tau_\Delta$ and a kinematic viscosity is a "Reynolds number" (see section 1.4 in Chandrasekhar (1961) for more examples). These quantities determine the so-called "regime" of the system i.e. the "kind" of dynamics which develops. Whenever the ℓ_Δ and τ_Δ of different systems give rise to similar values to these characteristic numbers, the dynamics of the systems is ultimately similar (see for instance paragraph 19 in Landau & Lifshits (1987)). In particular, whenever any of these numbers assumes values much smaller or much bigger than unity it means that some term of those appearing in the equations describing the system is negligible or predominant with respect to some other. In these cases, the equations can be simplified as some terms can be substituted by appropriate constants. To individuate whether simplifications are possible, or whether one can draw analogies with systems where the dynamics is known, it might be of relevance to determine the parameter space of the system considered, as in Fig. 7.1, panel on the left.

At some scales, it might be possible to recognise that the dynamics can be decomposed into motions of basic "units" of the system which can be taken approximately uniform in space and time by themselves, and which make it possible, therefore, to interpret the system's evolution as a re-arrangement of such units, generally described by the

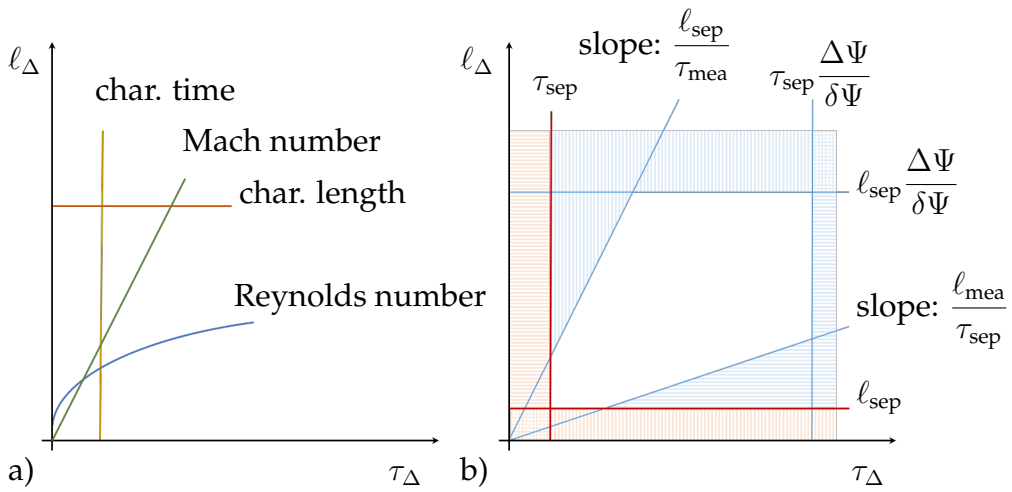

FIGURE 7.1: a) Parameter space of τ_Δ and ℓ_Δ in which different regimes can be recognised as different areas, with frontiers denoted by characteristic lengths and times, or by the locations where Mach or Reynolds numbers equal one (own image). Whenever two systems the characteristic scales under study, ℓ_Δ and τ_Δ, are far from one of such frontiers, one can simplify some terms in the system of equations describing the dynamics (see text).
b) Parameter space of τ_Δ and ℓ_Δ in which different zones have been highlighted if the characteristic scales there are sampled ineffectively and/or oversampled with respect to the capabilities of a data-set (own image). Dynamics is undersampled in all red-shaded regions, while oversampling happens for all areas shaded azure; undersampling and oversampling are spatial if the shading is vertical, temporal if shading is horizontal. Systems with characteristic scales falling in the white region are the only ones which can be "optimally" sampled, least when $\tau_{mea} > \tau_{sep}$ and/or $\ell_{mea} > \ell_{sep}$ i.e. when any scale resolved in the dataset is oversampled.

known fluid equations. Expressing these requirements more formally, it is necessary to introduce the characteristic space $\ell_\square$ and time $\tau_\square$ scales for internal relaxation of the fluid element, and one between the following two: either the element's lifetime $\tau_\#$ (determined by processes that tend to disperse in unorderly fashion the material initially contained within a space of characteristic dimension $\ell_\square$) or the blurring length $\ell_\#$ (which characterises processes which disrupt the unitariety of the element, acting over a time $\tau_\square$).

Now, it is possible to intend a "piece" of the system of characteristic dimension $\ell_\square$ as fluid element with respect to some dynamics whenever its length is negligible with respect to the spatial scales considered (i.e. $\ell_\square \ll \ell_\Delta$) and its relaxation time $\tau_\square$ is negligible with respect to the characteristic time intervals of the dynamics studied ($\tau_\square \ll \tau_\Delta$). These requirements reflect the idea that the fluid element should be negligible in all dimensions, temporal and spatial, at the scales of the dynamics considered. Moreover, it must be required either that the element's "lifetime" is much longer than the temporal scale over which the system is followed (i.e. $\tau_\# \gg \tau_\Delta$) or, equivalently, that the "blurring" length is much smaller than the element's own (read $\ell_\# \ll \ell_\square$). Without any of the last two requests, the element would be nothing but an arbitrary portion of system which has been "cut out" but cannot be understood as a well-defined, material unit whose dynamics can be given a proper description.

7.1.3 Discrete sampling of the continuum

In a variety of different situations, the continuum cannot be known analytically (i.e. "with infinite precision") but, rather, one has to settle with imperfect estimates of values assumed by the fields at certain times only in a number of positions located at finite distance from each other. This is the case of multi-satellite spacecraft missions sampling the interplanetary space, or that of a numerical simulation, in which a finite number of values is used to approximate the continuous change of the physical quantities in time and space alike.

Now, consider our knowledge of the continuum fields as limited to values taken at locations distant ℓ_{sep} from each other, and separated in time by the intervals τ_{sep}. Moreover, known field values result from averaging the real values over some spatial and temporal scale, here indicated by ℓ_{mea} and τ_{mea}, respectively, plus some error which for the generic Ψ field will be indicated by $\delta\Psi$. Given this scenario, let me now try to determine how well any characteristic scales ℓ_Δ and τ_Δ can be resolved.

First, the scales ℓ_Δ and τ_Δ at which the field can be resolved are larger than ℓ_{sep} and τ_{sep} respectively: below such threshold, dynamics is undersampled (see Shi *et al.* (2006) for instance). Once fields are resolved, however, in a variety of cases they can end up being oversampled, i.e. the information provided by data relative to locations close to each other, or at successive instants in time, will be somehow redundant. In other words, let us imagine to diminish progressively ℓ_{sep} and τ_{sep}, and note that smaller and smaller scales can be resolved. At some point, values from neighbouring locations and/or successive samples appear identical. This can happen either because we reached the limits of our resolution, ℓ_δ and τ_δ at which the error $\delta\Psi$ is as big as the characteristic variation of Ψ between close points, or because ℓ_{sep} and τ_{sep} have shrunk to the averaging scales themselves, i.e. ℓ_{mea} and τ_{mea}. A not-so-trivial feature of oversampling problems is that they tend to be "contagious": too large a ℓ_{mea} or ℓ_δ will end up to kill not only spatial resolution, but the temporal also. Analogously, a τ_{mea} or τ_δ too big will end up affecting spatial resolution (as noted in section 17.3 of Paschmann & Daly (1998)). All these considerations can be summarised in the following inequalities (as done in the annexes of Fadanelli *et al.* (2019)):

$$\underbrace{\frac{\tau_{\text{mea}}}{\tau_\Delta}, \frac{\ell_{\text{mea}}}{\ell_\Delta}, \frac{\delta\Psi}{\Delta\Psi}}_{\text{to avoid oversampling}} < \underbrace{\frac{\tau_{\text{sep}}}{\tau_\Delta}, \frac{\ell_{\text{sep}}}{\ell_\Delta}}_{\text{to avoid undersampling}} < 1 \qquad (7.1)$$

where by hypothesis a linear relation has been assumed between the sensibility scale and the characteristic scales we are interested in (i.e. $\tau_\delta/\tau_\Delta = \delta\Psi/\Delta\Psi = \ell_\delta/\ell_\Delta$). An easy visualisation of the relations 7.1 can be found in Fig. 7.1, right panel, where also it is specified whether the bad sampling (undersampling/oversampling) is spatial or temporal, i.e. whether it is $\ell_{\text{sep}}/\ell_\Delta$ or $\tau_{\text{sep}}/\tau_\Delta$ which does not obey the relations just presented.

One trivial remark here regards the effects of interpolating and/or filtering, by which it is possible to obtain datasets of various ℓ_{mea}, τ_{mea}, ℓ_{sep}, τ_{sep} from the original. Obviously, every time one of such operations is performed, interpolations or filtering, it is possible that different scales become well-resolved, not resolved or oversampled. The

art of data processing, obviously, consists in making it so that only the scales which are the most relevant for the study one is performing are the best-sampled ones.

Given the previous considerations one can deduce which scales will be not resolved, resolved or oversampled in the cases of multi-spacecraft missions or computer simulations. A most important observation, then, regards which kind of oversampling, temporal or spatial, one can allow in the aforementioned cases. Indeed, let me note that in a multi-spacecraft mission, with data collected at few locations but with high resolution in time, spatial oversampling would be fatal since it makes pointless to dispose of several satellites - this while temporal oversampling is even desirable, just to be sure that all relevant dynamics can be resolved. On the contrary, since in a numerical simulation generally one disposes of a large quantity of measures at different positions for the same time, but few times at which all these measures are taken (due to memory limitations), there spatial oversampling is not generally a concern, while concentrating all exits in times too close from each other is definitely an useless waste.

7.2 Magnetic structures and their evolution

Considering the primary role of magnetic fields in plasma dynamics, in plasma physics it is often important to describe magnetic structures and their evolution. In this section I introduce the reader to the basics of magnetic field description (subsection 7.2.1), then explain how to define the "velocity" of a magnetic field line (subsection 7.2.2) and that of a magnetic structure (subsection 7.2.3).

7.2.1 Relevant features of magnetic structures

Let me consider some bounded region of space where the magnetic field is nearly everywhere non-null: the "magnetic structure" which is determined in such a region is one of the fundamental elements in determining the system's behaviour i.e. for instance, to predict the accumulation of stresses and the propagation of perturbations (aside: this is going to be a very introductory presentation - for a wider look on the subject, see Ricca (2001)). Two aspects in particular are important in the characterisation of magnetic structures, namely the "topological" and the "geometrical" one. Topologically, one focuses on the "connectivity" which field lines establish by linking portions of the boundary where the field "enters" and "leaves" the region, i.e. by connecting boundaries with different "polarities" to each other. Geometrically, one considers the features relative to the three-dimensional shaping of the field lines (in some sense, this is the non-local extension of the local "magnetic configuration" which has been addressed in the main text - subsection 4.1.1).

As in the following I will present how magnetic structures can be characterised, I will consider three-dimensional systems first and then show what happens if we reduce to the two-dimensional, geometrically simpler case, which has often been used

in the literature. Indeed, even if it is somewhat unnatural to expect any real system to obey the strict symmetry under which a reduced system evolves (as noted in Boozer (2019a)), it must be noted that reduced models are not only more practical to implement both in analytical analyses and numerical computations, but also their results are generally easier to visualise and understand physically. Traditionally, two kinds of reduced models have been extensively employed for magnetised plasma systems: periodic three-dimensional and two-dimensional. Even if here I will only present the latter case, it should be pointed out that the former can effectively provide an interesting "trait d'union" between two-dimensional models and the fully three-dimensional truth (see for instance in Yeates & Hornig (2013) and Yeates & Hornig (2014)).

Among the most important aspects of a magnetic structure, there is its "topology". In order to individuate it, it is useful to start by defining a "continuously connected" volume by some in which any two field lines end up to coincide whenever any point in one of them is moved arbitrarily close to some point in the other. The so-called "separatrix surfaces" divide continuously connected zones from one another, and are obviously characterised by the fact that field lines on either of their sides, no matter how close to each other in some part of the domain, are always separated by some

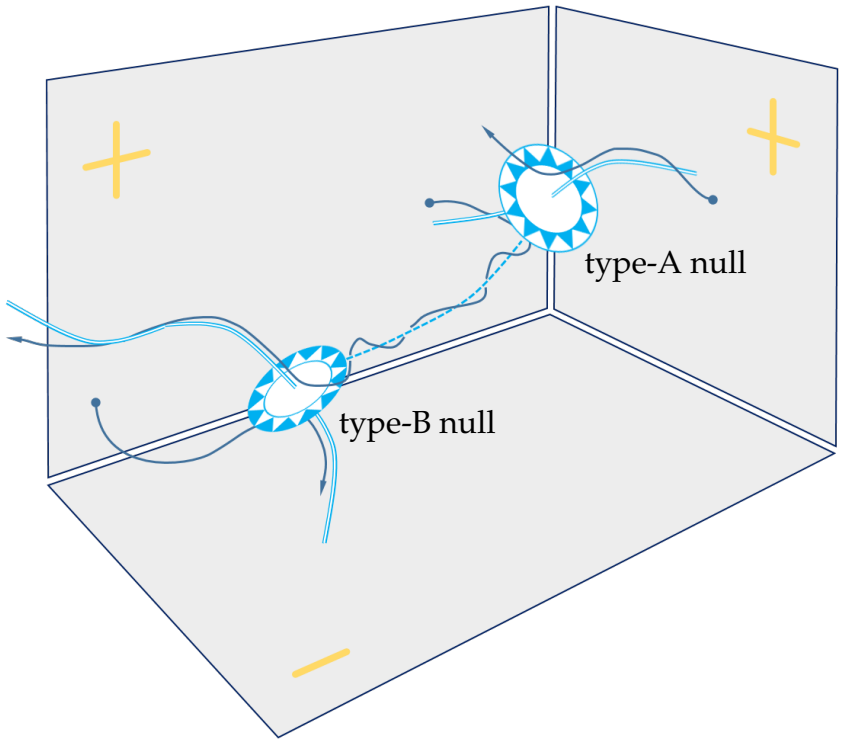

FIGURE 7.2: Schematic representation of the topological skeleton of a magnetic structure with positive polarity on two vertical yellow plates, and negative polarity on the horizontal one (own image). Two nondegenerate nulls are present in this structure, each at the centre of a spine-fan structure, with the spine represented by the white-azure line and the fan by the white-azure plate. Note that the two nulls are of different type (with inward fan lines for the null on the left and outward fan lines for the null on the right). A separator, connecting the nulls, is represented by the dashed azure line. As example, three magnetic field lines are also shown.

finite distance in some part of the system. Lines at the intersection of separatrices are called "separators", and together with separatrix surfaces, they build up the so-called "topological skeleton" of the magnetic structure (see Bungey *et al.* (1996) and section 8.4 of Priest & Forbes (2000)). It is interesting to note that the topological skeleton is always linked with magnetic nulls, i.e. the points where $\vec{B} = \vec{0}$. An intuitive explanation of this fact comes from noting that, since $\vec{B}$ is solenoidal, field lines approaching a null very close to each other generally end up abandoning it while pointing in very different directions, and this while the whole concept of connectivity loses sense for those lines which actually touch the null. This behaviour can be well recognised in the analysis of nondegenerate magnetic nulls, i.e. those in which the trace of $\vec{\nabla}\vec{B}$ is not zero (which is generally the case), where one can always recognise a "spine" curve and a "fan" plane where magnetic field lines "accumulate" as they approach or leave the null's neighbourhood (see Fig. 7.2). Due to the solenoidal nature of $\vec{B}$, obviously, an inward-pointing fan is associated with a "divergent" spine, and a "convergent" spine appears always with outward-pointing fans: in the first case, the null is known as "negative" or "type-A" while in the second case it is said to be "positive" or of "type-B" (see Parnell *et al.* (1996) and section 2.4 in Birn & Priest (2007)).

Alongside to the topological characterisation just presented, it is often useful to take into consideration also some "geometrical" aspects of a magnetic structure. Such aspect can be intended as a refinement of the concept of magnetic topology: while in a topological analysis one considers whether two lines can be made coincident as their foot-points are brought together, however, in determining magnetic geometry one focuses on "how fast" two lines can merge into one, i.e. how "far" apart do field lines "end" whenever they "start" from points "close" to each other. More formally, as the magnetic connectivity projects boundary zones of different polarity onto each other, one can define a mathematical estimator of the "squashing" in the foot-point mapping and thus obtain a geometrical characterisation of the magnetic structure (see for reference Démoulin (2006)). By analogy with the elements of a topological skeleton, in the geometrical analysis we generally recognise "quasi-separatrix layers" as the magnetic surfaces composed by lines for which the squashing in the connectivity map attains some constant value, and "quasi separators" as the lines at which such squashing is locally maximum (see Titov *et al.* (2002), - aside: note that these concepts are analogous to the "Lagrangian Coherent Structures" used in hydrodynamics by Haller (2011), Haller & Beron-Vera (2013), Haller (2014)). In order to obtain a more complete characterisation of magnetic geometry, however, it is possible to introduce more quantities, either focusing on the magnetic linkage, either characterising the in-volume behaviour of the field. As example of the former class let me quote the "orthogonal parquet" (see Titov *et al.* (2002)) while for the latter I will note the magnetic configuration estimators presented before (subsection 4.1.1) and the "exponentiation factor" which evaluates "how fast" is it that "close" field lines separate from each other (see Boozer (2012b), Daughton *et al.* (2014))).

In a two-dimensional system the description of magnetic structures can be incredibly simplified, since the magnetic field can be written in terms of two scalar functions only.

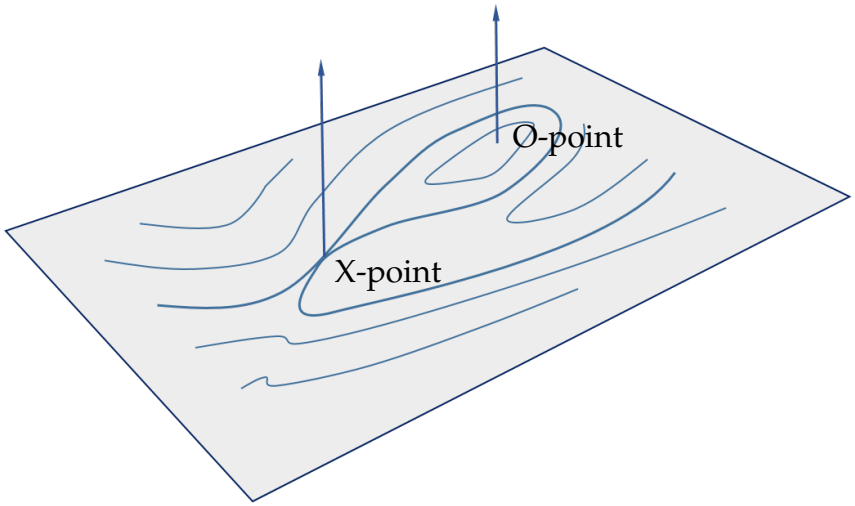

FIGURE 7.3: A two-dimensional magnetic structure, invariant in the direction perpendicular to the yellow surface (own image). In grey-blue, in-plane projection of some field lines crossing the yellow surface, which can be easily identified as contour lines of ψ. In-plane null points can be recognised as elliptic (O-points) or hyperbolic (X-points) according to the behaviour of neighbouring lines.

Indeed, choosing $\vec{e}_z$ as the out-of-plane direction, the following decomposition holds:

$$\vec{B} = \vec{B}_{/\!/} + \vec{B}_z = \vec{e}_z \times \vec{\nabla}\psi + B_z\vec{e}_z$$

where we can recognise ψ as the in-plane magnetic flux. By this description, one can immediately recognise that the sole flux function ψ fully determines both topology and geometry. For what concerns topology, note that continuously connected zones are divided by lines called "separatrices" which intersect at some of the in-plane nulls, called "hyperbolic" or "X-points" due to the characteristic arrangement of the in-plane field. All other in-plane nulls must be "elliptic" i.e. "O-points" (see Fig. 7.3). All geometrical aspects of the magnetic structure can be simply evaluated from the gradient of ψ.

7.2.2 The evolution of magnetic structures: line velocity

Let us now focus on the evolution of the magnetic field. While it is - we know from Maxwell - the electric field that governs magnetic evolution, here we prefer to define a magnetic field velocity. Wherever such a velocity can be obtained, the magnetic field lines can be understood as if they were "dragged" by it, and for this reason it provides an intuitive way to envision and represent how the magnetic field changes. So, let us call it $\vec{c}_B$, and define it by requiring it conserves either the line integral of some magnetic potential $\vec{A}$, either the surface integral of $\vec{B}$, either the volume integral of some $\vec{A}\cdot\vec{B}$ (note that the "some" in this requirements are due to the gauge indetermination of electromagnetic potentials, and see subsection 7.1.1 for quick notes on integrals over lines, surfaces and volumes). A simple check shows that the three conditions defining $\vec{c}_B$ are not only equivalent to each other - obviously - but also that they are equivalent to the request that $\vec{c}_B$ obeys:

$$\vec{E} + \vec{\nabla}\Upsilon = -\frac{\vec{c}_B \times \vec{B}}{c} \tag{7.2}$$

with Υ being an arbitrary scalar which must be set at some value in one point (at least) for each field line (see for instance Birn & Priest (2007) at page 29). At this point, the "classical" way to obtain field velocity from $\vec{B}$ and $\vec{E}$ consists in splitting Eq. 7.2 into parallel and perpendicular components with respect to the local magnetic field: by integrating the parallel equation along field lines one gets Υ from which $\vec{c}_B$ follows thanks to the perpendicular equation.

Writing the procedure to get $\vec{c}_B$, I implicitly recognised two important features of the field velocity. Let me now point them out explicitly. The first note on $\vec{c}_B$ regards all cases in which it cannot be defined. This happens either because Eq. 7.2 cannot be split because of some null, either because forward and backward integration along a closed field line results in different values for $\vec{c}_B$ at the same point. Without closed field lines and nulls, however, it can be demonstrated that some $\vec{c}_B$ does always exist ("anti-reconnection theorem" - see Newcomb (1958), Hornig & Schindler (1996) or Boozer (2012a)). The second note on field velocity is about the fact that, where it exists, $\vec{c}_B$ is not uniquely defined. On one hand, $\vec{c}_B$ is always dependent on the choice of the value of Υ at some (arbitrary) point of every field line. On the other hand, the $\vec{B}$-parallel component of $\vec{c}_B$ must always be set arbitrarily since field velocity has been derived via the $\vec{B}$-perpendicular component of Eq. 7.2 only. For these two reasons, in general $\vec{c}_B$ is not unique. This indetermination substantially reflects the fact that there's no "natural" way to move a field line, but rather field line "motion" must be intended as the change in field line that follows from the motion of the "seed" point from which the line is drawn.

Let me now move to the two-dimensional case, and define a reduced field velocity which is required only to conserve the in-plane flux, and will be called $\vec{c}_\psi$ so to avoid confusion with the general case. In the reduced system, the request that $\vec{c}_\psi$ carries only in-plane flux implies that Eq. 7.2 gets simplified into:

$$\vec{E}_z + v\,\vec{e}_z = -\frac{\vec{c}_\psi \times \vec{B}_{/\!/}}{c} = -\frac{\vec{c}_\psi \cdot \vec{\nabla}\psi}{c}\vec{e}_z \tag{7.3}$$

in which instead of the gradient of Υ appears the constant v (aside: such a profound change is due to the the in-plane vs. out-of-plane distinction which in the case discussed here "preceeds" the otherwise "natural" separation into parallel and perpendicular components). Therefore, determining $\vec{c}_\psi$ requires only to choose the value of v once the out-of-plane $\vec{E}$ and the in-plane $\vec{B}$ are known.

Similar to its three-dimensional counterpart, two-dimensional line velocity fails at in-plane nulls, but contrary to $\vec{c}_B$ it is well defined on closed field lines since it does not need any kind of field-integration to be determined. Moreover, also $\vec{c}_\psi$ is not completely determined due to the arbitrariety of v and the non-definitedness of its component parallel to the in-plane field, reflecting the fact that only a field-perpendicular velocity "makes sense" when it comes to "move" field lines.

7.2.3 The evolution of magnetic structures: structure velocity

Having introduced line velocity, here I turn onto structure velocity i.e. the speed $\vec{c}_X$ which can be associated to a certain magnetic structure which "moves around" in time but does not "change" by itself. In other words, $\vec{c}_X$ can be defined whenever it is supposed that the timescale of a magnetic structure's "intrinsic" evolution is much longer than the time scales under consideration. Under such an hypothesis, obviously, for every magnetic structure a frame must exist such that the structure appears stationary in that frame. In this situation, for any other reference one can write the relation $\vec{0} = [\partial_t + \vec{c}_X \cdot \vec{\nabla}]\vec{B}$ and hence is provided with the expression for structure velocity:

$$\vec{c}_X = -[\partial_t \vec{B}] \cdot [\vec{\nabla}\vec{B}]^{-1} = c\,[\vec{\nabla} \times \vec{E}] \cdot [\vec{\nabla}\vec{B}]^{-1} \tag{7.4}$$

originally derived by Shi *et al.* (2006), which is valid in three-dimensional system as well as in all reduced cases. The quantity $\vec{c}_X$ can be clearly recognised different from $\vec{c}_B$ already introduced since the former takes by hypothesis that the magnetic field is advected in a Lagrangian manner, while the latter is built on the assumption of a flux-conserving flow (for the distinction between the two, see subsection 7.1.1 in Appendix). This is because the magnetic structure which a number of lines form at some instant can be formed by other lines at some other time, which have replaced the original ones but maintain the overall disposition identical (in some sense, note that this distinction is similar to that between phase and group velocity for waves).

Among other things, a particularly interesting use of $\vec{c}_X$ is to find the velocity of magnetic nulls, which can be considered "structures" as long as they are stable in time, i.e. as long as they do not "bifurcate" into two. Indeed, in several numerical experiments the $\vec{c}_X$ calculated from the magnetic field near the magnetic null is in excellent agreement with the null's speed deduced by confronting successive times in the simulation output, this in one-dimensional (see Murphy (2010)), two-dimensional (see Juusola *et al.* (2018)) and even three-dimensional systems (see Murphy *et al.* (2015)).

The note on nulls lead us to the last point of discussion, before going on: can we characterise the evolution of every geometrical and/or topological feature as that of a "magnetic structure" i.e. advecting it by some $\vec{c}_X$? The answer is generally negative: velocity of a geometrical and/or topological feature is not necessarily the $\vec{c}_X$ just introduced even in those cases in which it can be well defined. The easiest way to recognise this is to note that identification of such features follows from the study of the whole system, hence their motions cannot be derived from local parameters and therefore $\vec{c}_X$, which is defined locally, cannot represent such a motion (see Murphy *et al.* (2015)).

7.3 Magnetic reconnection

Within the evolution of magnetised plasmas, particular interest must be given to a class of processes dubbed "reconnections" that are discussed in detail throughout all this section. After the general definition of magnetic reconnection (subsection 7.3.1), I introduce the reader to

reconnection rate, a fundamental parameter to characterise reconnection processes (subsection 7.3.2) and I discuss of the context in which reconnection appears, i.e. what micro and macro physical processes are seen to accompany reconnection (subsection 7.3.3). To conclude the section, I present the reader with the "classical" approach to the study of a single reconnection site (subsection 7.3.4).

7.3.1 Defining magnetic reconnection

Let me begin by reminding the reader (from subsection 2.2.1) that a magnetised plasma is said to be "frozen" wherever magnetic field lines can be thought as co-moving with $\vec{u}$, while the failing of this condition individuates a so-called "diffusion region" in the system. Now, according to the "general magnetic reconnection theory" (developed by Schindler *et al.* (1988) and Hesse & Schindler (1988)), a reconnection site is defined by presence of a localised diffusion region inside a frozen plasma, a condition equivalent to a local failure of the plasma velocity to be flux-preserving (see subsection 2.2.2).

It is interesting to express the criterion for reconnection by supposing some magnetic field velocity $\vec{c}_B$ can be defined (nearly) everywhere in the region of interest (see subsection 7.2.2). Then the perpendicular component of Eq. 7.2 implies that:

$$\vec{c}_B = \frac{[c\vec{E} + c\vec{\nabla}\Upsilon] \times \vec{B}}{B^2} = \vec{u}_\perp + \frac{[c\vec{E} + \vec{u} \times \vec{B} + c\vec{\nabla}\Upsilon] \times \vec{B}}{B^2} \tag{7.5}$$

By this re-writing it is possible to recognise that where $c\vec{E} + \vec{u} \times \vec{B}$ cannot be approximated as the gradient of some scalar, there the perpendicular component of $\vec{u}$ cannot match $\vec{c}_B$ and therefore magnetic surfaces can't "move" as if the plasma advected them, hence magnetic connectivity changes with time.

Including $\vec{c}_B$ in the study of reconnection is important especially in the regard that it allows the distinction between "local" and "global" reconnection processes (as defined in Schindler *et al.* (1988)). In order to understand it, let me say that $\vec{c}_B$ is "anchored" over some finite volume whenever Υ is set so that there $\vec{c}_B$ equals the field-perpendicular plasma velocity. Clearly, $\vec{c}_B$ cannot be anchored on the totality of a volume when this contains reconnection sites, and yet, it is also not necessarily true that $\vec{c}_B$ can be anchored to all the volume outside of the diffusion regions. This circumstance leads to the distinction between "local" and "global" reconnections: whenever it is not possible to find a scalar Υ such that $\vec{c}_B = \vec{u}_\perp$ over all the system not occupied by reconnection sites, reconnection is called "global" while it is "local" if $\vec{c}_B$ can be anchored over all the non-reconnection volume. This distinction is particularly important once recognised that in local reconnection magnetic connectivity is maintained among all plasma elements which travel outside reconnection sites but this cannot be in the global case, since by definition there's no $\vec{c}_B$ which equals $\vec{u}_\perp$ everywhere outside reconnections.

Let me now rephrase the considerations just presented for a two-dimensional system. In this case, reconnection happens wherever a zone of non-null volume has nonvanishing $\vec{E}_z + \vec{u}_{\not z} \times \vec{B}_{\not z}/c$, since in this case in-plane field lines are not advected with the reduced field velocity $\vec{c}_\psi$. Similar to the three-dimensional case, let me consider a

finite-volume zone where $\vec{c}_\psi$ is well defined and write the equivalent of Eq. 7.5 from Eq. 7.3:

$$\vec{c}_\psi = \frac{[c\vec{E}_z + c\,\upsilon\,\vec{e}_z] \times \vec{B}_{/\!/}}{B_{/\!/}^2} = [\vec{u}_{/\!/}]_\perp + \frac{[c\vec{E}_z + \vec{u}_{/\!/} \times \vec{B}_{/\!/} + c\,\upsilon\,\vec{e}_z] \times \vec{B}_{/\!/}}{B_{/\!/}^2} \tag{7.6}$$

where the first term in the rightmost side indicates the in-plane velocity projected perpendicular to the in-plane magnetic field (aside: considering only the $\upsilon = 0$ case, this formula is reported by Liu *et al.* (2018b) and, in simplified fashion, by Liu & Hesse (2016) and Swisdak *et al.* (2003)).

In two-dimensional reconnection the arbitrariety of anchoring vanishes, since taking $\upsilon = 0$ implies that $\vec{c}_\psi$ matches the component of $\vec{u}_{/\!/}$ perpendicular to $\vec{B}_{/\!/}$ throughout all non-reconnecting regions. Given the disappearance of different but equally valid anchoring possibilities, in two dimensions also the distinction of "global" and "local" reconnections stops being meaningful.

Before moving on, let me note here that not all authors recognise for reconnection the definition just presented (see for instance the note which concludes Priest & Démoulin (1995)). As an example, I can report of some who intend "reconnection" as a failure in $\vec{c}_B$ being well-defined (see for instance Boozer (2002)) or as a failure of a more general four-velocity of the electromagnetic field (as in Hornig & Rastätter (1998)). If we were to take the first alternative definition, however, note that all zeros in the magnetic field and some closed field lines become reconnection sites while a series of "commonly accepted" reconnection processes don't get recognised as such (this was recognised for instance in the discussion on plasmoids in Schindler *et al.* (1988)). The second alternative definition I quoted, though seemingly more solid, seems to have been treated really marginally in literature and this makes it difficult to discuss it thoroughly. Even another possible definition of reconnection is that often advocated by A. Boozer (see Boozer (2012a), Boozer (2014), Boozer (2019a), Boozer (2019b)), in which the diffusion region is not characterised by a "diffusivity" which is stronger than the surroundings, but by a stronger exponentiation of field lines. In other words, in this paradigma reconnection appears wherever the magnetic structure of the system allows the microscopic, inherently diffusive, nature of the plasma to emerge macroscopically due to a stochastic, exponentially growing separation of magnetic field lines. While the interested reader is kindly invited to dig into the amusing panorama of the many alternative definitions for reconnection, however, from now on I will stick to the "general" definition of magnetic reconnection just presented, and to that only.

7.3.2 The reconnection rate

One of the most important characteristics of a reconnecting system is given by how much plasma gets "involved" in a reconnection, per unit time, which is generally evaluated by the amount of magnetic flux which gets "mismatched" in each time interval inside a certain surface: this is the so-called "reconnection rate" (aside: always remember the equivalence of line preservation and flux transport for a localised nonideal

region, demonstrated in Hesse & Schindler (1988)). In this subsection, I will briefly discuss the reconnection rate, focusing on how it can be expressed in three-dimensional and two-dimensional systems, and noting how it generally depends on the system's characteristics.

In fully three-dimensional systems, one can express the infinitesimal mismatched magnetic flux i.e. the reconnection rate density, that I will call $\vec{R}_B$, thanks to the usual transport equations (see subsection 7.1.1):

$$\begin{aligned} \vec{R}_B := d_t\vec{B} + \vec{B}\vec{\nabla}\cdot\vec{u} - \vec{B}\cdot\vec{\nabla}\vec{u} \quad &= -\vec{\nabla}\times[c\vec{E} + \vec{u}\times\vec{B}] \\ &= \vec{\nabla}\times[(\vec{c}_B - \vec{u})\times\vec{B}] \end{aligned} \tag{7.7}$$

Reconnected flux through some open surface, per unit time, can be found by integrating any of the three equivalent expression in the previous equation or, by the Kelvin-Stokes theorem, integrating $-c\vec{E} - \vec{u}\times\vec{B}$ or $(\vec{c}_B - \vec{u})\times\vec{B}$ along the surface's contour. Let me quickly remark that the previous expression shows the obvious idea that the variation in magnetic flux across a surface advected with the plasma must be given by the difference of $\vec{u}$ and any field velocity $\vec{c}_B$, which by definition perfectly advects the magnetic flux (aside: notice that while $\vec{c}_B$ is dependent on the choice of Υ, $\vec{R}_B$ is not).

Reconnection rate can also be re-expressed in the two-dimensional case, denoting how much the in-plane flux changes across surfaces advected with the in-plane velocity. Obviously, all relevant surfaces are those constructed by translation of an in-plane curve in the out-of-plane direction (the flux of $\vec{B}_{\not z}$ is identically zero across all surfaces obtained from some portion of the plane, and "oblique" surfaces are not consistent with the system's symmetries). At each point, the mismatched infinitesimal in-plane flux per unit time, i.e. $\vec{R}_\psi$, is given by:

$$\begin{aligned} \vec{R}_\psi := d_t\vec{B}_{\not z} + \vec{B}_{\not z}\vec{\nabla}\cdot\vec{u}_{\not z} - \vec{B}_{\not z}\cdot\vec{\nabla}\vec{u}_{\not z} \quad &= -\vec{\nabla}\times[c\vec{E}_z + \vec{u}_{\not z}\times\vec{B}_{\not z}] \\ &= \vec{\nabla}\times[(\vec{c}_\psi - \vec{u}_{\not z})\times\vec{B}_{\not z}] \end{aligned} \tag{7.8}$$

and the flux reconnected through a surface which is built over some in-plane curve is the difference of the quantity $-c\vec{E}_z - \vec{u}_{\not z}\times\vec{B}_{\not z}$ or $(\vec{c}_\psi - \vec{u}_{\not z})\times\vec{B}_{\not z}$ between the extremes of the said curve (aside: as in the three-dimensional case, also here the ambiguity in defining $\vec{c}_\psi$ does not imply a similar ambiguity in $\vec{R}_\psi$, which is defined regardless of υ).

Now, in dealing with a reconnection site it is customary not to refer to the $\vec{R}_B$ and $\vec{R}_\psi$ quantities just defined, but rather to present one value only, obtained by integrating the rate densities over a certain surface which is deemed representative of the reconnection site considered. In particular, such a reconnection rate $\mathcal{R}$ can be intended as a good indicator of the "strength" of connectivity change between plasma elements, i.e. in some sense it indicates the "fitness" of the reconnection process inside the plasma considered. For this reason $\mathcal{R}$ is the most important parameter characterising reconnection sites (aside: this does not mean that other suggestions have not been advanced, such as those in Scudder *et al.* (2015), but $\mathcal{R}$ remains by far the most widespread of all these).

7.3.3 Contextualising reconnection

Which are the plasma dynamics in which reconnections do generally develop? How does reconnection interact with a mostly ideal plasma system? It is in answering these questions that the full complexity of reconnection's role in plasma physics comes to light, since both small-scale and large-scale plasma processes must be considered at the same time. Indeed, if on the one hand the understanding of reconnection requires to determine how a diffusion region is established, so all small-scale physics is involved in the answer. On the other hand, whether reconnection can proceed is regulated by the overall energetic convenience of novel magnetic connectivities, and determining this requires looking at the large-scale dynamics of the system. The fact that large-scale and small-scale physics must be considered at once when contextualising reconnection, it shouldn't come as surprise that determining the interplay between reconnections and many other processes in plasma physics is, as of today, an open field of research (see Bhattacharjee (2004), Zweibel & Yamada (2009), Hesse & Cassak (2020)).

In the creation of a diffusion region, the heart of a reconnection site, several micro-scale processes might play a part. To identify which these processes are, the most immediate approach is supposing some generalised Ohm's law and investigate how the different terms inside it do contribute to the quantity $\vec{R}_B$ or $\vec{R}_\psi$ which quantifies local mismatching of magnetic flux through fluid-advected infinitesimal surfaces. This kind of investigations (especially considering a generalised Ohm's law equivalent to the electron's Euler equation) has been the object of generous efforts in the past years (see Hesse & Winske (1998), Kuznetsova *et al.* (2000), Hesse (2002), Ricci *et al.* (2004), Hesse *et al.* (2005), Hesse *et al.* (2011a), Hesse *et al.* (2014), Hesse *et al.* (2016), Hesse *et al.* (2018b), Genestreti *et al.* (2018b), Egedal *et al.* (2018), Egedal *et al.* (2019)). More than the exact mechanism underlying the "diffusion" allowing reconnection (see Birn *et al.* (2001) and references therein), however, it has been found that $\mathcal{R}$ depends on the spatial extension of the DR established by such processes. Transverse to the magnetic field, too large a diffusion region has been reported to slow down reconnection by hampering the release of energy stored at large scales (see Karimabadi *et al.* (2007)). Therefore, standing fluid structures (see Petschek (1964)) or instabilities (like those discussed in Daughton *et al.* (2006) for instance) which affect the transverse scales of non-ideal regions have been historically regarded as the main responsibles for "fast" reconnections. Along the magnetic field, however, it is generally expected that reducing a nonideal region's length below some critical, macroscopic value would ultimately diminish reconnection rate, but this topic has scarcely been explored (see for instance Huang *et al.* (2019)). In some cases (see Karimabadi *et al.* (2007), Cassak *et al.* (2007b), Cassak *et al.* (2007a)) reconnection rate has been seen responding abruptly to changes in the extension of the diffusion region, and such non-linearity clearly constitutes an added difficulty in determining what is the exact relationship between $\mathcal{R}$ and DR dimensions.

Determining the "energetic convenience" of reconnection, one must consider a number of elements in large-scale plasma dynamics. Usually, the main contribution to energy release is given by the relaxation of field lines, i.e. the discharge of "magnetic tension" which is accounted by the $\vec{B} \cdot \vec{\nabla}\vec{B}/4\pi$ term inside the Lorenz force density (see

Liu *et al.* (2017), Liu *et al.* (2018b)). In order for the magnetic field to release its energy, however, it is crucial to analyse more than the magnetic structure: for instance, one of the main elements in determining whether such release is allowed is the pattern of plasma motions around a reconnection site. Indeed, it has been evidenced in multiple occasions that processes leading to modifications of plasma flows inside and around the reconnection site are associated with changes in $\mathcal{R}$ (see Drake *et al.* (2006b), Matteini *et al.* (2013) for instance). Also the presence of fluid drifts can modify flow patterns leading to diminution of reconnection rate, possibly until reconnection gets altogether suppressed (this possibility was recognised in Swisdak *et al.* (2003), Liu & Hesse (2016), and several observations in space seem to support it - see for reference only Sawyer *et al.* (2019), Fuselier *et al.* (2020), Vernisse *et al.* (2020)), and velocity shears advecting the foot-points of reconnected lines can make reconnection more or less energetically favoured (see Doss *et al.* (2015) or Doss *et al.* (2016) for cases in which advection of footpoints resulted in diminished reconnection rate, and Ma *et al.* (2016), Liu *et al.* (2018b) for situations in which this does not seem to happen). Understanding the exact dependency of $\mathcal{R}$ on flow patterns, however, is not trivial since in some cases even slight perturbations of the latter result into sudden changes of the former (e.g. note how slight local variations in a temperature-generated diamagnetic drifts lead to reconnection "bursts" in Liu & Hesse (2016)).

The problem of contextualising reconnection within the micro and macro scales of plasma processes is particularly evident in the conflict between the "inside-out" and "outside-in" perspectives of reconnection physics which have been advanced and discussed throughout the years. Basically, in the "inside-out" view of reconnection it is the local physics "at or near" the reconnection site to be the main element in determining the rate. On the other hand, taking the "outside-in" view one supposes that $\mathcal{R}$ is primarily given by the dynamics of plasma over an extended volume around the reconnection site. As of today, it is not completely understood the extent to which each of these two views is correct and the debate remains open, stimulating an improvement in theoretical and observational studies of reconnection (see Hesse & Cassak (2020)).

Before closing, an important note is due on the dimensionality we consider as approaching the study of reconnections. Even if the magnetic configurations in which reconnection develops are generally three-dimensional, yet the study of two-dimensional reconnections has filled the overwhelming majority of the literature since reduced problems ultimately offer easier treatment and better understanding of the physics. Passing from three to two dimensions and thus neglecting several features of the whole system, however, means that such simplifications can lead to problematic situations.

- In two dimensions, it is possible that some characteristics of reconnection processes come to be "distorted" with respect to the way they appear in the three-dimensional reality. For instance, allowing wavevectors to develop only in-plane might result in reduced reconnection proceeding with a rate which is artificially diminished with respect to the one which would have developed in three dimensions. While in systems characterised by one single reconnection process it is sometimes possible to orient the two-dimensional plane so to recover the three-

dimensional rate (see Hesse *et al.* (2013) and Liu *et al.* (2018a)), this becomes increasingly unlikely for systems in which multiple reconnections develop (see for instance in Nakamura *et al.* (2013) and Karimabadi et al. in Balogh *et al.* (2014)).

- In two dimensions, some characteristics of the three-dimensional system cannot be attained at all. This is the case, for instance, of some bundling which magnetic field lines can attain only in three dimensions. In particular, it is impossible to have locally "exponentially diverging" field lines, and therefore cannot allow some forms of reconnection, which might be indeed relevant in many cases of practical application (see Boozer (2019a)). Another example is the distinction between "global" and "local" reconnections (which we have seen in subsection 7.3.1) which just lose meaning as one passes into two-dimensional systems.

For these reasons, while the study of reconnection in a two-dimensional geometry is ultimately easier to carry on, yet it is important to keep in mind that its relative simplicity comes at the prize of a distortion which should be carefully taken into account every time one wants to infer from it the properties of three-dimensional plasma dynamics.

7.3.4 The study of specific reconnection sites

Let us put aside for some moment the problems discussed in the previous subsection, and focus on a single, isolated reconnection site by considering only a small volume around the diffusion region, supposing some form for the fields and plasma inside it and determining the others under the assumption of time-stationarity. This is the so-called "kinematic" approach to the reconnection physics, and has proved to be enormously useful in making clear some characteristics of several reconnection sites. As a working hypothesis, note that neglecting temporal evolution is not particularly limiting because one can generally find a zone encompassing the whole reconnection site which is large enough to determine all features of the reconnection process but is yet so small that its "relaxation" can be virtually assumed to take no time compared to the physics of interest (this is noted in Biskamp (2005), section 3.3). One must remember, however, that only a non-stationary, dynamical study can provide the information required as starting point for a kinematic analysis, i.e. a wider inquiry of plasma dynamics is always necessary to identify the structure of magnetic field and flows to study in kinematic approach.

As an example of how kinematic analyses are carried on, let me present here a viable procedure to apply in such studies, declined both in the three-dimensional and in the two-dimensional cases. In a three-dimensional system one can suppose an analytical form for $\vec{B}$ and $c\vec{E} + \vec{u} \times \vec{B}$, which determines how the diffusion region is shaped, then retrieve $\vec{E}$ and $\vec{u}_\perp$ once specified the value of either of them on a reference surface that crosses all the field lines. This can be done, for instance, by exploiting the trivial solution $\vec{c}_B = \vec{0}$ which is given by time stationarity: the simplified form of Eq. 7.5 given by $\vec{c}_B = \vec{0}$ allows to retrieve the values of Υ on the reference surface first, then determine $\vec{E}$ and $\vec{u}_\perp$ once Υ has been calculated over the whole of the volume via field-line integra-

tion of $c\vec{E} + \vec{u} \times \vec{B}$. If the system is two-dimensional instead, the very same procedure can be carried on by assuming first $\vec{B}_{/\!/}$ and $c\vec{E}_z + \vec{u}_{/\!/} \times \vec{B}_{/\!/}$, with $\vec{E}_z$ and the fluid velocity perpendicular to the in-plane field following from specifying either of them at some point of the system. Similarly to the three-dimensional case, a strategy can be to use Eq. 7.6 simplified by assuming $\vec{c}_\psi = \vec{0}$ thanks to time stationarity: the value of υ determined at the reference point allows to find $\vec{E}_z$ and the fluid velocity perpendicular to the in-plane field everywhere. From this point, in both tree-dimensional and two-dimensional systems it is possible to proceed by considering more physical variables (such as density, pressure etc.) and establish their values in relation to the quantities already assumed and/or determined; however, here I will not discuss possible strategies to include such quantities in the kinematic analysis.

In a three-dimensional reconnection site, the most natural way to analyse the change of magnetic connectivity is through a machinery based on the introduction of two line velocities, a machinery which can be put in place whenever (nearly) all magnetic lines traversing the region considered have their foot-points on the boundary of the volume considered. Indeed, in this case at (nearly) every point one can define $\vec{c}_B^{\,+}$ by requiring it is anchored on the plasma on the boundary through which the field enters, and $\vec{c}_B^{\,-}$ anchored where the field exits (positive and negative polarity boundaries). Alongside with the two field velocities, obviously, by forward and backward integration of the parallel electric field along the magnetic line one obtains the two scalars Υ^+ and Υ^- over (nearly) the whole volume. Now, by definition reconnection happens wherever at least one of $\vec{c}_B^{\,+}$, $\vec{c}_B^{\,-}$, $\vec{u}_\perp$ differs from the other two, and reconnection rate density is easily found at every point by inserting either field velocity in Eq. 7.7. The advantage of introducing two field velocity becomes apparent when in need to distinguish between local and global reconnection events (classification introduced in subsection 7.3.1), since reconnection caused by $\vec{u}_\perp$ differing from $\vec{c}_B^{\,+} = \vec{c}_B^{\,-}$ is local while it is global only if the two field velocities are distinct from each other (see Priest *et al.* (2003) - note also that Titov *et al.* (2009) provides a sound mathematical framework allowing the identification of global reconnections from a refinement of the $\vec{c}_B^{\,+} \neq \vec{c}_B^{\,-}$ condition just stated). The need of two field velocities, however, disappears completely in the two-dimensional case since $\vec{c}_\psi$ is always uniquely anchorable to the whole of ideal plasma by setting υ to zero and there's no distinction between local and global processes. In this scenario, connectivity changes occur whenever the $\vec{c}_\psi$ with $\upsilon = 0$ differs from the in-plane, field-perpendicular fluid velocity and the reconnection rate is simply given by Eq. 7.8.

Let me focus now on a series of reconnection sites for which kinematic studies have been carried on. In particular, in three dimensions I will consider two cases, one in which the field never vanishes and the other in which the diffusion region contains a null-point. In two dimensions instead I will consider only the case in which the diffusion region contains a X-point (hyperbolic null of the in-plane field) which can be considered a limit situation for both the three-dimensional configurations discussed here (see Fig. 7.4 for an overview).

In global three-dimensional reconnection without nulls, performing a kinematic anal-

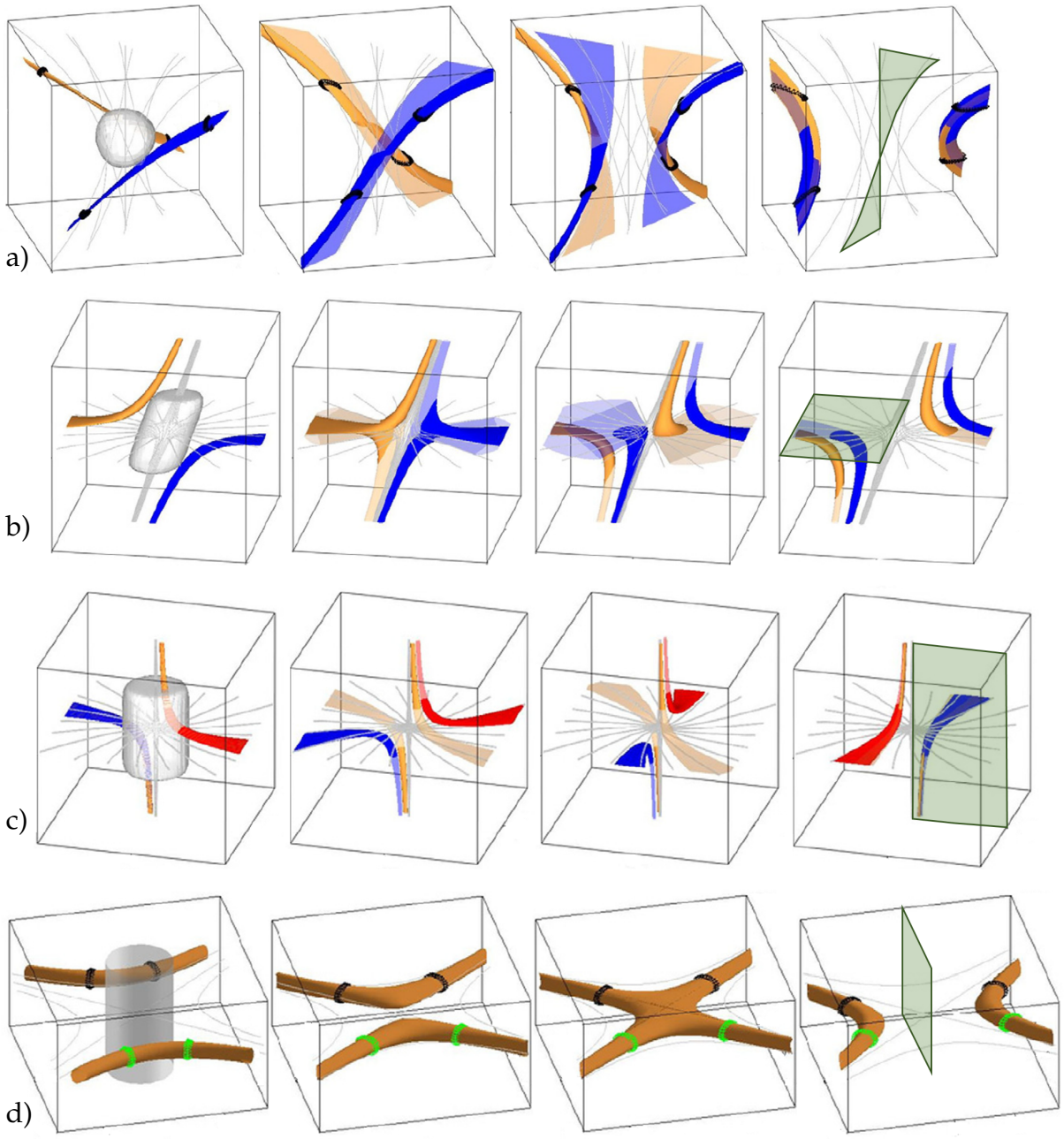

FIGURE 7.4: Different reconnection sites, in which the flux tubes connected to some plasma particles have been highlighting so to rend the motion of field lines close to a nonideal region (adapted from Pontin (2011)). In the leftmost column, the shading shows the extension of the nonideal region considered. In the rightmost column, the surface used to evaluate the characteristic reconnection rate for each site.
a) Non-null, three-dimensional reconnection ("magnetic flipping").
b) Three-dimensional reconnection with null and nonideality: fan-aligned current.
c) Three-dimensional reconnection with null and nonideality: spine-aligned current.
d) Two-dimensional reconnection with in-plane null and nonideality, represented in a three-dimensional box for the sake of uniformity within the figure.
Aside: note how the presence of a current impacts the neighbourhood of a magnetic null, bending the spine whenever it is fan-aligned and torquing the fan's field lines when it flows along the spine instead.

ysis reveals that an ongoing connectivity change must be accompanied by the apparition of a counter-rotating component in the plasma flows traversed by the reconnecting field lines (see Hornig & Priest (2003) or section 2.3 in Birn & Priest (2007)). In particular, the combination of such counter-rotating flows with an hyperbolic velocity pattern across the diffusion region determines the characteristic "magnetic flipping" movement which can be recognised for the field lines connected with the material passing close to the diffusion region (see top row of Fig. 7.4). In particular, magnetic flipping is indicative of the difference between the $\vec{c}_B^{+}$ and $\vec{c}_B^{-}$ which develop in this case. To determine the site's reconnection rate one usually considers field-parallel surfaces which is partially immersed inside the diffusion region: reconnection rate across such surfaces is given by the value $|\Upsilon^+ - \Upsilon^-|$ at the magnetic line on each surface's contour across the nonideal region (see Hesse & Schindler (1988)). Sometimes, the maximum among all rates obtained by this method is intended as "the" rate for the whole reconnection site even if more complex scenarios might require a more delicate approach which takes in consideration more than one quantity (see Hesse & Birn (1993), Wyper & Hesse (2015)).

If a magnetic null is embedded inside the diffusion region, then the magnetic field's structure of the reconnection site can be recognised in the characteristic "spine and fan" configuration (as mentioned in subsection 7.2.1, see the two central rows of Fig. 7.4). Within this case, kinematic studies have been focused on two sub-cases in particular, namely, that of a fan-aligned current or that of a spine-aligned current. In the first sub-case a cross-fan flux of plasma must be present (as in Pontin *et al.* (2005)) while in the second one reconnection assumes the characteristics of a "rotational slippage" around the spine (see Pontin *et al.* (2004)) very similar to what one can see in a non-null reconnection (recall the counter-rotating flow pattern which was necessary in that case). Depending on the situation, then, one can recognise different surfaces to estimate a single reconnection rate for the whole reconnection site. Similar to the non-null reconnection case, also here the surfaces considered are composed by field lines, and generally the null falls on their boundary. For instance, reconnection rate for a spine-aligned current can be estimated by the spine-integral of the parallel electric field, while in the case of a fan-aligned current a good measure can be found by integrating $\vec{E}$ along the magnetic field line which encounters the null parallel to $\vec{J}$ there (see Pontin *et al.* (2004), Pontin *et al.* (2005), and Wyper & Jain (2013)).

If up to now we have seen three-dimensional examples, it is in two dimensions that we find the most extensively studied reconnection site, namely, the X-point surrounded by a nonideal region. In some regards, this case can be seen as the "extraction" of a plane from the fan-aligned null-point reconnection or as a two-dimensional "compression" of the non-null case (see 2.3.5 in Birn & Priest (2007)). For instance, by carrying on the same kinematic analysis performed in three dimensions it is immediate to recognise that by the presence of a diffusion region the flow must develop into an hyperbolic pattern characterised by a stagnation situated at the so-called "S-point" within the nonideal region, a situation which is similar to fan-aligned null-reconnection in three dimensions (aside: this was recognised by Nickeler *et al.* (2012) via a procedure which is somewhat different to the one discussed here, but ultimately equivalent). The strict two-dimensional constraint of the dynamics, however, results into distinct peculiari-

ties also. For instance, flux tubes advected toward the X-point get reconnected in pairs i.e. the two portions of a severed flux tube always recombine with the two halves of another flux tube, instead of each getting connected with different one (see the bottom row of Fig. 7.4). In this case any curve with one extreme at the X-point and the other in the ideal plasma defines a surface to compute the reconnection rate, implying that $\mathcal{R}$ here is given by the out-of-plane electric field (note that E_z at the X-point is the same as everywhere else because of time-stationarity). A variety of kinematic studies tries to provide additional detail to this picture. Among these, particularly fortunate have been the so-called "scaling analyses" in which several variables are assumed constant and uniform in the inflow and outflow sufficiently far from the diffusion region, and analytical relations have been established between them (see Cassak & Shay (2007), Hesse *et al.* (2009), Birn *et al.* (2010), Hesse *et al.* (2011b), or the more complicated Divin *et al.* (2012)).

Concluding this subsection, it is important to recall that while kinematic analyses are well suited to understand the relations between quantities appearing in a reconnection site supposed stationary in time, only a dynamical study of reconnection physics can establish which stationary configurations are the ones in which a system generally evolves, or which ones are improbable. Since dynamical studies tend to be technically challenging, however, only in very few cases they have been carried on by analytical calculations, the custom being resorting to numerical experiments instead (aside: as examples of dynamical studies conducted analytically, consider for instance the "collapse" analyses of unstable magnetic structures, such as Longcope & Cowley (1996), Mellor *et al.* (2002), Mellor *et al.* (2003), Pontin & Craig (2005)). In particular, by numerical analysed it has been determined that all the reconnection cases just discussed in kinematic fashion are indeed representative of situations which come to be realised by the plasma evolution (see Al-Hachami (2019) for the non-null case, and Pontin (2011) reporting that if the diffusion region contains a null the development of fan-aligned/spine-aligned current can be achieved by a shear-like/rotational perturbation; to assess that two-dimensional reconnection models are also viable, or how to intend them within the three-dimensional space, see Hesse *et al.* (2013), Sauppe & Daughton (2018), Liu *et al.* (2018a)). Before closing, it might be worth also adding that not only simulations can establish the dynamics of a reconnecting plasma, but these also allow to get into the micro-physics involved in such process - an aspect of reconnection in which interest has recently been substantial (see subsections 7.5.1 and 7.5.2).

7.4 Gyrations and guiding centres

Here I provide a quick overview of single-particle behaviours in plasmas, which are fundamental whenever one is interested into some details of small-scale plasma dynamics (as for instance while dealing with diffusion-region physics). To this aim, first I show that under some circumstances the orbit of a charge in a magnetic field can be separated into the motion of a guiding centre and a gyration, and how it is possible to devise a dynamics for each of these (subsection

7.4.1). For a gyrating particle, gain or loss of energy can be recognised locally as the effect of the so-called "type-A" and "type-B" Fermi processes (as I detail in subsection 7.4.2) while statistically one must distinguish between the "first-order" and "second-order" energisation scenarios (subsection 7.4.3). The section ends with an overview of the so-called "adiabatic invariants" i.e. quantities which characterise the quasi-periodicities in a particle motion and can allow useful insight on single-charge motions (subsection 7.4.4).

7.4.1 Decomposing the dynamics

Let me suppose that a charge moves in an environment where the electric and magnetic field have characteristic scales ℓ_Δ and τ_Δ much larger, respectively, than the characteristic length and time of the charge's motion. It is clear that in this situation the charge's behaviour can be locally approximated as if the background was uniform, a case in which the charge's orbit is an helix coaxial with the magnetic field. For this reason in a nearly-uniform environment it is natural to decompose charges' motions into a "guiding centre" i.e. low-frequency, large-scale component and a "gyration" which constitutes the high-frequency and small-scale behaviour. Performing such decomposition also on the motion laws gives us the so-called "guiding centre" treatment of the charge's dynamics.

Let me begin by recognising the "average" and "gyration" motions by indices "a" and "g" respectively:

$$\vec{r} = \vec{r}_a + \vec{r}_g \qquad\qquad \vec{v} = \vec{v}_a + \vec{v}_g$$

with the prescriptions that the spatial and temporal scales of gyrations, i.e. ℓ_g and τ_g, are much smaller than those of the average motion, i.e. ℓ_a and τ_a, and that $\vec{r}_g$ and $\vec{v}_g$ average to zero over ℓ_g and τ_g. Now, calling ϵ the small parameter by which the scales are separated (for simplicity, here I suppose $\ell_g/\ell_a = \epsilon = \tau_g/\tau_a$), the acceleration term in Newton's law can be expanded into:

$$m d_t \vec{v} = \underbrace{m d_t \vec{v}_{g0}}_{\epsilon^0} + \underbrace{m[d_t \vec{v}_{a0} + d_t \vec{v}_{g1}]}_{\epsilon^1} + \dots$$

thanks to the previous considerations (aside: a rigorous derivation of the order expansion just presented might be achieved by the method described in Hazeltine & Waelbroeck (2018): basically, one understands the gyrations as functions of a "time" t/ϵ instead of using t and in this way $\vec{r}_g$ and $\vec{v}_g$ can be correctly expanded in ϵ, hence the previous result). Also the electromagnetic fields at the point where the particle is located can be obtained via Taylor's expansion about the average point, i.e. at the so-called "gyrocentre":

$$\underbrace{\vec{E}}_{\epsilon^0} + \underbrace{\vec{r}_g \cdot \vec{\nabla}\vec{E}}_{\epsilon^1} + \dots \qquad \underbrace{\vec{B}}_{\epsilon^0} + \underbrace{\vec{r}_g \cdot \vec{\nabla}\vec{B}}_{\epsilon^1} + \dots$$

Inserting the expanded fields and acceleration term into Newton's law one obtains a

series of motion equations, one for each power of ϵ:

$$m d_t \vec{v}_{g0} = q\left[\vec{E} + \frac{[\vec{v}_{g0} + \vec{v}_{a0}] \times \vec{B}}{c}\right] \tag{7.9}$$

$$m[d_t \vec{v}_{g1} + d_t \vec{v}_{a0}] = q\left[\vec{r}_g \cdot \vec{\nabla}\vec{E} + \frac{[\vec{v}_{g1} + \vec{v}_{a1}] \times \vec{B} + [\vec{v}_{g0} + \vec{v}_{a0}] \times [\vec{r}_g \cdot \vec{\nabla}\vec{B}]}{c}\right] \tag{7.10}$$

From this series of equations one can extract the laws of gyrocentre motion just by averaging over one gyration. The difference between Eqs. 7.9, 7.10 and their gyration-averages determine the gyration motion approximated to zeroth and first order in ϵ.

Let me start by considering the gyration. Defining the Larmor frequency $\omega_g := qB/mc$, at order zero, Eq. 7.9 becomes:

$$m d_t \vec{v}_{g0} = m[\vec{v}_g \times \omega_g \vec{e}_{||}]$$

which implies that in zeroth approximation the gyration is an uniform, circular motion in the plane perpendicular to $\vec{B}$:

$$\vec{v}_{g0} = \vec{r}_g \times \omega_g \vec{e}_{||}$$

All successive orders will keep track of corrections to this perfectly circular behaviour, but in general their exact form is of little interest here. Passing to average motion, defining the Larmor moment $M_g := m v_{g0}^2/2B$, the gyration averages of Eqs. 7.9 and 7.10 appear:

$$\vec{0} = q\vec{E} + [q/c][\vec{v}_{a0} \times \vec{B}]$$
$$m d_t \vec{v}_{a0} = [q/c][\vec{v}_{a1} \times \vec{B}] - M_g \vec{\nabla} B$$

with the last term in the motion equation following from the series of equivalences:

$$\begin{aligned}
\langle \vec{v}_{g0} \times [\vec{r}_g \cdot \vec{\nabla}\vec{B}] \rangle_g &= \omega_g \langle [\vec{r}_g \times \vec{e}_{||}] \times [\vec{r}_g \cdot \vec{\nabla}\vec{B}] \rangle_g \\
&= \omega_g \langle \vec{r}_g : \vec{\nabla}\vec{B}\, \vec{e}_{||} - \vec{r}_g \cdot \vec{\nabla}\vec{B} \cdot \vec{e}_{||} \rangle_g \\
&\overset{\bullet}{=} [\omega_g r_g^2/2] \left[[\vec{\vec{1}} - \vec{\vec{e}}_{||}] : \vec{\nabla}\vec{B}\, \vec{e}_{||} - [\vec{\vec{1}} - \vec{\vec{e}}_{||}] \cdot \vec{\nabla}\vec{B} \cdot \vec{e}_{||} \right] \\
&= [\omega_g r_g^2/2] \left[\vec{\nabla} \cdot \vec{B} - \vec{\nabla} B \right] \\
&= -[\omega_g r_g^2/2] \vec{\nabla} B \\
&= -[c/q]\, M_g\, \vec{\nabla} B
\end{aligned}$$

the $\langle \ldots \rangle_g$ being gyration average, and "$\bullet$" denoting a passage based on the mathematical relation:

$$\langle \vec{\vec{r}}_g \rangle_g = [r_g^2/2]\, [\vec{\vec{1}} - \vec{\vec{e}}_{||}]$$

Now, one can extract easily the gyrocentre velocity from these equations. In particular, introducing the "magnetic drift velocity" relative to some force as:

$$\vec{c}_{...} := \frac{c}{q} \frac{\vec{F}_{...} \times \vec{B}}{B^2}$$

it is possible to individuate that field-perpendicular gyrocentre motion is given by the "E-cross-B" drift at order zero, and at order one the "gradient-B", "inertial" and "polarisation" drifts:

$$\begin{aligned} \vec{F}_E &:= q\vec{E} \qquad \Rightarrow \qquad \vec{v}_{a0} = \vec{v}_{\|_0} + \vec{c}_E \\ \vec{F}_G &:= -M_g \vec{\nabla} B \\ \vec{F}_K &:= -m d_t \vec{v}_{\|_0} \qquad \Rightarrow \qquad \vec{v}_{a1} = \vec{v}_{\|_1} + \vec{c}_G + \vec{c}_K + \vec{c}_\Pi \\ \vec{F}_\Pi &:= -m d_t \vec{c}_E \end{aligned}$$

In particular, when the magnetic field direction $\vec{e}_\|$ varies mainly parallel to the magnetic field itself, the "inertial" drift term can be approximated by the "curvature" drift:

$$\begin{aligned} \vec{F}_K &= m[\vec{e}_\| d_t v_{\|_0} + v_{\|_0} d_t \vec{e}_\|] \\ &= m\Big[\vec{e}_\| d_t v_{\|_0} + v_{\|_0}[\partial_t \vec{e}_\| + \vec{v}_{a0} \cdot \vec{\nabla}\vec{e}_\|]\Big] \\ &\simeq m\Big[\vec{e}_\| d_t v_{\|_0} + v_{\|_0}^2 \underbrace{[\vec{e}_\| \cdot \vec{\nabla}\vec{e}_\|]}_{=:\vec{\kappa}}\Big] =: \vec{e}_\| m d_t v_{\|_0} + \vec{F}_C \end{aligned} \qquad \Rightarrow \qquad \vec{c}_K \simeq \vec{c}_C$$

All drifts just introduced can be "physically" interpreted by noting that some change in the length of the particle's Larmor radius will result in moving the gyrocentre closer or further to the gyration orbit - a motion that the guiding centre theory interprets as drift. Now, the Larmor radius can be affected either by the magnitude of B (this is the mechanism underlying the "gradient-B" drift) either by some change in gyration velocity, that is, by any perpendicular acceleration. When this mechanism is driven by some electric force we get the "E-cross-B" drift, that is of order zero, while a change in order-zero gyrocentre motion gives the "inertial" and "polarization" drifts, of order one.

Before closing the section, it is important to remark that in some cases macroscopic plasma processes can be recognised as the product of the gyration effects just presented. For instance, magnetic drifts can appear also at fluid level when the gyratoric behaviour which determines them contributes equally to the dynamics of the whole plasma. Instead, "drift currents" are an example of what happens when gyratoric effects act differently on particles with different mass, charge and/or velocity (see Parker (1957)). The complete understanding of such phenomena, however, requires a through presentation of gyro-kinetic and/or gyro-fluid theories, a presentation which falls beyond the scope of this work.

7.4.2 Fermi processes: type-A and type-B

The investigation of particle energisation in magnetised plasmas presents two quite distinct aspects linked to Fermi's name, and one of these is the categorization of energisations as "type-A" and "type-B" Fermi processes. In order to understand this categorisation, let me begin by expressing energisations in single-particle guiding centre theory. I begin by writing the equations describing the evolution of kinetic energy due to the particle's gyration $\mathcal{E}_g$ and due to gyro-averaged motions $\mathcal{E}_{a\|}$ and $\mathcal{E}_{a\perp}$, separated

according to velocity parallel and perpendicular to the magnetic field. Approximating the guiding centre velocity by $\vec{v}_{||} + \vec{c}_E$ (as in Northrop (1963)) one gets:

$$\begin{aligned} d_t\mathcal{E}_g &= M_g\, d_t B &&= \vec{v}_{||} \cdot M_g \vec{\nabla} B + M_g[\partial_t + \vec{c}_E \cdot \vec{\nabla}]B \\ d_t\mathcal{E}_{a||} &= \vec{v}_{||} \cdot m d_t \vec{v}_{||} &&= \vec{v}_{||} \cdot \left[q\vec{E} - M_g \vec{\nabla} B\right] + \vec{c}_E \cdot \left[m v_{||}^2 \vec{\kappa} + m v_{||}[\partial_t + \vec{c}_E \cdot \vec{\nabla}]\vec{e}_{||}\right] \\ d_t\mathcal{E}_{a\perp} &= \vec{c}_E \cdot m d_t \vec{c}_E &&= \dots \end{aligned} \tag{7.11}$$

where for our limited aims the $m d_t \vec{c}_E$ in the last equation has not been expanded. Indeed, it is enough to me to recognise in the previous expressions the following elements:

"curvature term"	$\vec{c}_E \cdot m v_{||}^2 \vec{\kappa}$
"betatron term"	$M_g[\partial_t + \vec{c}_E \cdot \vec{\nabla}]B$
"mirroring term"	$\vec{v}_{||} \cdot M_g \vec{\nabla} B$

and note that the "curvature term" contributes to parallel particle energy, the "betatron term" contributes to perpendicular energy and the "mirroring term" regulates exchanges between $\mathcal{E}_g$ and $\mathcal{E}_{a||}$. Summing up parallel and perpendicular contributions we get:

$$d_t\mathcal{E} = \vec{v}_{||} \cdot [q\vec{E}] + \vec{c}_E \cdot \left[m v_{||}^2 \vec{\kappa} + m v_{||}[\partial_t + \vec{c}_E \cdot \vec{\nabla}]\vec{e}_{||} + m d_t \vec{c}_E\right] + M_g[\partial_t + \vec{c}_E \cdot \vec{\nabla}]B$$

in which we can recognise all processes behind the energisation or de-energisation of a gyrating charge.

Let's consider now a physical system in which there's no electric field and the magnetic structure is static in some particular frame of reference. Whenever one takes another reference frame, however, particles will appear to be accelerated or decelerated by some non-zero electric field which is linked to the magnetic structure velocity $\vec{c}_X$ (for more details on $\vec{c}_X$ see subsection 7.2.3). Such an acceleration can be determined by frame-transforming the energy-evolution equation for the velocity boost $\vec{c}_X$, obtaining:

$$d_t\mathcal{E} = -\vec{c}_{X||} \cdot [M_g \vec{\nabla} B] + \vec{c}_{X\perp} \cdot [m(v_{||} - c_{X||})^2 \vec{\kappa}] \tag{7.12}$$

where the two terms on the right determine the so-called "type-A" and "type-B" Fermi processes. Looking into the derivation of this last equation, one notes that the betatron term is related with type-A processes while curvature acceleration leads to type-B energisation, with the former increasing $\mathcal{E}_g$ and the latter acting upon $\mathcal{E}_{a||}$. Both these acceleration mechanisms can be intuitively understood by recognising that in a static magnetic structure the magnetic gradient and/or magnetic curvature can change only the direction (but not modulus) of a charge's velocity: taking a reference frame in which the same structure is seen moving implies that the same charge's velocity will be recorded to vary also in modulus (this argument is schematically represented in Fig. 7.5). As no change in reference frame can vary the magnetic-field-parallel component of $\vec{E}$, no "Fermi-type" energisation is linked to the field-parallel term.

To conclude this presentation, let me stress the fact that even if up to now we have considered particles singularly, also it is possible to deduce from the considerations

just presented some of the overall effects which type-A and type-B processes have on a gyrating plasma population. In particular, it can be noted that since type-A acceleration acts proportional to the gyration velocity squared, it tends to widen the ƒ on the field-perpendicular plane. With type-B process being proportional to the parallel guiding centre velocity squared, ƒ extends along the field-parallel direction. By exploiting the peculiarity of such effects, it is possible to infer which processes have acted upon some plasma within some time interval by comparing its initial and final velocity distributions, provided that other processes impacting on ƒ (such as some collisional scattering or instability-driven isotropization) act on times which are characteristically much longer than the interval considered (see Wu *et al.* (2006)).

7.4.3 Fermi processes: first-order and second-order

While up to this point the focus has been on a single, local event of acceleration, in this section I will focus on how the large-scale configuration of the system determines the cumulative result of multiple acceleration events. In particular, we can recognise "first-order" and "second-order" scenarios of Fermi acceleration whenever the charge undergoes multiple energisations and/or de-energisations, for instance due to repeated type-A or type-B processes (subsection 7.4.2). In particular, the "first-order" case happens if the charge is bound to follow some "track" leading them from one acceleration to another or from one deceleration to the following, while a "second-order" scenario

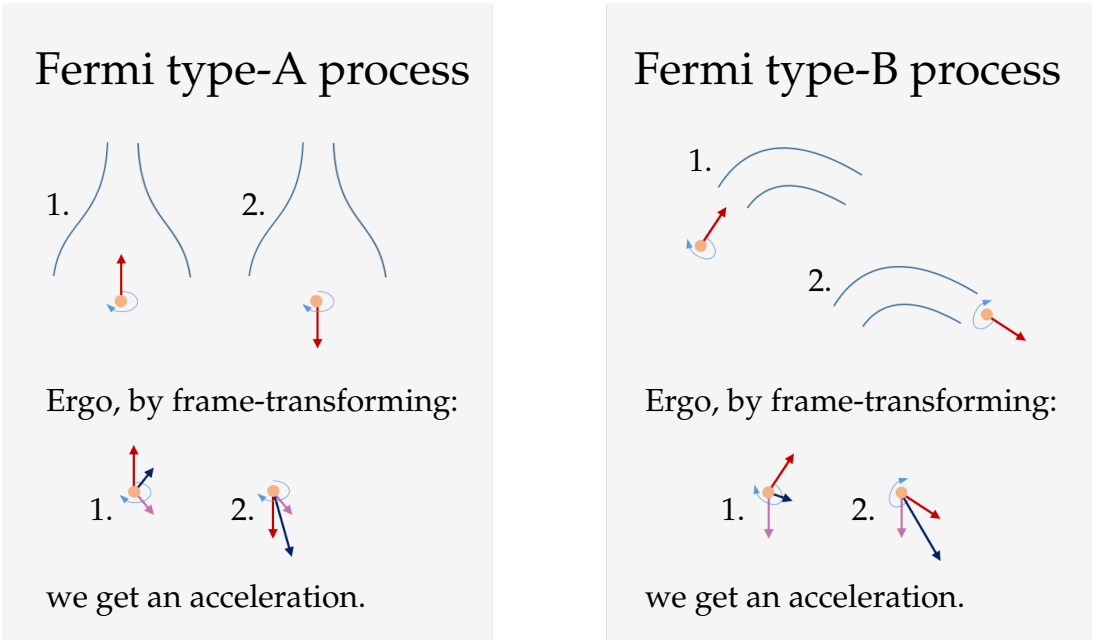

FIGURE 7.5: Schematic representation of Fermi's type-A and type-B processes: the guiding centre is marked in orange, and its velocity in the frame solidal with the magnetic structure is the red arrow (own image). In the lower portions of the schemes, frame-transforming (boost) velocity is the light purple arrow, and dark blue is the velocity as seen in the transformed reference. While the length of red arrows is always the same, meaning that in the structure's frame, the guiding centre's velocity only changes in direction, the dark blue arrows are also different in magnitude, showing that in the transformed frame the particle is seen to accelerate (aside: note that even if type-A processes primarily influence the $\mathcal{E}_g$ energy, here it is intended that this energy variation is transferred into $\mathcal{E}_{a\parallel}$ via the mirroring term).

is recognised if the charge encounters energisation and/or de-energisation sites randomly.

First-order scenarios are realised whenever some kind of re-injection mechanism is capable of re-iterating a charge's interaction with one or more energisation sites, thus leading to a repeated deceleration or to a series of accelerations. Two examples might clarify how a first-order scenario is attained.

- Consider a magnetised shock structure: here the particle accelerates by repeatedly mirroring on local maxima in the field's intensity situated on both sides of the shock, i.e. by a repeated type-A process (for reference, see section 8.2.2 in Meyer-Vernet (2007)). Now, the reason for which these random local maxima must be interpreted as coherently contributing to the acceleration of particles is that, when co-moving with the material on one side of the shock, material on the other side will always be perceived either as incoming, if the shock is compressional, either as outgoing, if the shock is decompressional. Given the relative motion, therefore, particles bouncing from one side of the shock to the other will be statistically trapped in "magnetic bottles" which either continuously expand, either continuously shrink. In the last scenario, it is obvious to understand that the collapsing "bottle" leads to energisation of the trapped particles until the moment in which their energy is sufficient to escape away.

- Inside an expanding or contracting flux rope, a charge is continuously energised or de-energised by repeated type-B processes (as recognised by Drake *et al.* (2006a)). In particular, squeezing the flux rope results in particles orbiting faster and faster around the flux rope's axis, eventually reaching an energy that allows them to escape altogether.

In the second-order scenario, particles are not following "tracks" of accelerations and/or decelerations but rather get energised and de-energised statistically. An interesting point to note is that if energisations and de-energisations are due to random type-A and type-B processes, then the ultimate result is that energy gains statistically predominate over losses. That in this case a charge gets ultimately energised becomes apparent once considered the statistics of particle encounters with local maxima of the magnetic field and/or curved field lines, randomly distributed in the system and randomly moving around. Indeed, suppose that some local maxima and/or curved line moves with a structure velocity $\vec{c}_X$ much smaller in modulus than $\langle v \rangle$ and consider the statistics of charges interacting with thir energisation site, taking the angle θ as the deviation from the $\vec{c}_X$ direction. Since interactions at some θ scale with the approximate factor of $1 + [c_X/\langle v \rangle] \cos\theta$, the number of "head on" encounters, which energise the particles, is more than "rear-end" impacts, which de-energise the particles instead. Therefore, in a chaotic scenario particle energisation is bit more likely than particle de-energisation, but the statistical nature of this imbalance makes it so that it takes a lot of accelerations and decelerations for the single particle to end up with a substantial energy gain.

A quick note might now be due on is the origin of "first-order" and "second-order"

denominations. Under the hypotheses of acceleration sites unperturbed by the interaction with particles and moving with a characteristic velocity c_X much smaller than $\langle v \rangle$, it is possible to show that the energy variation linked with acceleration processes is proportional to c_X (see next paragraph). Therefore, as in the chaotic acceleration scenario it is necessary to scale such energy variation by another c_X (this emerges from the $1 + [c_X/\langle v \rangle] \cos\theta$ factor discussed in the previous paragraph), it is evident that in the "organised" scenario particles will gain energy proportional to c_X while in the "disorganised" case the statistical energy increase will be proportional to c_X^2 instead - hence the denominations of first-order and second-order processes.

To understand that c_X scales the energy transferred in one cycle, let us evaluate it quickly through a three-step procedure: transpose energy and linear momentum into a magnetic structure's frame, then calculate there the final energy and momentum to transpose them finally back into the initial reference. Denoting by primes the quantity in the frame of the magnetic structure, the three couples of relations appear:

$$\begin{aligned} \mathcal{E}' &= [1 - c_X^2/c^2]^{-1/2}\Big[\mathcal{E} + pc_X \cos\theta\Big] \\ p' &= [1 - c_X^2/c^2]^{-1/2}\Big[\mathcal{E}c_X[c^2\cos\theta]^{-1} + p\Big] \end{aligned} \qquad \begin{aligned} \mathcal{E}' + \Delta\mathcal{E}' &= \mathcal{E}' \\ p' + \Delta p' &= -p' \end{aligned}$$

$$\begin{aligned} \mathcal{E} + \Delta\mathcal{E} &= [1 - c_X^2/c^2]^{-1/2}\Big[[\mathcal{E}' + \Delta\mathcal{E}'] - [p' + \Delta p']c_X \cos\theta\Big] \\ p + \Delta p &= [1 - c_X^2/c^2]^{-1/2}\Big[[\mathcal{E}' + \Delta\mathcal{E}']c_X[c^2\cos\theta]^{-1} - [p' + \Delta p']\Big] \end{aligned}$$

Putting these together, we can easily obtain the final energy in terms of the initial one, which simplifies once considered that magnetic structures move much slower than the speed of light:

$$\begin{aligned} \mathcal{E} + \Delta\mathcal{E} &= [1 - c_X^2/c^2]^{-1/2}\Big[[\mathcal{E}' + \Delta\mathcal{E}'] - [p' + \Delta p']c_X \cos\theta\Big] \\ &= [1 - c_X^2/c^2]^{-1/2}\Big[\mathcal{E}' + p'c_X \cos\theta\Big] \\ &= [1 - c_X^2/c^2]^{-1}\Big[\mathcal{E} + 2pc_X \cos\theta + \mathcal{E}c_X^2/c^2\Big] \\ &\underset{c_X/c\to 0}{\sim} \mathcal{E} + 2pc_X \cos\theta + 2\mathcal{E}c_X^2/c^2 \\ &= \mathcal{E}\Big[1 + 2[pc_X \cos\theta]/\mathcal{E} + 2c_X^2/c^2\Big] \\ &\underset{c_X/c\to 0}{\sim} \mathcal{E}\Big[1 + 2(c_X/c)\cos\theta + 2c_X^2/c^2\Big] \end{aligned}$$

hence:

$$\frac{\Delta\mathcal{E}}{\mathcal{E}} \underset{c_X/c\to 0}{\sim} 2\frac{c_X}{c}\cos\theta + 2\frac{c_X^2}{c^2} \tag{7.13}$$

from which one recognises that the relative energy gain scales as c_X/c, as stated.

7.4.4 Adiabatic invariants

In Hamiltonian theory, it is well known that any quantity defined as the line integral of the system's total momentum $\vec{p}$ over some close orbit $\mathcal{C}$ parametrised by s, that is of

the form:

$$\text{Pinv} := \oint_{\mathcal{C}} \vec{p} \cdot d\vec{r} = \oint_{s} \vec{p} \cdot \partial_s \vec{r}\, ds$$

in constant in time; hence the name of "Poincaré invariants" for all such objects (after the study of periodic dynamical systems performed by H. Poincaré - see in Abraham *et al.* (2003)). Demonstrating that such quantities are indeed constant can be easily done:

$$\begin{aligned} d_t\text{Pinv} &= \oint_s [\partial_t \vec{p} \cdot \partial_s \vec{r} + \vec{p} \cdot \partial_t \partial_s \vec{r}]\, ds = \oint_s [\partial_t \vec{p} \cdot \partial_s \vec{r} - \partial_s \vec{p} \cdot \partial_t \vec{r}]\, ds \\ &= -\oint_s [\vec{\nabla}_r \mathcal{H} \cdot \partial_s \vec{r} + \vec{\nabla}_p \mathcal{H} \cdot \partial_s \vec{p}]\, ds = -\oint \partial_s \mathcal{H}\, ds = 0 \end{aligned}$$

where $\mathcal{H}$ is the system's Hamiltonian, and the second passage has been performed integrating by parts. Now, supposing that $\mathcal{C}$ is an "approximately close" orbit, and to parametrise it by s, the quantity:

$$\text{Ainv} := \int_{\mathcal{C}} \vec{p} \cdot d\vec{r} = \int_{s} \vec{p} \cdot \partial_s \vec{r}\, ds$$

will be approximately an invariant, that is its temporal variation will take much longer than the particle in performing the approximately closed orbit. Because of this, such quantities are called "adiabatic invariants" (see section 2.8 in Fitzpatrick (2014)).

Three adiabatic invariants can be individuated for a charged particle if it moves in a magnetic field with characteristic scales ℓ_Δ and τ_Δ much larger than those of the particle's motion. The first adiabatic invariant arises whenever the gyration motion is approximately closed, while the second and third arise due to nearly periodic gyrocentre paths, the former regarding mostly parallel motions and the latter mostly perpendicular ones (precessions). Let us present each of them in detail, remembering that:

$$\vec{p} = m\vec{v} + [q/c]\vec{A}$$

is the total momentum for a magnetised particle (see chapter 3 in Landau *et al.* (1975)).

The first adiabatic invariant is proportional to the magnetic moment relative to the gyration motion of the particle, as it can be shown by the equivalences:

$$\begin{aligned} \text{Ainv}_1 :&= \int_s \vec{p} \cdot \partial_s \vec{r}_g\, ds \simeq \langle \Big[m[\vec{v}_a + \vec{v}_g] + [q/c][\vec{A} + \vec{r}_g \cdot \vec{\nabla}\vec{A}] \Big] \cdot [\vec{r}_g \times \vec{e}_{||}] \rangle_g \\ &= \langle \Big[[m\omega_g]\, \vec{r}_g \times \vec{e}_{||} + [m\omega_g/B]\, \vec{r}_g \cdot \vec{\nabla}\vec{A} \Big] \cdot [\vec{r}_g \times \vec{e}_{||}] \rangle_g \\ &= \langle \Big[m\omega_g r_g^2 - [m\omega_g/B]\, \vec{e}_{||} \cdot \vec{\vec{\epsilon}} : [\vec{r}_g \cdot \vec{\nabla}\vec{A}] \Big] \rangle_g \\ &\overset{\bullet}{=} m\omega_g r_g^2 - [m\omega_g r_g^2/2B]\, \vec{e}_{||} \cdot \vec{\vec{\epsilon}} : [[\vec{\vec{1}} - \vec{e}_{||}] \cdot \vec{\nabla}\vec{A}] \\ &= m\omega_g r_g^2/2 = [mc/q][mv_g^2/2B] = [mc/q]\, M_g \end{aligned} \tag{7.14}$$

with $\vec{\vec{\epsilon}}$ being the Levi-Civita "symbol" (see Arfken *et al.* (2013)) and "$\bullet$" denoting a passage based on:

$$\langle \vec{r}_g \rangle_g = [r_g^2/2]\, [\vec{\vec{1}} - \vec{\vec{e}}_{||}]$$

Therefore, the magnetic moment linked to the particle's gyration is approximately conserved over the Larmor time scale, or equivalently it varies much slower than the particle's gyration. This fact becomes incredibly useful, for instance, in situations where we need to quantify a variation in $\mathcal{E}_g$ since the invariance of M_g allows to deduce it immediately from the change in magnetic intensity.

The second adiabatic invariant is present whenever the motion of the gyrocentre parallel to the magnetic field approximately closes:

$$\text{Ainv}_2 := \int_s \vec{p} \cdot \partial_s \vec{r}_{a||}\, ds = \int_s \left[m\vec{v}_a + [q/c]\vec{A} \right] \cdot \partial_s \vec{r}_{a||}\, ds = \int_s m\vec{v}_a \cdot \partial_s \vec{r}_{a||}\, ds \tag{7.15}$$

where the last equality holds because while $\partial_s \vec{r}_a$ and $\vec{v}_a$ change sign after each bounce, the vector potential doesn't and therefore its averaged contribute is null. The invariance of this quantity can be exploited, for example, to deduce changes of $\mathcal{E}_{a||}$ in time.

The third adiabatic invariant is conserved whenever perpendicular (precession) motions draw nearly closed orbits:

$$\begin{aligned} \text{Ainv}_3 &:= \int_s \vec{p} \cdot \partial_s \vec{r}_{a\perp}\, ds = \int_s \left[m\vec{v}_a + [q/c]\vec{A} \right] \cdot \partial_s \vec{r}_{a\perp}\, ds \\ &\simeq [q/c] \int_s \vec{A} \cdot \partial_s \vec{r}_{a\perp}\, ds \simeq [q/c] \int_\Sigma \vec{B} \cdot d\vec{\Sigma} \end{aligned} \tag{7.16}$$

where the first approximation follows from the fact that velocity contributes are usually negligible with respect to magnetic ones, and the second is due to the nearly-exact circuitation of $\vec{A}$ being close to the magnetic flux passing trough the precession orbit considered (under the gauge hypothesis of $\vec{A}$ being solenoidal). If we were to know exactly the integral of the $\vec{A}$ term above, instead, conservation of this adiabatic invariant could allow us to deduce the variation of $\mathcal{E}_{a\perp}$ experienced by the charge during its precession.

The main reason beneath the distinction of the second and third adiabatic invariants lies in the usually good separation between the time scales on which a gyrocentre completes a "parallel" and a "perpendicular" orbit. Indeed, in absence of a strong external electric field (a situation that is the usual standard in plasmas due to the strong dielectric properties of these media) the gyrocentre perpendicular velocity is negligible with respect to the parallel one. That Ainv_2 and Ainv_3 are similar to some degree, however, can be recognised by noting that they are both related to large-scale periodicities in gyrocentre motions, and their constancy leads to first-order Fermi accelerations or decelerations (described in subsection 7.4.3) whenever there's a variation of $\vec{B}$.

The classical example to see all three adiabatic invariants "in action" is the study of charged particle motions inside the dipolar magnetic field generated by a circular current loop, supposed to vary temporally and spatially on scales much larger than those proper of particle dynamics so that charges can gyrate. Obviously, gyrating behaviour allows for the first invariant. To recognise the second invariant, instead, one must consider two limit situations: near the current loop and far away from it. In the first case

field lines are arranged in a helical fashion, gyrocentres can move at quasi-constant pace in orbits winding around the current loop, nearly along field lines, and the discrete translational symmetry of such orbits determines the second adiabatic invariant. In the second case the field is in good approximation dipolar, and gyrocentres set about to follow field lines are bound to encounter high-latitude magnetic mirrors (the enhanced intensity of the magnetic field implies that field-parallel gyrocentre velocity must be reversed), hence they oscillate back-and-forth into quasi-closed orbits which imply the presence of a second adiabatic invariant. A third adiabatic invariant is found in both limit cases by taking into account the cumulative effects of small, field-perpendicular longitudinal drifts: due to the system's symmetry these must add up into a precession motion which is linked to an approximately conserved quantity.

The previous example can be intended also as a very approximate model of the near-Earth plasma environment dominated by the terrestrial magnetic field. In particular, by adiabatic theory one can understand the basic reason behind the existence of a low-latitude particle trapping in the magnetosphere, a phenomenon particularly evident in the so-called "Van Allen radiation belts" (see section 2.10 in Fitzpatrick (2014)). Indeed, while conservation of the Ainv_1 traps particles latitudinally, forcing them to bounce about the magnetic equator, conservation of the second and third accounts for the relative stability of this trapping. By Ainv_2 particles cannot move directly outward or inward, but can at most precede around the Earth's magnetic axis - by Ainv_3 instead we are made sure that precessing particles will approximately return to their initial bouncing position when the precession has resulted into a complete revolution. The necessity to keep all these invariants implies that slow variations of the magnetospheric field cause the position and energy of trapped charges to change. More specifically, if the field's strength experiences a diminution, trapped particle regions will forcedly shift outward and expand in latitude, while an increase of field magnitude results in these zones getting closer to Earth, and latitudinally more compact. In the first scenario, clearly, particles are de-energised while in the second they gain energy instead. Now, changes of magnetospheric field intensity leading to such energy variations are possible as a consequence of the interplanetary plasma dynamics (as an example, see Wu *et al.* (2006) in which it is recognised that during substorm-induced rearrangements of the magnetosphere, type-A processes dominate for particles trapped closer to Earth while mostly type-B processes energise the plasma which precipitates from the magnetotail). This way, space weather influences the spatial distribution of trapped magnetospheric particles, as well as their energy.

7.5 Micro-anatomy of reconnections

Up to now, reconnection was approached in its large-scale characteristics and there has been no detail about processes which follow from multi-species dynamics. Here, however, I briefly overview multi-species and small-scale effects which arise in correspondence with reconnection. To this aim, first I note how the micro-physics associated with the presence of more than one

species or pseudo-species introduces a fine shaping of the electromagnetic field in the neighbourhood of a reconnection site (subsection 7.5.1). Then I recognise how a plasma gets "processed" while passing through such a complex environment (subsection 7.5.2). Contrary to most discussion of such themes, rather than focusing on peculiarities which emerge in a specific kind of reconnection site here I will be reporting only on considerations which hold in all generality wherever the plasma reconnects.

7.5.1 A structured electromagnetic environment

Wherever a multi-species plasma develops small-scale dynamics one generally finds series of nested diffusion regions, each one being recognised where one the species breaks ideality. In the ion-electron case, for instance, the ions will generally develop a larger diffusion region (in short "IDR"), which will contain the smaller diffusion region of electrons (or "EDR") - and a finer distinction can be made, obviously, whenever one wants to divide any species into multiple pseudo-species. Now, while one could think that the IDRs and EDRs are simply the re-scaled version of one another, actually the micro-dynamics of ions and electrons at the reconnection site generally makes it so that the two differ sensibly from each other, thus creating a variegated environment (see Karimabadi *et al.* (2007), Divin *et al.* (2012), Karimabadi et al. in Balogh *et al.* (2014)). Hereafter, I will present the main traits of the IDR-EDR environment, the focus being foremost on the $\vec{E}$ and $\vec{B}$ fields inside reconnection regions.

In order to understand the micro-anatomy of nested diffusion regions, two facts about the flow of a magnetised plasma are to be kept in mind. The first is the trivial remark that the field-perpendicular velocity is generally the same as that of magnetic lines. The second fact regards field-parallel fluid velocity instead, and density: where a portion of magnetic flux tube expands, there parallel velocity increases and density goes down - the opposite happens with contracting magnetic tubes (while this behaviour is somehow intuitive, it can be appreciated at best in the framework of guiding centre theory - see subsection 7.4.4). Given this note, one understands that since some portions of inflowing/outflowing magnetic tubes are generally found expanding/contracting, alongside the magnetic field there must be a (field-parallel) converging/diverging flow pattern in inflows/outflows, respectively. These considerations will suffice in order to picture the micro-fluid aspects of multi-species reconnection.

As introduced before, in an ion-electron plasma the ion nonideal regions are wider since ions are by far the easiest species to de-idealise. This makes it so that the ion dynamics will generally be characterised by nothing more than the de-idealisation and re-idealisation processes. Electrons, instead, get also sensibly affected by the compression and decompression of magnetic flux tubes, creating strong fluxes around the reconnection site. In particular, inside the IDR and outside the EDR, where ions cannot follow these motions, it is possible to develop zones with relevant currents and charge unbalances which result into magnetic and electric fields. These electromagnetic structures are known as "Hall" fields and constitute the foremost characteristic of multi-species reconnection neighbourhoods (see Uzdensky & Kulsrud (2006), then Rogers (2003) for its changes in different external conditions and Le *et al.* (2010b) for an estimation of its

intensity).

Alongside with the ones just described, two other micro-fluid effects can be generally important, and both result from the different rates at which particles of different species can escape from the nonideal region.

- First, an electrostatic field pointing outward from the reconnection site generally follows from the fact that ions and electrons are differently accelerated in the outflow. Basically, if no electrostatic field were to develop, the difference in ion and electron flows would imply a violation of quasineutrality, with too many ions inside the reconnection site (see Egedal & Fasoli (2001), Egedal *et al.* (2008)). For the sake of brevity, I will call this feature "Egedal" field in the following.

- Second, acceleration along the inflows can lead to the so-called "Larmor" field: whenever a reconnection site is lays in between zones of high and low densities, it is possible that demagnetised plasma from the high-density side ends up "overflowing" into the low-density region, where it get re-idealised and deviated due to the magnetic field there. Obviously, the electric fields associated with deviated particles are different among the species, since ions and electrons "overflow" differently into the low-density ideal region: the Larmor field appears as the result of this difference (see Malakit *et al.* (2013), Ek-In *et al.* (2017)).

If the previous discussion regards structures that will remain steady under fixed external conditions, diffusion regions have been also identified as preferential sites for the excitation of waves and instabilities (see Fujimoto (2014), Lapenta *et al.* (2015a)). This generally makes it so that locally a turbulent plasma dynamics develops, which has been the object of numerous studies (see Lapenta (2008), Daughton *et al.* (2011), Nakamura *et al.* (2016), Price *et al.* (2016), Price *et al.* (2017), Le *et al.* (2018), Lapenta *et al.* (2019), Price *et al.* (2020) but note also that in computational studies, boundary conditions might impact the turbulence retrieved - see Liu *et al.* (2018a)) and, due to its inherent complexity, might not have been completely characterised yet.

To conclude this subsection, let me note that observations of the microphysics just presented in general seem to fit well with predictions, even when reconnection is assumed only two-dimensional (for a representation of Hall, Larmor and potential fields in two-dimensional reconnection with a X-point, see Fig. 7.6). The Hall structure has been, for instance, an evergreen objective of observation analyses (from those relying on statistics such as Nagai (2003) to the analysis of single events, such as via THEMIS , CLUSTER and most recently in MMS data - see for instance Mozer *et al.* (2008), Eastwood *et al.* (2010) and Denton *et al.* (2016b), Peng *et al.* (2017), Zhang *et al.* (2017)). The large-scale electrostatic potential has also been repeatedly observed (in particular, with THEMIS and CLUSTER - see Egedal *et al.* (2005), Egedal *et al.* (2010)) while the Larmor field tends to be more elusive (I refer the reader only to Phan *et al.* (2016)). However, satellite detection of fine structures (see Cozzani *et al.* (2019)) and waves (see Zhou *et al.* (2014), Zhou *et al.* (2016), Graham *et al.* (2017b), Graham *et al.* (2017a), Burch *et al.* (2018b), Wilder *et al.* (2019)) in IDRs and EDRs also point at a complex variety of

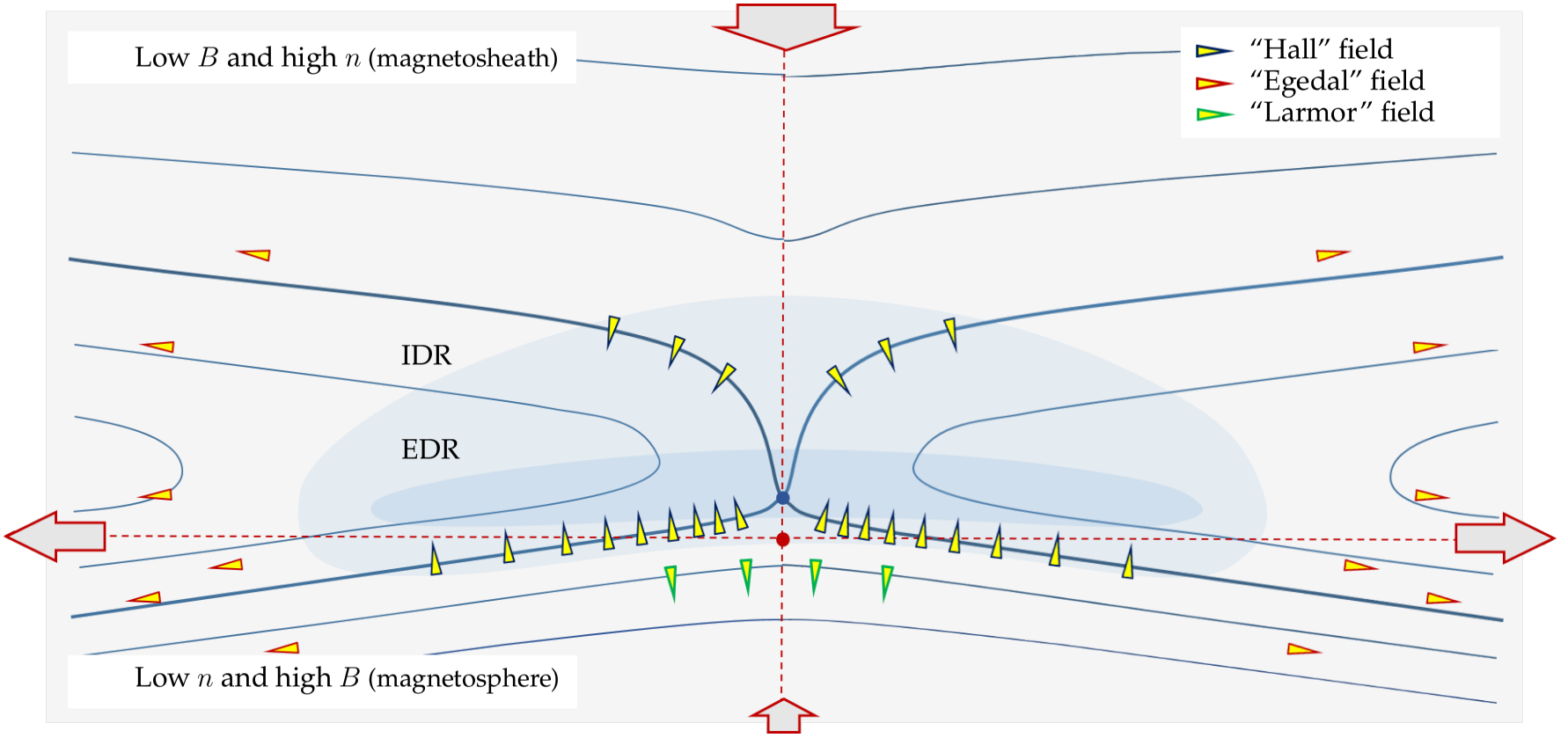

FIGURE 7.6: Schematic representation of a two-dimensional reconnection region constituted of an in-plane null surrounded by a non-ideal region, assumed stationary (own image). Blue lines indicate the in-plane magnetic field lines while red slashed lines determine the "skeleton" of the hyperbolic flow. Note that for generality reconnection here is supposed with asymmetric inflow conditions, even though without a significant out-of-plane (guide) field - a situation similar to that at the dayside magnetopause (hence the small labels in parenthesis, indicating magnetosphere and magnetosheath). In particular, asymmetry makes it so that the X-point of magnetic degeneracy does not coincide with the S-point where the fluid stagnates: this can be recognised as the point at the centre of the red slashed cross does not coincide with that in which the four magnetic separatrices converge. In this geometry, the Hall electric fields develop into an asymmetric, dipolar structure while their magnetic counterpart form an asymmetric quadrupole (not shown). The Egedal field is dispersed over large scales in the outflows while the Larmor electric field is concentrated in the low-density inflow.

electromagnetic phenomena developing in tandem with magnetic reconnection.

7.5.2 Plasma micro-physics of a reconnection site

Once that the electromagnetic shaping of fields inside a reconnection region is known, it is possible also to understand in detail how the plasma gets affected by the passage through a reconnection site. While this kind of studies has often been focused onto the identification of some microscopic processes leading to the macroscopic diffusion (see Egedal (2002), Che *et al.* (2011), Che (2017)), in the following I will not deal with this topic but rather present a brief summary of what is known about particle orbits in a reconnection neighbourhood.

In order to keep this discussion clean, from now on all processes discussed will be recognised into two broad categories: on one side, those in which particles can be understood to "gyrate" in the plane perpendicular to the local field, drawing an approximate helix with characteristic scale ℓ_g in a characteristic time τ_g - on the other side, those in which particles cannot "gyrate" since the ℓ_g and τ_g they would need are larger than the characteristic scales on which the field varies (see subsection 7.4.1). For clarity, let me call these two kinds of motions "gyratoric" and "nongyratoric" respectively, from now on. Obviously, since both ℓ_g and τ_g are species-dependent, in the same reconnection site there can be a significant difference among species in the regard of how much of their dynamics must be understood as gyratoric or nongyratoric.

As already remarked, the characteristic motion of ions in a multi-species reconnection is generally the simplest: ions enter the reconnection zone, get de-idealised and as they get re-idealised they exit it, generally heated and accelerated. Gyratoric processes contributing to ion acceleration are usually recognised via the drift decomposition of the field-perpendicular velocity (see Li *et al.* (2017)), while increments in temperature in this regime generally follow from field-parallel mixing of bouncing populations (see Drake *et al.* (2009b), Drake & Swisdak (2014)). Regarding nongyratoric processes, in certain situations it has been found that as ions bounce in the reversing Hall field, the motional $\vec{E}$ provides an acceleration which leads to a temperature increase by a mechanism analogous to the energisation of pick-up ions in the solar wind (see Drake *et al.* (2009a), Drake *et al.* (2009b), Aunai *et al.* (2011b), Drake & Swisdak (2014), and Haggerty *et al.* (2015), which consider also how the Egedal field modifies the field-parallel velocity of ions), while regions of highly curved field lines have been recognised prone to nongyratoric scattering (see Sergeev *et al.* (1983) and Shen *et al.* (2014) for an experimental detection). In any case, the complex shaping of a reconnection site implies that many of these acceleration/scattering processes are strongly localised and/or region-dependent (see for instance Eastwood *et al.* (2018) discussing the effects of a density cavity in exhaust heating patterns).

Also the electrons generally get energised as they pass through a reconnection site. As for the ions, transiting through different zones in a reconnection site does generally result into different energisations (see Wang *et al.* (2016), Li *et al.* (2017)), with field-parallel electrostatic acceleration being the most diffused (see Egedal *et al.* (2012), Le

et al. (2012), Zhou *et al.* (2018c), Zhou *et al.* (2018b)) and dominating the whole energisation processes when a strong ambient magnetic field is present (see Dahlin *et al.* (2014), Dahlin *et al.* (2017)). Field-perpendicular gyratoric energisation is usually decomposed following the recognition of different drifts (see subsection 7.4.1). This way it was recognised, for instance, that curvature-drift acceleration is diminished by a guide field (see Dahlin *et al.* (2014), Dahlin *et al.* (2017)) while the more compressional the material and the stronger the impact of the component related to the magnetic field gradient (see Borovikov *et al.* (2017)). Nongyratoric electron dynamics is present, as for ions, in the form of pitch-angle scattering at curved field lines (see Sergeev *et al.* (1983), Zhang *et al.* (2016), Lavraud *et al.* (2016), Norgren *et al.* (2018)) but also in a series of other effects from small-scale fields, concentrated in the innermost EDR and at separatrices (see Lapenta *et al.* (2015b), Egedal *et al.* (2016a), Burch *et al.* (2018b), Hesse *et al.* (2018a), Norgren *et al.* (2019), Khotyaintsev *et al.* (2020)). Again, it is worth remarking the strongly zone-dependent character of all acceleration and scattering processes (see Drake *et al.* (2005), Eastwood *et al.* (2018), Burch *et al.* (2018a), Swisdak *et al.* (2018)).

One last note is due, before concluding the subsection, about the shaping of distribution functions f inside the reconnection neighbourhood. Since a distribution function can be recognised constant along particle orbits (this follows from Vlasov's equation, Eq. 2.1), supposing to know that f has a particular form "sufficiently far" from the region considered, then at each point inside the zone of interest f can be simply reconstructed as a "patchwork" of pieces of distribution functions which have been "advected" along particle orbits. This means that understanding f in the reconnection neighbourhood generally calls for a detailed study of single-particle motions from "sufficiently far" into the region considered (see for instance how f is interpreted in Zenitani & Nagai (2016), Zenitani *et al.* (2017), Hesse *et al.* (2017) - interestingly, this kind of study can still be analytically performed in approximated way whenever the motion of particles is gyratoric). In this regard, the most important distinction one can make inside a distribution function is between those particles which have enough energy to stream along field lines basically unbothered by the microphysics and those other particles which must bounce instead many times along the "same" segments of field line while getting advected by the large-scale plasma flows. These two quasi-species that microphysics distinguishes are usually called "trapped" and "passing" (see Le *et al.* (2009), Le *et al.* (2010a), Divin *et al.* (2010), Egedal *et al.* (2013)). Whenever distribution functions "far away" are different on different sides of the reconnection, the trapped population at some point can be superposed with a passing population coming from another region, returning an unusually shaped f, possibly displaying crescents and multiple beams which have been recently individuated in spacecraft measures and numerical simulations (see Burch *et al.* (2016a), Bessho *et al.* (2016), Egedal *et al.* (2016b), Egedal *et al.* (2018), Wang *et al.* (2019)).

Bibliography

Abraham, R., Marsden, J., & Ratiu, T. 2003. *Manifolds, ternsor analysis and applications*. 84, 111

Al-Hachami, A. 2019. Magnetic Reconnection in the Absence of Three-Dimension Null Point. *Herald of the bauman moscow state technical university. series natural sciences*, Dec., 50–66. 103

Alm, L., Argall, M. R., Torbert, R. B., Farrugia, C. J., Burch, J. L., Ergun, R. E., Russell, C. T., Strangeway, R. J., Khotyaintsev, Y. V., Lindqvist, P.-A., Marklund, G. T., Giles, B. L., & Shuster, J. 2017. EDR signatures observed by MMS in the 16 October event presented in a 2-D parametric space. *Journal of geophysical research: Space physics*, **122**(3), 3262–3276. 41

Andriopoulou, M., Nakamura, R., Torkar, K., Baumjohann, W., Torbert, R. B., Lindqvist, P.-A., Khotyaintsev, Y. V., Dorelli, J., Burch, J. L., & Russell, C. T. 2016. Study of the spacecraft potential under active control and plasma density estimates during the MMS commissioning phase. *Geophysical research letters*, **43**(10), 4858–4864. 35

Arfken, George B., Weber, Hans-Jurgen, & Harris, F. 2013. Mathematical methods for physicists. *Pages i–ii of: Mathematical Methods for Physicists*. Elsevier. 111

Argall, Matthew R., Small, Colin R., Piatt, Samantha, Breen, Liam, Petrik, Marek, Kokkonen, Kim, Barnum, Julie, Larsen, Kristopher, Wilder, Frederick D., Oka, Mitsuo, Paterson, William R., Torbert, Roy B., Ergun, Robert E., Phan, Tai, Giles, Barbara L., & Burch, James L. 2020. MMS SITL Ground Loop: Automating the Burst Data Selection Process. *Frontiers in astronomy and space sciences*, **7**(Sept.), 54. 41

Aunai, N., Belmont, G., & Smets, R. 2011a. Energy budgets in collisionless magnetic reconnection: Ion heating and bulk acceleration. *Physics of plasmas*, **18**(12), 122901. 66

Aunai, N., Belmont, G., & Smets, R. 2011b. Proton acceleration in antiparallel collisionless magnetic reconnection: Kinetic mechanisms behind the fluid dynamics: PROTON DYNAMICS IN MAGNETIC RECONNECTION. *Journal of geophysical research: Space physics*, **116**(A9), n/a–n/a. 117

Baker, D. N., Riesberg, L., Pankratz, C. K., Panneton, R. S., Giles, B. L., Wilder, F. D., & Ergun, R. E. 2016. Magnetospheric Multiscale Instrument Suite Operations and Data System. *Space science reviews*, **199**(1-4), 545–575. 32

Balogh, André, Bykov, Andrei, Cargill, Peter, Dendy, Richard, Dudok de Wit, Thierry, & Raymond, John (eds). 2014. *Microphysics of Cosmic Plasmas*. Space Sciences Series of ISSI, vol. 47. Boston, MA: Springer US. 27, 40, 99, 114

Barrie, A. C., Cipriani, F., Escoubet, C. P., Toledo-Redondo, S., Nakamura, R., Torkar, K., Sternovsky, Z., Elkington, S., Gershman, D., Giles, B., & Schiff, C. 2019. Char-

acterizing spacecraft potential effects on measured particle trajectories. *Physics of plasmas*, **26**(10), 103504. 34

Beresnyak, Andrey, & Li, Hui. 2016. FIRST-ORDER PARTICLE ACCELERATION IN MAGNETICALLY DRIVEN FLOWS. *The astrophysical journal*, **819**(2), 90. 70

Bessho, N., Chen, L.-J., & Hesse, M. 2016. Electron distribution functions in the diffusion region of asymmetric magnetic reconnection: DISTRIBUTION IN ASYMMETRIC RECONNECTION. *Geophysical research letters*, **43**(5), 1828–1836. 118

Bhattacharjee, A. 2004. Impulsive Magnetic Reconnection in the Earth's Magnetotail and the Solar Corona. *Annual review of astronomy and astrophysics*, **42**(1), 365–384. 97

Birn, J., & Hesse, M. 2005. Energy release and conversion by reconnection in the magnetotail. *Annales geophysicae*, **23**(10), 3365–3373. 69

Birn, J., & Hesse, M. 2010. Energy release and transfer in guide field reconnection. *Physics of plasmas*, **17**(1), 012109. 64, 66, 68, 69

Birn, J, & Priest, E R. 2007. *RECONNECTION OF MAGNETIC FIELDS: Magnetohydrodynamics and Collisionless Theory and Observations*. 27, 29, 84, 90, 92, 102

Birn, J., Drake, J. F., Shay, M.A., Rogers, B. N., Denton, R. E., Hesse, M., Kuznetsova, Masha, Ma, Z., Bhattacharjee, A., Otto, Antonius, & Pritchett, P. L. 2001. GEM Magnetic Reconnection Challenge. 97

Birn, J., Hesse, M., & Schindler, K. 2006. Entropy conservation in simulations of magnetic reconnection. *Physics of plasmas*, **13**(9), 092117. 66, 69

Birn, J., Borovsky, J. E., Hesse, M., & Schindler, K. 2010. Scaling of asymmetric reconnection in compressible plasmas. *Physics of plasmas*, **17**(5), 052108. 66, 103

Birn, J., Artemyev, A. V., Baker, D. N., Echim, M., Hoshino, M., & Zelenyi, L. M. 2012. Particle Acceleration in the Magnetotail and Aurora. *Space science reviews*, **173**(1-4), 49–102. 13, 15

Biskamp, Dieter. 2005. *Magnetic Reconnection*. 26, 99

Blake, J. B., Mauk, B. H., Baker, D. N., Carranza, P., Clemmons, J. H., Craft, J., Crain, W. R., Crew, A., Dotan, Y., Fennell, J. F., Friedel, R. H., Friesen, L. M., Fuentes, F., Galvan, R., Ibscher, C., Jaynes, A., Katz, N., Lalic, M., Lin, A. Y., Mabry, D. M., Nguyen, T., Pancratz, C., Redding, M., Reeves, G. D., Smith, S., Spence, H. E., & Westlake, J. 2016. The Fly's Eye Energetic Particle Spectrometer (FEEPS) Sensors for the Magnetospheric Multiscale (MMS) Mission. *Space science reviews*, **199**(1-4), 309–329. 34

Boozer, Allen H. 2002. Reconnection and the Ideal Evolution of Magnetic Fields. *Physical review letters*, **88**(21), 215005. 95

Boozer, Allen H. 2012a. Magnetic reconnection in space. *Physics of plasmas*, **19**(9), 092902. 92, 95

Boozer, Allen H. 2012b. Separation of magnetic field lines. *Physics of plasmas*, **19**(11), 112901. 82, 90

Boozer, Allen H. 2014. Formation of current sheets in magnetic reconnection. *Physics of plasmas*, **21**(7), 072907. 95

Boozer, Allen H. 2019a. Fast magnetic reconnection and the ideal evolution of a magnetic field. *Physics of plasmas*, **26**(4), 042104. 89, 95, 99

Boozer, Allen H. 2019b. Magnetic reconnection with null and X-points. *Physics of plasmas*, **26**(12), 122902. arXiv: 1907.08062. 95

Borovikov, D., Tenishev, V., Gombosi, T. I., Guidoni, S. E., DeVore, C. R., Karpen, J. T.,

& Antiochos, S. K. 2017. ELECTRON ACCELERATION IN CONTRACTING MAGNETIC ISLANDS DURING SOLAR FLARES. *The astrophysical journal*, **835**(1), 48. 118

Borovsky, Joseph E., & Valdivia, Juan Alejandro. 2018. The Earth's Magnetosphere: A Systems Science Overview and Assessment. *Surveys in geophysics*, **39**(5), 817–859. 12

Boyd, T., & Sanderson, J. 2003. *The Physics of Plasmas*. 18, 19

Bruno, Roberto, & Carbone, Vincenzo. 2016. *Turbulence in the Solar Wind*. Lecture Notes in Physics, vol. 928. Cham: Springer International Publishing. 34, 35

Bungey, T. N., Titov, V. S., & Priest, E. R. 1996. Basic topological elements of coronal magnetic fields. 90

Burch, J. L., Torbert, R. B., Phan, T. D., Chen, L.-J., Moore, T. E., Ergun, R. E., Eastwood, J. P., Gershman, D. J., Cassak, P. A., Argall, M. R., Wang, S., Hesse, M., Pollock, C. J., Giles, B. L., Nakamura, R., Mauk, B. H., Fuselier, S. A., Russell, C. T., Strangeway, R. J., Drake, J. F., Shay, M. A., Khotyaintsev, Yu. V., Lindqvist, P.-A., Marklund, G., Wilder, F. D., Young, D. T., Torkar, K., Goldstein, J., Dorelli, J. C., Avanov, L. A., Oka, M., Baker, D. N., Jaynes, A. N., Goodrich, K. A., Cohen, I. J., Turner, D. L., Fennell, J. F., Blake, J. B., Clemmons, J., Goldman, M., Newman, D., Petrinec, S. M., Trattner, K. J., Lavraud, B., Reiff, P. H., Baumjohann, W., Magnes, W., Steller, M., Lewis, W., Saito, Y., Coffey, V., & Chandler, M. 2016a. Electron-scale measurements of magnetic reconnection in space. *Science*, **352**(6290), aaf2939. 40, 118

Burch, J. L., Moore, T. E., Torbert, R. B., & Giles, B. L. 2016b. Magnetospheric Multiscale Overview and Science Objectives. *Space science reviews*, **199**(1-4), 5–21. 31, 33, 35, 79

Burch, J. L., Ergun, R. E., Cassak, P. A., Webster, J. M., Torbert, R. B., Giles, B. L., Dorelli, J. C., Rager, A. C., Hwang, K.-J., Phan, T. D., Genestreti, K. J., Allen, R. C., Chen, L.-J., Wang, S., Gershman, D., Le Contel, O., Russell, C. T., Strangeway, R. J., Wilder, F. D., Graham, D. B., Hesse, M., Drake, J. F., Swisdak, M., Price, L. M., Shay, M. A., Lindqvist, P.-A., Pollock, C. J., Denton, R. E., & Newman, D. L. 2018a. Localized Oscillatory Energy Conversion in Magnetopause Reconnection. *Geophysical research letters*, **45**(3), 1237–1245. 74, 118

Burch, J. L., Webster, J. M., Genestreti, K. J., Torbert, R. B., Giles, B. L., Fuselier, S. A., Dorelli, J. C., Rager, A. C., Phan, T. D., Allen, R. C., Chen, L.-J., Wang, S., Le Contel, O., Russell, C. T., Strangeway, R. J., Ergun, R. E., Jaynes, A. N., Lindqvist, P.-A., Graham, D. B., Wilder, F. D., Hwang, K.-J., & Goldstein, J. 2018b. Wave Phenomena and Beam-Plasma Interactions at the Magnetopause Reconnection Region. *Journal of geophysical research: Space physics*, **123**(2), 1118–1133. 115, 118

Carrington, R. C. 1859. Description of a Singular Appearance seen in the Sun on September 1, 1859. *Monthly notices of the royal astronomical society*, **20**(Nov.), 13–15. 15

Cassak, P. A. 2016. Inside the Black Box: Magnetic Reconnection and the Magnetospheric Multiscale Mission. *Space weather*, **14**(3), 186–197. 31

Cassak, P. A., & Shay, M. A. 2007. Scaling of asymmetric magnetic reconnection: General theory and collisional simulations. *Physics of plasmas*, **14**(10), 102114. 103

Cassak, P. A., Drake, J. F., & Shay, M. A. 2007a. Catastrophic onset of fast magnetic reconnection with a guide field. *Physics of plasmas*, **14**(5), 054502. 97

Cassak, P. A., Drake, J. F., Shay, M. A., & Eckhardt, B. 2007b. Onset of Fast Magnetic Reconnection. *Physical review letters*, **98**(21), 215001. 97

Cassak, P. A., Liu, Y.-H., & Shay, M. A. 2017. A Review of the 0.1 Reconnection Rate Problem. *Journal of plasma physics*, **83**(5), 715830501. arXiv: 1708.03449. 27

Chandrasekhar, S. 1961. *Hydrodynamic and Hydromagnetic stability*. 85

Chanteur, G. 2000. Accuracy of fields gradients estimations by CLUSTER: explanation of its dependency upon elongation and planarity of the tetrahedron. 38

Chasapis, Alexandros, Yang, Y., Matthaeus, W. H., Parashar, T. N., Haggerty, C. C., Burch, J. L., Moore, T. E., Pollock, C. J., Dorelli, J., Gershman, D. J., Torbert, R. B., & Russell, C. T. 2018. Energy Conversion and Collisionless Plasma Dissipation Channels in the Turbulent Magnetosheath Observed by the Magnetospheric Multiscale Mission. *The astrophysical journal*, **862**(1), 32. 82

Che, H. 2017. How anomalous resistivity accelerates magnetic reconnection. *Physics of plasmas*, **24**(8), 082115. 117

Che, H., Drake, J. F., & Swisdak, M. 2011. A current filamentation mechanism for breaking magnetic field lines during reconnection. *Nature*, **474**(7350), 184–187. 117

Cozzani, Giulia, Retinò, A., Califano, F., Alexandrova, A., Le Contel, O., Khotyaintsev, Y., Vaivads, A., Fu, H. S., Catapano, F., Breuillard, H., Ahmadi, N., Lindqvist, P.-A., Ergun, R. E., Torbert, R. B., Giles, B. L., Russell, C. T., Nakamura, R., Fuselier, S., Mauk, B. H., Moore, T., & Burch, J. L. 2019. *In situ* spacecraft observations of a structured electron diffusion region during magnetopause reconnection. *Physical review e*, **99**(4), 043204. 74, 115

Dahlin, J. T., Drake, J. F., & Swisdak, M. 2014. The mechanisms of electron heating and acceleration during magnetic reconnection. *Physics of plasmas*, **21**(9), 092304. 70, 118

Dahlin, J. T., Drake, J. F., & Swisdak, M. 2015. Electron acceleration in three-dimensional magnetic reconnection with a guide field. *Physics of plasmas*, **22**(10), 100704. 70, 83

Dahlin, J. T., Drake, J. F., & Swisdak, M. 2016. Parallel electric fields are inefficient drivers of energetic electrons in magnetic reconnection. *Physics of plasmas*, **23**(12), 120704. 70

Dahlin, J. T., Drake, J. F., & Swisdak, M. 2017. The role of three-dimensional transport in driving enhanced electron acceleration during magnetic reconnection. *Physics of plasmas*, **24**(9), 092110. 70, 118

Darwin, C.G. 1920. The dynamical motions of charged particles. *The london, edinburgh, and dublin philosophical magazine and journal of science*, **39**(233), 537–551. 22

Daughton, W., Roytershteyn, V., Karimabadi, H., Yin, L., Albright, B. J., Bergen, B., & Bowers, K. J. 2011. Role of electron physics in the development of turbulent magnetic reconnection in collisionless plasmas. *Nature physics*, **7**(7), 539–542. 115

Daughton, W., Nakamura, T. K. M., Karimabadi, H., Roytershteyn, V., & Loring, B. 2014. Computing the reconnection rate in turbulent kinetic layers by using electron mixing to identify topology. *Physics of plasmas*, **21**(5), 052307. 45, 90

Daughton, William, Scudder, Jack, & Karimabadi, Homa. 2006. Fully kinetic simulations of undriven magnetic reconnection with open boundary conditions. *Physics of plasmas*, **13**(7), 072101. 97

Del Sarto, Daniele, & Pegoraro, Francesco. 2018. Shear-induced pressure anisotropization and correlation with fluid vorticity in a low collisionality plasma. *Monthly notices of the royal astronomical society*, **475**(1), 181–192. 42

Denton, R. E., Sonnerup, B. U. Ö., Birn, J., Teh, W.-L., Drake, J. F., Swisdak, M., Hesse,

M., & Baumjohann, W. 2010. Test of methods to infer the magnetic reconnection geometry from spacecraft data: MAGNETIC RECONNECTION GEOMETRY. *Journal of geophysical research: Space physics*, **115**(A10), n/a–n/a. 51

Denton, R. E., Sonnerup, B. U. Ö., Swisdak, M., Birn, J., Drake, J. F., & Hesse, M. 2012. Test of Shi et al. method to infer the magnetic reconnection geometry from spacecraft data: MHD simulation with guide field and antiparallel kinetic simulation: MAGNETIC RECONNECTION GEOMETRY. *Journal of geophysical research: Space physics*, **117**(A9), n/a–n/a. 51

Denton, R. E., Sonnerup, B. U. Ö., Hasegawa, H., Phan, T. D., Russell, C. T., Strangeway, R. J., Giles, B. L., Gershman, D., & Torbert, R. B. 2016a. Motion of the MMS spacecraft relative to the magnetic reconnection structure observed on 16 October 2015 at 1307 UT: RECONNECTION STRUCTURE ON 16 OCTOBER 2015. *Geophysical research letters*, **43**(11), 5589–5596. 41

Denton, R. E., Sonnerup, B. U. Ö., Hasegawa, H., Phan, T. D., Russell, C. T., Strangeway, R. J., Giles, B. L., & Torbert, R. B. 2016b. Reconnection guide field and quadrupolar structure observed by MMS on 16 October 2015 at 1307 UT: GUIDE FIELD AND QUADRUPOLAR STRUCTURE. *Journal of geophysical research: Space physics*, **121**(10), 9880–9887. 115

Denton, R. E., Sonnerup, B. U. Ö., Russell, C. T., Hasegawa, H., Phan, T.-D., Strangeway, R. J., Giles, B. L., Ergun, R. E, Lindqvist, P.-A., Torbert, R. B., Burch, J. L, & Vines, S. K. 2018. Determining $\boldsymbol{L}$ - $\boldsymbol{M}$ - $\boldsymbol{N}$ Current Sheet Coordinates at the Magnetopause From Magnetospheric Multiscale Data. *Journal of geophysical research: Space physics*, Mar. 40

Divin, A., Markidis, S., Lapenta, G., Semenov, V. S., Erkaev, N. V., & Biernat, H. K. 2010. Model of electron pressure anisotropy in the electron diffusion region of collisionless magnetic reconnection. *Physics of plasmas*, **17**(12), 122102. 118

Divin, A., Lapenta, G., Markidis, S., Semenov, V. S., Erkaev, N. V., Korovinskiy, D. B., & Biernat, H. K. 2012. Scaling of the inner electron diffusion region in collisionless magnetic reconnection: ELECTRON DIFFUSION REGION SCALING. *Journal of geophysical research: Space physics*, **117**(A6), n/a–n/a. 103, 114

Doss, C. E., Komar, C. M., Cassak, P. A., Wilder, F. D., Eriksson, S., & Drake, J. F. 2015. Asymmetric magnetic reconnection with a flow shear and applications to the magnetopause. *Journal of geophysical research: Space physics*, **120**(9), 7748–7763. 98

Doss, C. E., Cassak, P. A., & Swisdak, M. 2016. Particle-in-cell simulation study of the scaling of asymmetric magnetic reconnection with in-plane flow shear. *Physics of plasmas*, **23**(8), 082107. 98

Drake, J. F., & Swisdak, M. 2014. The onset of ion heating during magnetic reconnection with a strong guide field. *Physics of plasmas*, **21**(7), 072903. 117

Drake, J. F., Shay, M. A., Thongthai, W., & Swisdak, M. 2005. Production of Energetic Electrons during Magnetic Reconnection. *Physical review letters*, **94**(9), 095001. 118

Drake, J. F., Swisdak, M., Che, H., & Shay, M. A. 2006a. Electron acceleration from contracting magnetic islands during reconnection. *Nature*, **443**(7111), 553–556. 109

Drake, J. F., Swisdak, M., Schoeffler, K. M., Rogers, B. N., & Kobayashi, S. 2006b. Formation of secondary islands during magnetic reconnection. *Geophysical research letters*, **33**(13), L13105. 98

Drake, J. F., Swisdak, M., Phan, T. D., Cassak, P. A., Shay, M. A., Lepri, S. T., Lin,

R. P., Quataert, E., & Zurbuchen, T. H. 2009a. Ion heating resulting from pickup in magnetic reconnection exhausts: ION PICKUP. *Journal of geophysical research: Space physics*, **114**(A5), n/a–n/a. 117

Drake, J. F., Cassak, P. A., Shay, M. A., Swisdak, M., & Quataert, E. 2009b. A MAGNETIC RECONNECTION MECHANISM FOR ION ACCELERATION AND ABUNDANCE ENHANCEMENTS IN IMPULSIVE FLARES. *The astrophysical journal*, **700**(1), L16–L20. 117

Du, Senbei, Guo, Fan, Zank, Gary P., Li, Xiaocan, & Stanier, Adam. 2018. Plasma Energization in Colliding Magnetic Flux Ropes. *The astrophysical journal*, **867**(1), 16. 66

Du, Senbei, Zank, Gary P., Guo, Fan, & Li, Xiaocan. 2019. Energy Dissipation and Entropy in Collisionless Plasma. *arxiv:1911.08086 [astro-ph, physics:physics]*, Nov. arXiv: 1911.08086. 66

Dunlop, M.W., Southwood, D.J., Glassmeier, K.-H., & Neubauer, F.M. 1988. Analysis of multipoint magnetometer data. *Advances in space research*, **8**(9-10), 273–277. 38

Démoulin, P. 2006. Extending the concept of separatrices to QSLs for magnetic reconnection. *Advances in space research*, **37**(7), 1269–1282. 90

Eastwood, J. P., Shay, M. A., Phan, T. D., & Øieroset, M. 2010. Asymmetry of the Ion Diffusion Region Hall Electric and Magnetic Fields during Guide Field Reconnection: Observations and Comparison with Simulations. *Physical review letters*, **104**(20), 205001. 115

Eastwood, J. P., Phan, T. D., Drake, J. F., Shay, M. A., Borg, A. L., Lavraud, B., & Taylor, M. G. G. T. 2013. Energy Partition in Magnetic Reconnection in Earth's Magnetotail. *Physical review letters*, **110**(22), 225001. 68

Eastwood, J. P., Hietala, H., Toth, G., Phan, T. D., & Fujimoto, M. 2015. What Controls the Structure and Dynamics of Earth's Magnetosphere? *Space science reviews*, **188**(1-4), 251–286. 12, 14

Eastwood, J. P., Phan, T. D., Cassak, P. A., Gershman, D. J., Haggerty, C., Malakit, K., Shay, M. A., Mistry, R., Øieroset, M., Russell, C. T., Slavin, J. A., Argall, M. R., Avanov, L. A., Burch, J. L., Chen, L. J., Dorelli, J. C., Ergun, R. E., Giles, B. L., Khotyaintsev, Y., Lavraud, B., Lindqvist, P. A., Moore, T. E., Nakamura, R., Paterson, W., Pollock, C., Strangeway, R. J., Torbert, R. B., & Wang, S. 2016. Ion-scale secondary flux ropes generated by magnetopause reconnection as resolved by MMS. *Geophysical research letters*, **43**(10), 4716–4724. 54, 55

Eastwood, J. P., Biffis, E., Hapgood, M. A., Green, L., Bisi, M. M., Bentley, R. D., Wicks, R., McKinnell, L.-A., Gibbs, M., & Burnett, C. 2017. The Economic Impact of Space Weather: Where Do We Stand?: Perspective. *Risk analysis*, **37**(2), 206–218. 16

Eastwood, J. P., Mistry, R., Phan, T. D., Schwartz, S. J., Ergun, R. E., Drake, J. F., Øieroset, M., Stawarz, J. E., Goldman, M. V., Haggerty, C., Shay, M. A., Burch, J. L., Gershman, D. J., Giles, B. L., Lindqvist, P. A., Torbert, R. B., Strangeway, R. J., & Russell, C. T. 2018. Guide Field Reconnection: Exhaust Structure and Heating. *Geophysical research letters*, **45**(10), 4569–4577. 117, 118

Ebihara, Yusuke, & Tanaka, Takashi. 2020. Evolution of auroral substorm as viewed from MHD simulations: dynamics, energy transfer and energy conversion. *Reviews of modern plasma physics*, **4**(1), 2. 14, 30

Egedal, J. 2002. A drift kinetic approach to stationary collisionless magnetic reconnec-

tion in an open cusp plasma. *Physics of plasmas*, **9**(4), 1095–1103. 117

Egedal, J., & Fasoli, A. 2001. Single-Particle Dynamics in Collisionless Magnetic Reconnection. *Physical review letters*, **86**(22), 5047–5050. 115

Egedal, J., Øieroset, M., Fox, W., & Lin, R. P. 2005. *In Situ* Discovery of an Electrostatic Potential, Trapping Electrons and Mediating Fast Reconnection in the Earth's Magnetotail. *Physical review letters*, **94**(2), 025006. 115

Egedal, J., Fox, W., Katz, N., Porkolab, M., Øieroset, M., Lin, R. P., Daughton, W., & Drake, J. F. 2008. Evidence and theory for trapped electrons in guide field magnetotail reconnection: TRAPPED ELECTRONS IN GUIDE FIELD RECONNECTION. *Journal of geophysical research: Space physics*, **113**(A12), n/a–n/a. 115

Egedal, J., Lê, A., Katz, N., Chen, L.-J., Lefebvre, B., Daughton, W., & Fazakerley, A. 2010. Cluster observations of bidirectional beams caused by electron trapping during antiparallel reconnection: ELECTRON TRAPPING IN RECONNECTION. *Journal of geophysical research: Space physics*, **115**(A3), n/a–n/a. 115

Egedal, J., Daughton, W., & Le, A. 2012. Large-scale electron acceleration by parallel electric fields during magnetic reconnection. *Nature physics*, **8**(4), 321–324. 117

Egedal, J., Wetherton, B., Daughton, W., & Le, A. 2016a. Processes setting the structure of the electron distribution function within the exhausts of anti-parallel reconnection. *Physics of plasmas*, **23**(12), 122904. 118

Egedal, J., Le, A., Daughton, W., Wetherton, B., Cassak, P. A., Chen, L.-J., Lavraud, B., Trobert, R. B., Dorelli, J., Gershman, D. J., & Avanov, L. A. 2016b. Spacecraft observations and analytic theory of crescent-shaped electron distributions in asymmetric magnetic reconnection. *Physical review letters*, **117**(18), 185101. arXiv: 1607.05670. 118

Egedal, J., Le, A., Daughton, W., Wetherton, B., Cassak, P.A., Burch, J.L., Lavraud, B., Dorelli, J., Gershman, D.J., & Avanov, L.A. 2018. Spacecraft Observations of Oblique Electron Beams Breaking the Frozen-In Law During Asymmetric Reconnection. *Physical review letters*, **120**(5), 055101. 97, 118

Egedal, J., Ng, J., Le, A., Daughton, W., Wetherton, B., Dorelli, J., Gershman, D., & Rager, A. 2019. Pressure Tensor Elements Breaking the Frozen-In Law During Reconnection in Earth's Magnetotail. *Physical review letters*, **123**(22), 225101. 97

Egedal, Jan, Le, Ari, & Daughton, William. 2013. A review of pressure anisotropy caused by electron trapping in collisionless plasma, and its implications for magnetic reconnection. *Physics of plasmas*, **20**(6), 061201. 21, 118

Ek-In, Surapat, Malakit, Kittipat, Ruffolo, David, Shay, Michael A., & Cassak, Paul A. 2017. Effects of a Guide Field on the Larmor Electric Field and Upstream Electron Temperature Anisotropy in Collisionless Asymmetric Magnetic Reconnection. *The astrophysical journal*, **845**(2), 113. 115

Euler, L. 1761. Principia motus fluidorum. *Novi commentarii academiae scientiarum imp. petropolitanae*, 271–311. 20

Fadanelli, S., Faganello, M., Califano, F., Cerri, S. S., Pegoraro, F., & Lavraud, B. 2018. North-South Asymmetric Kelvin-Helmholtz Instability and Induced Reconnection at the Earth's Magnetospheric Flanks. *Journal of geophysical research: Space physics*, **123**(11), 9340–9356. 80, 81

Fadanelli, S., Lavraud, B., Califano, F., Jacquey, C., Vernisse, Y., Kacem, I., Penou, E., Gershman, D. J., Dorelli, J., Pollock, C., Giles, B. L., Avanov, L. A., Burch, J., Chandler, M. O., Coffey, V. N., Eastwood, J. P., Ergun, R., Farrugia, C. J., Fuselier, S. A., Genot,

V. N., Grigorenko, E., Hasegawa, H., Khotyaintsev, Y., Le Contel, O., Marchaudon, A., Moore, T. E., Nakamura, R., Paterson, W. R., Phan, T., Rager, A. C., Russell, C. T., Saito, Y., Sauvaud, J.-A., Schiff, C., Smith, S. E., Toledo Redondo, S., Torbert, R. B., Wang, S., & Yokota, S. 2019. Four-Spacecraft Measurements of the Shape and Dimensionality of Magnetic Structures in the Near-Earth Plasma Environment. *Journal of geophysical research: Space physics*, **124**(8), 6850–6868. 39, 46, 48, 49, 50, 52, 55, 56, 57, 58, 59, 60, 61, 87

Faganello, M., Califano, F., Pegoraro, F., & Andreussi, T. 2012. Double mid-latitude dynamical reconnection at the magnetopause: An efficient mechanism allowing solar wind to enter the Earth's magnetosphere. *Epl (europhysics letters)*, **100**(6), 69001. 81

Faganello, Matteo, & Califano, Francesco. 2017. Magnetized Kelvin–Helmholtz instability: theory and simulations in the Earth's magnetosphere context. *Journal of plasma physics*, **83**(6), 535830601. 14

Fargette, N., Lavraud, B., Øieroset, M., Phan, T. D., Toledo-Redondo, S., Kieokaew, R., Jacquey, C., Fuselier, S. A., Trattner, K. J., Petrinec, S., Hasegawa, H., Garnier, P., Génot, V., Lenouvel, Q., Fadanelli, S., Penou, E., Sauvaud, J.-A., Avanov, D. L. A., Burch, J., Chandler, M. O., Coffey, V. N., Dorelli, J., Eastwood, J. P., Farrugia, C. J., Gershman, D. J., Giles, B. L., Grigorenko, E., Moore, T. E., Paterson, W. R., Pollock, C., Saito, Y., Schiff, C., & Smith, S. E. 2020. On the Ubiquity of Magnetic Reconnection Inside Flux Transfer Event-Like Structures at the Earth's Magnetopause. *Geophysical research letters*, **47**(6). 30

Farrugia, C. J., Gratton, F. T., Bender, L., Biernat, H. K., Erkaev, N. V., Quinn, J. M., Torbert, R. B., & Dennisenko, V. 1998. Charts of joint Kelvin-Helmholtz and Rayleigh-Taylor instabilites at the dayside magnetopause for strongly northward interplanetary magnetic field. *Journal of geophysical research: Space physics*, **103**(A4), 6703–6727. 14

Fitzpatrick, Richard. 2014. *Plasma Physics: an introduction*. 10, 18, 19, 111, 113

Frisch, Uriel. 1995. *Turbulence*. 44

Frühauff, Dennis, Mieth, Johannes Z. D., & Glassmeier, Karl-Heinz. 2017. Average plasma sheet polytropic index as observed by THEMIS. *Annales geophysicae*, **35**(2), 253–262. 21, 66, 69, 82

Fujimoto, Keizo. 2014. Wave activities in separatrix regions of magnetic reconnection. *Geophysical research letters*, **41**(8), 2721–2728. 115

Furth, Harold P, Killeen, John, & Rosenbluth, Marshall N. 1963. Finite-Resistivity Instabilities of a Sheet Pinch. 27. 28

Fuselier, S. A., Lewis, W. S., Schiff, C., Ergun, R., Burch, J. L., Petrinec, S. M., & Trattner, K. J. 2016. Magnetospheric Multiscale Science Mission Profile and Operations. *Space science reviews*, **199**(1-4), 77–103. 32

Fuselier, S. A., Petrinec, S. M., Sawyer, R. P., Mukherjee, J., & Masters, A. 2020. Suppression of Magnetic Reconnection at Saturn's Low-Latitude Magnetopause. *Journal of geophysical research: Space physics*, **125**(5). 98

Galtier, Sebastien. 2016. *Introduction to Modern Magnetohydrodynamics*. Cambridge: Cambridge University Press. 23

Genestreti, K. J., Nakamura, T. K. M., Nakamura, R., Denton, R. E., Torbert, R. B., Burch, J. L., Plaschke, F., Fuselier, S. A., Ergun, R. E., Giles, B. L., & Russell, C. T. 2018a. How Accurately Can We Measure the Reconnection Rate $\boldsymbol{E}_{m}$ for the MMS

Diffusion Region Event of 11 July 2017? *Journal of geophysical research: Space physics*, **123**(11), 9130–9149. 41

Genestreti, K. J., Varsani, A., Burch, J. L., Cassak, P. A., Torbert, R. B., Nakamura, R., Ergun, R. E., Phan, T.-D., Toledo-Redondo, S., Hesse, M., Wang, S., Giles, B. L., Russell, C. T., Vörös, Z., Hwang, K.-J., Eastwood, J. P., Lavraud, B., Escoubet, C. P., Fear, R. C., Khotyaintsev, Y., Nakamura, T. K. M., Webster, J. M., & Baumjohann, W. 2018b. MMS Observation of Asymmetric Reconnection Supported by 3-D Electron Pressure Divergence: OHM'S LAW FOR NEW MMS EDR EVENT. *Journal of geophysical research: Space physics*, Mar. 97

Goedbloed, Hans Peter, & Poedts, Stefaan. 2005. *Principles of magnetohydrodynamics: with applications to laboratory and astrophysical plasmas*. Vol. 42. 23

Goldman, M. V., Newman, D. L., & Lapenta, G. 2016. What Can We Learn about Magnetotail Reconnection from 2D PIC Harris-Sheet Simulations? *Space science reviews*, **199**(1-4), 651–688. 45

Goldman, M. V., Newman, D. L., Eastwood, J. P., & Lapenta, G. 2020. Multibeam Energy Moments of Multibeam Particle Velocity Distributions. *Journal of geophysical research: Space physics*, **125**(12). 21

Gonzalez, Walter, & Parker, Eugene (eds). 2016. *Magnetic Reconnection: Concepts and Applications*. Astrophysics and Space Science Library, vol. 427. Cham: Springer International Publishing. 40, 45, 68

Graham, D. B., Khotyaintsev, Yu. V., Norgren, C., Vaivads, A., André, M., Toledo-Redondo, S., Lindqvist, P.-A., Marklund, G. T., Ergun, R. E., Paterson, W. R., Gershman, D. J., Giles, B. L., Pollock, C. J., Dorelli, J. C., Avanov, L. A., Lavraud, B., Saito, Y., Magnes, W., Russell, C. T., Strangeway, R. J., Torbert, R. B., & Burch, J. L. 2017a. Lower hybrid waves in the ion diffusion and magnetospheric inflow regions. *Journal of geophysical research: Space physics*, **122**(1), 517–533. 115

Graham, D.B., Khotyaintsev, Yu.V., Vaivads, A., Norgren, C., André, M., Webster, J.M., Burch, J.L., Lindqvist, P.-A., Ergun, R.E., Torbert, R.B., Paterson, W.R., Gershman, D.J., Giles, B.L., Magnes, W., & Russell, C.T. 2017b. Instability of Agyrotropic Electron Beams near the Electron Diffusion Region. *Physical review letters*, **119**(2), 025101. 115

Greene, John M. 1992. Locating Three- Dimensional Roots by a Bisection Method. 5. 45

Griton, L., & Pantellini, F. 2020. Magnetohydrodynamic simulations of a Uranus-at-equinox type rotating magnetosphere. *Astronomy & astrophysics*, **633**(Jan.), A87. 12

Haaland, S., Sonnerup, B. U. Ö., Dunlop, M. W., Georgescu, E., Paschmann, G., Klecker, B., & Vaivads, A. 2004a. Orientation and motion of a discontinuity from Cluster curlometer capability: Minimum variance of current density: MAGNETOPAUSE ORIENTATION FROM CURRENT DENSITY. *Geophysical research letters*, **31**(10), n/a–n/a. 39

Haaland, S. E., Sonnerup, B. U. Ö., Dunlop, M. W., Balogh, A., Georgescu, E., Hasegawa, H., Klecker, B., Paschmann, G., Puhl-Quinn, P., Rème, H., Vaith, H., & Vaivads, A. 2004b. Four-spacecraft determination of magnetopause orientation, motion and thickness: comparison with results from single-spacecraft methods. *Annales geophysicae*, **22**(4), 1347–1365. 40

Haggerty, C. C., Shay, M. A., Drake, J. F., Phan, T. D., & McHugh, C. T. 2015. The

competition of electron and ion heating during magnetic reconnection: PARTITION OF HEATING IN RECONNECTION. *Geophysical research letters*, **42**(22), 9657–9665. 117

Haller, G., & Beron-Vera, F. J. 2013. Coherent Lagrangian vortices: the black holes of turbulence. *Journal of fluid mechanics*, **731**(Sept.), R4. 90

Haller, George. 2011. A variational theory of hyperbolic Lagrangian Coherent Structures. *Physica d: Nonlinear phenomena*, **240**(7), 574–598. 90

Haller, George. 2014. Lagrangian Coherent Structures. 28. 90

Hasegawa, H., Sonnerup, B. U. Ö., Denton, R. E., Phan, T.-D., Nakamura, T. K. M., Giles, B. L., Gershman, D. J., Dorelli, J. C., Burch, J. L., Torbert, R. B., Russell, C. T., Strangeway, R. J., Lindqvist, P.-A., Khotyaintsev, Y. V., Ergun, R. E., Cassak, P. A., Kitamura, N., & Saito, Y. 2017. Reconstruction of the electron diffusion region observed by the Magnetospheric Multiscale spacecraft: First results: ELECTRON DIFFUSION REGION SEEN BY MMS. *Geophysical research letters*, **44**(10), 4566–4574. 40

Hazeltine, R. D, & Waelbroeck, F. 2018. *The framework of plasma physics*. OCLC: 1028553216. 104

Hesse, M., & Birn, J. 1993. Parallel electric fields as acceleration mechanisms in three-dimensional magnetic reconnection. *Advances in space research*, **13**(4), 249–252. 102

Hesse, M., & Cassak, P. A. 2020. Magnetic Reconnection in the Space Sciences: Past, Present, and Future. *Journal of geophysical research: Space physics*, **125**(2). 17, 27, 97, 98

Hesse, M., & Schindler, K. 1988. A theoretical foundation of general magnetic reconnection. *Journal of geophysical research*, **93**(A6), 5559. 26, 94, 96, 102

Hesse, M., Chen, L.J., Liu, Y.-H., Bessho, N., & Burch, J.L. 2017. Population Mixing in Asymmetric Magnetic Reconnection with a Guide Field. *Physical review letters*, **118**(14), 145101. 118

Hesse, M., Norgren, C., Tenfjord, P., Burch, J. L., Liu, Y.-H., Chen, L.-J., Bessho, N., Wang, S., Nakamura, R., Eastwood, J. P., Hoshino, M., Torbert, R. B., & Ergun, R. E. 2018a. On the role of separatrix instabilities in heating the reconnection outflow region. *Physics of plasmas*, **25**(12), 122902. 118

Hesse, M., Liu, Y.-H., Chen, L.-J., Bessho, N., Wang, S., Burch, J. L., Moretto, T., Norgren, C., Genestreti, K. J., Phan, T. D., & Tenfjord, P. 2018b. The physical foundation of the reconnection electric field. *Physics of plasmas*, **25**(3), 032901. 97

Hesse, Michael. 2002. The structure of the dissipation region for component reconnection: Particle simulations. *Geophysical research letters*, **29**(12), 1563. 97

Hesse, Michael, & Winske, Dan. 1998. Electron dissipation in collisionless magnetic reconnection. *Journal of geophysical research: Space physics*, **103**(A11), 26479–26486. 97

Hesse, Michael, Kuznetsova, Masha, Schindler, Karl, & Birn, Joachim. 2005. Three-dimensional modeling of electron quasiviscous dissipation in guide- field magnetic reconnection. *Phys. plasmas*, 5. 97

Hesse, Michael, Zenitani, Seiji, Kuznetsova, Masha, & Klimas, Alex. 2009. A simple, analytical model of collisionless magnetic reconnection in a pair plasma. *Physics of plasmas*, **16**(10), 102106. 103

Hesse, Michael, Neukirch, Thomas, Schindler, Karl, Kuznetsova, Masha, & Zenitani, Seiji. 2011a. The Diffusion Region in Collisionless Magnetic Reconnection. *Space science reviews*, **160**(1-4), 3–23. 97

Hesse, Michael, Birn, Joachim, & Zenitani, Seiji. 2011b. Magnetic reconnection in a

compressible MHD plasma. *Physics of plasmas*, **18**(4), 042104. 103

Hesse, Michael, Aunai, Nicolas, Zenitani, Seiji, Kuznetsova, Masha, & Birn, Joachim. 2013. Aspects of collisionless magnetic reconnection in asymmetric systems. *Physics of plasmas*, **20**(6), 061210. 99, 103

Hesse, Michael, Aunai, Nicolas, Sibeck, David, & Birn, Joachim. 2014. On the electron diffusion region in planar, asymmetric, systems: diffusion region in asymmetric systems. *Geophysical research letters*, **41**(24), 8673–8680. 97

Hesse, Michael, Liu, Yi-Hsin, Chen, Li-Jen, Bessho, Naoki, Kuznetsova, Masha, Birn, Joachim, & Burch, James L. 2016. On the electron diffusion region in asymmetric reconnection with a guide magnetic field. *Geophysical research letters*, **43**(6), 2359–2364. 97

Hewett, D. 1985. Elimination of electromagnetic radiation in plasma simulation: The Darwin or magneto inductive approximation. 12. 22

Hietala, H., & Plaschke, F. 2013. On the generation of magnetosheath high-speed jets by bow shock ripples: JETS, RIPPLES, AND M'SHEATH. *Journal of geophysical research: Space physics*, **118**(11), 7237–7245. 14

Hietala, H., Phan, T. D., Angelopoulos, V., Oieroset, M., Archer, M. O., Karlsson, T., & Plaschke, F. 2018. In Situ Observations of a Magnetosheath High-Speed Jet Triggering Magnetopause Reconnection. *Geophysical research letters*, **45**(4), 1732–1740. 14

Hoilijoki, Sanni, Ganse, Urs, Pfau-Kempf, Yann, Cassak, Paul A., Walsh, Brian M., Hietala, Heli, Alfthan, Sebastian, & Palmroth, Minna. 2017. Reconnection rates and X line motion at the magnetopause: Global 2D-3V hybrid-Vlasov simulation results. *Journal of geophysical research: Space physics*, **122**(3), 2877–2888. 30

Hornig, G., & Schindler, K. 1996. Magnetic topology and the problem of its invariant definition. *Physics of plasmas*, **3**(3), 781–791. 92

Hornig, Gunnar, & Priest, Eric. 2003. Evolution of magnetic flux in an isolated reconnection process. *Physics of plasmas*, **10**(7), 2712–2721. 102

Hornig, Gunnar, & Rastätter, Lutz. 1998. The magnetic structure of B 0-reconnection. *Physica scripta*, **T74**(Jan.), 34–39. 95

Hoshino, Masahiro. 2018. Energy Partition between Ion and Electron of Collisionless Magnetic Reconnection. *The astrophysical journal*, **868**(2), L18. 66, 69

Huang, Kai, Liu, Yi-Hsin, Lu, Quanming, & Hesse, Michael. 2019. Scaling of magnetic reconnection with a limited x-line extent. *arxiv:1912.00841 [physics]*, Dec. arXiv: 1912.00841. 97

Huang, Shiyong, Zhao, Pufan, He, Jiansen, Yuan, Zhigang, Zhou, Meng, Fu, Huishan, Deng, Xiaohua, Pang, Ye, Wang, Dedong, Yu, Xiongdong, Li, Haimeng, Torbert, Roy, & Burch, James. 2018. A new method to identify flux ropes in space plasmas. *Annales geophysicae*, **36**(5), 1275–1283. 40

Huynh, Du Q. 2009. Metrics for 3D Rotations: Comparison and Analysis. *Journal of mathematical imaging and vision*, **35**(2), 155–164. 51

Hwang, K.-J., Sibeck, D. G., Burch, J. L., Choi, E., Fear, R. C., Lavraud, B., Giles, B. L., Gershman, D., Pollock, C. J., Eastwood, J. P., Khotyaintsev, Y., Escoubet, Philippe, Fu, H., Toledo-Redondo, S., Torbert, R. B., Ergun, R. E., Paterson, W. R., Dorelli, J. C., Avanov, L., Russell, C. T., & Strangeway, R. J. 2018. Small-Scale Flux Transfer Events Formed in the Reconnection Exhaust Region Between Two X Lines. *Journal of geophysical research: Space physics*, **123**(10), 8473–8488. 30

Inc., Auth. 1859. Auroral Display. *The louisville daily courier*, Sept., 3. 15

Juusola, Liisa, Hoilijoki, Sanni, Pfau-Kempf, Yann, Ganse, Urs, Jarvinen, Riku, Battarbee, Markus, Kilpua, Emilia, Turc, Lucile, & Palmroth, Minna. 2018. Fast plasma sheet flows and X line motion in the Earth's magnetotail: results from a global hybrid-Vlasov simulation. *Annales geophysicae*, **36**(5), 1183–1199. 30, 93

Kacem, I., Jacquey, C., Génot, V., Lavraud, B., Vernisse, Y., Marchaudon, A., Le Contel, O., Breuillard, H., Phan, T. D., Hasegawa, H., Oka, M., Trattner, K. J., Farrugia, C. J., Paulson, K., Eastwood, J. P., Fuselier, S. A., Turner, D., Eriksson, S., Wilder, F., Russell, C. T., Øieroset, M., Burch, J., Graham, D. B., Sauvaud, J.-A., Avanov, L., Chandler, M., Coffey, V., Dorelli, J., Gershman, D. J., Giles, B. L., Moore, T. E., Saito, Y., Chen, L.-J., & Penou, E. 2018. Magnetic Reconnection at a Thin Current Sheet Separating Two Interlaced Flux Tubes at the Earth's Magnetopause. *Journal of geophysical research: Space physics*, Mar. 54, 56, 57

Karimabadi, H., Daughton, W., & Scudder, J. 2007. Multi-scale structure of the electron diffusion region: STRUCTURE OF THE ELECTRON DIFFUSION REGION. *Geophysical research letters*, **34**(13), n/a–n/a. 97, 114

Khotyaintsev, Yu.V., Graham, D.B., Steinvall, K., Alm, L., Vaivads, A., Johlander, A., Norgren, C., Li, W., Divin, A., Fu, H.S., Hwang, K.-J., Burch, J.L., Ahmadi, N., Le Contel, O., Gershman, D.J., Russell, C.T., & Torbert, R.B. 2020. Electron Heating by Debye-Scale Turbulence in Guide-Field Reconnection. *Physical review letters*, **124**(4), 045101. 118

Khrabrov, Alexander V., & Sonnerup, Bengt U. Ö. 1998. Orientation and motion of current layers: minimization of the Faraday residue. *Geophysical research letters*, **25**(13), 2373–2376. 40

Kieokaew, Rungployphan, Foullon, Claire, & Lavraud, Benoit. 2018. Four-Spacecraft Magnetic Curvature and Vorticity Analyses on Kelvin-Helmholtz Waves in MHD Simulations: CURVATURE AND VORTICITY OF KH WAVES. *Journal of geophysical research: Space physics*, **123**(1), 513–529. 38

Kivelson, M., & Russell, C.T. 1995. *Introduction to space physics*. 36

Kuznetsova, Masha M., Hesse, Michael, & Winske, Dan. 2000. Toward a transport model of collisionless magnetic reconnection. *Journal of geophysical research: Space physics*, **105**(A4), 7601–7616. 97

Landau, L. D., & Lifshits, E. M. 1987. *Fluid mechanics*. 2nd edn. Course of theoretical physics, vol. 6. 85

Landau, L. D., Lifshits, E. M., & Landau, L. D. 1975. *The classical theory of fields*. 4th rev. english ed edn. Course of theoretical physics, vol. 2. Oxford ; New York: Pergamon Press. 111

Lang, Kenneth R. 2011. *Cambridge Guide to the Solar System*. 11, 14

Lang, Kenneth R. 2013. *Essential Astrophysics*. Undergraduate Lecture Notes in Physics. Berlin, Heidelberg: Springer Berlin Heidelberg. 11

Langmuir, Irving, Co, GsERALu EIXCTRIc, & NsCTADY, SCH. 1928. Oscillations in ionized gases. **14**, 11. 10

Lapenta, G., Pucci, F., Goldman, M. V., & Newman, D. L. 2019. A violin sonata for reconnection. *arxiv:1904.02094 [astro-ph, physics:physics]*, Apr. arXiv: 1904.02094. 115

Lapenta, Giovanni. 2008. Self-Feeding Turbulent Magnetic Reconnection on Macroscopic Scales. *Physical review letters*, **100**(23), 235001. arXiv: 0805.0426. 115

Lapenta, Giovanni, Markidis, Stefano, Goldman, Martin V., & Newman, David L. 2015a. Secondary reconnection sites in reconnection-generated flux ropes and reconnection fronts. *Nature physics*, **11**(8), 690–695. 45, 115

Lapenta, Giovanni, Markidis, Stefano, Divin, Andrey, Newman, David, & Goldman, Martin. 2015b. Separatrices: The crux of reconnection. *Journal of plasma physics*, **81**(1), 325810109. 118

Laundal, K. M., & Richmond, A. D. 2017. Magnetic Coordinate Systems. *Space science reviews*, **206**(1-4), 27–59. 37

Lavraud, B., Thomsen, M. F., Lefebvre, B., Schwartz, S. J., Seki, K., Phan, T. D., Wang, Y. L., Fazakerley, A., Rème, H., & Balogh, A. 2006. Evidence for newly closed magnetosheath field lines at the dayside magnetopause under northward IMF. *Journal of geophysical research*, **111**(A5), A05211. 40

Lavraud, B., Zhang, Y. C., Vernisse, Y., Gershman, D. J., Dorelli, J., Cassak, P. A., Dargent, J., Pollock, C., Giles, B., Aunai, N., Argall, M., Avanov, L., Barrie, A., Burch, J., Chandler, M., Chen, L.-J., Clark, G., Cohen, I., Coffey, V., Eastwood, J. P., Egedal, J., Eriksson, S., Ergun, R., Farrugia, C. J., Fuselier, S. A., Génot, V., Graham, D., Grigorenko, E., Hasegawa, H., Jacquey, C., Kacem, I., Khotyaintsev, Y., MacDonald, E., Magnes, W., Marchaudon, A., Mauk, B., Moore, T. E., Mukai, T., Nakamura, R., Paterson, W., Penou, E., Phan, T. D., Rager, A., Retino, A., Rong, Z. J., Russell, C. T., Saito, Y., Sauvaud, J.-A., Schwartz, S. J., Shen, C., Smith, S., Strangeway, R., Toledo-Redondo, S., Torbert, R., Turner, D. L., Wang, S., & Yokota, S. 2016. Currents and associated electron scattering and bouncing near the diffusion region at Earth's magnetopause. *Geophysical research letters*, **43**(7), 3042–3050. 53, 118

Lavraud, Benoit, & Larson, Davin E. 2016. Correcting moments of in situ particle distribution functions for spacecraft electrostatic charging. *Journal of geophysical research: Space physics*, **121**(9), 8462–8474. 33

Le, A., Egedal, J., Daughton, W., Fox, W., & Katz, N. 2009. Equations of State for Collisionless Guide-Field Reconnection. *Physical review letters*, **102**(8), 085001. 21, 118

Le, A., Egedal, J., Fox, W., Katz, N., Vrublevskis, A., Daughton, W., & Drake, J. F. 2010a. Equations of state in collisionless magnetic reconnection. *Physics of plasmas*, **17**(5), 055703. 21, 118

Le, A., Egedal, J., Daughton, W., Drake, J. F., Fox, W., & Katz, N. 2010b. Magnitude of the Hall fields during magnetic reconnection: HALL FIELDS DURING RECONNECTION. *Geophysical research letters*, **37**(3), n/a–n/a. 114

Le, A., Karimabadi, H., Egedal, J., Roytershteyn, V., & Daughton, W. 2012. Electron energization during magnetic island coalescence. *Physics of plasmas*, **19**(7), 072120. 117

Le, A., Daughton, W., Ohia, O., Chen, L.-J., Liu, Y.-H., Wang, S., Nystrom, W. D., & Bird, R. 2018. Drift turbulence, particle transport, and anomalous dissipation at the reconnecting magnetopause. *Physics of plasmas*, **25**(6), 062103. 115

Li, Xiaocan, Guo, Fan, Li, Hui, & Li, Gang. 2015. NONTHERMALLY DOMINATED ELECTRON ACCELERATION DURING MAGNETIC RECONNECTION IN A LOW- PLASMA. *The astrophysical journal*, **811**(2), L24. 70

Li, Xiaocan, Guo, Fan, Li, Hui, & Li, Gang. 2017. Particle Acceleration during Magnetic Reconnection in a Low-beta Plasma. *The astrophysical journal*, **843**(1), 21. 70, 117

Li, Xiaocan, Guo, Fan, Li, Hui, & Birn, Joachim. 2018. The Roles of Fluid Compression and Shear in Electron Energization during Magnetic Reconnection. *The astrophysical journal*, **855**(2), 80. 70

Liu, Yi-Hsin, & Hesse, Michael. 2016. Suppression of collisionless magnetic reconnection in asymmetric current sheets. *Physics of plasmas*, **23**(6), 060704. 95, 98

Liu, Yi-Hsin, Daughton, W., Karimabadi, H., Li, H., & Roytershteyn, V. 2013. Bifurcated Structure of the Electron Diffusion Region in Three-Dimensional Magnetic Reconnection. *Physical review letters*, **110**(26), 265004. 29

Liu, Yi-Hsin, Hesse, M., Guo, F., Daughton, W., Li, H., Cassak, P.A., & Shay, M.A. 2017. Why does Steady-State Magnetic Reconnection have a Maximum Local Rate of Order 0.1? *Physical review letters*, **118**(8), 085101. 98

Liu, Yi-Hsin, Hesse, Michael, Li, Tak Chu, Kuznetsova, Masha, & Le, Ari. 2018a. Orientation and stability of asymmetric magnetic reconnection x-line. *Journal of geophysical research: Space physics*, **123**(6), 4908–4920. arXiv: 1805.07774. 99, 103, 115

Liu, Yi-Hsin, Hesse, M., Guo, F., Li, H., & Nakamura, T. K. M. 2018b. Strongly localized magnetic reconnection by the super-Alfvénic shear flow. *Physics of plasmas*, **25**(8), 080701. 95, 98

Livadiotis, George. 2018. Long-Term Independence of Solar Wind Polytropic Index on Plasma Flow Speed. *Entropy*, **20**(10), 799. 82

Longcope, D. W., & Cowley, S. C. 1996. Current sheet formation along three-dimensional magnetic separators. *Physics of plasmas*, **3**(8), 2885–2897. 103

Lundin, R., Yamauchi, M., Sauvaud, J.-A., & Balogh, A. 2005. Magnetospheric plasma boundaries: a test of the frozen-in magnetic field theorem. *Annales geophysicae*, **23**(7), 2565–2578. 25

Lyon, J. G. 2000. The Solar Wind-Magnetosphere-Ionosphere System. *Science*, **288**(5473), 1987–1991. 16

Ma, Xuanye, & Otto, Antonius. 2014. Nonadiabatic heating in magnetic reconnection. *Journal of geophysical research: Space physics*, **119**(7), 5575–5588. 66, 69

Ma, Xuanye, Otto, Antonius, & Delamere, Peter A. 2016. Magnetic reconnection with a fast perpendicular sheared flow: RECONNECTION WITH FAST FLOW SHEAR. *Journal of geophysical research: Space physics*, **121**(10), 9427–9442. 98

Malakit, K., Shay, M. A., Cassak, P. A., & Ruffolo, D. 2013. New Electric Field in Asymmetric Magnetic Reconnection. *Physical review letters*, **111**(13), 135001. 115

Mangeney, A., Califano, F., Cavazzoni, C., & Travnicek, P. 2002. A Numerical Scheme for the Integration of the Vlasov–Maxwell System of Equations. *Journal of computational physics*, **179**(2), 495–538. 22

Manuzzo, R., Belmont, G., Rezeau, L., Califano, F., & Denton, R. E. 2019. Crossing of Plasma Structures by Spacecraft: A Path Calculator. *Journal of geophysical research: Space physics*, **124**(12), 10119–10140. 39

Matteini, L., Landi, S., Velli, M., & Matthaeus, W. H. 2013. PROTON TEMPERATURE ANISOTROPY AND MAGNETIC RECONNECTION IN THE SOLAR WIND: EFFECTS OF KINETIC INSTABILITIES ON CURRENT SHEET STABILITY. *The astrophysical journal*, **763**(2), 142. 98

Mauk, B. H., Blake, J. B., Baker, D. N., Clemmons, J. H., Reeves, G. D., Spence, H. E., Jaskulek, S. E., Schlemm, C. E., Brown, L. E., Cooper, S. A., Craft, J. V., Fennell, J. F., Gurnee, R. S., Hammock, C. M., Hayes, J. R., Hill, P. A., Ho, G. C., Hutcheson,

J. C., Jacques, A. D., Kerem, S., Mitchell, D. G., Nelson, K. S., Paschalidis, N. P., Rossano, E., Stokes, M. R., & Westlake, J. H. 2016. The Energetic Particle Detector (EPD) Investigation and the Energetic Ion Spectrometer (EIS) for the Magnetospheric Multiscale (MMS) Mission. *Space science reviews*, **199**(1-4), 471–514. 34

McFadden, J. P., Carlson, C. W., Larson, D., Bonnell, J., Mozer, F., Angelopoulos, V., Glassmeier, K.-H., & Auster, U. 2008. THEMIS ESA First Science Results and Performance Issues. *Space science reviews*, **141**(1-4), 477–508. 34

Mellor, C., Titov, V. S., & Priest, E. R. 2002. Linear collapse of spatially linear, two-dimensional null points. *Journal of plasma physics*, **68**(3), 221–235. 103

Mellor, C., Titov, V.S., & Priest, E.R. 2003. Linear collapse of spatially linear, three-dimensional, potential null points. *Geophysical & astrophysical fluid dynamics*, **97**(6), 489–505. 103

Meyer-Vernet, Nicole. 2007. *Basics of the solar wind*. Cambridge atmospheric and space science series. Cambridge ; New York: Cambridge University Press. OCLC: ocm71808112. 11, 109

Molokov, Sergei S., Moreau, René, & Moffatt. 2007. *Magnetohydrodynamics: historical evolution and trends*. Fluid mechanics and its applications, no. 80. Dordrecht: Springer. OCLC: 255466599. 23

Mott-Smith, H. M. 1971. History of "Plasmas". 10

Mozer, F. S., & Retinò, A. 2007. Quantitative estimates of magnetic field reconnection properties from electric and magnetic field measurements: QUANTITATIVE RECONNECTION RATES. *Journal of geophysical research: Space physics*, **112**(A10), n/a–n/a. 39

Mozer, F. S., Angelopoulos, V., Bonnell, J., Glassmeier, K. H., & McFadden, J. P. 2008. THEMIS observations of modified Hall fields in asymmetric magnetic field reconnection. *Geophysical research letters*, **35**(17), L17S04. 115

Murphy, N. A. 2010. Resistive magnetohydrodynamic simulations of X-line retreat during magnetic reconnection. *Physics of plasmas*, **17**(11), 112310. 93

Murphy, Nicholas A., Parnell, Clare E., & Haynes, Andrew L. 2015. The appearance, motion, and disappearance of three-dimensional magnetic null points. *Physics of plasmas*, **22**(10), 102117. 93

Nagai, T. 2003. Structure of the Hall current system in the vicinity of the magnetic reconnection site. *Journal of geophysical research*, **108**(A10), 1357. 115

Nakamura, R., Torkar, K., Andriopoulou, M., Jeszenszky, H., Escoubet, C. P., Cipriani, F., Lindqvist, P. A., Fuselier, S. A., Pollock, C. J., Giles, B. L., & Khotyaintsev, Y. 2017a. Initial Results From the Active Spacecraft Potential Control Onboard Magnetospheric Multiscale Mission. *Ieee transactions on plasma science*, **45**(8), 1847–1852. 35

Nakamura, T. K. M., Daughton, W., Karimabadi, H., & Eriksson, S. 2013. Three-dimensional dynamics of vortex-induced reconnection and comparison with THEMIS observations: VORTEX-INDUCED RECONNECTION IN 3-D. *Journal of geophysical research: Space physics*, **118**(9), 5742–5757. 99

Nakamura, T. K. M., Nakamura, R., Narita, Y., Baumjohann, W., & Daughton, W. 2016. Multi-scale structures of turbulent magnetic reconnection. *Physics of plasmas*, **23**(5), 052116. 115

Nakamura, T. K. M., Eriksson, S., Hasegawa, H., Zenitani, S., Li, W. Y., Genestreti, K. J.,

Nakamura, R., & Daughton, W. 2017b. Mass and Energy Transfer Across the Earth's Magnetopause Caused by Vortex-Induced Reconnection: Mass and Energy Transfer by KH Vortex. *Journal of geophysical research: Space physics*, **122**(11), 11,505–11,522. 29

Nakamura, T. K. M., Nakamura, R., Varsani, A., Genestreti, K. J., Baumjohann, W., & Liu, Y.-H. 2018. Remote Sensing of the Reconnection Electric Field From In Situ Multipoint Observations of the Separatrix Boundary. *Geophysical research letters*, **45**(9), 3829–3837. 41

Newcomb, W. A. 1958. Motion of Magnetic Lines of Force. 92

Nguyen, Gautier, Aunai, Nicolas, Fontaine, Dominique, Pennec, Erwan Le, Bossche, Joris Van den, Jeandet, Alexis, Bakkali, Brice, Vignoli, Louis, & Blancard, Bruno Regaldo-Saint. 2019. Automatic Detection of Interplanetary Coronal Mass Ejections from In Situ Data: A Deep Learning Approach. *The astrophysical journal*, **874**(2), 145. 41

Nickeler, D. H., Karlický, M., & Bárta, M. 2012. Topological skeleton of the 2-D slightly non-ideal MHD system close to X-type magnetic null points – an analysis of the general solution for the generic case. *Annales geophysicae*, **30**(6), 1015–1023. 102

Nicolaou, Georgios, Livadiotis, George, & Wicks, Robert T. 2019. On the Calculation of the Effective Polytropic Index in Space Plasmas. *Entropy*, **21**(10), 997. 82

Norgren, C., Graham, D. B., Khotyaintsev, Yu. V., André, M., Vaivads, A., Hesse, M., Eriksson, E., Lindqvist, P.-A., Lavraud, B., Burch, J., Fuselier, S., Magnes, W., Gershman, D. J., & Russell, C. T. 2018. Electron Reconnection in the Magnetopause Current Layer. *Journal of geophysical research: Space physics*, **123**(11), 9222–9238. 118

Norgren, C., Hesse, M., Tenfjord, P., Graham, D. B., Khotyaintsev, Yu V., Vaivads, A., Steinvall, K., Xu, Y., Gershman, D. J., Lindqvist, P.-A., & Burch, J. L. 2019. Electron acceleration and thermalization at magnetotail separatrices. *arxiv:1908.11138 [physics]*, Aug. arXiv: 1908.11138. 118

Northrop, Theodore G. 1963. Adiabatic charged-particle motion. *Reviews of geophysics*, **1**(3), 283. 107

Parker, E. N. 1957. Newtonian Development of the Dynamical Properties of Ionized Gases of Low Density. *Physical review*, **107**(4), 924–933. 106

Parker, E. N. 2004. Tangential discontinuities in untidy magnetic topologies. *Physics of plasmas*, **11**(5), 2328–2332. 63, 79

Parks, George K. 2018. *Characterizing Space Plasmas: A Data Driven Approach*. Astronomy and Astrophysics Library. Cham: Springer International Publishing. 34

Parnell, C. E., Smith, J. M., Neukirch, T., & Priest, E. R. 1996. The structure of three-dimensional magnetic neutral points. *Physics of plasmas*, **3**(3), 759–770. 90

Paschmann, G., Papamastorakis, I., Baumjohann, W., Sckopke, N., Carlson, C. W., Sonnerup, B. U. Ö., & Lühr, H. 1986. The magnetopause for large magnetic shear: AMPTE/IRM observations. *Journal of geophysical research*, **91**(A10), 11099. 40

Paschmann, G., Sonnerup, B., Papamastorakis, I., Baumjohann, W., Sckopke, N., & Lühr, H. 1990. The magnetopause and boundary layer for small magnetic shear: Convection electric fields and reconnection. *Geophysical research letters*, **17**(11), 1829–1832. 39

Paschmann, G., Haaland, S. E., Phan, T. D., Sonnerup, B. U. Ö., Burch, J. L., Torbert, R. B., Gershman, D. J., Dorelli, J. C., Giles, B. L., Pollock, C., Saito, Y., Lavraud, B., Russell, C. T., Strangeway, R. J., Baumjohann, W., & Fuselier, S. A. 2018. Large-Scale

Survey of the Structure of the Dayside Magnetopause by MMS. *Journal of geophysical research: Space physics*, Mar. 41

Paschmann, Goetz, & Daly, Patrick W. 1998. *Analysis Methods for Multi-Spacecraft Data*. 37, 38, 40, 48, 50, 87

Paschmann, Goetz, & Daly, Patrick W. 2008. *Multi-Spacecraft Analysis Methods Revisited*. 37

Peng, F. Z., Fu, H. S., Cao, J. B., Graham, D. B., Chen, Z. Z., Cao, D., Xu, Y., Huang, S. Y., Wang, T. Y., Khotyaintsev, Y. V., Andre, M., Russell, C. T., Giles, B., Lindqvist, P.-A., Torbert, R. B., Ergun, R. E., & Burch, J. L. 2017. Quadrupolar pattern of the asymmetric guide-field reconnection: Asymmetric Reconnection at Magnetopause. *Journal of geophysical research: Space physics*, **122**(6), 6349–6356. 115

Perri, Silvia, Servidio, Sergio, Vaivads, Andris, & Valentini, Francesco. 2017. Numerical Study on the Validity of the Taylor Hypothesis in Space Plasmas. *The astrophysical journal supplement series*, **231**(1), 4. 37

Petschek, H. E. 1964. Magnetic field annihilation. 97

Peucker, Thomas K., & Douglas, David H. 1975. Detection of Surface-Specific Points by Local Parallel Processing of Discrete Terrain Elevation Data. *Computer graphics and image processing*, **4**(4), 375–387. 45

Peyret, R., & Taylor, T. D. 1983. *Computational Methods for Fluid Flow*. 1 edn. Scientific Computation. Springer-Verlag, Berlin Heidelberg. 44

Pezzi, Oreste, Cozzani, Giulia, Califano, Francesco, Valentini, Francesco, Guarrasi, Massimiliano, Camporeale, Enrico, Brunetti, Gianfranco, Retinò, Alessandro, & Veltri, Pierluigi. 2019. ViDA: a Vlasov-DArwin solver for plasma physics at electron scales. *Journal of plasma physics*, **85**(5), 905850506. arXiv: 1905.02953. 22

Phan, T. D., Shay, M. A., Gosling, J. T., Fujimoto, M., Drake, J. F., Paschmann, G., Oieroset, M., Eastwood, J. P., & Angelopoulos, V. 2013. Electron bulk heating in magnetic reconnection at Earth's magnetopause: Dependence on the inflow Alfvén speed and magnetic shear: ELECTRON BULK HEATING IN RECONNECTION. *Geophysical research letters*, **40**(17), 4475–4480. 68

Phan, T. D., Drake, J. F., Shay, M. A., Gosling, J. T., Paschmann, G., Eastwood, J. P., Oieroset, M., Fujimoto, M., & Angelopoulos, V. 2014. Ion bulk heating in magnetic reconnection exhausts at Earth's magnetopause: Dependence on the inflow Alfvén speed and magnetic shear angle: ION HEATING IN RECONNECTION. *Geophysical research letters*, **41**(20), 7002–7010. 68

Phan, T. D., Shay, M. A., Haggerty, C. C., Gosling, J. T., Eastwood, J. P., Fujimoto, M., Malakit, K., Mozer, F. S., Cassak, P. A., Oieroset, M., & Angelopoulos, V. 2016. Ion Larmor radius effects near a reconnection X line at the magnetopause: THEMIS observations and simulation comparison: ION LARMOR RADIUS EFFECTS NEAR X LINE. *Geophysical research letters*, **43**(17), 8844–8852. 115

Pollock, C., Moore, T., Jacques, A., Burch, J., Gliese, U., Saito, Y., Omoto, T., Avanov, L., Barrie, A., Coffey, V., Dorelli, J., Gershman, D., Giles, B., Rosnack, T., Salo, C., Yokota, S., Adrian, M., Aoustin, C., Auletti, C., Aung, S., Bigio, V., Cao, N., Chandler, M., Chornay, D., Christian, K., Clark, G., Collinson, G., Corris, T., De Los Santos, A., Devlin, R., Diaz, T., Dickerson, T., Dickson, C., Diekmann, A., Diggs, F., Duncan, C., Figueroa-Vinas, A., Firman, C., Freeman, M., Galassi, N., Garcia, K., Goodhart, G., Guererro, D., Hageman, J., Hanley, J., Hemminger, E., Holland, M., Hutchins,

M., James, T., Jones, W., Kreisler, S., Kujawski, J., Lavu, V., Lobell, J., LeCompte, E., Lukemire, A., MacDonald, E., Mariano, A., Mukai, T., Narayanan, K., Nguyan, Q., Onizuka, M., Paterson, W., Persyn, S., Piepgrass, B., Cheney, F., Rager, A., Raghuram, T., Ramil, A., Reichenthal, L., Rodriguez, H., Rouzaud, J., Rucker, A., Saito, Y., Samara, M., Sauvaud, J.-A., Schuster, D., Shappirio, M., Shelton, K., Sher, D., Smith, D., Smith, K., Smith, S., Steinfeld, D., Szymkiewicz, R., Tanimoto, K., Taylor, J., Tucker, C., Tull, K., Uhl, A., Vloet, J., Walpole, P., Weidner, S., White, D., Winkert, G., Yeh, P.-S., & Zeuch, M. 2016. Fast Plasma Investigation for Magnetospheric Multiscale. *Space science reviews*, **199**(1-4), 331–406. 34

Pontin, D. I., & Craig, I. J. D. 2005. Current singularities at finitely compressible three-dimensional magnetic null points. *Physics of plasmas*, **12**(7), 072112. 103

Pontin, D.I. 2011. Three-dimensional magnetic reconnection regimes: A review. *Advances in space research*, **47**(9), 1508–1522. 101, 103

Pontin, D.I., Hornig, G., & Priest, E.R. 2004. Kinematic reconnection at a magnetic null point: spine-aligned current. *Geophysical & astrophysical fluid dynamics*, **98**(5), 407–428. 102

Pontin, D.I., Hornig, G., & Priest, E.R. 2005. Kinematic reconnection at a magnetic null point: fan-aligned current. *Geophysical & astrophysical fluid dynamics*, **99**(1), 77–93. 102

Price, L., Swisdak, M., Drake, J. F., Cassak, P. A., Dahlin, J. T., & Ergun, R. E. 2016. The effects of turbulence on three-dimensional magnetic reconnection at the magnetopause: TURBULENCE DURING 3D RECONNECTION. *Geophysical research letters*, **43**(12), 6020–6027. 115

Price, L., Swisdak, M., Drake, J. F., Burch, J. L., Cassak, P. A., & Ergun, R. E. 2017. Turbulence in Three-Dimensional Simulations of Magnetopause Reconnection: TURBULENCE DURING 3-D RECONNECTION. *Journal of geophysical research: Space physics*, **122**(11), 11,086–11,099. 115

Price, L., Swisdak, M., Drake, J. F., & Graham, D. B. 2020. Turbulence and Transport During Guide Field Reconnection at the Magnetopause. *Journal of geophysical research: Space physics*, **125**(4). 115

Priest, E. R., & Démoulin, P. 1995. Three-dimensional magnetic reconnection without null points: 1. Basic theory of magnetic flipping. *Journal of geophysical research*, **100**(A12), 23443. 95

Priest, E. R., & Forbes, Terry. 2000. *Magnetic reconnection: MHD theory and applications*. Cambridge ; New York: Cambridge University Press. 14, 90

Priest, E. R., Hornig, G., & Pontin, D. I. 2003. On the nature of three-dimensional magnetic reconnection. *Journal of geophysical research*, **108**(A7), 1285. 100

Priest, E. R., Longcope, D. W., & Janvier, M. 2016. Evolution of Magnetic Helicity During Eruptive Flares and Coronal Mass Ejections. *Solar physics*, **291**(7), 2017–2036. 29

Priest, Eric. 2017. Our dynamic sun: 2017 Hannes Alfvén Medal lecture at the EGU. *Annales geophysicae*, **35**(4), 805–816. 14

Pucci, F., Usami, S., Ji, H., Guo, X., Horiuchi, R., Okamura, S., Fox, W., Jara-Almonte, J., Yamada, M., & Yoo, J. 2018. Energy transfer and electron energization in collisionless magnetic reconnection for different guide-field intensities. *Physics of plasmas*, **25**(12), 122111. 66, 74

Pucci, Fulvia, & Velli, Marco. 2013. RECONNECTION OF QUASI-SINGULAR CUR-

RENT SHEETS: THE "IDEAL" TEARING MODE. *The astrophysical journal*, **780**(2), L19. 28

Pucci, Fulvia, Velli, Marco, & Tenerani, Anna. 2017. Fast Magnetic Reconnection: "Ideal" Tearing and the Hall Effect. *The astrophysical journal*, **845**(1), 25. 28

Pudovkin, Mikhail I., Meister, Claudia-Veronika, Besser, Bruno P., & Biernat, Helfried K. 1997. The effective polytropic index in a magnetized plasma. *Journal of geophysical research: Space physics*, **102**(A12), 27145–27149. 69

Rana, S. 2004. *Topological Data Structures.pdf*. 45

Rappazzo, A. F. 2015. EQUILIBRIA, DYNAMICS, AND CURRENT SHEET FORMATION IN MAGNETICALLY CONFINED CORONAE. *The astrophysical journal*, **815**(1), 8. 82

Rappazzo, A. F., & Parker, E. N. 2013. CURRENT SHEETS FORMATION IN TANGLED CORONAL MAGNETIC FIELDS. *The astrophysical journal*, **773**(1), L2. 82

Rezeau, L., Belmont, G., Manuzzo, R., Aunai, N., & Dargent, J. 2018. Analyzing the Magnetopause Internal Structure: New Possibilities Offered by MMS Tested in a Case Study: ANALYSE OF THE MAGNETOPAUSE INTERNAL STRUCTURE WITH MMS. *Journal of geophysical research: Space physics*, **123**(1), 227–241. 39, 47

Ricca, Renzo L. (ed). 2001. *An Introduction to the Geometry and Topology of Fluid Flows*. Dordrecht: Springer Netherlands. 88

Ricci, Paolo, Brackbill, J. U., Daughton, W., & Lapenta, Giovanni. 2004. Collisionless magnetic reconnection in the presence of a guide field. *Physics of plasmas*, **11**(8), 4102–4114. 97

Rogers, B. N. 2003. Signatures of collisionless magnetic reconnection. *Journal of geophysical research*, **108**(A3), 1111. 114

Rong, Z. J., Wan, W. X., Shen, C., Zhang, T. L., Lui, A. T. Y., Wang, Yuming, Dunlop, M. W., Zhang, Y. C., & Zong, Q.-G. 2013. Method for inferring the axis orientation of cylindrical magnetic flux rope based on single-point measurement: ORIENTATION OF FLUX ROPES. *Journal of geophysical research: Space physics*, **118**(1), 271–283. 39

Sauppe, J. P., & Daughton, W. 2018. Kinetic-scale flux rope reconnection in periodic and line-tied geometries. *Physics of plasmas*, **25**(1), 012901. 103

Sawyer, R. P., Fuselier, S. A., Mukherjee, J., & Petrinec, S. M. 2019. An Investigation of Flow Shear and Diamagnetic Drift Effects on Magnetic Reconnection at Saturn's Dawnside Magnetopause. *Journal of geophysical research: Space physics*, **124**(11), 8457–8473. 98

Schindler, K., Hesse, M., & Birn, J. 1988. General magnetic reconnection, parallel electric fields, and helicity. *Journal of geophysical research*, **93**(A6), 5547. 26, 94, 95

Scholer, M., Ipavich, F. M., Gloeckler, G., Hovestadt, D., & Klecker, B. 1981. Leakage of magnetospheric ions into the magnetosheath along reconnected field lines at the dayside magnetopause. *Journal of geophysical research*, **86**(A3), 1299. 40

Scudder, J. D., Karimabadi, H., Daughton, W., & Roytershteyn, V. 2015. Frozen flux violation, electron demagnetization and magnetic reconnection. *Physics of plasmas*, **22**(10), 101204. 96

Sergeev, V.A., Sazhina, E.M., Tsyganenko, N.A., Lundblad, J.Å., & Søraas, F. 1983. Pitch-angle scattering of energetic protons in the magnetotail current sheet as the dominant source of their isotropic precipitation into the nightside ionosphere. *Planetary and space science*, **31**(10), 1147–1155. 117, 118

Servidio, S., Matthaeus, W. H., Shay, M. A., Cassak, P. A., & Dmitruk, P. 2009. Magnetic Reconnection in Two-Dimensional Magnetohydrodynamic Turbulence. *Physical review letters*, **102**(11), 115003. 45

Servidio, S., Matthaeus, W. H., Shay, M. A., Dmitruk, P., Cassak, P. A., & Wan, M. 2010. Statistics of magnetic reconnection in two-dimensional magnetohydrodynamic turbulence. *Physics of plasmas*, **17**(3), 032315. 45

Servidio, S., Valentini, F., Perrone, D., Greco, A., Califano, F., Matthaeus, W. H., & Veltri, P. 2015. A kinetic model of plasma turbulence. *Journal of plasma physics*, **81**(1), 325810107. 41, 44, 83

Sharma Pyakurel, P., Shay, M. A., Phan, T. D., Matthaeus, W. H., Drake, J. F., TenBarge, J. M., Haggerty, C. C., Klein, K. G., Cassak, P. A., Parashar, T. N., Swisdak, M., & Chasapis, A. 2019. Transition from ion-coupled to electron-only reconnection: Basic physics and implications for plasma turbulence. *Physics of plasmas*, **26**(8), 082307. 73

Shay, M. A., Haggerty, C. C., Phan, T. D., Drake, J. F., Cassak, P. A., Wu, P., Oieroset, M., Swisdak, M., & Malakit, K. 2014. Electron heating during magnetic reconnection: A simulation scaling study. *Physics of plasmas*, **21**(12), 122902. 66, 68

Shen, C., Li, X., Dunlop, M., Liu, Z. X., Balogh, A., Baker, D. N., Hapgood, M., & Wang, X. 2003. Analyses on the geometrical structure of magnetic field in the current sheet based on cluster measurements: GEOMETRICAL STRUCTURE OF TAIL MAGNETIC FIELD. *Journal of geophysical research: Space physics*, **108**(A5). 39, 47

Shen, C., Li, X., Dunlop, M., Shi, Q. Q., Liu, Z. X., Lucek, E., & Chen, Z. Q. 2007a. Magnetic field rotation analysis and the applications: MAGNETIC FIELD ROTATION ANALYSIS. *Journal of geophysical research: Space physics*, **112**(A6), n/a–n/a. 39, 46, 47, 79

Shen, C., Dunlop, M., Li, X., Liu, Z. X., Balogh, A., Zhang, T. L., Carr, C. M., Shi, Q. Q., & Chen, Z. Q. 2007b. New approach for determining the normal of the bow shock based on Cluster four-point magnetic field measurements: NORMAL OF EARTH'S BOW SHOCK. *Journal of geophysical research: Space physics*, **112**(A3), n/a–n/a. 40

Shen, C., Yang, Y. Y., Rong, Z. J., Li, X., Dunlop, M., Carr, C. M., Liu, Z. X., Baker, D. N., Chen, Z. Q., Ji, Y., & Zeng, G. 2014. Direct calculation of the ring current distribution and magnetic structure seen by Cluster during geomagnetic storms: DISTORTIONS BY RING CURRENTS. *Journal of geophysical research: Space physics*, **119**(4), 2458–2465. 117

Shi, Q. Q., Shen, C., Pu, Z. Y., Dunlop, M. W., Zong, Q.-G., Zhang, H., Xiao, C. J., Liu, Z. X., & Balogh, A. 2005. Dimensional analysis of observed structures using multipoint magnetic field measurements: Application to Cluster: STRUCTURE DIMENSIONALITY DETERMINATION. *Geophysical research letters*, **32**(12), n/a–n/a. 39, 46, 79

Shi, Q. Q., Shen, C., Dunlop, M. W., Pu, Z. Y., Zong, Q.-G., Liu, Z. X., Lucek, E., & Balogh, A. 2006. Motion of observed structures calculated from multi-point magnetic field measurements: Application to Cluster. *Geophysical research letters*, **33**(8), L08109. 87, 93

Shi, Q. Q., Tian, A. M., Bai, S. C., Hasegawa, H., Degeling, A. W., Pu, Z. Y., Dunlop, M., Guo, R. L., Yao, S. T., Zong, Q.-G., Wei, Y., Zhou, X.-Z., Fu, S. Y., & Liu, Z. Q. 2019. Dimensionality, Coordinate System and Reference Frame for Analysis of In-Situ Space Plasma and Field Data. *Space science reviews*, **215**(4), 35. 39, 51

Shuster, J. R., Argall, M. R., Torbert, R. B., Chen, L.-J., Farrugia, C. J., Alm, L., Wang, S., Daughton, W., Gershman, D. J., Giles, B. L., Russell, C. T., Burch, J. L., & Pollock, C. J. 2017. Hodographic approach for determining spacecraft trajectories through magnetic reconnection diffusion regions: HODOGRAPHIC TRAJECTORY ALGORITHM. *Geophysical research letters*, **44**(4), 1625–1633. 41

Siscoe, George. 2011. Aspects of global coherence of magnetospheric behavior. *Journal of atmospheric and solar-terrestrial physics*, **73**(4), 402–419. 12

Song, P., Singer, Howard J., & Siscoe, George L. (eds). 2001. *Space weather*. Geophysical monograph, no. 125. Washington, DC: American Geophysical Union. 16

Sonnerup, B. U. Ö. 2004. Orientation and motion of a discontinuity from single-spacecraft measurements of plasma velocity and density: Minimum mass flux residue. *Journal of geophysical research*, **109**(A3), A03221. 40

Sonnerup, B. U. Ö, & Cahill, L. J. 1967. Magnetopause structure and attitude from Explorer 12 observations. *Journal of geophysical research*, **72**(1), 171. 39

Sonnerup, B. U. Ö, Papamastorakis, I., Paschmann, G., & Lühr, H. 1987. Magnetopause properties from AMPTE/IRM observations of the convection electric field: Method development. *Journal of geophysical research*, **92**(A11), 12137. 40

Stawarz, J. E., Eastwood, J. P., Genestreti, K. J., Nakamura, R., Ergun, R. E., Burgess, D., Burch, J. L., Fuselier, S. A., Gershman, D. J., Giles, B. L., Le Contel, O., Lindqvist, P.-A., Russell, C. T., & Torbert, R. B. 2018. Intense Electric Fields and Electron-Scale Substructure Within Magnetotail Flux Ropes as Revealed by the Magnetospheric Multiscale Mission. *Geophysical research letters*, **45**(17), 8783–8792. 30

Stephenson, F. Richard, Willis, David M., Hayakawa, Hisashi, Ebihara, Yusuke, Scott, Christopher J., Wilkinson, Julia, & Wild, Matthew N. 2019. Do the Chinese Astronomical Records Dated AD 776 January 12/13 Describe an Auroral Display or a Lunar Halo? A Critical Re-examination. *Solar physics*, **294**(4), 36. 15

Sulem, P. L., & Passot, T. 2015. Landau fluid closures with nonlinear large-scale finite Larmor radius corrections for collisionless plasmas. *Journal of plasma physics*, **81**(1), 325810103. 20, 42

Sun, T. R., Tang, B. B., Wang, C., Guo, X. C., & Wang, Y. 2019a. Large-Scale Characteristics of Flux Transfer Events on the Dayside Magnetopause. *Journal of geophysical research: Space physics*, Apr., 2018JA026395. 30

Sun, W. J., Slavin, J. A., Tian, A. M., Bai, S. C., Poh, G. K., Akhavan-Tafti, M., Lu, San, Yao, S. T., Le, G., Nakamura, R., Giles, B. L., & Burch, J. L. 2019b. MMS Study of the Structure of Ion-Scale Flux Ropes in the Earth's Cross-Tail Current Sheet. *Geophysical research letters*, **46**(12), 6168–6177. 30

Swisdak, M., Rogers, B. N., Drake, J. F., & Shay, M. A. 2003. Diamagnetic suppression of component magnetic reconnection at the magnetopause: DIAMAGNETIC SUPPRESSION OF RECONNECTION. *Journal of geophysical research: Space physics*, **108**(A5). 95, 98

Swisdak, M., Drake, J. F., Price, L., Burch, J. L., Cassak, P. A., & Phan, T.-D. 2018. Localized and Intense Energy Conversion in the Diffusion Region of Asymmetric Magnetic Reconnection. *Geophysical research letters*, **45**(11), 5260–5267. 74, 118

Tanaka, T., Watanabe, M., Den, M., Fujita, S., Ebihara, Y., Kikuchi, T., Hashimoto, K. K., & Kataoka, R. 2016. Generation of field-aligned current (FAC) and convection through the formation of pressure regimes: Correction for the concept of Dungey's

convection. *Journal of geophysical research: Space physics*, **121**(9), 8695–8711. 13
Taylor, G I. 1938. The Spectrum of Turbulence. 16. 37
Taylor, J. B. 2000. Relaxation revisited. *Physics of plasmas*, **7**(5), 1623–1629. 62
Tenerani, Anna, Rappazzo, Antonio Franco, Velli, Marco, & Pucci, Fulvia. 2015. THE TEARING MODE INSTABILITY OF THIN CURRENT SHEETS: THE TRANSITION TO FAST RECONNECTION IN THE PRESENCE OF VISCOSITY. *The astrophysical journal*, **801**(2), 145. 28
Threlfall, J., Hood, A. W., & Priest, E. R. 2018. Flux Rope Formation Due to Shearing and Zipper Reconnection. *Solar physics*, **293**(6), 98. 29
Titov, V. S., Forbes, T. G., Priest, E. R., Mikić, Z., & Linker, J. A. 2009. SLIP-SQUASHING FACTORS AS A MEASURE OF THREE-DIMENSIONAL MAGNETIC RECONNECTION. *The astrophysical journal*, **693**(1), 1029–1044. 100
Titov, Vyacheslav S., Hornig, Gunnar, & Démoulin, Pascal. 2002. Theory of magnetic connectivity in the solar corona: THE THEORY OF MAGNETIC CONNECTIVITY. *Journal of geophysical research: Space physics*, **107**(A8), SSH 3–1–SSH 3–13. 90
Toledo-Redondo, S., Lavraud, B., Fuselier, S. A., André, M., Khotyaintsev, Yu. V., Nakamura, R., Escoubet, C. P., Li, W. Y., Torkar, K., Cipriani, F., Barrie, A. C., Giles, B., Moore, T. E., Gershman, D., Lindqvist, P.-A., Ergun, R. E., Russell, C. T., & Burch, J. L. 2019. Electrostatic Spacecraft Potential Structure and Wake Formation Effects for Characterization of Cold Ion Beams in the Earth's Magnetosphere. *Journal of geophysical research: Space physics*, **124**(12), 10048–10062. 34
Tonks, Lewi. 1967. The Birth of "Plasma". *American journal of physics*, **35**(9), 857–858. 10
Torbert, R. B., Russell, C. T., Magnes, W., Ergun, R. E., Lindqvist, P.-A., LeContel, O., Vaith, H., Macri, J., Myers, S., Rau, D., Needell, J., King, B., Granoff, M., Chutter, M., Dors, I., Olsson, G., Khotyaintsev, Y. V., Eriksson, A., Kletzing, C. A., Bounds, S., Anderson, B., Baumjohann, W., Steller, M., Bromund, K., Le, Guan, Nakamura, R., Strangeway, R. J., Leinweber, H. K., Tucker, S., Westfall, J., Fischer, D., Plaschke, F., Porter, J., & Lappalainen, K. 2016. The FIELDS Instrument Suite on MMS: Scientific Objectives, Measurements, and Data Products. *Space science reviews*, **199**(1-4), 105–135. 35
Tsurutani, B. T. 2003. The extreme magnetic storm of 1–2 September 1859. *Journal of geophysical research*, **108**(A7), 1268. 15
Uzdensky, Dmitri A., & Kulsrud, Russell M. 2006. Physical origin of the quadrupole out-of-plane magnetic field in Hall-magnetohydrodynamic reconnection. *Physics of plasmas*, **13**(6), 062305. 114
Vaivads, Andris, Retinò, Alessandro, & André, Mats. 2009. Magnetic reconnection in space plasma. *Plasma physics and controlled fusion*, **51**(12), 124016. 17
Valentini, F., Trávníček, P., Califano, F., Hellinger, P., & Mangeney, A. 2007. A hybrid-Vlasov model based on the current advance method for the simulation of collisionless magnetized plasma. *Journal of computational physics*, **225**(1), 753–770. 41, 71
Vasyliunas, Vytenis M. 1975. Theoretical models of magnetic field line merging. *Reviews of geophysics*, **13**(1), 303. 26
Vernisse, Y., Lavraud, B., Faganello, M., Fadanelli, S., Sisti, M., Califano, F., Eriksson, S., Gershman, D. J., Dorelli, J., Pollock, C., Giles, B., Avanov, L., Burch, J., Dargent, J., Ergun, R. E., Farrugia, C. J., Génot, V., Hasegawa, H., Jacquey, C., Kacem, I.,

Kieokaew, R., Kuznetsova, M., Moore, T., Nakamura, T., Paterson, W., Penou, E., Phan, T. D., Russell, C. T., Saito, Y., Sauvaud, J.-A., & Toledo-Redondo, S. 2020. Latitudinal Dependence of the Kelvin-Helmholtz Instability and Beta Dependence of Vortex-Induced High-Guide Field Magnetic Reconnection. *Journal of geophysical research: Space physics*, **125**(5). 98

Vinogradov, A. A., Vasko, I. Y., Artemyev, A. V., Yushkov, E. V., Petrukovich, A. A., & Zelenyi, L. M. 2016. Kinetic models of magnetic flux ropes observed in the Earth magnetosphere. *Physics of plasmas*, **23**(7), 072901. 29

Wan, M., Matthaeus, W.H., Roytershteyn, V., Karimabadi, H., Parashar, T., Wu, P., & Shay, M. 2015. Intermittent Dissipation and Heating in 3D Kinetic Plasma Turbulence. *Physical review letters*, **114**(17), 175002. 83

Wang, Shan, Chen, Li-Jen, Bessho, Naoki, Kistler, Lynn M., Shuster, Jason R., & Guo, Ruilong. 2016. Electron heating in the exhaust of magnetic reconnection with negligible guide field: Electron Heating in Reconnection. *Journal of geophysical research: Space physics*, **121**(3), 2104–2130. 70, 117

Wang, Shan, Chen, Li-Jen, Bessho, Naoki, Hesse, Michael, Yoo, Jongsoo, Yamada, Masaaki, Liu, Yi-Hsin, Gershman, Danial J., Giles, Barbara L., & Moore, Thomas E. 2018. Energy Conversion and Partition in the Asymmetric Reconnection Diffusion Region. *Journal of geophysical research: Space physics*, **123**(10), 8185–8205. 66, 68

Wang, Z., Fu, H. S., Liu, C. M., Liu, Y. Y., Cozzani, G., Giles, B. L., Hwang, K.-J., & Burch, J. L. 2019. Electron Distribution Functions Around a Reconnection X-Line Resolved by the FOTE Method. *Geophysical research letters*, **46**(3), 1195–1204. 118

Wasserman, Larry. 2004. *All of Statistics: A Concise Course in Statistical Inference*. Springer Texts in Statistics. New York, NY: Springer New York. 51

Webster, J. M., Burch, J. L., Reiff, P. H., Daou, A. G., Genestreti, K. J., Graham, D. B., Torbert, R. B., Ergun, R. E., Sazykin, S. Y., Marshall, A., Allen, R. C., Chen, L.-J., Wang, S., Phan, T. D., Giles, B. L., Moore, T. E., Fuselier, S. A., Cozzani, G., Russell, C. T., Eriksson, S., Rager, A. C., Broll, J. M., Goodrich, K., & Wilder, F. 2018. Magnetospheric Multiscale Dayside Reconnection Electron Diffusion Region Events. *Journal of geophysical research: Space physics*, **123**(6), 4858–4878. 40

Wendel, Deirdre E., & Reiff, Patricia H. 2009. Magnetopause reconnection impact parameters from multiple spacecraft magnetic field measurements. *Geophysical research letters*, **36**(20), L20108. 41

Wendel, Deirdre E., Liu, Yi-Hsin, Giles, Barbara L., & Torbert, Roy B. 2018. Violation of Field Line Conservation and Associated Spatial Scales in Particle-in-Cell Simulations and MMS Data. *Journal of geophysical research: Space physics*, Mar. 40, 45

Wilder, F. D., Ergun, R. E., Hoilijoki, S., Webster, J., Argall, M. R., Ahmadi, N., Eriksson, S., Burch, J. L., Torbert, R. B., Le Contel, O., Strangeway, R. J., & Giles, B. L. 2019. A Survey of Plasma Waves Appearing Near Dayside Magnetopause Electron Diffusion Region Events. *Journal of geophysical research: Space physics*, **124**(10), 7837–7849. 115

Wu, P., Fritz, T. A., Larvaud, B., & Lucek, E. 2006. Substorm associated magnetotail energetic electrons pitch angle evolutions and flow reversals: Cluster observation. *Geophysical research letters*, **33**(17), L17101. 108, 113

Wyper, P. F., & Hesse, M. 2015. Quantifying three dimensional reconnection in fragmented current layers. *Physics of plasmas*, **22**(4), 042117. 102

Wyper, P. F., & Jain, Rekha. 2013. Reconnection at three dimensional magnetic null

points: Effect of current sheet asymmetry. *Physics of plasmas*, **20**(5), 052901. 102

Yang, Yan, Matthaeus, William H., Parashar, Tulasi N., Haggerty, Colby C., Roytershteyn, Vadim, Daughton, William, Wan, Minping, Shi, Yipeng, & Chen, Shiyi. 2017. Energy transfer, pressure tensor, and heating of kinetic plasma. *Physics of plasmas*, **24**(7), 072306. 64, 66, 68, 69

Yeates, A. R., & Hornig, G. 2013. Unique topological characterization of braided magnetic fields. *Physics of plasmas*, **20**(1), 012102. 89

Yeates, A R, & Hornig, G. 2014. A complete topological invariant for braided magnetic fields. *Journal of physics: Conference series*, **544**(Oct.), 012002. 89

Young, D. T., Burch, J. L., Gomez, R. G., De Los Santos, A., Miller, G. P., Wilson, P., Paschalidis, N., Fuselier, S. A., Pickens, K., Hertzberg, E., Pollock, C. J., Scherrer, J., Wood, P. B., Donald, E. T., Aaron, D., Furman, J., George, D., Gurnee, R. S., Hourani, R. S., Jacques, A., Johnson, T., Orr, T., Pan, K. S., Persyn, S., Pope, S., Roberts, J., Stokes, M. R., Trattner, K. J., & Webster, J. M. 2016. Hot Plasma Composition Analyzer for the Magnetospheric Multiscale Mission. *Space science reviews*, **199**(1-4), 407–470. 34

Zenitani, Seiji, & Nagai, Tsugunobu. 2016. Particle dynamics in the electron current layer in collisionless magnetic reconnection. *Physics of plasmas*, **23**(10), 102102. 118

Zenitani, Seiji, Hesse, Michael, Klimas, Alex, & Kuznetsova, Masha. 2011. New Measure of the Dissipation Region in Collisionless Magnetic Reconnection. *Physical review letters*, **106**(19), 195003. 65

Zenitani, Seiji, Hasegawa, Hiroshi, & Nagai, Tsugunobu. 2017. Electron dynamics surrounding the X line in asymmetric magnetic reconnection. *Journal of geophysical research: Space physics*, **122**(7), 7396–7413. 118

Zhang, Lei, He, Jiansen, Tu, Chuanyi, Yang, Liping, Wang, Xin, Marsch, Eckart, & Wang, Linghua. 2015. OCCURRENCE RATES AND HEATING EFFECTS OF TANGENTIAL AND ROTATIONAL DISCONTINUITIES AS OBTAINED FROM THREE-DIMENSIONAL SIMULATION OF MAGNETOHYDRODYNAMIC TURBULENCE. *The astrophysical journal*, **804**(2), L43. 82

Zhang, Y. C., Shen, C., Marchaudon, A., Rong, Z. J., Lavraud, B., Fazakerley, A., Yao, Z., Mihaljcic, B., Ji, Y., Ma, Y. H., & Liu, Z. X. 2016. First in situ evidence of electron pitch angle scattering due to magnetic field line curvature in the Ion diffusion region: Pitch Angle Scattering. *Journal of geophysical research: Space physics*, **121**(5), 4103–4110. 118

Zhang, Y. C., Lavraud, B., Dai, L., Wang, C., Marchaudon, A., Avanov, L., Burch, J., Chandler, M., Dorelli, J., Duan, S. P., Ergun, R. E., Gershman, D. J., Giles, B., Khotyaintsev, Y. V., Lindqvist, P. A., Paterson, W., Russell, C. T., Schiff, C., Tang, B. B., & Torbert, R. 2017. Quantitative analysis of a Hall system in the exhaust of asymmetric magnetic reconnection: Hall System in Asymmetric Exhaust. *Journal of geophysical research: Space physics*, **122**(5), 5277–5289. 115

Zhou, M., Ashour-Abdalla, M., Berchem, J., Walker, R. J., Liang, H., El-Alaoui, M., Goldstein, M. L., Lindqvist, P.-A., Marklund, G., Khotyaintsev, Y. V., Ergun, R. E., Wilder, F. D., Russell, C. T., Strangeway, R. J., Zhao, C., Paterson, W. R., Giles, B. L., Pollock, C. J., Torbert, R. B., Burch, J. L., Dorelli, J. C., Gershman, D. J., Avanov, L. A., Lavraud, B., & Chandler, M. O. 2016. Observation of high-frequency electrostatic waves in the vicinity of the reconnection ion diffusion region by the spacecraft of

the Magnetospheric Multiscale (MMS) mission. *Geophysical research letters*, **43**(10), 4808–4815. 115

Zhou, M., Berchem, J., Walker, R. J., El-Alaoui, M., Goldstein, M. L., Lapenta, G., Deng, X., Li, J., Le Contel, O., Graham, D. B., Lavraud, B., Paterson, W. R., Giles, B. L., Burch, J. L., Torbert, R. B., Russell, C. T., Strangeway, R. J., Zhao, C., Ergun, R. E., Lindqvist, P.-A., & Marklund, G. 2018a. Magnetospheric Multiscale Observations of an Ion Diffusion Region With Large Guide Field at the Magnetopause: Current System, Electron Heating, and Plasma Waves. *Journal of geophysical research: Space physics*, Mar. 57

Zhou, Meng, Li, Huimin, Deng, Xiaohua, Huang, Shiyong, Pang, Ye, Yuan, Zhigang, Xu, Xiaojun, & Tang, Rongxin. 2014. Characteristic distribution and possible roles of waves around the lower hybrid frequency in the magnetotail reconnection region: LHW IN RECONNECTION. *Journal of geophysical research: Space physics*, **119**(10), 8228–8242. 115

Zhou, Meng, El-Alaoui, Mostafa, Lapenta, Giovanni, Berchem, Jean, Richard, Robert L., Schriver, David, & Walker, Raymond J. 2018b. Suprathermal Electron Acceleration in a Reconnecting Magnetotail: Large-Scale Kinetic Simulation. *Journal of geophysical research: Space physics*, **123**(10), 8087–8108. 118

Zhou, X., Büchner, J., Widmer, F., & Muñoz, P. A. 2018c. Electron acceleration by turbulent plasmoid reconnection. *Physics of plasmas*, **25**(4), 042904. 118

Zweibel, Ellen G., & Yamada, Masaaki. 2009. Magnetic Reconnection in Astrophysical and Laboratory Plasmas. *Annual review of astronomy and astrophysics*, **47**(1), 291–332. 97

Zweibel, Ellen G., & Yamada, Masaaki. 2016. Perspectives on magnetic reconnection. *Proceedings of the royal society a: Mathematical, physical and engineering sciences*, **472**(2196), 20160479. 17

First of all, the breath grew feebler; then it missed its regularity of return; then it wholly intermitted, and the upper lip was slightly convulsed; after this there followed one feeble respiration or sigh; and after that no more; but the pulse still beat for a few seconds - slower and fainter, till it ceased altogether; the mechanism stopped; the last motion was at an end; and exactly at that moment the clock struck eleven.

T. P. D. Q.